

# **An Evaluation of g-C<sub>3</sub>N<sub>4</sub> and BiVO<sub>4</sub> for Photocatalytic Water Treatment and Disinfection**

**Amit Kumar Singhal**

**B.Tech, M.Tech (Nanotechnology)**

**Faculty of Computing, Engineering, and the Built Environment**



**Thesis submitted for the degree of Doctor of Philosophy**

**November 2021**

*I confirm that the word count of this thesis is less than 100,000 words*

## Table of Contents

<b>Table of Contents .....</b>	<b>i</b>
<b>Acknowledgements .....</b>	<b>vii</b>
<b>Note on Access to Contents.....</b>	<b>viii</b>
<b>Publications and Presentations .....</b>	<b>ix</b>
<b>List of Abbreviations .....</b>	<b>xi</b>
<b>List of Figures.....</b>	<b>xii</b>
<b>List of Tables .....</b>	<b>xviii</b>
<b>Abstract .....</b>	<b>xx</b>
<b>Chapter 1. Introduction.....</b>	<b>1</b>
<b>1.1 Background.....</b>	<b>1</b>
<b>1.2 Semiconductor photocatalysis.....</b>	<b>2</b>
1.2.1 Basic principle of photocatalysis .....	2
1.2.2 Photocatalyst and its prerequisites for photocatalysis.....	4
1.2.3 Photocatalytic organic degradation .....	6
1.2.4 Photocatalytic microbial disinfection.....	7
<b>1.3 Aim and objectives .....</b>	<b>8</b>
1.3.1 Aim.....	8
1.3.2 Objectives.....	8
<b>1.4 Thesis structure .....</b>	<b>9</b>
<b>1.5 References .....</b>	<b>11</b>
<b>Chapter 2. Literature review .....</b>	<b>15</b>
<b>2.1 Introduction .....</b>	<b>15</b>
<b>2.2 Graphitic carbon nitride (g-C<sub>3</sub>N<sub>4</sub>) .....</b>	<b>16</b>
2.2.1 Carbon nitride from the beginning.....	16
2.2.2 Crystal structure and different phases of C <sub>3</sub> N <sub>4</sub> and stability .....	17
2.2.3 Surface physicochemical properties.....	21
2.2.4 Design and performance of g-C <sub>3</sub> N <sub>4</sub> -based photocatalyst for water remediation .....	25

2.2.4.1 Unitary structure - effect of precursors and exfoliation methods .....	26
2.2.4.2 g-C <sub>3</sub> N <sub>4</sub> based binary/ternary/multi heterostructures .....	28
<b>2.3 Bismuth vanadate (BiVO<sub>4</sub>) .....</b>	<b>33</b>
2.3.1 Crystal and electronic structure of BiVO <sub>4</sub> .....	33
2.3.2 Synthesis of BiVO <sub>4</sub> .....	35
2.3.2.1 Morphology-controlled synthesis .....	35
2.3.2.2 Facet-controlled synthesis .....	38
2.3.2.3 Formation of heterostructures .....	39
<b>2.4 Other photocatalysts for water remediation.....</b>	<b>40</b>
<b>2.5 Challenges and future perspectives .....</b>	<b>42</b>
<b>2.6 References .....</b>	<b>51</b>
<b>Chapter 3. Materials and methods .....</b>	<b>65</b>
<b>3.1 Materials .....</b>	<b>65</b>
3.1.1 List of chemicals, materials, source, and purity.....	65
<b>3.2 Synthesis methods of photocatalysts .....</b>	<b>67</b>
3.2.1 Thermal polymerization of g-C <sub>3</sub> N <sub>4</sub> .....	67
3.2.2 Thermal exfoliation g-C <sub>3</sub> N <sub>4</sub> .....	68
3.2.3 Hydrothermal synthesis of BiVO <sub>4</sub> .....	69
3.2.4 Nucleation/seed mediated synthesis of BiVO <sub>4</sub> .....	71
<b>3.3 Electrode preparation .....</b>	<b>71</b>
3.3.1 Substrate and its cleaning.....	72
3.3.2 Spray coating on FTO substrates .....	72
3.3.3 Electrical contact on FTO substrates .....	72
<b>3.4 Materials characterization .....</b>	<b>73</b>
3.4.1 X-ray diffraction (XRD) .....	73
3.4.2 Field emission scanning electron microscopy (FESEM).....	74
3.4.3 Fourier transform infrared spectroscopy (FTIR).....	74
3.4.4 Raman spectroscopy .....	74
3.4.5 X-ray and ultraviolet photoelectron spectroscopy (XPS/UPS).....	75
3.4.6 Ultraviolet-visible diffuse reflectance spectroscopy .....	76
3.4.7 BET surface area analysis (BET).....	77
<b>3.5 Photoelectrochemical measurements .....</b>	<b>77</b>

3.5.1 Photoelectrochemical cell .....	77
3.5.2 Photoelectrochemical methods .....	79
3.5.2.1 Linear sweep voltammetry (LSV).....	79
3.5.2.2 Chronoamperometry .....	80
3.5.2.3 Spectral photocurrent response .....	80
3.5.2.4 Open-circuit potential and open circuit photopotential.....	81
3.5.2.5 Electrochemical impedance spectroscopy.....	82
3.5.2.6 Mott-Schottky analysis .....	83
<b>3.6 Photocatalysis experiments .....</b>	<b>83</b>
3.6.1 Experimental setup for photocatalytic testing .....	83
3.6.2 Photocatalytic degradation of organic pollutants .....	85
3.6.3 Phenol analysis by high-performance liquid chromatography (HPLC).....	85
3.6.4 Photocatalytic disinfection.....	86
3.6.5 GInaFiT modelling tool for disinfection kinetics.....	87
<b>3.7 References .....</b>	<b>88</b>

## **Chapter 4. The effect of precursors and synthesis parameters on the physicochemical properties and photocatalytic activity of g-C<sub>3</sub>N<sub>4</sub> ..92**

<b>4.1 Aim and objectives .....</b>	<b>92</b>
4.1.1 Aim.....	92
4.1.2 Objectives.....	92
<b>4.2 Introduction .....</b>	<b>93</b>
<b>4.3 Experimental Section .....</b>	<b>96</b>
4.3.1 Materials .....	96
4.3.2 Synthesis of bulk g-C <sub>3</sub> N <sub>4</sub> .....	96
4.3.3 Thermal exfoliation of g-C <sub>3</sub> N <sub>4</sub> .....	96
4.3.4 Characterizations .....	97
4.3.5 Photocatalysis experiment .....	97
4.3.5.1 Water disinfection .....	97
4.3.5.1.1 Preparation of bacterial culture .....	97
4.3.5.1.2 Inactivation of <i>E. coli</i> .....	98
4.3.5.2 Photocatalytic degradation of phenol .....	98
<b>4.4 Results and discussion .....</b>	<b>99</b>

4.4.1 Physicochemical properties.....	99
4.4.1.1 Effect of synthesis reaction temperature.....	99
4.4.1.2 Effect of reaction time.....	108
4.4.1.3 Effect of precursors.....	114
4.4.1.4 Effect of exfoliation.....	120
4.4.2 Photocatalytic activity.....	130
4.4.2.1 Phenol degradation.....	130
4.4.2.1 Bacterial inactivation.....	132
<b>4.5 The possible photocatalytic mechanism of g-C<sub>3</sub>N<sub>4</sub>.....</b>	<b>139</b>
<b>4.6 Conclusions.....</b>	<b>140</b>
<b>4.7 References.....</b>	<b>142</b>

<b>Chapter 5. Photoelectrochemical properties of exfoliated graphitic carbon nitride (g-C<sub>3</sub>N<sub>4</sub>).....</b>	<b>147</b>
<b>5.1 Aim and objectives.....</b>	<b>147</b>
5.1.1 Aim.....	147
5.1.2 Objectives.....	147
<b>5.2 Introduction.....</b>	<b>148</b>
<b>5.3 Experimental Section.....</b>	<b>150</b>
5.3.1 Synthesis of exfoliated g-C <sub>3</sub> N <sub>4</sub> .....	150
5.3.2 Working electrode preparation.....	150
5.3.3 Analytical characterization.....	151
5.3.4 Photoelectrochemical methods.....	152
<b>5.4 Results and discussion.....</b>	<b>152</b>
5.4.1 Electronic properties.....	152
5.4.1.1 Elemental mapping by EDX.....	153
5.4.1.2 Optical bandgap determination.....	155
5.4.1.3 X-ray photoelectron spectroscopy analysis.....	156
5.4.1.4 Band edge positions and work function determination.....	160
<b>5.4.2 Photoelectrochemical measurements.....</b>	<b>163</b>
5.4.2.1 Linear sweep voltammetry.....	163
5.4.2.2 Chronoamperometry.....	169
5.4.2.3 Spectral photocurrent response.....	170

5.4.2.4 Open-circuit potential ( $E_{ocp}$ ) and open circuit photopotential ( $E_{oph}$ ).....	173
5.4.2.5 Electrochemical impedance spectroscopy.....	174
5.4.2.6 Mott-Schottky analysis .....	177
5.4.3 A proposed energy band diagram .....	178
<b>5.5 Conclusions .....</b>	<b>180</b>
<b>5.6 References .....</b>	<b>181</b>

## **Chapter 6 - Synthesis of BiVO<sub>4</sub> micro/nano structures with different morphologies: characterization and photocatalytic activities ..... 186**

<b>6.1 Aim and objectives .....</b>	<b>186</b>
6.1.1 Aim .....	186
6.1.2 Objectives.....	186
<b>6.2 Introduction .....</b>	<b>187</b>
<b>6.3 Experimental Section .....</b>	<b>188</b>
6.3.1 Materials .....	188
6.3.2 Synthesis of BiVO <sub>4</sub> .....	188
6.3.2.1 Spheres: hydrothermal synthesis.....	189
6.3.2.2 Nanoplates: hydrothermal synthesis .....	189
6.3.2.3 Pyramids/thorns: seed-mediated aqueous growth.....	190
6.3.3 Electrode preparation .....	191
6.3.4 Analytical characterization .....	192
6.3.5 Photoelectrochemical methods .....	192
6.3.6 Photocatalysis experiment .....	193
<b>6.4 Results and discussion .....</b>	<b>193</b>
6.4.1 Morphology and micro/nanostructures .....	193
6.4.2 Structure and composition .....	195
6.4.2.1 X-ray diffraction analysis.....	195
6.4.2.2 Raman spectroscopy .....	197
6.4.2.3 Elemental mapping by EDX .....	198
6.4.3 Optical bandgap determination .....	202
6.4.4 X-ray photoelectron spectroscopy analysis .....	202
6.4.5 Photoelectrochemical measurements .....	214
6.4.5.1 Current-potential measurements (LSV).....	215

6.4.5.2 Current-time measurements at fixed potential .....	219
6.4.6 Photocatalytic activity .....	221
6.4.7 Chemical probe study.....	222
<b>6.5 Conclusions .....</b>	<b>224</b>
<b>6.6 References .....</b>	<b>226</b>
<b>Chapter 7. Conclusions and future work .....</b>	<b>230</b>
<b>7.1 Conclusions .....</b>	<b>230</b>
<b>7.2 Future work and recommendations .....</b>	<b>236</b>
<b>7.3 References .....</b>	<b>238</b>

## Acknowledgement

First of all, bowing down to Almighty God, I would like to express my gratitude to the selection committee for choosing me as a PhD candidate and providing me the opportunity to work at NIBEC, Ulster University. I am very grateful to the Doctoral College for funding me through the Vice Chancellor's Research Scholarship which made this PhD possible.

With sincere gratitude and respect, I acknowledge the Chair of my supervisory team, Prof. Tony Byrne, for his continued encouragement, guidance, and exceptional support, which helped complete my research project in the challenging COVID-19 period. I would like to acknowledge my other supervisors Dr Patrick Dunlop and Dr Pilar Fernandez for their support, advice, and inspiration throughout my research.

I would like to thank; Dr Jeremy Hamilton for his assistance and informative discussions; Dr Preetam Sharma for his initial support and providing SEM, EDX, photoelectrochemical measurement training; Dr Helen Lubarsky for microbiological training as well as Dr Maria Ana Cortes for her assistance in microbiology.

I would also like to acknowledge; Dr Adrian Boyd for giving me training on XRD, FTIR, and Raman; Prof. Davide Mariotti for allowing me to access the UUPS facility as well as Dr Chiranjeevi Maddi for his assistance with XPS measurements and Dr Gourav Bhattacharya for his assistance with photoelectrochemical measurements.

Special thanks to Mrs Ann Blair, Mr Brian McGrath, and Mr Damien McDonald for their administrative and technical support. Additionally, I would like to thank all the staff, fellow PhDs and friends for their help and support provided during this research.

Finally, I would like to dedicate this work to my late grandparents without their blessings I would not have been here. I would like to heartily thank my parents, in-laws, brothers, sisters for their blessings, unconditional love, and moral support. My biggest thanks to my wife Maya Gupta and my stress reliever, son Avyukt Singhal, for being my greatest strength and honest support, who had to endure my stress and moans during the anxious days of PhD.

Thank you all for being with me on this journey.

Amit Kumar Singhal



## **Note on Access to Contents**

“I hereby declare that the with the effect from the date on which the thesis is deposited in the Library of the Ulster University, I permit

1. The Librarian of the University to allow the thesis to be copied in the whole or in part without reference to me on the understanding that such authority applies to the provision of single copies made for study purposes or for the inclusion within the stock of another library.
2. The thesis to be made available through the Ulster Institutional Respiratory and/or EThOS under the terms of the Ulster eThesis Deposit Agreement which I have signed.

IT IS A CONDITION OF USE OF THIS THESIS THAT ANYONE WHO CONSULTS IT MUST RECOGNISE THAT THE COPYRIGHT RESTS WITH THE AUTHOR AND THAT NO QUOTATION FROM THE THESIS AND NO INFORMATION DERIVED FROM IT MAY BE PUBLISHED UNLESS THE SOURCE IS PROPERLY ACKNOWLEDGED.”

Amit Kumar Singhal

November 2021

## Publications and Presentations

### *Book Chapters*

1. **Singhal, A.**, Fernandez-Ibañez, P., and Byrne, J. A. (2021), Photocatalytic and Photoelectrocatalytic treatment of water and wastewater. in ‘Industrial Applications of Nano particles/Nano technologies’ (**under review**)
2. Fernandez-Ibañez, P., Byrne, J. A., Polo López M. I., Singh, A., McMichael, S., **Singhal, A.**, (2020), Photocatalytic inactivation of microorganisms in water (chapter 8). in ‘Nanostructured Photocatalysts: From Materials to Applications in Solar Fuels and Environmental Remediation’, Elsevier, Editors: Rabah Boukherroub, Satishchandra B. Ogale, and Neil Robertson. ISBN: 9780128178362

### *Manuscripts under preparation*

1. **Singhal, A. K.**, Fernandez-Ibañez, P., Dunlop, P. S. M, Byrne, J. A., “A Review on Graphitic Carbon Nitride (g-C<sub>3</sub>N<sub>4</sub>) for Photocatalytic Water Disinfection”
2. **Singhal, A. K.**, Fernandez-Ibañez, P., Dunlop, P. S. M, Byrne, J. A., “The effect of precursors and synthesis parameters on the physicochemical properties and photocatalytic activity of g-C<sub>3</sub>N<sub>4</sub>”
3. **Singhal, A. K.**, Fernandez-Ibañez, P., Dunlop, P. S. M., Byrne, J. A., “Understanding the poor photocatalytic activities of g-C<sub>3</sub>N<sub>4</sub> using photo electrochemistry”
4. **Singhal, A. K.**, Fernandez-Ibañez, P., Dunlop, P. S. M., Byrne, J. A., “Synthesis of BiVO<sub>4</sub> micro/nano structures with different morphologies: characterization and photocatalytic activities”

***Presentations (Chronological order)***

1. **Singhal, A. K.**, Sharma, P. K., Hamilton, J. W. J., Fernandez-Ibañez, P., Dunlop, P. S. M, and Byrne, J. A., “Investigation into Photocatalytic Behaviour of g-C<sub>3</sub>N<sub>4</sub> and BiVO<sub>4</sub> using Photoelectrochemistry” at 11<sup>th</sup> European Conference on Solar Chemistry and Photocatalysis: Environmental Applications (SPEA-11), June 2022, Turin, Italy **(Oral, accepted)**
2. McMichael, S., **Singhal, A.**, Fernandez-Ibanez, P.A., and Byrne, J.A., “An overview of photoactive coatings to prevent the transmission of pathogens” at Royal Society of Chemistry: Materials tackling infectious disease-a networking workshop, November 2021. **(Oral, accepted)**
3. **Singhal, A. K.**, Fernandez-Ibañez, P., Dunlop, P. S. M, Byrne, J. A., “Urea-derived Graphitic Carbon Nitride (u-g-C<sub>3</sub>N<sub>4</sub>) Films for Photocatalytic Water Remediation” at Environ 2021, June 2021. **(Oral)**
4. **Singhal, A. K.**, Fernandez-Ibañez, P., Dunlop, P. S. M, Byrne, J. A., “Transient Photocurrent Response of Exfoliated Graphitic Carbon Nitride (g-C<sub>3</sub>N<sub>4</sub>)”, at *Royal Society of Chemistry, Chemical Nanosciences & Nanotech Early Career Virtual Poster Symposium-2021*, March 2021. **(Poster)**
5. **Singhal, A. K.**, Fernandez-Ibañez, P., Dunlop, P. S. M, Byrne, J. A., “Non-photocatalytic Activity of g-C<sub>3</sub>N<sub>4</sub> for Water Remediation”, at *Czech Society for Applied Photocatalysis–UK & Ireland Semiconductor Photochemistry EURO-NETWORK PHOTOCATALYSIS MEETING-2019*, September 2019, University of Chemistry and Technology Prague, Czech Republic. **(Oral)**
6. **Singhal, A. K.**, Sharma, P. K., Singh, A., Lubarsky, H., Hamilton, J. W. J., Fernandez-Ibañez, P., Dunlop, P. S. M, and Byrne, J. A., “The effect of precursors and reaction parameters on the physicochemical properties and photocatalytic activity of graphitic carbon nitride” *European Materials Research Society Spring Meeting-2019*, May 2019, Nice, France. **(Poster)**

## List of Abbreviations

AM	Air mass
BE	Binding energy
CB	Conduction band
CFU	Colony-forming units
DRS	Diffuse reflectance spectroscopy
EDX	Energy dispersive X-ray analysis
$E_f$	Fermi energy level
$E_{fb}$	Flat band potential
$E_g$	Band gap energy
EIS	Electrochemical impedance spectroscopy
$E_{OCP}$	Open circuit potential
eV	Electron volt
FESEM	Field emission scanning electron microscopy
FRA	Frequency response analyser
FTIR	Fourier transform infrared spectroscopy
FTO	Fluorine doped tin oxide
FWHM	Full width half maximum
IPCE	Incident photon-to-current conversion efficiency
$J_{ph}$	Photocurrent density
LSV	Linear sweep voltammetry
NHE	Normal hydrogen electrode
PC	Photocatalyst
ROS	Reactive oxygen species
SCE	Saturated calomel electrode
$U_{CB}$	Conduction band potential
UPS	Ultraviolet photoelectron spectroscopy
$U_{VB}$	Valence band potential
UV-Vis	Ultraviolet-visible
VB	Valence band
VBXPS	Valence band X-ray photoelectron spectroscopy
XRD	X-ray diffraction
$\nu$	Frequency
$\phi_s$	Work function

## List of Figures

<b>Fig. 1.1.</b> Schematic of a photocatalytic process across semiconductor interface (A - Acceptor, D - Donor) .....	<b>3</b>
<b>Fig. 1.2.</b> Schematic of band gap and band edge energies of various semiconductors.	<b>5</b>
<b>Fig. 2.1.</b> Crystal structure of three g-C <sub>3</sub> N <sub>4</sub> phases (a) g-h-triazine, (b) g-o-triazine, and (c) g-h-heptazine .....	<b>18</b>
<b>Fig. 2.2.</b> The redox potentials of the relevant reactions with respect to the band edge potentials of the g-C <sub>3</sub> N <sub>4</sub> at pH 7.....	<b>24</b>
<b>Fig. 2.3.</b> (a) Photocurrent–time dependence of bulk g-C <sub>3</sub> N <sub>4</sub> and SL g-C <sub>3</sub> N <sub>4</sub> electrodes under visible light irradiation ( $\lambda > 400$ nm), and (b) Photocatalytic disinfection efficiencies under different conditions.....	<b>27</b>
<b>Fig. 2.4.</b> Schematic representation of the band structures of different g-C <sub>3</sub> N <sub>4</sub> based materials .....	<b>29</b>
<b>Fig. 2.5.</b> Type-II (a) and Z-scheme (b) charge transfer models and corresponding proposed surface redox reactions for HT-CN/TiO <sub>2</sub> composite.....	<b>31</b>
<b>Fig. 2.6.</b> Mechanism of photocatalytic disinfection treated with Ag <sub>2</sub> WO <sub>4</sub> /g-C <sub>3</sub> N <sub>4</sub> composite under visible light irradiation .....	<b>32</b>
<b>Fig. 2.7.</b> Schematic representations of antibacterial activity for g-C <sub>3</sub> N <sub>4</sub> -SnO <sub>2</sub> /TiO <sub>2</sub> nanotubes/Ti plate toward <i>E. coli</i> under visible light irradiation.....	<b>32</b>
<b>Fig. 2.8.</b> Crystal structure of BiVO <sub>4</sub> such as monoclinic scheelite (ms, space group: C2/c), tetragonal scheelite (ts, space group: I41/a), and tetragonal zircon (tz, space group: I41/amd) .....	<b>34</b>
<b>Fig. 2.9.</b> Schematic diagram of the microemulsion synthesis of BiVO <sub>4</sub> carried out at pH = 1, 4, 7 and 10.....	<b>36</b>
<b>Fig. 2.10.</b> The effect of different pH values on the crystalline phase and morphology of the as-prepared BiVO <sub>4</sub> .....	<b>37</b>
<b>Fig. 2.11.</b> SEM images of samples of (a) BiVO <sub>4</sub> -a without TiCl <sub>3</sub> and (b) BiVO <sub>4</sub> -d with TiCl <sub>3</sub> , HRTEM images of samples of c) BiVO <sub>4</sub> -a and d) BiVO <sub>4</sub> -d with its SEAD pattern. Schematic illustrations for e) BiVO <sub>4</sub> -a and f) BiVO <sub>4</sub> -d.....	<b>38</b>
<b>Fig. 3.1.</b> The illustration for the layer exfoliation and splitting mechanism of g-C <sub>3</sub> N <sub>4</sub> with the correlation between layer thickness of g-C <sub>3</sub> N <sub>4</sub> and the pyrolysis time .....	<b>68</b>
<b>Fig. 3.2.</b> Hydrothermal Parr reactor (Parr Instruments) used for BiVO <sub>4</sub> synthesis ...	<b>69</b>

<b>Fig. 3.3.</b> Flowchart for the hydrothermal synthesis of (a) BiVO <sub>4</sub> spheres and (b) BiVO <sub>4</sub> nanoplates.....	<b>70</b>
<b>Fig. 3.4.</b> Flowchart for the seed mediated synthesis of BiVO <sub>4</sub> pyramids/thorns.....	<b>71</b>
<b>Fig. 3.5.</b> A schematic representation of photoelectrochemical cell used for PEC measurements.....	<b>78</b>
<b>Fig. 3.6.</b> – Spectral emission of the 450 W Xe lamp (250 – 800 nm) .....	<b>79</b>
<b>Fig. 3.7.</b> – Monochromatic spectral intensity for 450 W Xe lamp from 270-430 nm at 10 nm intervals.....	<b>81</b>
<b>Fig. 3.8.</b> Schematic of stirred tank reactor used for photocatalytic experiments.....	<b>84</b>
<b>Fig. 3.9.</b> Spectral irradiance for the 1 kW Xe lamp for UV-Vis irradiation (250-800 nm) with and without AM 1.5 filter.....	<b>84</b>
<b>Fig. 3.10.</b> Eight types of inactivation curves included in GInaFiT modelling tool ...	<b>87</b>
<b>Fig. 4.1.</b> Possible mechanisms of the reaction pathways of polymeric carbon nitride formation using (a) Cyanamide (b) Urea, and (c) Thiourea, as precursor .....	<b>94</b>
<b>Fig. 4.2.</b> XRD patterns of g-C <sub>3</sub> N <sub>4</sub> samples synthesized at different temperatures using melamine as a precursor.....	<b>100</b>
<b>Fig. 4.3.</b> FTIR spectra of g-C <sub>3</sub> N <sub>4</sub> samples synthesized at different temperatures using melamine as a precursor.....	<b>102</b>
<b>Fig. 4.4.</b> Raman spectra of g-C <sub>3</sub> N <sub>4</sub> samples synthesized at different temperatures using melamine.....	<b>103</b>
<b>Fig. 4.5.</b> (a) Nitrogen adsorption-desorption isotherms, (b) Specific surface area by five-point BET, and (c) corresponding pore size distribution curves for g-C <sub>3</sub> N <sub>4</sub> samples synthesized at different temperatures using melamine .....	<b>104</b>
<b>Fig. 4.6.</b> Digital photograph of melamine derived g-C <sub>3</sub> N <sub>4</sub> samples at different temperatures. ....	<b>106</b>
<b>Fig. 4.7.</b> (a) UV-Vis diffuse reflectance spectra, (b) Tauc plots for the band gap energy calculation, of melamine derived g-C <sub>3</sub> N <sub>4</sub> samples synthesized at different temperatures, and (c) Correlation between bandgap and calcination temperature ..	<b>107</b>
<b>Fig. 4.8.</b> XRD patterns of melamine derived g-C <sub>3</sub> N <sub>4</sub> samples calcinated for different time period .....	<b>109</b>
<b>Fig. 4.9.</b> FTIR-spectra of melamine derived g-C <sub>3</sub> N <sub>4</sub> samples calcinated for different time period .....	<b>110</b>

<b>Fig. 4.10.</b> Raman spectra of melamine derived g-C <sub>3</sub> N <sub>4</sub> samples calcinated for different time period .....	<b>110</b>
<b>Fig. 4.11.</b> (a) Nitrogen adsorption-desorption isotherms, (b) Specific surface area by five-point BET, and (c) corresponding pore size distribution curves for g-C <sub>3</sub> N <sub>4</sub> samples synthesized at different temperatures using melamine .....	<b>112</b>
<b>Fig. 4.12.</b> (a) UV-Vis diffuse reflectance spectra, and (b) Tauc plots for the band gap energy calculation, of melamine derived g-C <sub>3</sub> N <sub>4</sub> samples calcinated for different time period. ....	<b>113</b>
<b>Fig. 4.13.</b> XRD patterns of g-C <sub>3</sub> N <sub>4</sub> prepared using different precursors for same reaction conditions .....	<b>115</b>
<b>Fig. 4.14.</b> FTIR-spectra of g-C <sub>3</sub> N <sub>4</sub> prepared using different precursors for same reaction conditions .....	<b>115</b>
<b>Fig. 4.15.</b> Raman spectra of melamine derived g-C <sub>3</sub> N <sub>4</sub> samples prepared using different precursors for same reaction conditions.....	<b>116</b>
<b>Fig. 4.16.</b> (a) Nitrogen adsorption-desorption isotherms, (b) Specific surface area by five-point BET, and (c) corresponding pore size distribution curves for g-C <sub>3</sub> N <sub>4</sub> samples synthesized using different precursors. ....	<b>117</b>
<b>Fig. 4.17.</b> (a) UV-Vis diffuse reflectance spectra, and (b) Tauc plots for the band gap energy calculation, for g-C <sub>3</sub> N <sub>4</sub> samples synthesized using different precursors .....	<b>119</b>
<b>Fig. 4.18.</b> XRD patterns of bulk and exfoliated g-C <sub>3</sub> N <sub>4</sub> samples prepared using (a) melamine, (b) thiourea, and (c) urea as precursor.....	<b>122</b>
<b>Fig. 4.19.</b> FTIR spectra of bulk and exfoliated g-C <sub>3</sub> N <sub>4</sub> samples prepared using (a) melamine, (b) thiourea, and (c) urea as precursor.....	<b>123</b>
<b>Fig. 4.20.</b> Raman spectra of bulk and exfoliated g-C <sub>3</sub> N <sub>4</sub> samples prepared using (a) melamine, (b) thiourea, and (c) urea as precursor.....	<b>124</b>
<b>Fig. 4.21.</b> (a) Nitrogen adsorption-desorption isotherms, (b) Specific surface area by five-point BET, and (c) corresponding pore size distribution curves for exfoliated g-C <sub>3</sub> N <sub>4</sub> samples synthesized using different precursor .....	<b>126</b>
<b>Fig. 4.22.</b> (a) UV-Vis diffuse reflectance spectra, and (b) Tauc plots for the band gap energy calculation, for exfoliated g-C <sub>3</sub> N <sub>4</sub> samples synthesized using different precursors .....	<b>127</b>
<b>Fig. 4.23.</b> FESEM micrograph of melamine derived bulk g-C <sub>3</sub> N <sub>4</sub> sample (MCN-545-4h) .....	<b>128</b>

<b>Fig. 4.24.</b> FESEM micrograph of melamine derived exfoliated g-C <sub>3</sub> N <sub>4</sub> sample (MCN-exf) .....	<b>128</b>
<b>Fig. 4.25.</b> FESEM micrograph of thiourea derived bulk g-C <sub>3</sub> N <sub>4</sub> sample (TCN-545-4h) .....	<b>129</b>
<b>Fig. 4.26.</b> FESEM micrograph of thiourea derived exfoliated g-C <sub>3</sub> N <sub>4</sub> sample (TCN-exf) .....	<b>129</b>
<b>Fig. 4.27.</b> FESEM micrograph of urea derived bulk g-C <sub>3</sub> N <sub>4</sub> sample (UCN-545-4h) .....	<b>129</b>
<b>Fig. 4.28.</b> FESEM micrographs of urea derived exfoliated g-C <sub>3</sub> N <sub>4</sub> sample (UCN-exf) .....	<b>130</b>
<b>Fig. 4.29.</b> Photolytic and photocatalytic phenol degradation using different g-C <sub>3</sub> N <sub>4</sub> samples and P25-TiO <sub>2</sub> under UV-Vis irradiation .....	<b>131</b>
<b>Fig. 4.30.</b> <i>E. coli</i> disinfection shown by exfoliated g-C <sub>3</sub> N <sub>4</sub> samples synthesized using different precursors and P25-TiO <sub>2</sub> at 100 mg L <sup>-1</sup> concentration.....	<b>132</b>
<b>Fig. 4.31.</b> The schematic of possible photocatalytic mechanism of g-C <sub>3</sub> N <sub>4</sub> explicating degradation of phenol and <i>E. coli</i> disinfection .....	<b>140</b>
<b>Fig. 5.1.</b> (a) FESEM image of exfoliated g-C <sub>3</sub> N <sub>4</sub> , and corresponding EDX elemental mapping for (b) C, (c) N, (d) Si, and (e) EDX spectrum .....	<b>154</b>
<b>Fig. 5.2.</b> (a) UV-Vis diffuse reflectance spectra, and (b) Tauc plots for the band gap energy calculation, for melamine derived exfoliated g-C <sub>3</sub> N <sub>4</sub> .....	<b>155</b>
<b>Fig. 5.3.</b> XPS survey spectrum for exfoliated g-C <sub>3</sub> N <sub>4</sub> .....	<b>156</b>
<b>Fig. 5.4.</b> Structure of the repeating heptazine carbon nitride unit with the corresponding atomic assignment according to XPS analysis.....	<b>157</b>
<b>Fig. 5.5.</b> High resolution C 1s spectrum of exfoliated g-C <sub>3</sub> N <sub>4</sub> .....	<b>158</b>
<b>Fig. 5.6.</b> High resolution N 1s spectrum of exfoliated g-C <sub>3</sub> N <sub>4</sub> .....	<b>158</b>
<b>Fig. 5.7.</b> High resolution O 1s spectrum of exfoliated g-C <sub>3</sub> N <sub>4</sub> .....	<b>159</b>
<b>Fig. 5.8.</b> Valence band XPS spectrum of exfoliated g-C <sub>3</sub> N <sub>4</sub> .....	<b>160</b>
<b>Fig. 5.9.</b> UPS spectrum of exfoliated g-C <sub>3</sub> N <sub>4</sub> .....	<b>161</b>
<b>Fig. 5.10.</b> Magnified UPS spectrum of exfoliated g-C <sub>3</sub> N <sub>4</sub> near valence band region .....	<b>162</b>
<b>Fig. 5.11.</b> Schematic band diagram for g-C <sub>3</sub> N <sub>4</sub> showing the position of its Fermi level .....	<b>162</b>
<b>Fig. 5.12.</b> LSV of exfoliated g-C <sub>3</sub> N <sub>4</sub> from -1.0 to +1.0 V .....	<b>164</b>



<b>Fig. 5.13.</b> Enlarged area A from LSV (Fig. 5.12) of exfoliated g-C <sub>3</sub> N <sub>4</sub> , showing anodic (n-type) to cathodic (p-type) photocurrent transition.....	<b>165</b>
<b>Fig. 5.14.</b> Enlarged area B from LSV (Fig. 5.12) of exfoliated g-C <sub>3</sub> N <sub>4</sub> , showing cathodic (p-type) to anodic (n-type) photocurrent transition .....	<b>166</b>
<b>Fig. 5.15.</b> Enlarged area C from LSV (Fig. 5.12) of exfoliated g-C <sub>3</sub> N <sub>4</sub> showing photocurrent onset potential.....	<b>166</b>
<b>Fig. 5.16.</b> Chopped LSV of g-C <sub>3</sub> N <sub>4</sub> (magnified in the range of -0.2 to +0.5 V). Point B showing cathodic (p-type) to anodic (n-type) photocurrent transition.....	<b>167</b>
<b>Fig. 5.17.</b> Photocurrent response for exfoliated g-C <sub>3</sub> N <sub>4</sub> at various potentials (a) ranging from 0.0 V to 1.0 V, and (b) showing photocurrent transition potential.....	<b>170</b>
<b>Fig. 5.18.</b> Spectral response for exfoliated g-C <sub>3</sub> N <sub>4</sub> measured at (a) +1 V, and (b) 0 V varying the incident irradiation wavelength from 280 to 460 nm at 10 nm periods and 30 s exposure-delay cycle .....	<b>171</b>
<b>Fig. 5.19.</b> IPCE (%) for exfoliated g-C <sub>3</sub> N <sub>4</sub> plotted as a function of wavelength ....	<b>172</b>
<b>Fig. 5.20.</b> Open circuit potential for exfoliated g-C <sub>3</sub> N <sub>4</sub> under dark and UV-vis irradiation .....	<b>173</b>
<b>Fig. 5.21.</b> The EIS Nyquist plot for exfoliated g-C <sub>3</sub> N <sub>4</sub> measured at OCP = -0.09 V under dark and UV-vis irradiation .....	<b>175</b>
<b>Fig. 5.22.</b> The EIS Bode phase plot for exfoliated g-C <sub>3</sub> N <sub>4</sub> measured at OCP = -0.09 V under dark and UV-vis irradiation .....	<b>176</b>
<b>Fig. 5.23.</b> The electrochemical equivalent circuit obtained after simulating impedance data for exfoliated g-C <sub>3</sub> N <sub>4</sub> (a) in dark, and (b) UV-Vis irradiation .....	<b>176</b>
<b>Fig. 5.24.</b> Mott-Schottky plot for exfoliated g-C <sub>3</sub> N <sub>4</sub> sample in the potential range of -1.0 to +1.0 V, step potential 0.02V .....	<b>178</b>
<b>Fig. 5.25.</b> Schematic energy band diagram of g-C <sub>3</sub> N <sub>4</sub> derived from DRS, VBXPS and UPS measurements.....	<b>179</b>
<b>Fig. 6.1.</b> Experimental setup for (a) Hydrothermal synthesis of spherical and plate shape BiVO <sub>4</sub> particles, (b) Reflux set up for seed mediated synthesis of pyramid/thorn shape BiVO <sub>4</sub> particles .....	<b>191</b>
<b>Fig. 6.2.</b> FESEM images of BiVO <sub>4</sub> samples synthesized by different methods: BiV-1 (a) BiVO <sub>4</sub> Spheres, and (b) BiVO <sub>4</sub> spheres at high magnification showing clusters of nano-size particles. BiV-2 (c) BiVO <sub>4</sub> plates, and (d) BiVO <sub>4</sub> plates at high magnification. BiV-3 (e) seed layer, (f) BiVO <sub>4</sub> pyramids/thorns, (g) Sea urchin-like structures, and (h) BiVO <sub>4</sub> pyramids/thorns at high magnification.....	<b>194</b>

<b>Fig. 6.3.</b> (a) XRD patterns of BiVO <sub>4</sub> samples synthesized by different methods (b) XRD patterns of seed layer stage and final annealed BiV-3 sample synthesized by seed mediated method .....	<b>196</b>
<b>Fig. 6.4.</b> Raman spectra of BiVO <sub>4</sub> samples synthesized by different methods, (laser 532 nm) .....	<b>198</b>
<b>Fig. 6.5.</b> FESEM image and corresponding EDX elemental mapping for Bi, V, O, and EDX spectrum for BiVO <sub>4</sub> sample having spherical shape (BiV-1) Scale = 2.5μm	<b>199</b>
<b>Fig. 6.6.</b> FESEM image and corresponding EDX elemental mapping for Bi, V, O, and EDX spectrum for BiVO <sub>4</sub> sample having nanoplates shape (BiV-2). Scale = 2.5μm .....	<b>200</b>
<b>Fig. 6.7.</b> FESEM image and corresponding EDX elemental mapping for Bi, V, O, and EDX spectrum for BiVO <sub>4</sub> sample having pyramid/thorns shape (BiV-3). Scale = 2.5μm .....	<b>201</b>
<b>Fig. 6.8.</b> Tauc plots for the band gap energy calculation, for as-prepared BiVO <sub>4</sub> samples.....	<b>202</b>
<b>Fig. 6.9.</b> Typical XPS survey spectra for BiV-1 .....	<b>203</b>
<b>Fig. 6.10.</b> High-resolution spectra of Bi 4f for BiV-1 .....	<b>203</b>
<b>Fig. 6.11.</b> High-resolution spectra of V 2p for BiV-1.....	<b>204</b>
<b>Fig. 6.12.</b> High-resolution spectra of C 1s for BiV-1 .....	<b>204</b>
<b>Fig. 6.13.</b> High-resolution spectra of O 1s for BiV-1 .....	<b>205</b>
<b>Fig. 6.14.</b> Typical XPS survey spectra for BiV-2.....	<b>208</b>
<b>Fig. 6.15.</b> High-resolution spectra of Bi 4f for BiV-2 .....	<b>208</b>
<b>Fig. 6.16.</b> High-resolution spectra of V 2p for BiV-2.....	<b>209</b>
<b>Fig. 6.17.</b> High-resolution spectra of C 1s for BiV-2 .....	<b>209</b>
<b>Fig. 6.18.</b> High-resolution spectra of O 1s for BiV-2 .....	<b>210</b>
<b>Fig. 6.19.</b> Typical XPS survey spectra for BiV-3 .....	<b>211</b>
<b>Fig. 6.20.</b> High-resolution spectra of Bi 4f for BiV-3 .....	<b>211</b>
<b>Fig. 6.21.</b> High-resolution spectra of V 2p for BiV-3.....	<b>212</b>
<b>Fig. 6.22.</b> High-resolution spectra of C 1s for BiV-3 .....	<b>213</b>
<b>Fig. 6.23.</b> High-resolution spectra of O 1s for BiV-3 .....	<b>213</b>
<b>Fig. 6.24.</b> Chopped linear sweep voltammogram of BiV-1 from -0.2 V to +1.0 V under UV-vis irradiation .....	<b>215</b>

- Fig. 6.25.** Linear sweep voltammogram for BiV-3 while sweeping from negative to positive potential under (a) continuous light condition in the range, -0.6 V to +1.0 V, and (b) Chopped light in the range +0.2 V to +1.0 V under UV-vis irradiation..... **217**
- Fig. 6.26.** Linear sweep voltammogram for BiV-3 while sweeping from positive to negative potential (a) continuous light condition in the range, -0.4 V to +1.0 V, and (b) Chopped light in the range -0.4 V to +1.0 V under UV-vis irradiation. .... **218**
- Fig. 6.27.** Photocurrent response for BiV-1 at various potentials ranging from, (a) 1.0 V to 0.0 V, (b) 0.0 to -0.1 V ..... **219**
- Fig. 6.28.** Photocurrent response for BiV-3 at various potentials ranging from +1.0 V to -0.4 V ..... **220**
- Fig. 6.29.** Photolytic and photocatalytic phenol degradation using BiV-1 and BiV-2 samples under UV-Vis irradiation ..... **222**
- Fig. 6.30.** Photolytic and photocatalytic RNO degradation using BiV-1 and BiV-2 samples under UV-Vis irradiation ..... **224**

## List of Tables

<b>Table 2.1.</b> Structural parameters and band gaps of different phases of C <sub>3</sub> N <sub>4</sub> .....	<b>19</b>
<b>Table 2.2.</b> Summary of g-C <sub>3</sub> N <sub>4</sub> based photocatalysts for water treatment and remediation.....	<b>44</b>
<b>Table 2.3.</b> List of other reported photocatalysts for water remediation .....	<b>47</b>
<b>Table 3.1.</b> List of chemicals with their molecular formula, source, and purity.....	<b>65</b>
<b>Table 4.1.</b> Summary of all the prepared g-C <sub>3</sub> N <sub>4</sub> samples with their reaction parameters .....	<b>97</b>
<b>Table 4.2.</b> Abbreviated names of synthesized samples with their reaction parameters .....	<b>99</b>
<b>Table 4.3.</b> Effect of calcination temperature of g-C <sub>3</sub> N <sub>4</sub> on BET parameters and band gap energy .....	<b>105</b>
<b>Table 4.4.</b> Table 4.4. Abbreviated names of synthesized samples with their reaction parameters .....	<b>109</b>
<b>Table 4.5.</b> Effect of calcination time of g-C <sub>3</sub> N <sub>4</sub> on BET parameters and band gap energy .....	<b>111</b>
<b>Table 4.6.</b> Abbreviated names of synthesized samples with their reaction parameters .....	<b>114</b>
<b>Table 4.7.</b> Role of precursors on BET parameters and band gap energy .....	<b>118</b>
<b>Table 4.8.</b> Abbreviated names of synthesized samples with their reaction parameters. ....	<b>120</b>
<b>Table 4.9.</b> Combined impact of precursor and exfoliation on BET parameters and band gap energy .....	<b>125</b>
<b>Table 4.10.</b> Initial rate of zero order reaction (k), coefficient of regression (R <sup>2</sup> ) shown by g-C <sub>3</sub> N <sub>4</sub> samples in phenol degradation.....	<b>131</b>
<b>Table 4.11.</b> Images of <i>E. coli</i> colonies on solid culture medium showing photocatalytic disinfection performance by exfoliated g-C <sub>3</sub> N <sub>4</sub> samples (MCN-exf, TCN-exf and UCN-exf) under 5 h of UV-Vis irradiation. (Sampling- 100 µl of 103 dilution).....	<b>135</b>
<b>Table 4.12.</b> Statistical measures and parameter values obtained when applying nine models available in GInaFiT Version 1.6 on the experimental data set of light control .....	<b>136</b>

<b>Table 4.13.</b> Statistical measures and parameter values obtained when applying nine models available in GInaFiT Version 1.6 on the experimental data set of MCN-exf .....	<b>136</b>
<b>Table 4.14.</b> Statistical measures and parameter values obtained when applying nine models available in GInaFiT Version 1.6 on the experimental data set of TCN-exf .....	<b>137</b>
<b>Table 4.15.</b> Statistical measures and parameter values obtained when applying nine models available in GInaFiT Version 1.6 on the experimental data set of UCN-exf .....	<b>137</b>
<b>Table 4.16.</b> The best fitting model and obtained parameter values on the experimental data set of <i>E. coli</i> disinfection .....	<b>138</b>
<b>Table 5.1.</b> Redox reactions, redox couples, and their corresponding redox potentials to form reactive oxygen species .....	<b>149</b>
<b>Table 5.2.</b> C, N and O bonding compositions and corresponding binding energies estimated from deconvolution of high-resolution spectrum obtained by XPS .....	<b>159</b>
<b>Table 6.1.</b> Bi, V, C and O bonding compositions and corresponding binding energies estimated from deconvolution of high-resolution spectrum of BiV-1 obtained by XPS .....	<b>206</b>
<b>Table 6.2.</b> Bi, V, C and O bonding compositions and corresponding binding energies estimated from deconvolution of high-resolution spectrum of BiV-2 obtained by XPS .....	<b>207</b>
<b>Table 6.3.</b> Bi, V, C and O bonding compositions and corresponding binding energies estimated from deconvolution of high-resolution spectrum of BiV-3 obtained by XPS .....	<b>214</b>

## Abstract

Photocatalysis has been found to be effective for the degradation of organic pollutants and for the inactivation of various pathogenic microorganisms in water, including disinfection resistant species. Development of a semiconductor photocatalyst that has a narrow band gap, responsive to visible light and suitable energy band structure is needed for effective redox capacity. In this study, we explored two different materials *i.e.*, graphitic carbon nitride (g-C<sub>3</sub>N<sub>4</sub>) and bismuth vanadate (BiVO<sub>4</sub>) as photocatalysts for water treatment and attempted to correlate their physiochemical properties to the photocatalytic activity.

g-C<sub>3</sub>N<sub>4</sub> was investigated to analyse the effect of different precursors and reaction parameters on its physiochemical properties *i.e.*, porosity, morphology, crystal structure, *etc.* and photocatalytic performance for phenol degradation and *E. coli* inactivation. The urea derived exfoliated g-C<sub>3</sub>N<sub>4</sub> displayed high specific surface area (183.9 m<sup>2</sup> g<sup>-1</sup>). The thiourea and urea derived exfoliated g-C<sub>3</sub>N<sub>4</sub> samples exhibited better phenol degradation and *E. coli* disinfection performance than all other prepared g-C<sub>3</sub>N<sub>4</sub> samples. However, the photocatalytic efficiency demonstrated by all the g-C<sub>3</sub>N<sub>4</sub> samples is still far behind the photocatalytic efficiency of P25-TiO<sub>2</sub> under UV-Vis irradiation.

The inefficient photocatalytic performance of g-C<sub>3</sub>N<sub>4</sub> was explained through its physiochemical properties, *i.e.*, bandgap energy, band edge positions, work function, photocurrent, open circuit photopotential, and flat band potential, *etc.* It was found to behave as an intrinsic semiconductor as the Fermi level of g-C<sub>3</sub>N<sub>4</sub> was quantified approximately in the middle of the forbidden gap. A very small photocurrent and photoelectrochemical photocurrent switching (PEPS) effect was observed in photoelectrochemical results.

Another photocatalyst  $\text{BiVO}_4$  was successfully synthesized with different morphologies (spheres, plates, pyramids/thorns) using hydrothermal and seed mediated methods. Although prepared samples did not show any photocatalytic activity for phenol degradation despite producing  $\cdot\text{OH}$  radicals (detected by RNO photocatalytic discolouration), possibly due to its positive conduction band edge potential which is insufficient to reduce oxygen.

# Chapter 1 – Introduction

## 1.1 Background

Water is the most important among all natural resources for health perspective and economic development which must be systematically conserved, treated, and recycled. Fast growing industrialization and modern development are posing a threat to life for every living species on this planet because of overuse of finite resources and pollution of the natural environment. Access to safe drinking water is a basic human right; However, the availability of safe drinking water is still a crucial issue in many countries.<sup>1-3</sup>

The WHO and UNICEF JMP report (2021) states that in 2020 only 74% of the global population had access to safely managed drinking water services. Of this, 86% of urban population had access to safely managed drinking water services, whereas only 60% of rural population had access. This means that 4 out of 10 individuals in rural areas are still consuming contaminated water. The WHO defines safely managed drinking-water services as drinking water from an improved source that is accessible on premises, available when needed and free from faecal and priority chemical contamination.<sup>4</sup> The consumption of contaminated water can spread diseases such as diarrhoea, cholera, dysentery, typhoid, and polio due to presence of pathogenic microorganisms.<sup>5</sup>

According to WHO report (2019), it is estimated that contaminated drinking water is the individual cause of 829,000 diarrheal deaths each year.<sup>6</sup> Most of these deaths occur in rural areas of developing and low income nations where the water source remains polluted and adequate sanitation is unavailable. Substantial efforts have been made to address this issue by different global organizations, but the target is still



unmet. The United Nations have set an agenda for 2030 as “17 sustainable development goals (SDGs) to improve the lives and future prospects of everyone, everywhere”. SDG 6 aims ensure availability and sustainable management of water and sanitation for all by 2030.<sup>7</sup>

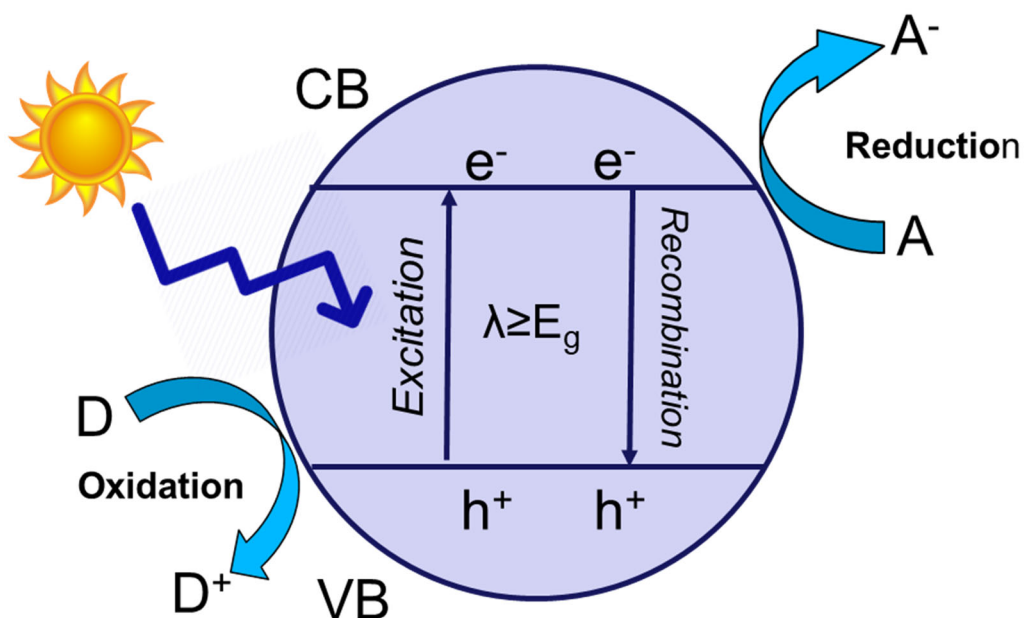
So far, various traditional approaches including coagulation-flocculation, sedimentation, reverse osmosis, filtration, solar disinfection, chemical and biological methods have been exercised for water treatment process but unfortunately these processes have their own limitations and side effects.<sup>3</sup> Hence a collective demand and effort has arisen for the development of low-cost, efficient, and technically sound method for producing clean water. In this regard, the most widely studied processes are Advanced Oxidation Processes (AOPs) such as UVC/H<sub>2</sub>O<sub>2</sub>, sonolysis, ozonation, Fenton-like oxidation, electrochemical oxidation, photocatalysis, and their combinations. Semiconductor photocatalysis appears to be a promising and low-cost method among above-mentioned AOPs for water remediation, because it can utilize solar energy as a source of energy which is freely available and does not require the addition of consumable chemicals other than oxygen from air.<sup>8,9</sup> This photochemical process has been shown to be an effective solution for water disinfection *i.e.*, inactivation of various pathogenic microorganisms in water, including some that are resistant to chlorination, UVC or ozonation.<sup>10</sup>

## **1.2 Semiconductor photocatalysis**

### **1.2.1 Basic principle of photocatalysis**

In a photocatalytic process, when a semiconductor is irradiated by photons having energy equal to or greater than its band gap, valence band electrons get excited to the conduction band while leaving holes in the valence band. Thus, produced e<sup>-</sup>/h<sup>+</sup> pairs

can either recombine releasing the energy as heat or radiation, or they can react at the surface interface in redox reactions. Thus, the whole process revolves around excitons or charge carriers (Fig. 1.1).



**Fig. 1.1.** Schematic of a photocatalytic process across semiconductor interface (A - Acceptor, D - Donor)

The terms photokatalyse and photokatalytisch was first viewed in the 1910 in “Textbook on Photochemistry” by Plotnikov.<sup>11</sup> The word photocatalyst was later introduced in France in 1913 by Landau<sup>12</sup> but real concern was shown towards applications of photocatalysis by scientists after the publication of Fujishima and Honda<sup>13</sup> in Nature in 1972 addressing water splitting through TiO<sub>2</sub> electrode. Photocatalysis has the ability to eliminate low level concentration of resistant organic pollutants as well as microorganisms present in water.<sup>14</sup> In 1977, Frank and Bard reported on the photocatalytic decomposition of cyanide in the presence of aqueous TiO<sub>2</sub> powder.<sup>15</sup> Later in 1985 Matsunaga *et al.* for the first time reported the photocatalytic microbial inactivation by platinum doped TiO<sub>2</sub>.<sup>16</sup> Since then, semiconductor photocatalysis has been widely studied and explored with more

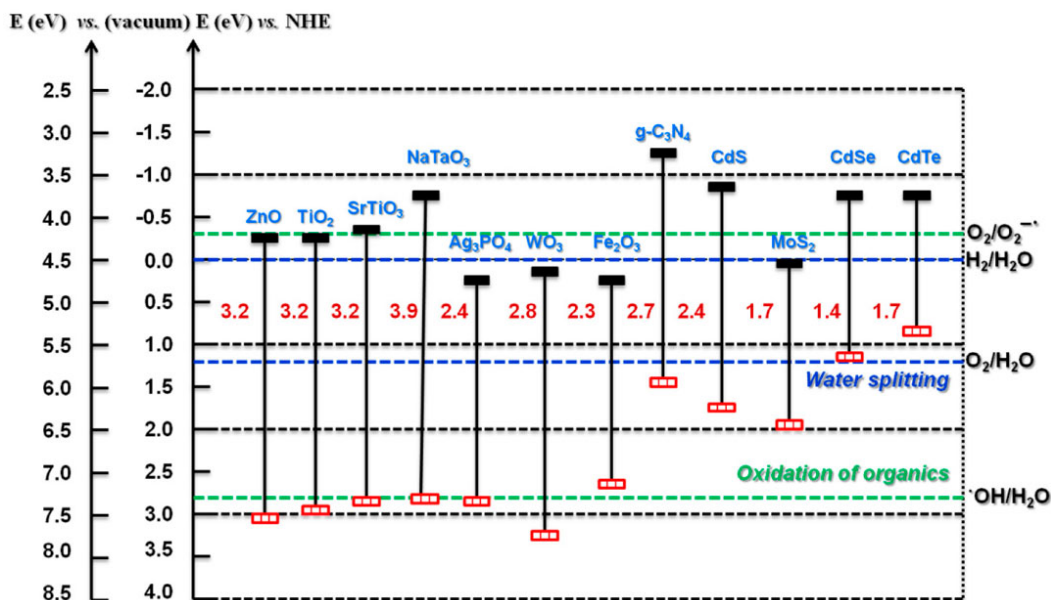
emphasis to energy and environmental subjects such as CO<sub>2</sub> reduction, water splitting, organic degradation, microbial inactivation, *etc.*

### 1.2.2 Photocatalyst and its prerequisites for photocatalysis

A photocatalyst is a semiconductor, a material with conductivity between insulator and conductor. Its photoelectronic property is characterized by its energy band structure which mainly consists of a valence band and a conduction band (CB). At low temperature, a semiconductor has fully occupied valence band and empty conduction band and it behaves as an insulator at 0 K. The energy difference between the lowest energy level of conduction band ( $U_{CB}$ ) and the uppermost energy level of valence band ( $U_{VB}$ ) is termed as the optical band gap ( $E_g$ ).<sup>17</sup>

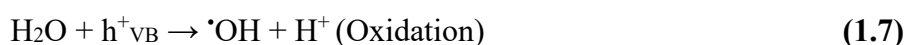
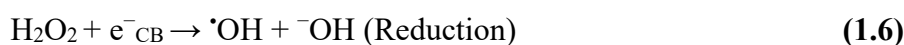
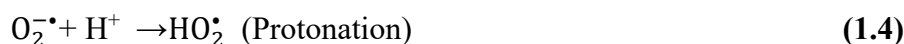
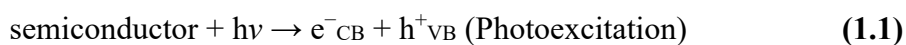
The main concept of semiconductor photocatalysis is the formation of electron-hole ( $e^-$ - $h^+$ ) pairs upon the absorption of photons with energy equal or greater than the band gap of semiconductor (photocatalyst). The redox capacity of these photogenerated carriers is closely related with the positions of corresponding VB and CB. The photoinduced  $h^+$  has a stronger oxidation capacity when the VB potential of a photocatalyst is more positive than  $e^-$  donor species, while photoinduced  $e^-$  exhibits more powerful reduction capacity when the CB potential of a photocatalyst is more negative than  $e^-$  acceptor species. The charge carriers, which do not undergo recombination process, can drift, or migrate to the surface of the material, and can participate in the redox reactions. The VB holes behave as good oxidizers between a potential of +1.0 to +3.5 V (NHE) and the CB electrons are good reducers between a potential of +0.5 to -1.5 V (NHE).<sup>18</sup> For example, TiO<sub>2</sub> in anatase phase has the CB potential ( $U_{CB} = -0.51$  V, pH 7) which permits the reduction of absorbed oxygen ( $E_{(O_2/O_2^{\cdot-})}^0 = -0.33$  V and  $E_{(O_2/HO_2^{\cdot})}^0 = -0.45$  V), both vs. NHE while the VB

potential ( $U_{VB} = +2.69\text{V}$ , pH 7) allows the oxidation of water and hydroxyl ion ( $E_{(H_2O/O_2)}^0 = +0.82\text{V}$  and  $E_{(OH^-/HO^*)}^0 = +2.29\text{V}$ ). Likewise, g-C<sub>3</sub>N<sub>4</sub> has the CB potential (-1.3 V) and the VB potential (+1.4 V) both vs. NHE.<sup>9,13,14,19</sup> For some other semiconductors, band gap and band edge energies are shown in Fig. 1.2.



**Fig. 1.2.** Schematic of band gap and band edge energies of various semiconductors [Reproduced from Kumar *et al.*, *Catalysts*, 2018, **8**, 74]<sup>14</sup>

The photoexcited  $e^-$  in the CB may transfer to oxygen to form superoxide ( $\cdot O_2^-$ ) or hydroperoxide radicals ( $\cdot HO_2$ ), whereas photoinduced  $h^+$  in the valence band may oxidize water to form hydroxyl radicals ( $\cdot OH$ ) (equations 1.1-1.7).



These produced reactive oxygen species (ROS) can contribute to the inactivation of microorganisms and the degradation of organic pollutants.<sup>20,21</sup> Hence, a semiconductor photocatalyst should have an appropriate energy band structure in order to remove organic pollutants and disinfect pathogens effectively. In the past few decades many materials such as ZnO, TiO<sub>2</sub>, SnO<sub>2</sub>, CdS, Fe<sub>2</sub>O<sub>3</sub>, C<sub>3</sub>N<sub>4</sub>, Cu<sub>2</sub>O, BiVO<sub>4</sub>, Bi<sub>2</sub>WO<sub>6</sub>, WO<sub>3</sub> *etc.*, have been investigated for their efficacy for various photocatalytic applications.<sup>22</sup>

### 1.2.3 Photocatalytic organic degradation

Organic pollutants in water come from various sources such as industrial spills, leakage in chemical tanks, pesticides, household wastes, medicine, *etc.* These organic contaminants can be categorized into dyes, surfactants, phenolic compounds, hydrocarbons, organohalides, plasticizers *etc.* Their chemical stability, water solubility, toxicity, carcinogenicity, difficult to degrade, make them a risk to the environment and/or human health. Many studies of organic pollutant degradation have been reported so far.<sup>23–26</sup> Although, depending on its chemical structure and functional groups, each organic pollutant can have a different degradation pathway<sup>27,28</sup> but a general photocatalytic degradation pathway for organic compounds can be given by equation 1.8 where each organic substance decomposes into simple organic and inorganic molecules and finally mineralized into carbon dioxide and water or eventually simple inorganic compounds containing heteroatoms.



Phenol is commonly used as a model organic pollutant to test the efficacy of prepared semiconductor photocatalyst for photocatalytic organic degradation. Phenol

(C<sub>6</sub>H<sub>5</sub>OH) is a common industrial pollutant which is toxic and available in many household products, pharmaceutical drugs *etc.*<sup>29-31</sup>

#### 1.2.4 Photocatalytic microbial disinfection

The use of semiconductor photocatalysis has also been explored for removing microbiological contaminants from water. The common wastewater microorganisms include adenoviruses that cause respiratory diseases, enteroviruses that cause a variety of gastrointestinal diseases, coronaviruses that cause tracheitis, diarrhoea, and pneumonia, and *Salmonella* that cause dysentery, colitis, and meningitis.<sup>30</sup> A microbial cell commonly made up of 70-90% water and compounds such as nucleic acids, lipids, proteins, polysaccharides, and lipopolysaccharides. Hence, reactive oxygen species (ROS) have ability to attack and render them inactive.<sup>32</sup> Matsunaga *et al.*<sup>16</sup> were the first who demonstrated the photoelectrochemical bacterial inactivation using platinized TiO<sub>2</sub>.

Photocatalytic microbial inactivation is thought to be caused by number of processes. The key steps of mechanism of ROS to destroy microbial cell reported by Matsunaga and his co-workers are as follows: ROS damages the coenzyme A present on the cell membrane which prevents the respiratory activity. Further ROS penetrates the cell and oxidizes the compounds present in the cell matrix, resulting in cell death.<sup>16,33</sup> Some researchers reported that ROS oxidizes the cell membrane resulting in destruction of outer layer of cell leading to the leakage of compounds present in cell matrix, resulting in cell death.<sup>34-36</sup>

*E. coli* is commonly chosen as a model microorganism to test the performance of photocatalyst for photocatalytic microbial disinfection. *E. coli* has also been

designated by the World Health Organization as a model indicator organism for the faecal pollution of drinking water.<sup>37</sup>

### 1.3 Aim and objectives

#### 1.3.1 Aim

The overall aim of this research was to explore the different materials *i.e.*, carbon nitride and bismuth vanadate as photocatalysts for water treatment and disinfection, and to correlate their physicochemical and photoelectrochemical properties to the photocatalytic activity.

#### 1.3.2 Objectives

- i. To conduct a comprehensive literature review on emerging photocatalytic materials for their application in photocatalytic water disinfection and organic degradation.
- ii. To synthesize graphitic carbon nitride (g-C<sub>3</sub>N<sub>4</sub>) and exfoliated g-C<sub>3</sub>N<sub>4</sub> using different precursors under varying reactions conditions by thermal polymerization route.
- iii. To determine the effect of changing reactions parameters on physicochemical properties of g-C<sub>3</sub>N<sub>4</sub> using different analytical techniques.
- iv. To study the impact of thermal exfoliation of g-C<sub>3</sub>N<sub>4</sub> on its physicochemical properties using different analytical techniques.
- v. To study the effect of precursors and synthesis parameters on the photocatalytic activity of g-C<sub>3</sub>N<sub>4</sub> for water disinfection and organic degradation under UV-visible light irradiation and to compare it with a model photocatalyst (P25-TiO<sub>2</sub>).

- vi. To determine the optical bandgap and band edge positions of exfoliated g-C<sub>3</sub>N<sub>4</sub>
- vii. To investigate the photoelectrochemical properties of exfoliated g-C<sub>3</sub>N<sub>4</sub>.
- viii. To present an energy band diagram of exfoliated g-C<sub>3</sub>N<sub>4</sub> based on the obtained results.
- ix. To synthesize different morphologies of bismuth vanadate (BiVO<sub>4</sub>) using different methods.
- x. To study the morphology and elemental mapping of as-prepared BiVO<sub>4</sub> through FESEM-EDX
- xi. To determine the elemental composition and chemical states present in the as-prepared BiVO<sub>4</sub> using XPS.
- xii. To explore the photoelectrochemical properties of BiVO<sub>4</sub> photoelectrodes
- xiii. To investigate the photocatalytic activity of BiVO<sub>4</sub> for the degradation of a model organic pollutant under UV-Vis irradiation

## 1.4 Thesis structure

The thesis is structured in seven chapters as follows:

**Chapter 2** presents a comprehensive literature review appropriate to the thesis title. This review begins with the brief introduction and the historical traces of carbon nitride. After that, characteristics, pioneering studies in design, and photocatalytic efficiency of g-C<sub>3</sub>N<sub>4</sub> based photocatalysts for water remediation will be discussed. The latter section will be focused on another photocatalyst, BiVO<sub>4</sub> where we will discuss pioneer work on the controlled synthesis of BiVO<sub>4</sub> and approaches to improve the photocatalytic efficacy of BiVO<sub>4</sub> for water disinfection and organic degradation. At the end, it will be concluded with recently reported photocatalysts, challenges ahead, and future perspectives, for water remediation.



**Chapter 3** includes a description of materials, synthesis methods and characterization techniques that were used during the course of this research work.

**Chapter 4** describes the synthesis of graphitic carbon nitride (g-C<sub>3</sub>N<sub>4</sub>) and exfoliated g-C<sub>3</sub>N<sub>4</sub> using different precursors under varying reactions conditions by thermal polymerization route. It further investigates the effect of changing reactions parameters on physicochemical properties of as-prepared g-C<sub>3</sub>N<sub>4</sub> samples using XRD, FTIR, Raman, BET and DRS techniques. It also explores the work on the impact of thermal exfoliation of g-C<sub>3</sub>N<sub>4</sub> on its physicochemical properties using XRD, FTIR, Raman, BET, DRS and FESEM techniques. At the end, it studies the effect of precursors and synthesis parameters on the photocatalytic activity of g-C<sub>3</sub>N<sub>4</sub> for water disinfection and organic degradation under UV-visible light irradiation and also includes the comparison with model photocatalyst (P25-TiO<sub>2</sub>).

**Chapter 5** investigates the optical, electronic and photoelectrochemical properties of exfoliated g-C<sub>3</sub>N<sub>4</sub> and determines its optical bandgap and band edge positions. It concludes with the energy band diagram of exfoliated g-C<sub>3</sub>N<sub>4</sub> drawn on the basis of the acquired data.

**Chapter 6** explores the synthesis of BiVO<sub>4</sub> with three distinct morphologies using different methods. It then investigates the physicochemical, electronic and photoelectrochemical properties as well as their photocatalytic activities of as-prepared BiVO<sub>4</sub> samples.

**Chapter 7** presents the overall conclusions of this research with discussion on potential future work and recommendations.

## 1.5 References

1. Byrne, J. A., Fernández-Ibáñez, P., & Sharma P. K. Water scarcity in developing regions. in *Sustainable Water Management and Technologies* (ed. Chen, D. H.), CRC Press, 2016, 227–248. (doi:10.1201/9781315373850)
2. Gogoi A., Mazumder P., Tyagi V. K., Tushara Chaminda G.G., An A.K., & Kumar M. Occurrence and fate of emerging contaminants in water environment: A review. *Groundw. Sustain. Dev.* 2018, **6**, 169–180.
3. Bethi, B., Sonawane, S. H., Bhanvase, B. A. & Gumfekar, S. P. Nanomaterials-based advanced oxidation processes for wastewater treatment: A review. *Chem. Eng. Process. – Process Intensif.* 2016, **109**, 178–189.
4. Progress on household drinking water, sanitation and hygiene 2000-2020: five years into the SDGs. Geneva: World Health Organization (WHO) and the United Nations Children’s Fund (UNICEF), 2021.
5. Pandit, A. B. & Kumar, J. K. Clean Water for Developing Countries. *Annu. Rev. Chem. Biomol. Eng.* 2015, **6**, 217–246.
6. Drinking-water Key facts. *World Health Organization*, 2019. Available at: <http://www.who.int/en/news-room/fact-sheets/detail/drinking-water>. (Accessed on 11 Oct, 2021).
7. *The Sustainable Development Goals Report 2017*. World Health Organization, 2017.
8. Razavi-Khosroshahi, H., Edalati, K., Wu, J., Nakashima, Y., Arita, M., Ikoma, Y., Sadakiyo, M., Inagaki, Y., Staykov, A., Yamauchi, M., Horitab, Z., & Fuji, M. High-pressure zinc oxide phase as visible-light-active photocatalyst with narrow band gap. *J. Mater. Chem. A*, 2017, **5**, 20298–20303.
9. Belver, C., Bedia, J., Gómez-Avilés, A., Peñas-Garzón, M. & Rodriguez, J. J. Semiconductor Photocatalysis for Water Purification. in *Nanoscale Materials in Water Purification*, Elsevier, 2019, 581–651. (doi:10.1016/B978-0-12-813926-4.00028-8)
10. Byrne, J. A., Dunlop, P. S. M., Hamilton, J. W. J., Fernández-Ibáñez, P., Polo-López, I., Sharma, P. K., & Vennard, A. S. M. A Review of Heterogeneous Photocatalysis for Water and Surface Disinfection. *Molecules*, 2015, **20**, 5574–5615.
11. Plotnikow, J. Textbook of Photochemistry, Verlag von Willhelm Knapp,

- Berlin, 1910, p. 72.
12. Landau, M. Le phénomène de la photocatalyse, *Compt. Rend.*, 1913, **156**, 1894–1896.
  13. Fujishima, A. & Honda, K. Electrochemical Photolysis of Water at a Semiconductor Electrode. *Nature*, 1972, **238**, 37–38.
  14. Kumar, S., Karthikeyan, S. & Lee, A. g-C<sub>3</sub>N<sub>4</sub>-Based Nanomaterials for Visible Light-Driven Photocatalysis. *Catalysts*, 2018, **8**, 74.
  15. Frank, S. N. and Bard, A. J. Heterogeneous photocatalytic oxidation of cyanide ion in aqueous solutions at titanium dioxide powder. *J. Am. Chem. Soc.* 1977, **99(1)**, 303–304.
  16. Matsunaga, T., Tomoda, R., Nakajima, T. & Wake, H. Photoelectrochemical sterilization of microbial cells by semiconductor powders. *FEMS Microbiol. Lett.* 1985, **29**, 211–214.
  17. Kittel, C. Introduction to solid state physics (8<sup>th</sup> ed.). John Wiley & Sons, 2004.
  18. Gołębiewska, A., Kobylański, M. P. & Zaleska-Medynska, A. Fundamentals of metal oxide-based photocatalysis. in *Metal Oxide-Based Photocatalysis*, Elsevier, 2018, 3–50. (doi:10.1016/B978-0-12-811634-0.00002-0)
  19. Serpone, N., Emeline, A. V., Horikoshi, S., Kuznetsov, V. N. & Ryabchuk, V. K. On the genesis of heterogeneous photocatalysis: a brief historical perspective in the period 1910 to the mid-1980s. *Photochem. Photobiol. Sci.* 2012, **11**, 1121.
  20. Cruz-Ortiz, B. R., Hamilton, J. W. J., Pablos, C., Díaz-Jiménez, L., Cortés-Hernández, D. A., Sharma, P. K., Castro-Alfárez, M., Fernández-Ibañez, P., Dunlop, P. S. M., & Byrne, J. A. Mechanism of photocatalytic disinfection using titania-graphene composites under UV and visible irradiation. *Chem. Eng. J.* 2017, **316**, 179–186.
  21. Banerjee, S., Pillai, S. C., Falaras, P., O'shea, K. E., Byrne, J. A., & Dionysiou, D. D. New Insights into the Mechanism of Visible Light Photocatalysis. *J. Phys. Chem. Lett.* 2014, **5**, 2543–2554.
  22. Cao, S., Low, J., Yu, J. & Jaroniec, M. Polymeric Photocatalysts Based on Graphitic Carbon Nitride. *Adv. Mater.* 2015, **27**, 2150–2176.
  23. Rajamanickam, D. & Shanthi, M. Photocatalytic degradation of an organic pollutant by zinc oxide – solar process. *Arab. J. Chem.* 2016, **9**, S1858–S1868.
  24. Chen, D., Cheng, Y., Zhou, N., Chen, P., Wang, Y., Li, K., Huo, S., Cheng, P.,

- Peng, P., Zhang, R., Wang, L., Liu, H., Liu, Y., & Ruan, R. Photocatalytic degradation of organic pollutants using TiO<sub>2</sub>-based photocatalysts: A review. *J. Clean. Prod.* 2020, **268**, 121725.
25. Sun, Y., Wang, C., Gu, G., Ma, Y., Xiong, Z., & Liu, Y. Facile synthesis of free-metal ternary composites for ultra-fast photocatalytic degradation of organic pollutant. *Catal. Today* 2020, **340**, 294–301.
26. Sanakousar, F. M., Vidyasagar, C., Jiménez-Pérez, V. M. & Prakash, K. Recent progress on visible-light-driven metal and non-metal doped ZnO nanostructures for photocatalytic degradation of organic pollutants. *Mater. Sci. Semicond. Process.* 2022, **140**, 106390.
27. Dabrowska, D., Kot-Wasik, A. & Namieśnik, J. Pathways and analytical tools in degradation studies of organic pollutants. *Crit. Rev. Anal. Chem.* 2005, **35**, 155–176.
28. Antoniou, M. G., Zhao, C., O'Shea, K. E., Zhang, G., Dionysiou, D. D., Zhao, C., Han, C., Nadagouda, M. N., Choi, H., Fotiou, T., Triantis, T. M., Hiskia, A. *Photocatalytic degradation of organic contaminants in water: Process optimization and degradation pathways. RSC Energy and Environment Series*, The Royal Society of Chemistry, 2016.
29. Bodzek, M. & Rajca, M. Photocatalysis in the treatment and disinfection of water. Part I. Theoretical backgrounds / Fotokataliza w oczyszczaniu i dezynfekcji wody część I. podstawy teoretyczne. *Ecol. Chem. Eng. S*, 2012, **19**, 489–512.
30. Ren, G., Han, H., Wang, Y., Liu, S., Zhao, J., Meng, X., & Li, Z. Recent Advances of Photocatalytic Application in Water Treatment: A Review. *Nanomaterials*, 2021, **11**, 1804.
31. Chong, M. N., Jin, B., Chow, C. W. K. & Saint, C. Recent developments in photocatalytic water treatment technology: A review. *Water Res.*, 2010, **44**, 2997–3027.
32. Dalrymple, O. K., Stefanakos, E., Trotz, M. A. & Goswami, D. Y. A review of the mechanisms and modeling of photocatalytic disinfection. *Appl. Catal. B Environ.* 2010, **98**, 27–38.
33. Wu, P., Imlay, J. A. & Shang, J. K. Mechanism of *Escherichia coli* inactivation on palladium-modified nitrogen-doped titanium dioxide. *Biomaterials*, 2010, **31**, 7526–7533.

34. Tran, T. H., Nosaka, A. Y. & Nosaka, Y. Adsorption and Photocatalytic Decomposition of Amino Acids in TiO<sub>2</sub> Photocatalytic Systems. *J. Phys. Chem. B*, 2006, **110**, 25525–25531.
35. Yang, X. & Wang, Y. Photocatalytic effect on plasmid DNA damage under different UV irradiation time. *Build. Environ.* 2008, **43**, 253–257.
36. Wang, W., Yu, Y., An, T., Li, G., Yip, H. Y., Yu, J. C., & Wong, P. K. Visible-Light-Driven Photocatalytic Inactivation of *E. coli* K-12 by Bismuth Vanadate Nanotubes: Bactericidal Performance and Mechanism. *Environ. Sci. Technol.* 2012, **46**, 4599–4606.
37. *Guidelines for drinking-water quality: fourth edition incorporating the first addendum*. Geneva: World Health Organization; 2017.

## Chapter 2 - Literature review

### 2.1 Introduction

The world population currently stands at 7.9 billion and is projected to reach 9.8 billion by 2050, with an annual increase of around 83 million.<sup>1</sup> Population growth, accelerated industrialization and technological development have an adverse effect on water quality, which is caused by various kinds of chemical and microbiological pollutants/contaminants.<sup>2-5</sup> Therefore, demand for safe water is growing rapidly and has become a major global concern. Conserving natural water resources and developing new technologies for wastewater treatment have emerged as critical environmental challenges for the twenty-first century.

Solar energy is an inexhaustible and free energy resource that has proven to be an alternative solution to replace or improve existing techniques for addressing energy and environmental issues. Semiconductor photocatalysis is a potentially solar-powered photochemical process that has demonstrated to be an effective technology for water treatment. Briefly, a semiconductor photocatalytic reaction may include four key steps: (a) generation of charge carriers, (b) migration, (c) recombination, and (d) charge utilization. The occurrence of these steps largely determined by the electronic band structure of the photocatalyst which absorbs solar irradiation and converts it into chemical energy.<sup>6</sup>

In recent years, much effort has been made to develop novel and effective semiconductor photocatalyst focusing photocatalytic water treatment including organic degradation and microbial disinfection. Several compounds have been explored as potential semiconductor photocatalysts such as ZnO, TiO<sub>2</sub>, SnO<sub>2</sub>, CdS, Fe<sub>2</sub>O<sub>3</sub>, C<sub>3</sub>N<sub>4</sub>, Cu<sub>2</sub>O, BiVO<sub>4</sub>, Bi<sub>2</sub>WO<sub>6</sub>, WO<sub>3</sub> *etc.*<sup>7</sup> Among various photocatalytic

materials, TiO<sub>2</sub> is still the most extensively explored photocatalyst but wide bandgap (3.2 eV) of TiO<sub>2</sub> confines its effectiveness under UV photons which accounts for only 4-5% of solar spectrum.<sup>8</sup> To more effectively utilize solar irradiation, there is a demand to develop visible light responsive photocatalysts since solar spectrum comprises 45% of visible light photons.<sup>9</sup> In this regard, graphitic carbon nitride (g-C<sub>3</sub>N<sub>4</sub>)<sup>10-12</sup> and bismuth vanadate (BiVO<sub>4</sub>)<sup>13,14</sup> have been intensively investigated as visible-light-driven photocatalyst because of their narrow bandgap (2.7 eV, 2.4 eV), high physicochemical stability, and ease of availability. This thesis will be focused on these two photocatalytic materials including investigation into their synthesis, characterization, and photocatalytic applications.

## 2.2 Graphitic carbon nitride (g-C<sub>3</sub>N<sub>4</sub>)

Carbon nitride (C<sub>3</sub>N<sub>4</sub>) is one of the primitive synthetic polymers reported in the scientific literatures. g-C<sub>3</sub>N<sub>4</sub>-based materials have been gone through extensive research as a photocatalyst for various environmental applications since the first reported use of g-C<sub>3</sub>N<sub>4</sub> as a metal-free semiconductor photocatalyst for H<sub>2</sub> evolution by Wang *et al.*<sup>15</sup> in 2009.

### 2.2.1 Carbon nitride from the beginning

The comprehensive picture of the historical background of C<sub>3</sub>N<sub>4</sub> has been reported by Zhang (2019),<sup>16</sup> Ong (2016),<sup>12</sup> Wang (2012),<sup>17</sup> Semencha (2010),<sup>18</sup> Thomas (2008),<sup>19</sup> Kroke (2004),<sup>20</sup> and Matsumoto *et. al* (1999)<sup>21</sup> in their review articles.

In brief, C<sub>3</sub>N<sub>4</sub> and its precursors have long back history since early days in 1834 when Liebig found melamine, melon, melem, and melam, and perceived as triazine and heptazine based compounds.<sup>22</sup> In 1922, Franklin studied and reinvestigated the

structure of compounds and revealed that the carbon nitride  $(C_3N_4)_x$  could be the last polymerization product of heating melon although he could not provide the evidences in support.<sup>23</sup> Pauling and Sturdivant came with evidences as X-ray crystallography studies in 1937 and a coplanar heptazine unit was suggested by them as a basic structure of these polymeric derivatives.<sup>24</sup> Three years later Redemann and Lucas found some analogies between graphite and melon.<sup>25</sup> Pauling's finding was further confirmed by Hosmane and his fellow scientists in 1982 when they reported the first crystal structure of a cyameluric derivative  $(C_6N_7H_3)$  and observed a coplanar arrangement in that.<sup>26</sup>

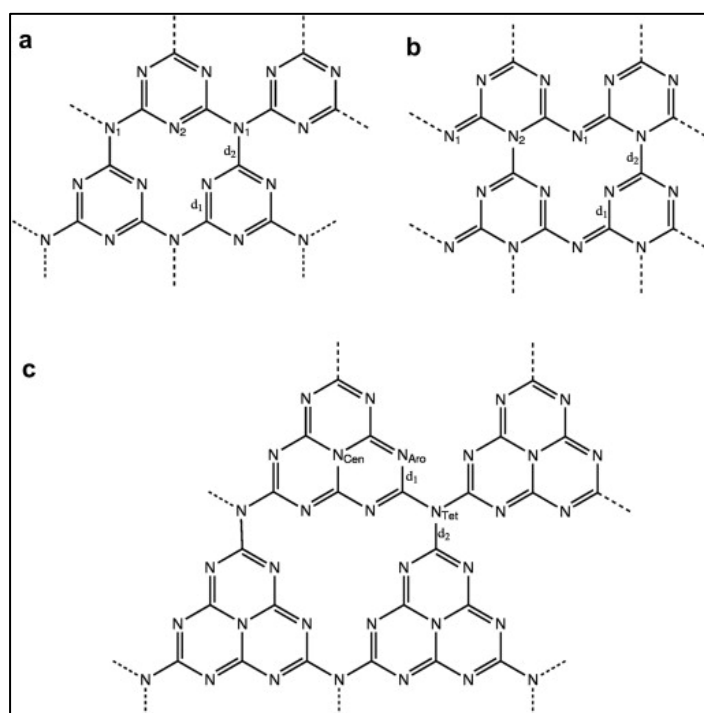
For an extensive stretch of time, the melon (which is a linear polymer of interconnected tri-s-triazine through secondary nitrogen) based  $C_3N_4$  had been overlooked as an unverified species because of its chemical inertness and insolubility in most solvents. Carbon nitride materials came in the limelight once again in 2006 since the expectation drawn by Goettmann with the finding of g- $C_3N_4$  as a metal free heterogenous catalyst for the benzene activation (Friedel–Crafts reaction).<sup>27</sup> Three years after that Wang and his co-workers reported first time g- $C_3N_4$  as a metal free photocatalyst for  $H_2$  evolution.<sup>15</sup> Since then, g- $C_3N_4$  have been gone through intense research to enhance its photoactivity.

### 2.2.2 Crystal structure and different phases of $C_3N_4$ and stability

Seven different phases are possessed by  $C_3N_4$  named as  $\alpha$ -  $C_3N_4$ ,  $\beta$ -  $C_3N_4$ , cubic  $C_3N_4$ , pseudocubic  $C_3N_4$ , g-h-triazine, g-o-triazine and g-h-heptazine, have been studied by Xu *et al.* using GW approximation.<sup>28,29</sup> Theoretical and experimental works demonstrated graphitic  $C_3N_4$  to be the most stable phase among all phases at ambient conditions and will be further discussed. Two phases (g-h-triazine and g-o-triazine)



are assembled on triazine ( $C_3N_3$ ) rings with a hexagonal (Fig. 2.1a) and orthorhombic (Fig. 2.1b) unit cell, respectively. g-h-triazine unit cell comprises 14 atoms and 3 coordinated N atoms that connect to the triazine rings, whereas g-o-triazine unit cell has direct C-N bonds between the rings. The third phase (g-h-heptazine) (Fig. 2.1c) is built from heptazine units ( $C_6N_7$ ), also called tri-s-triazine which contains 3 fused s-triazine rings linked by N atoms.



**Fig. 2.1.** Crystal structure of three g- $C_3N_4$  phases (a) g-h-triazine, (b) g-o-triazine, and (c) g-h-heptazine. [Reproduced from Xu *et al.*, *Int. J. Hydrogen Energy*, 2012, **37**, 11072–11080]<sup>29</sup>

Each primitive cell of  $\alpha$ -  $C_3N_4$ ,  $\beta$ -  $C_3N_4$ , cubic  $C_3N_4$ , pseudocubic-  $C_3N_4$ , g-h-triazine, g-o-triazine, and g-h-heptazine has 28, 14, 14, 7, 14, 14 and 28 atoms, respectively. The calculated lattice constant, 7.083 Å and inter planer distance, 3.3436 Å for g-h-heptazine was matched nearby with experimental outcomes obtained by X-ray diffraction (XRD) and High-resolution transmission electron microscopy (HRTEM). The other lattice parameters and band gap of all seven phases optimized by Xu *et al.* using GW approximation are listed in Table 2.1.

**Table 2.1.** Structural parameters and band gaps of different phases of  $C_3N_4$  [Adapted from Xu *et al.*, *Int. J. Hydrogen Energy*, 2012, **37**, 11072–11080]<sup>29</sup>

Phases of $C_3N_4$	Lattice parameter ( $\text{Å}$ )	$d_1$ ( $\text{Å}$ )	$d_2$ ( $\text{Å}$ )	Band gap (eV)	Type
$\alpha$ - $C_3N_4$	a = 6.465, c = 4.709			5.49	Indirect
$\beta$ - $C_3N_4$	a = 6.406, c = 2.406			4.85	Indirect
cubic $C_3N_4$	a = 5.411			4.30	Indirect
pseudocubic- $C_3N_4$	a = 3.426			4.13	Direct
g-h-triazine	a = 4.746, c = 6.586	1.320	1.444	2.97	Direct
g-o-triazine	a = 4.147, b = 4.754 c = 6.474	1.317	1.440	0.93	Indirect
g-h-heptazine	a = 7.083, b = 12.269 c = 6.871	1.335	1.458	2.88	Indirect

$d_1$  – Average C-N bond length in the aromatic rings

$d_2$  – Average C-N bond length that connects the rings

In the bulk form, most  $C_3N_4$  phases have direct band gap other than the pseudocubic and g-h-triazine phases which have indirect band gaps. Only g-h-triazine and g-h-heptazine phases are suitable for photocatalytic applications as they have appropriate band gaps for absorption of visible light photons. It has been established that tri-s-triazine based g- $C_3N_4$  was more energetically favoured and  $30 \text{ kJ mol}^{-1}$  more stable than the triazine based g- $C_3N_4$ .<sup>20</sup> In the recent works, it was found that the pyrolysis of dicyandiamide, cyanamide, or melamine produces a melon polymer composed of melem units confirming tri-s-triazine unit as the most stable tectonic unit of  $C_3N_4$ .<sup>30</sup> Therefore, the tri-s-triazine/heptazine tectonic unit has been widely accepted as the elementary structure for the g- $C_3N_4$ .

Graphitic carbon nitride is made of earth abundant elements, carbon (C), nitrogen (N) and a few impurities of hydrogen (H). Due to the presence of  $sp^2$ -hybridized C and N tends to form the  $\pi$ -conjugated plane (tri-s-triazine ring structure) and layered g- $C_3N_4$  shows high chemical and thermal stability ( $<600^\circ\text{C}$  in air) due to high

condensation properties which results in an alluring electronic structure, having a medium and indirect band gap ( $E_g \sim 2.7-2.8$  eV). g-C<sub>3</sub>N<sub>4</sub> is considered as a good photocatalyst because of having these exciting properties. Thus, it can be explored for photocatalytic applications. Polymeric characteristic enables g-C<sub>3</sub>N<sub>4</sub> to alter its surface properties easily through surface engineering at the molecular level including protonation, copolymerization, doping, *etc.* which may improve its performance.

It was widely reported the X-ray diffraction patterns of g-C<sub>3</sub>N<sub>4</sub> showing two characteristic diffraction peaks located at near 27.4° and 13.0° corresponding to the (002) and (100) planes (JCPDS 87-1526) respectively.<sup>31</sup> Wang *et al.* explained the XRD patterns in his paper for the g-C<sub>3</sub>N<sub>4</sub> which was synthesized by thermal condensation of cyanamide at 550°C. The results reveal the high intensity peak at nearby 27.4°, belonging to an interlayer distance of 0.326 nm, is due to the stacking of the conjugated aromatic system, as in graphite and the weak peak at 13.0°, which corresponds to distance 0.681 nm can be associated with an in-planer structural packing motif. It has been reported that hydrogen content in a material reduces with rise in condensation temperature.<sup>15</sup> Inspiring by this work, Thomas reported a detailed condensation study of cyanamide with the help of thermogravimetric analysis (TGA) and XRD to characterize the intermediates. The whole process involved polyaddition and polycondensation where cyanamide was first condensed to form melamine followed by ammonia elimination. The difference in products was also observed if condensation is performed in closed and open crucibles. Melamine based products were found up to 350°C, further heating to 390°C derived in the development of tri-s-triazine units via melamine rearrangements. Additional heating led to condensation of tri-s-triazine units into polymers and final polymerization of g-C<sub>3</sub>N<sub>4</sub> occurs at about 520°C and it turned in to an unstable form somewhat above 600°C. Heating above

700°C resulted in the disappearance of material due to formation of nitrogen and cyano fragments.<sup>19</sup>

Mo *et al.*<sup>32</sup> and Papailias *et al.*<sup>33</sup> also showed the similar XRD results for g-C<sub>3</sub>N<sub>4</sub> synthesized from melamine at different temperatures ranging 400–650°C and found similar results with 13.1° and 27.3° diffraction peaks. However, some researchers have been reported nanotubes of carbon nitride which exhibit one distinct diffraction peak than bulk carbon nitride at 17.4° indexed to an interplanar distance 0.49 nm, indicating the formation of the s-triazine units.<sup>34,35</sup> Single layer carbon nitride has also been informed which shows the weak diffraction peak at 27.4° indicating the destruction of inter layer structure of bulk g-C<sub>3</sub>N<sub>4</sub> after exfoliation.<sup>9</sup>

### 2.2.3 Surface physicochemical properties

Surface defects can form the multiple functionalities on the surface of polymeric carbon nitride. The basic primary (CNH<sub>2</sub>) and secondary amine (C<sub>2</sub>NH) functional groups could be created by hydrogen impurities (result of the incomplete polycondensation) on the edges of single layer g-C<sub>3</sub>N<sub>4</sub>, resulting the unique nucleophilic character. g-C<sub>3</sub>N<sub>4</sub> may contain several basic groups such as =N-, -NH-, -N-C=, and -NH<sub>2</sub> on its surface which are favourable for the removal of acidic pollutants such as phenol through chemical adsorption.<sup>36</sup> Hydrophobicity of g-C<sub>3</sub>N<sub>4</sub> could lead to the stacking of weakly interacted interfacial g-C<sub>3</sub>N<sub>4</sub> layers in aqueous environment, which can restrict the electron transport and separation and surface electrocatalytic reactions. Hydrophilicity of g-C<sub>3</sub>N<sub>4</sub> could be enhanced by chemical oxidation via introducing functional groups which contains oxygen such as hydroxyl and carboxyl. This will decrease the contact angle of water on surface of g-C<sub>3</sub>N<sub>4</sub>

particles which will improve their dispersion in aqueous solutions and will also enhance the photocatalytic activities.<sup>37</sup>

Fourier transform infrared spectroscopy (FTIR) can be used to identify these functional groups and C-N bonding information could be identified by measurement. The characteristic FTIR spectrum of g-C<sub>3</sub>N<sub>4</sub> shows characteristic peaks in three regions: 800-900 cm<sup>-1</sup>, 1200-1650 cm<sup>-1</sup> and 3000-3600 cm<sup>-1</sup>. The sharp absorption peak nearby 810 cm<sup>-1</sup> was indexed to heptazine/tri-s-triazine rings. The absorption peak at 883 cm<sup>-1</sup> was corresponded as the deformation mode of N-H in amino groups. Various strong bands (1241, 1322, 1406, 1571, and 1631 cm<sup>-1</sup>) found in the region between 1200 and 1650 cm<sup>-1</sup> were indexed to the typical stretching modes of CN heterocycles. The broad peaks between 3000 and 3600 cm<sup>-1</sup> were related to the stretching modes of terminal -NH<sub>2</sub> or -NH groups at the defect sites of the aromatic rings.<sup>38</sup>

The Raman spectra (A diode laser of 780 nm was used for excitation) of g-C<sub>3</sub>N<sub>4</sub> has several characteristic peaks at 1616, 1555, 1481, 1234, 751, 705, 543, and 479 cm<sup>-1</sup> which are indexed to vibration modes of CN heterocycles.<sup>39</sup> In case of single layer g-C<sub>3</sub>N<sub>4</sub>, a blue shift (1234 to 1250 cm<sup>-1</sup>) was observed which is related to the N=C (*sp*<sup>2</sup>) bending vibration (1250 cm<sup>-1</sup>) because exfoliated nanosheets shows a phonon confinement and quantum confinement effect of their ultrathin thickness. The ratio of peak heights is also described as characteristic feature *i.e.*, the ratios of peak heights of 751–705 cm<sup>-1</sup> (*I*<sub>751</sub>/*I*<sub>705</sub>) and 543–479 cm<sup>-1</sup> (*I*<sub>543</sub>/*I*<sub>479</sub>), indexed to layer–layer deformation vibrations or the correlation vibrations increased with reducing the g-C<sub>3</sub>N<sub>4</sub> layers. This feature of Raman spectroscopy can be utilized to figure out the layer numbers of g-C<sub>3</sub>N<sub>4</sub>.<sup>39,40</sup>

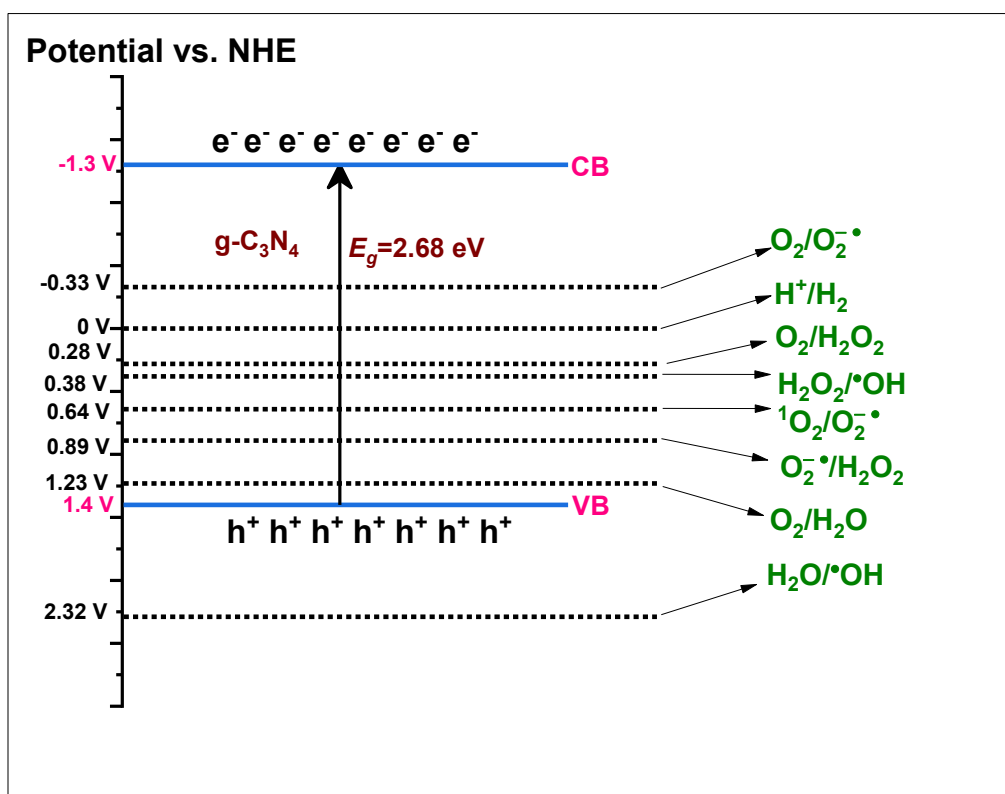
The elemental composition and chemical states of C and N in g-C<sub>3</sub>N<sub>4</sub> can be further quantitatively investigated by X-ray photoelectron spectroscopy (XPS). Ma *et al.*<sup>41</sup> reported the XPS spectra including the survey, C 1s, N 1s, and Ag 3d spectra for g-C<sub>3</sub>N<sub>4</sub> and Ag(3%)/g-C<sub>3</sub>N<sub>4</sub>. The survey XPS spectrum showed the presence of C, N, and O on the surface of g-C<sub>3</sub>N<sub>4</sub>, and presence of C, N, O and Ag on the surface of Ag(3%)/g-C<sub>3</sub>N<sub>4</sub>. Further, the two distinct peaks were displayed in C 1s spectra for both samples at 288.3 and 284.6 eV which relates to carbon atoms bonded with three adjacent N atoms in the g-C<sub>3</sub>N<sub>4</sub> lattice and the C-C bonding of reference carbon on the surface, respectively. The N 1s peak can be divided into three synthetic peaks positioned at 398.8, 400.3, 404.7 eV corresponding to the *sp*<sup>2</sup>-hybridized aromatic triazine rings (C=N-C), the tertiary nitrogen (N-(C)<sub>3</sub>) or amino functional groups carrying hydrogen ((C)<sub>2</sub>-NH) and charging effects or positive charge localization in heterocycles, respectively. The two peaks of an Ag 3d align with binding energies (BE) 374.3 eV (*3d*<sub>3/2</sub>) and 368.3 eV (*3d*<sub>5/2</sub>) related to metallic silver. In a line, with the combination of Raman spectra, IR spectra and XPS spectra, one can completely reveal the information about surface functional groups of g-C<sub>3</sub>N<sub>4</sub> based materials.

Moreover, the isoelectric point (IEP) can also be a valuable physicochemical parameter for various compounds such as hydroxides, sulphides, nitrides, and oxides, which had been broadly used to measure the surface charge of compound particles at different pH conditions. At pH 7, the zeta potential of g-C<sub>3</sub>N<sub>4</sub> prepared by melamine (MCN), thiourea (TCN) and urea (UCN) are -17.0, -30.7 and -19.9 mV respectively and their corresponding IEPs are 5.0, 4.4, and 5.1. At pH values below the IEP, the g-C<sub>3</sub>N<sub>4</sub> particles are positively charged, while above this point, they are negatively charged.<sup>42</sup> The optical properties of g-C<sub>3</sub>N<sub>4</sub> can be revealed by UV-Vis absorption spectroscopy and photoluminescence spectra. The typical absorption edge for the g-

C<sub>3</sub>N<sub>4</sub> obtained at 550°C was at 455 nm therefore absorbing in the visible. The estimated optical band gap of g-C<sub>3</sub>N<sub>4</sub> obtained by UV-Vis absorption curves and Kubelka–Munk function is about 2.7 eV calculated using the Tauc equation 2.1<sup>43,44</sup>

$$(\alpha \cdot h\nu)^{1/n} = B(h\nu - E_g) \quad (2.1)$$

Where  $\alpha$  - absorption coefficient,  $\nu$  - photon's frequency,  $B$  - proportionality constant, and  $E_g$  - bandgap.  $n=1/2$  for direct absorption and  $n=2$  for indirect absorption. Hence, the intercept of the tangents to the plots of  $(\alpha h\nu)^{1/n}$  vs. photon energy ( $h\nu$ ) can provide approximate bandgap.<sup>45</sup> Literature shows that the bandgap can be decreased by increasing the condensation temperature which increases the degree of polymerization.<sup>46</sup>



**Fig. 2.2.** The redox potentials of the relevant reactions with respect to the band edge potentials of the g-C<sub>3</sub>N<sub>4</sub> at pH 7

With an appropriate bandgap, positioning of conduction band (CB) and valence band (VB) edges of semiconductor photocatalyst should also match with the

redox potential for reactions of interest. X-ray photoelectron spectroscopy (XPS) can be used to determine the valence band energy, and electrochemical impedance spectroscopy (EIS) to determine the flat band potential. The VB potential can then be determined by the optical gap energy difference from CB potential (flat band potential). Researchers reported the positive slope of M-S plot, showing n-type semiconductor<sup>47</sup> and bottom edge of CB of g-C<sub>3</sub>N<sub>4</sub> is positioned at -1.3 V (vs NHE) at pH=7, sufficient for water reduction, whereas the top edge of VB is positioned at +1.4 V (vs NHE) at pH 7, resulting in a small thermodynamic driving force for oxidation.<sup>37</sup> Thus, to enhance the photooxidation ability of g-C<sub>3</sub>N<sub>4</sub>, modulation in the electronic band structure of g-C<sub>3</sub>N<sub>4</sub> is required to make the VB edge more positive which may improve the performance of g-C<sub>3</sub>N<sub>4</sub> as photocatalyst for water oxidation and water remediation applications. The redox potentials of the relevant reactions with respect to the estimated position of the g-C<sub>3</sub>N<sub>4</sub> band edges at pH 7 are shown in Fig. 2.2.<sup>37,48,49</sup>

Cheng *et al.*<sup>50</sup> measured the photoluminescence (PL) spectra of g-C<sub>3</sub>N<sub>4</sub> at 365 nm and found a broad emission band ranging from 400 to 650 nm, with the emission peak of around 470 nm. The intensity of PL signal is directly related to the recombination process of photo-generated electrons and holes upon photoexcitation. Generally, lower peak intensities in PL spectra reveal the improved charge separation and lower rates of recombination.

#### **2.2.4 Design and performance of g-C<sub>3</sub>N<sub>4</sub>-based photocatalyst for water remediation**

Since finding of photocatalytic properties of g-C<sub>3</sub>N<sub>4</sub>, researchers have investigated different ways to enhance the photocatalytic performance including modification in



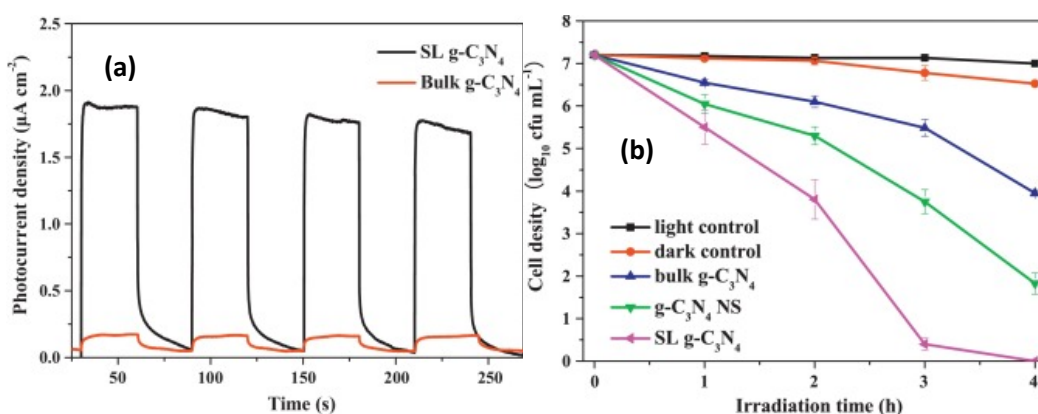
synthetic techniques, different shapes, metal doping, metal deposition, coupling with other semiconductors to form heterojunctions. The recent developments in design and performance of g-C<sub>3</sub>N<sub>4</sub>-based photocatalyst for photocatalytic water remediation are listed in Table 2.2.

#### 2.2.4.1 Unitary structure- effect of precursors and exfoliation methods

g-C<sub>3</sub>N<sub>4</sub> can be easily synthesized by thermal polymerization of various precursors such as cyanamide,<sup>51</sup> melamine,<sup>52</sup> dicyandiamide,<sup>53</sup> thiourea,<sup>54</sup> ammonium thiocyanate,<sup>55</sup> and urea<sup>56</sup> but the photocatalytic efficiency of the bulk g-C<sub>3</sub>N<sub>4</sub>, tested for H<sub>2</sub> evolution, organic degradation and microbial inactivation, is reported limited owing to fast recombination of photogenerated charge carriers (e<sup>-</sup> & h<sup>+</sup>) and its small surface area ca. ~10 m<sup>2</sup> g<sup>-1</sup>. Nano-engineering is an approach to achieving a large surface area and more surface reactive sites. It is known that large surface area and the porous structure of photocatalysts produce more reactive sites, which decreases the diffusion length necessary to reach the interface and facilitate the diffusion of photogenerated charge carriers thus enhancing photocatalytic efficiency. In order to enhance photocatalytic efficiency, Lee *et. al* (2012) first time used the urea as a precursor and silica as template to synthesize mesoporous g-C<sub>3</sub>N<sub>4</sub>. The sample having mass ratio 4, (ratio of urea to silica) exhibited the highest BET surface area, 224 m<sup>2</sup> g<sup>-1</sup> resulting in better photocatalytic activities for phenol removal than bulk g-C<sub>3</sub>N<sub>4</sub>.<sup>56</sup>

Comparative studies on the role of precursors on photocatalytic properties have also been reported by Zhang *et al.* (2013),<sup>57</sup> Teerthagiri *et al.* (2016),<sup>58</sup> and Devthde *et al.* (2018).<sup>59</sup> Their result reveals that urea derived g-C<sub>3</sub>N<sub>4</sub> outperformed among all in their photocatalytic behaviour but considering the cost, toxicity, and yield of the g-C<sub>3</sub>N<sub>4</sub>, melamine is recommended as best precursor.<sup>57</sup>

Preparation of 2D nanosheets by exfoliation of their bulk counterparts have been stimulated much interest due to their improved electrical, optical, and physicochemical properties. Huang *et al.*<sup>60</sup> first time reported the bacterial inactivation properties of g-C<sub>3</sub>N<sub>4</sub> on *E. coli* K-12. Silica template and cyanamide as precursor were used to prepare mesoporous g-C<sub>3</sub>N<sub>4</sub> whose surface area was 20 times (230 m<sup>2</sup> g<sup>-1</sup>) larger compared to the bulk g-C<sub>3</sub>N<sub>4</sub> (12 m<sup>2</sup> g<sup>-1</sup>). Results exhibited that the mesoporous g-C<sub>3</sub>N<sub>4</sub> inactivated 100% *E. coli* (2.5 × 10<sup>6</sup> CFU mL<sup>-1</sup>) after visible light irradiation for 4 h while the bulk counterpart only inactivated 50% bacterial in same conditions. Almost at the same time, Zhao and his co-workers reported the fabrication of atomic single layer g-C<sub>3</sub>N<sub>4</sub> with the thickness of 0.5 nm by tow step process.<sup>9</sup>



**Fig. 2.3** (a) Photocurrent–time dependence of bulk g-C<sub>3</sub>N<sub>4</sub> and SL g-C<sub>3</sub>N<sub>4</sub> electrodes under visible light irradiation ( $\lambda > 400$  nm), and (b) Photocatalytic disinfection efficiencies under different conditions. [Reproduced from Zhao *et al. Appl. Catal. B Environ.* 2014, **152–153**, 46–50]<sup>9</sup>

Bulk g-C<sub>3</sub>N<sub>4</sub> was processed into g-C<sub>3</sub>N<sub>4</sub> nanosheets by thermal etching, followed by an ultrasonication exfoliation of g-C<sub>3</sub>N<sub>4</sub> nanosheets. The prepared single layer g-C<sub>3</sub>N<sub>4</sub> exhibited the short charge-transfer distance which decrease the recombination probability, and the low charge-transfer resistance which promote the photo-generated charge separation. Correspondingly, single layer g-C<sub>3</sub>N<sub>4</sub> showed the 17 times enhanced photocurrent density (1.8 μA cm<sup>-2</sup>) than bulk g-C<sub>3</sub>N<sub>4</sub> (Fig. 2.3). Along with,

single layer g-C<sub>3</sub>N<sub>4</sub> was outperformed in bacterial inactivation than its other counterparts, bulk g-C<sub>3</sub>N<sub>4</sub> and g-C<sub>3</sub>N<sub>4</sub> nanosheets with 7 log, 3 log and 5 log reduction respectively, in 4 h under visible light irradiation.

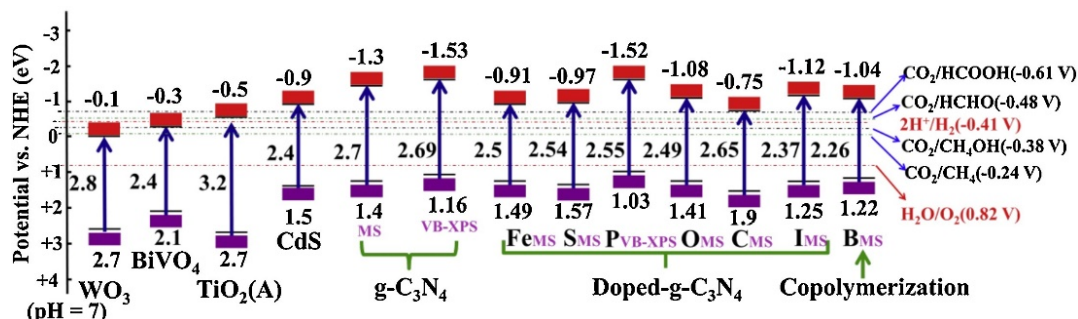
Very recently, a novel approach of ‘alternated cooling and heating’, was used by Kang *et al.* to fabricate highly crystalline g-C<sub>3</sub>N<sub>4</sub> nanosheets showing reduced band gap (2.62 eV), high crystallinity, improved specific surface area (88.59 m<sup>2</sup> g<sup>-1</sup>) and enhanced electron transport ability. As a result, complete photocatalytic inactivation of 2.5×10<sup>7</sup> CFU mL<sup>-1</sup> of *E. coli* within 120 min and 65% humic acid degradation after 70 min was observed.<sup>61</sup> Although the enhancement in photocatalytic properties further needs to be improved.

#### 2.2.4.2 g-C<sub>3</sub>N<sub>4</sub> based binary/ternary/multi heterostructures

Pristine g-C<sub>3</sub>N<sub>4</sub> shows low electrical conductivity, fast recombination of charge carriers, and limited absorption up to 460 nm which affect its photocatalytic activity. It is highly required to tune the physiochemical properties of g-C<sub>3</sub>N<sub>4</sub> to optimize the photoactivity. For this, introducing the impurities into the g-C<sub>3</sub>N<sub>4</sub> matrix or formation of heterostructures can be an effective approach which could be achieved by copolymerization, metal deposition, elemental doping (metal and non-metal), and coupling with other appropriate semiconductors, *etc.* as shown in Fig. 2.4.

Several studies have been published concerning nonmetal doping (O, C, P, S, B, I and F, *etc.*) and metal doping (Fe, Cu, Zn, Ni, and Ag, *etc.*) or their combination. Recently, Cui and his coworkers<sup>62</sup> discussed the formation of sulphur doped g-C<sub>3</sub>N<sub>4</sub> microspheres using in situ solvothermal condensation process and trithiocyanuric acid as a sulphur source and tested its photocatalytic activity for Cr (VI) reduction. Sulphur doping was confirmed with the formation of C-S and N-S into the hybrid structure

realizing improved conjugated structure, increase in visible light harvesting and elevated conduction band potential. In result, sulphur doped graphitic carbon nitride exhibited 24 times higher reduction rate of Cr (VI) than un-doped g-C<sub>3</sub>N<sub>4</sub>.



**Fig. 2.4.** Schematic representation of the band structures of different g-C<sub>3</sub>N<sub>4</sub> based materials. [Reproduced from Wen *et al.*, *Appl. Surf. Sci.*, 2017, **391**, 72–123]<sup>37</sup>

Ouyang *et al.* incorporated fullerenes (C<sub>60</sub>, C<sub>70</sub>) by hydrothermal method into carbon nitride matrix to make it metal-free photocatalysts (C<sub>60</sub>/C<sub>3</sub>N<sub>4</sub> and C<sub>70</sub>/C<sub>3</sub>N<sub>4</sub>) for bacterial disinfection minding the risk of the discharge of metals into treated water. Although researchers couldn't observe the XRD diffraction peak indexed to fullerene because of the thin layer of fullerene. However, they displayed higher *E. coli* inactivation efficiency.<sup>63</sup>

For metal doping, Gao *et al.* reported a novel synthesis approach for preparation of Cu-doped g-C<sub>3</sub>N<sub>4</sub> nanosheets. The surface area (40.86 m<sup>2</sup> g<sup>-1</sup>) of doped g-C<sub>3</sub>N<sub>4</sub> was seven times higher than pure g-C<sub>3</sub>N<sub>4</sub>. The strong optical absorption in visible region and extended absorption in IR region was also observed by the team which enabled the Cu-doped g-C<sub>3</sub>N<sub>4</sub> displaying improved photocatalytic activity for methylene blue dye degradation.<sup>64</sup> Xu *et al.* increased the photocatalytic activity of oxidized porous g-C<sub>3</sub>N<sub>4</sub> (PCNO) by loading of Ag nanoparticles using photo-assisted reduction method. Ag-PCNO could inactivate about 99.4% *Staphylococcus aureus* (10<sup>7</sup> CFU mL<sup>-1</sup>) after 3 h of visible light irradiation and it was found 2.4 times more effective

than PCNO for amaranth degradation.<sup>65</sup> The 99.4% inactivation shows that photocatalyst is quite effective.

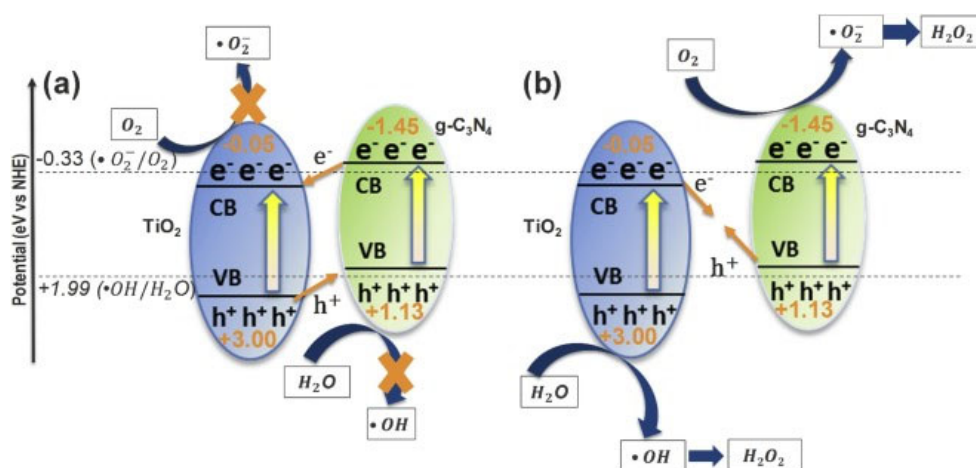
However, reporting the percent inactivation in photocatalytic disinfection results is not really appropriate because 99%, 99.9%, and 99.99% inactivation reflect only 2, 3, 4 log reduction, respectively. Therefore, one should prefer to report inactivation data in terms of log reduction rather than percentage when analysing photocatalyst efficacy.

Jourshabani *et al.*<sup>66</sup> combined both non-metal and metal doping and produced sulfur-doped mesoporous carbon nitride decorated with Cu particles. Characterization results of this study was indicating the improvement in the visible-light harvesting ability and facilitated the charge separation efficiency, and therefore, the photocatalytic activity was dramatically enhanced with 100% degradation of methylene blue dye in 90 min under visible light irradiation.

However, dyes should not be used as predictors for the photocatalytic activity of the photocatalysts because upon photoexcitation, dye degradation could be due to either a photocatalytic process, a dye sensitization or both. Upon photoexcitation, as many dyes absorb radiation and transfer an electron into the CB of a semiconductor photocatalyst, resulting in bleaching of the oxidised dye. This process is called dye sensitization.<sup>67-69</sup> Like percentage inactivation, reporting percentage degradation is also an inappropriate way of quantifying degradation because it does not provide any information about the reaction, instead, reporting the reaction rate is more informative and relevant.

In addition to doping, coupling of other semiconductors with g-C<sub>3</sub>N<sub>4</sub> and has also been practiced since last decades to be another effective approach for improving photo activity of g-C<sub>3</sub>N<sub>4</sub>. Various semiconductors such as TiO<sub>2</sub>, ZnO, Ag<sub>3</sub>PO<sub>4</sub>, BiVO<sub>4</sub>,

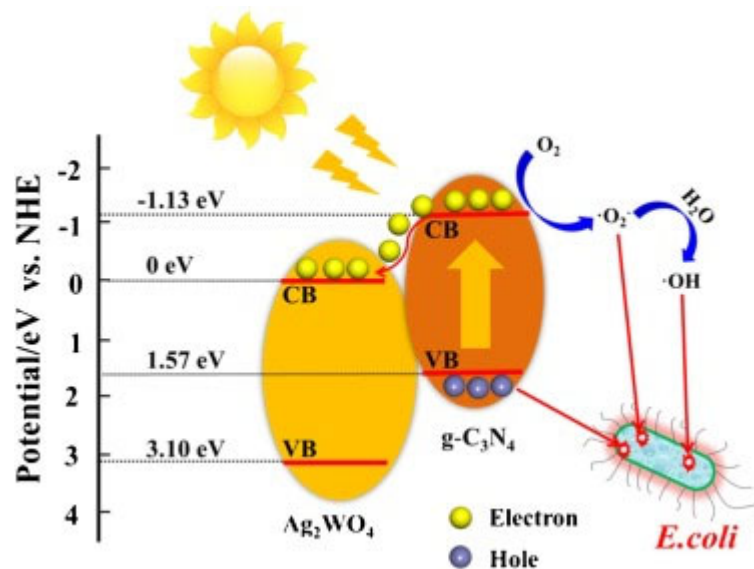
MoS<sub>2</sub>, SmVO<sub>4</sub>, WO<sub>3</sub>, GO, and many others have been coupled with g-C<sub>3</sub>N<sub>4</sub> to form heterostructures. Liu *et al.* has accepted TiO<sub>2</sub> as a proper partner to be combined with g-C<sub>3</sub>N<sub>4</sub> to form vertical Z-scheme heterojunction by hydrothermal method (Fig. 2.5). The resultant heterostructure were able to inactivate 10<sup>3</sup> CFU mL<sup>-1</sup> of *E. coli* within 30 min under sun light.<sup>70</sup>



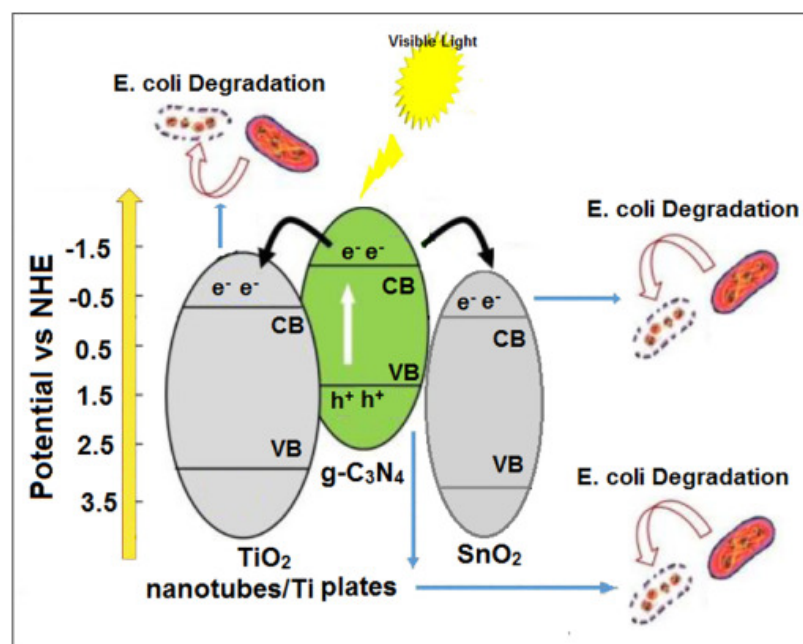
**Fig. 2.5.** Type-II (a) and Z-scheme (b) charge transfer models and corresponding proposed surface redox reactions for HT-CN/TiO<sub>2</sub> composite. [Reproduced from Liu *et al. Catal. Today* 2019, **335**, 243–25]<sup>70</sup>

Sun *et al.* prepared the graphene oxide/g-C<sub>3</sub>N<sub>4</sub> composite, a metal free heterostructure, through sonication method. They reported that 100 μg mL<sup>-1</sup> of GO/g-C<sub>3</sub>N<sub>4</sub> composite could inactivate 97.9% of 10<sup>7</sup> CFU mL<sup>-1</sup> *E. coli*.<sup>71</sup> Li *et al.* fabricated Bi<sub>2</sub>MoO<sub>6</sub>/g-C<sub>3</sub>N<sub>4</sub> heterojunctions by an in situ solvothermal method which exhibited higher efficiency for photocatalytic hydrogen production and photocatalytic disinfection of bacteria compared with pristine materials (Bi<sub>2</sub>MoO<sub>6</sub> or g-C<sub>3</sub>N<sub>4</sub>).<sup>72</sup> Li *et al.* reported the synthesis of Ag<sub>2</sub>WO<sub>4</sub>/g-C<sub>3</sub>N<sub>4</sub> composite by polymerization of thiourea and ammonia chloride followed by deposition-precipitation method. Ag<sub>2</sub>WO<sub>4</sub>(5%)/g-C<sub>3</sub>N<sub>4</sub> composites shown significantly enhanced photocatalytic activity compared with pure Ag<sub>2</sub>WO<sub>4</sub> and g-C<sub>3</sub>N<sub>4</sub> for *E. coli* disinfection. Increased light absorption, weaker PL intensity and reduced arc of Nyquist plots attributed to the effective separation and

transportation of the photo generated charge carriers and reduced recombination of free charges which support the efficiency of  $\text{Ag}_2\text{WO}_4/\text{g-C}_3\text{N}_4$  composite for water disinfection application. Schematic energy band diagram for  $\text{Ag}_2\text{WO}_4/\text{g-C}_3\text{N}_4$  composite proposed by Li *et al.* is represented in Fig. 2.6.<sup>73</sup>



**Fig. 2.6.** Mechanism of photocatalytic disinfection treated with  $\text{Ag}_2\text{WO}_4/\text{g-C}_3\text{N}_4$  composite under visible light irradiation. [Reproduced from Li *et al.* *J. Hazard. Mater.* 2017, **338**, 33–46]<sup>73</sup>



**Fig. 2.7.** Schematic representations of antibacterial activity for  $\text{g-C}_3\text{N}_4\text{-SnO}_2/\text{TiO}_2$  nanotubes/Ti plate toward *E. coli* under visible light irradiation. [Reproduced from Faraji *et al.* *J. Photochem. Photobiol. B Biol.* 2018, **178**, 124–132]<sup>74</sup>

g-C<sub>3</sub>N<sub>4</sub> can be coupled by more than two semiconductors with appropriate band gap to overcome the recombination problem for example, a ternary composite g-C<sub>3</sub>N<sub>4</sub>-SnO<sub>2</sub>/TiO<sub>2</sub> nanotubes/Ti plates were fabricated by Faraji *et al.* by simple dipping of TiO<sub>2</sub> nanotubes/Ti in a solution containing SnCl<sub>2</sub> and g-C<sub>3</sub>N<sub>4</sub> nanosheets followed by annealing and enhanced photocatalytic activities in both chemical (acetic acid and 2-propanol) and microbial (*E. coli*) systems were observed. The Schematic energy band diagram for the ternary composite g-C<sub>3</sub>N<sub>4</sub>-SnO<sub>2</sub>/TiO<sub>2</sub> nanotubes/Ti plates proposed by Faraji *et al.* is represented in Fig. 2.7.<sup>74</sup> Thus, by coupling with other metal, nonmetal, semiconductor, or combination of them and forming the heterostructures could reduce the recombination rate, increase the light harvesting resulting in enhancement in photocatalytic activities.

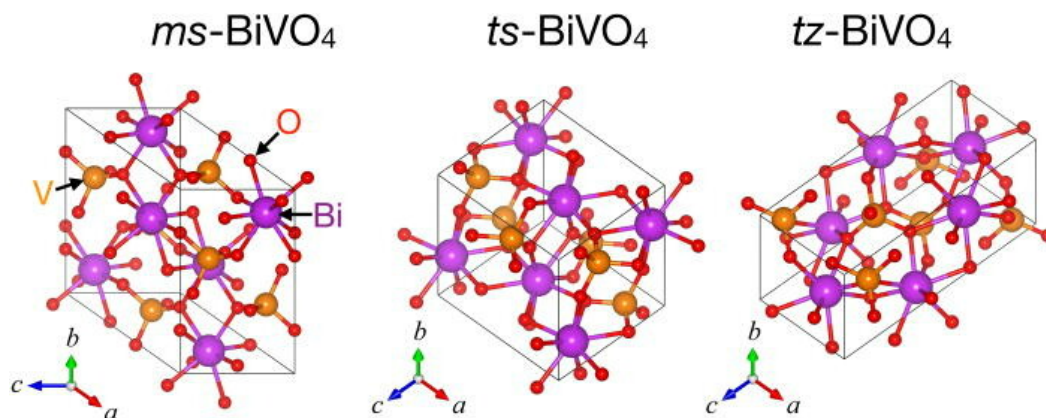
## 2.3 Bismuth vanadate (BiVO<sub>4</sub>)

BiVO<sub>4</sub> is another visible light responsive photocatalytic material that has been given considerable attention as a potential photocatalytic material because of its excellent characteristics such as narrow bandgap (~2.4 eV), non-toxicity, good photostability with photo corrosion resistance and easy fabrication.<sup>75</sup> Starting with Kudo *et al.* in 1999,<sup>76</sup> many other researchers have reported suggesting its use for diverse applications such as gas sensors, solid-state electrolytes, paints and batteries, and for photocatalytic applications such as water splitting, pollutant degradation.<sup>77,78</sup>

### 2.3.1 Crystal and electronic structure of BiVO<sub>4</sub>

BiVO<sub>4</sub> is an n-type semiconductor and found in three crystal phases: monoclinic-scheelite (m-s), tetragonal-zircon (t-z), and tetragonal-scheelite (t-s) as shown in Fig. 2.8.<sup>14,79,80</sup>





**Fig. 2.8.** Crystal structure of  $\text{BiVO}_4$  such as monoclinic scheelite (ms, space group:  $C2/c$ ), tetragonal scheelite (ts, space group:  $I41/a$ ), and tetragonal zircon (tz, space group:  $I41/amd$ ). [Reproduced from Choi *et al. Appl. Phys. Lett.*, 2021, **118**, 161901]<sup>80</sup>

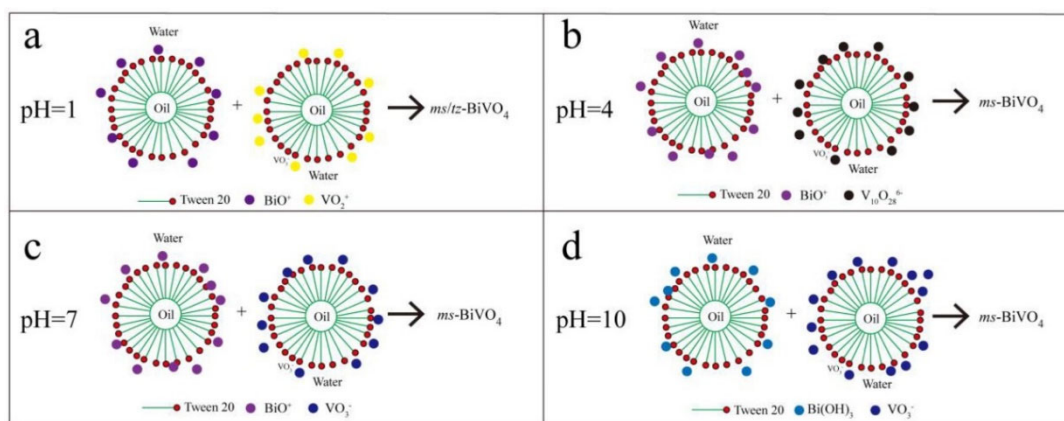
Tetragonal-zircon phase absorbs predominantly UV light with a bandgap of 2.9 eV, whereas monoclinic-scheelite phase absorbs light from both the visible and UV regions of the solar spectrum with a bandgap of 2.4 eV. UV light absorption in monoclinic and tetragonal phase are associated with the band transition from O 2p to V 3d and visible region absorption is caused by the transition from a valence band formed by Bi 6s or a hybrid orbital (made by overlapping of O 2p and Bi 6s) to a conduction band of V 3d.<sup>81</sup> Owing to distorted Bi-O band caused by  $6s^2$  lone pairs of  $\text{Bi}^{3+}$  which increases the separation efficiency of the photo-induced electrons and holes, the monoclinic phase is believed to be most photoactive phase among the three crystal phases.<sup>82</sup> Therefore, controlled synthesis is important to obtain monoclinic phase of  $\text{BiVO}_4$  to achieve good photocatalytic activity. Although  $\text{BiVO}_4$  is an n-type semiconductor but whether it is a direct semiconductor, or an indirect semiconductor is still a matter of debate. Walsh *et al.*<sup>83</sup> observed it to be a direct band gap semiconductor in their first-principles electronic structure analysis of  $\text{BiVO}_4$ , while Cooper *et al.*<sup>84</sup> found it to be indirect bandgap semiconductor in their study by resonant inelastic X-ray scattering.

### 2.3.2 Synthesis of BiVO<sub>4</sub>

It is well known that physiochemical properties and photocatalytic activities of BiVO<sub>4</sub> are highly influenced by its morphology, crystal structure and active facets, which are dependent on the preparation method and reaction conditions.<sup>85,86</sup> To achieve required physiochemical properties and good photocatalytic efficiency by BiVO<sub>4</sub>, researchers have been explored various approaches to do the controlled synthesis including morphology-controlled synthesis, facet-controlled synthesis, and formation of heterostructures, which are discussed in the following sections.,

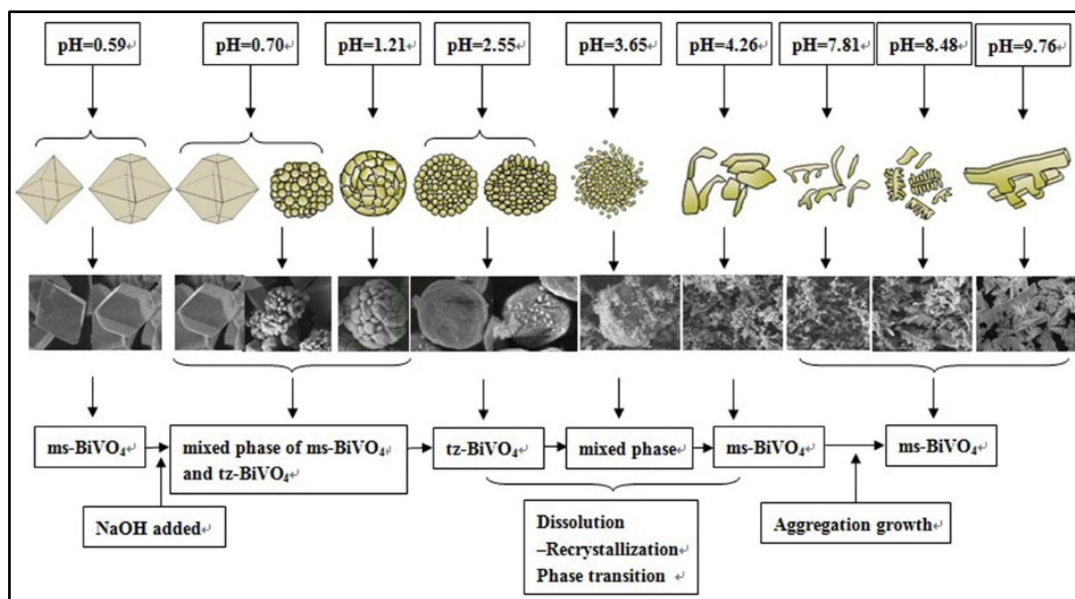
#### 2.3.2.1 Morphology-controlled synthesis

It has been demonstrated that the morphology of BiVO<sub>4</sub> has a significant impact on the efficiency of photocatalytic applications shown by BiVO<sub>4</sub> and the final morphology of BiVO<sub>4</sub> particle is strongly influenced by the preparation method and reaction parameters such as concentration and pH of precursor solution, reaction temperature, time, molar ratio of Bi<sup>3+</sup>/V<sup>5+</sup>, *etc.* The initial pH of the precursor solution is found to be a critical parameter in defining the phase and final morphology of BiVO<sub>4</sub> particles.<sup>78,82,85,87-89</sup> For example, Cao *et al.*<sup>88</sup> recently published an article on the effect of pH on the phase composition and photocatalytic activity of BiVO<sub>4</sub> produced via microemulsion method (Fig. 2.9). At pH = 1, they obtained a composite phase of monoclinic scheelite (ms-BiVO<sub>4</sub>), and tetragonal zircon (tz-BiVO<sub>4</sub>), while pure ms-BiVO<sub>4</sub> was formed in the pH range 4-10. In their study, the composite phase was shown to be more active for photocatalytic degradation of microcystin-LR than the pure ms-BiVO<sub>4</sub> phase because of the lower recombination rate of charge carriers.



**Fig. 2.9.** Schematic diagram of the microemulsion synthesis of  $\text{BiVO}_4$  carried out at  $\text{pH} = 1, 4, 7$  and  $10$ . [Reproduced from Cao *et al. Ceram. Int.*, 2020, **46**, 20788–20797]<sup>88</sup>

Earlier in 2013, Tan and his colleagues reported the detailed study on the effect of pH on crystal structure and morphology of  $\text{BiVO}_4$ . Various structures of  $\text{BiVO}_4$  were produced by the microwave hydrothermal method at different pH values, ranging from highly acidic pH (0.59) to highly basic (12.93) as shown in Fig. 2.10. They found monoclinic  $\text{BiVO}_4$  crystals with decahedron and octahedron microstructures at  $\text{pH}=0.59$  whereas spherical and polyhedral structures were obtained at strong acid condition ( $\text{pH} = 0.70\text{--}1.21$ ) which exhibited a mixed crystal phase (tetragonal and monoclinic). Pure monoclinic phase of  $\text{BiVO}_4$  having rodlike and dendritic structures were obtained in a pH range of 4.26 to 9.76. At pH 3.65, they found the phase transformation from tetragonal phase to monoclinic phase and pH above 9.76, nonstoichiometric crystals were formed which were either mixed-phase  $\text{BiVO}_4$  or non- $\text{BiVO}_4$  structures. In their study, the  $ms\text{-BiVO}_4$  phase obtained at pH 7.81 demonstrated high surface area and better photocatalytic activity than others for Rhodamine B (RhB) dye degradation.<sup>87</sup>



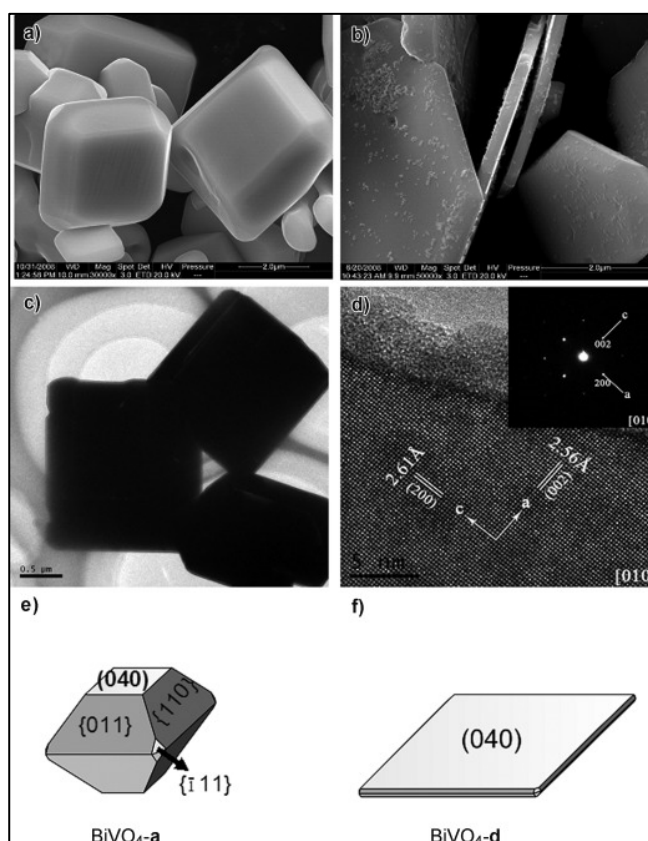
**Fig. 2.10.** The effect of different pH values on the crystalline phase and morphology of the as-prepared  $\text{BiVO}_4$  [Reproduced from Tan *et al.*, *ACS Appl. Mater. Interfaces*, 2013, **5**, 5186–5193]<sup>87</sup>

Likewise, Wu *et al.*<sup>90</sup> tuned the morphology of  $\text{BiVO}_4$  by adjusting the molar ratio of  $\text{Bi}^{3+}/\text{V}^{5+}$  during hydrothermal synthesis of  $\text{BiVO}_4$ . They obtained five different morphologies, dumbbell, rod, ellipsoid, sphere, and cake-like fabricated by varying molar ratio of  $\text{Bi}^{3+}/\text{V}^{5+}$  from 1.0 to 0.4. The cake-like  $\text{BiVO}_4$  microstructure showed higher photocatalytic degradation of RhB dye than other microstructures, which were prepared at 0.4 molar ratio of  $\text{Bi}^{3+}/\text{V}^{5+}$ .

In another report, Huang and his co-workers simultaneously investigated the influence of pH and reaction time during the hydrothermal synthesis of  $\text{BiVO}_4$ . According to their findings, the better photocatalytic activity of ms- $\text{BiVO}_4$  samples was found to be at low pH (=1) and a short period of hydrothermal reaction (12 h).<sup>82</sup> Similar to other parameters, reaction temperature and calcination temperature have also shown their influence on  $\text{BiVO}_4$  morphology leading in variation in their physiochemical and photocatalytic properties.<sup>91–95</sup>

### 2.4.2.2 Facet-controlled synthesis

Several researchers have explored the facet-based engineering on  $\text{BiVO}_4$  to see impact of exposed facet on photocatalytic activity of  $\text{BiVO}_4$ .<sup>81,96–99</sup> Among low indexed facets (*i.e.*  $\{001\}$ ,  $\{010\}$ , and  $\{110\}$  *etc.*),  $\{001\}$  is the preferred growth orientation which has also been proved to be favourable facet for photocatalytic water oxidation.



**Fig. 2.11.** SEM images of samples of (a)  $\text{BiVO}_4$ -a without  $\text{TiCl}_3$  and (b)  $\text{BiVO}_4$ -d with  $\text{TiCl}_3$ , HRTEM images of samples of (c)  $\text{BiVO}_4$ -a and (d)  $\text{BiVO}_4$ -d with its SEAD pattern. Schematic illustrations for (e)  $\text{BiVO}_4$ -a and (f)  $\text{BiVO}_4$ -d. [Reproduced from Wang *et al. Chem. - A Eur. J.*, 2011, **17**, 1275–1282]<sup>99</sup>

Han *et al.*<sup>100</sup> had reported that exposed facet  $\{001\}$  demonstrated sixteen times photocurrent density than randomly oriented  $\text{BiVO}_4$ . Another preferred orientation is  $\{010\}$  which exhibited its importance for photocatalytic degradation.<sup>97,99,101</sup> For example, Kamble and Ling recently carried out a facet dependent investigation and

found the sample with the {040} exposed facet as high-active facet for methylene blue degradation.<sup>97</sup> In an earlier report, Wang *et al.*<sup>99</sup> hydrothermally synthesized uniform decagonal monoclinic BiVO<sub>4</sub> crystals with different facet {040}, {011} and {110} using a directing agent, TiCl<sub>3</sub> as shown in Fig. 2.11a-f. The authors found a correlation between intensity ratio of {040}/{110} and photocatalytic oxidation of water. The higher {040}/{110} ratio means sample with {040} dominant exposed facet was found to be more efficient for the photocatalytic water oxidation.

#### 2.4.2.3 Formation of heterostructures

Researchers have explored morphology and facet-based engineering to obtain efficient BiVO<sub>4</sub> semiconductor, but the poor separation and fast recombination of charge pairs limits its photocatalytic efficiency. In comparison to a single semiconductor, a heterostructure semiconductor coupled with metal or another semiconductor having suitable band structure has been demonstrated an effective approach to improve photocatalytic performance of a semiconductor material. Many BiVO<sub>4</sub> heterostructures have been reported by researchers to investigate the impact on charge separation and transfer.<sup>102–105</sup> For instance, Rathi *et al.*<sup>104</sup> fabricated a BiVO<sub>4</sub>/g-C<sub>3</sub>N<sub>4</sub> heterostructure photocatalyst using hydrothermal method. The authors claimed that prepared heterostructure photocatalyst with 3:1 mass ratio of BiVO<sub>4</sub>/g-C<sub>3</sub>N<sub>4</sub> showed 3.7 times better photocatalytic activity for the 4-chlorophenol degradation than bare BiVO<sub>4</sub> which might be due to improved charge separation and transfer.

Dehdar and his co-workers prepared S-scheme heterostructure by coupling WO<sub>3</sub> with BiVO<sub>4</sub> through hydrothermal route. Their experimental results suggested for 97% degradation of 4-chlorophenol within one hour of visible irradiation by

LED.<sup>103</sup> Zou *et al.*<sup>105</sup> recently synthesized mixed phase BiVO<sub>4</sub> doped with Zn through hydrothermal method. They found that BiVO<sub>4</sub> with 2.5% Zn doping exhibited better photocatalytic efficiency for RhB degradation as 96% degradation in 90 min. Thus, heterostructure formation strategies may pave the way for designing high performance visible light active photocatalyst to be effective for water remediation. Summary of other g-C<sub>3</sub>N<sub>4</sub> based photocatalysts which are recently explored for water treatment and remediation, is given table 2.2.

## 2.4 Other photocatalysts for water remediation

Scientists have been developing a number of efficient, visible light driven photocatalysts to attain solar based applications such as organic degradation, disinfection of waterborne pathogens (bacteria, viruses, Fungai, *etc.*), water splitting and CO<sub>2</sub> reduction. However, here we are mainly giving attention to the photocatalysts being investigated for water treatment application. A summarized data of recently reported photocatalysts other than g-C<sub>3</sub>N<sub>4</sub>, tested for water treatment is listed in table 2.3 and some of them are discussed here.

Zhang *et al.*<sup>106</sup> successfully synthesized ZnSn(OH)<sub>6</sub> (ZSH) microspheres decorated with carbon quantum dots (CQDs) with three different morphologies solid, hollow and yolk-shell using hydrothermal method etching-second growth strategy. He tested pure ZSH and ZSH@CQDs composites for RhB degradation and *Staphylococcus aureus* disinfection under visible light and reported increased photocatalytic activity (70.4% degradation in 8h, 100% inactivation in 16h) of ZSH@CQDs as compared to parent material ZSH moreover among three different structures, ZSH@CQDs yolk shell outperformed. Based on scavenger studies he suggested that h<sup>+</sup> and <sup>•</sup>O<sub>2</sub><sup>-</sup> are the main reactive species for organic degradation while

for water disinfection of *Staphylococcus aureus*,  $\cdot\text{OH}$ ,  $\text{h}^+$  and  $\cdot\text{O}_2^-$  played major role. Unique up-conversion photoluminescence properties of CQDs and efficient charge separation contributed to enhance the photocatalytic activity of ZSH microspheres. Zeng *et al.*<sup>107</sup> fabricated the Z-scheme hetero-junction photocatalyst  $\text{TiO}_2/\text{rGO}/\text{WO}_3$  by hydrolysis - hydrothermal method. Photocatalytic activity of TRW and parent materials were evaluated for disinfection *E. coli* in water which showed the 97.3%, 67.5% bacterial inactivation efficiency in 80 min under simulated solar light and visible light respectively.

Shandilya *et al.*<sup>108</sup> prepared EV/FG24 nanocomposites by dispersing  $\text{EuVO}_4$  (EV) over fluorine doped graphene sheets (FG) where 24 represents the time period given for mechanical shaking in the synthesis of fluorine doped graphene. In their experiments, phenol and 2, 4-dinitrophenol (DNP) were fully degraded by EV/FG24 nanocomposites in 10 h and 89% *E. coli* inactivation was achieved in 3h under visible light. In other work they tried a similar process to prepare  $\text{GdVO}_4/\text{FG}$  and  $\text{SmVO}_4/\text{FG}$  composites which also showed the good photoinactivation properties.<sup>109,110</sup> Li. *et al.*<sup>111</sup> reported the synthesis of Z-scheme heterostructure by deposition of SnS nanoplates on the surface of  $\text{Bi}_2\text{WO}_6$  via bath sonication method. They reported that the photocatalytic activity of SnS- $\text{Bi}_2\text{WO}_6$  was better as compared to pure  $\text{Bi}_2\text{WO}_6$  typically, 68% *E. coli* inactivation and 5.8 times degradation of RhB dye in 60 min. Mazloom and Zamani prepared the  $\text{CeO}_2$ - $\text{SnO}_2$  nanocomposites doped with transition metals (Co, Ni and Mn) by sol-gel method. According to him, doping of transition metals reduced the crystallite size of cubic fluorite structure from 12.1 to 4.7 nm evidenced by XRD peak broadening by Williamson-Hall isotropic strain method and FESEM images. Moreover, decrease in optical bandgap was also observed from 3.23



to 2.91 eV by doping of transition metals. CeO<sub>2</sub>-SnO<sub>2</sub> doped with transition metal Mn showed a better photodegradation rate compared to other samples.<sup>112</sup>

A study was carried out by Zhang *et al.* in order to synthesize vanadium tetrasulfide (VS<sub>4</sub>) nanocomposites coupled by different carbon materials, including VS<sub>4</sub>/CP (carbon powder), VS<sub>4</sub>/rGO (reduced graphene oxides), VS<sub>4</sub>/CF (carbon fiber), and VS<sub>4</sub>/CNT (carbon nanotube). Among them, VS<sub>4</sub>/CP outperformed *E. coli* disinfection activity under simulated sunlight and visible light. It reduced the 9.7 log of *E. coli* in 30 min at 0.1 g L<sup>-1</sup> catalyst loading under visible light irradiation. However, it was not effective for *S. aureus* inactivation with 1.7 log reduction in 30 min.<sup>113</sup> Misra and his colleagues used co-precipitation method to synthesize Fe-doped ZnO nanoparticles impregnated on Kaolinite clay and was found more effective for photocatalytic disinfection of *Enterobacter sp.*, (a multidrug resistant enteric bacteria) than its parent material.<sup>114</sup>

## 2.5 Challenges and future perspectives

Although past few years have been witnessed enormous interest in the development of visible light active photocatalyst, their application in water disinfection has been somewhat overlooked if compared to other applications like H<sub>2</sub> evolution and CO<sub>2</sub> reduction. Some good results have been reported for g-C<sub>3</sub>N<sub>4</sub> and BiVO<sub>4</sub> based materials related to water remediation but the materials and studies in this field are still in primary stages and further focused research and developments are required. Altogether there are several challenges which need to be resolved to get promising g-C<sub>3</sub>N<sub>4</sub>/BiVO<sub>4</sub> based photocatalyst for water disinfection and organic degradation. These include, high recombination rate of charge carriers, limited light

absorption, stability after coupling with other semiconductors, dispersion, and recovery of photocatalyst.

Comparing experimental results from different laboratories is also a major challenge before the scientific community as many factors such as light source, light scattering and reactor design are involved to assess the photocatalytic activity of a photocatalyst during an experiment. According to recent studies, photocatalysts should be compared on the basis of photonic efficiencies or external quantum efficiency (EQE) which allows for reliable comparison and reproducibility of results.<sup>115,116</sup> Most of publications reported photocatalytic disinfection results in terms of percent inactivation which is not really appropriate and hard to analyse the actual efficiency of a photocatalyst because 99%, 99.9%, and 99.99% inactivation reflect only 2, 3, 4 log reduction, respectively. Therefore, one should prefer to report inactivation data in terms of log reduction rather than percentage when analysing photocatalyst efficacy. Similarly, reporting percentage degradation is also inappropriate because it does not provide any information about the reaction, instead, reporting the reaction rate would be more informative and relevant.

Also, there is still a demand to explore new visible light active photocatalyst which could be well effective for water remediation application. Some future perspective regarding effective visible light active photocatalyst comprise: (a) to explore new approaches for light harvesting to absorb the higher wavelengths ( $\lambda > 400$  nm), (b) Finding the way to increase the stability of the heterostructure photocatalysts, (c) finding the practical method for recovery of a photocatalyst. If above mentioned issues could be fixed, practical applications at pilot scale could be further explored.

Table 2.2: Summary of g-C<sub>3</sub>N<sub>4</sub> based photocatalysts for water treatment and remediation

Photocatalyst	Synthesis method	Target microorganism /Organic solvent	Operational Conditions			Inactivation/ Degradation efficiency		Year (Ref.)
			Light source	Catalyst loading	Initial Concentration	Time	Reduction/ Degradation	
g-C <sub>3</sub> N <sub>4</sub> /TiNT	Chemical vapor deposition	<i>E. coli</i>	Visible light			3 h	84%	(2018) <sup>117</sup>
BT-CN-2d g-C <sub>3</sub> N <sub>4</sub>	Delamination	<i>E. coli</i>	300 W Xe lamp Cut off $\lambda > 420$ nm	1 mg mL <sup>-1</sup>	10 <sup>7</sup> CFU mL <sup>-1</sup>	120 min	100%	(2018) <sup>118</sup>
g-C <sub>3</sub> N <sub>4</sub> /EP-520	Thermal method	<i>E. coli</i>	300 W Xe lamp Cut off $\lambda \geq 400$ nm	0.6 g/100 mL	10 <sup>8</sup> CFU mL <sup>-1</sup>	180 min	100%	(2018) <sup>119</sup>
		MS2				240 min		
2D- g-C <sub>3</sub> N <sub>4</sub>	Alternated cooling and heating	<i>E. coli</i>	300 W Xe lamp Cut off $\lambda > 420$ nm		2.5*10 <sup>7</sup> CFU mL <sup>-1</sup>	120 min	100%	(2018) <sup>61</sup>
		Humic acid				70 min	65%	
g-C <sub>3</sub> N <sub>4</sub> /TiO <sub>2</sub>	Hydrothermal	<i>E. coli</i>	300 W Xe lamp 1.5 AM filter	3 mg/30 mL	10 <sup>3</sup> CFU mL <sup>-1</sup>	30 min	> 96.8%	(2018) <sup>70</sup>
AgVO <sub>3</sub> QDs/g-C <sub>3</sub> N <sub>4</sub>	Ultrasonic reaction	Salmonella	300 W Xe lamp Cut off $\lambda > 410$ nm	0.75 mg mL <sup>-1</sup>	10 <sup>7</sup> CFU mL <sup>-1</sup>	10 min	96.4%	(2018) <sup>120</sup>
Boron-and phenyl-codoped g-C <sub>3</sub> N <sub>4</sub>	Thermal polycondensation	<i>E. coli</i>	300 W Xe lamp Cut off $\lambda > 420$ nm	0.15 mg mL <sup>-1</sup>	5*10 <sup>5</sup> CFU mL <sup>-1</sup>	180 min	99.9%	(2018) <sup>121</sup>
CHIT-CNP	Solution casting	<i>E. coli</i>	Sun light	10 mg/50 mL	10 <sup>6</sup> CFU mL <sup>-1</sup>	90 min	6 log	(2018) <sup>122</sup>

Photocatalyst	Synthesis method	Target microorganism /Organic solvent	Operational Conditions			Inactivation/ Degradation efficiency		Year (Ref.)
			Light source	Catalyst loading	Initial Concentration	Time	Reduction/ Degradation	
Ag(2%)/PCNO	Photo-assisted reduction	Amaranth	500 W Xe lamp Cut off $\lambda < 420$ nm	10 mg/50 mL	$1.5 \times 10^{-5}$ M	4 h	$k = 0.327 \text{ h}^{-1}$	(2018) <sup>123</sup>
		<i>S. aureus</i>		$0.2 \text{ g L}^{-1}$	$10^7 \text{ CFU mL}^{-1}$	3 h	99.4%	
g-C <sub>3</sub> N <sub>4</sub> -AgBr	Deposition	<i>E. coli</i> <i>S. aureus</i>	300 W Xe lamp Cut off $\lambda > 400$ nm	0.1 mg mL <sup>-1</sup>	$3 \times 10^6 \text{ CFU mL}^{-1}$	<i>E. coli</i> - 60 min S. <i>aureus</i> - 150 min	100%	(2017) <sup>124</sup>
Ag <sub>2</sub> WO <sub>4</sub> (5%)/g-C <sub>3</sub> N <sub>4</sub>	Polymerization & deposition-precipitation	<i>E. coli</i>	300 W Xe lamp Cut off $\lambda < 420$ nm	100 $\mu\text{g mL}^{-1}$	$10^7 \text{ CFU mL}^{-1}$	90 min	100%	(2017) <sup>73</sup>
g-C <sub>3</sub> N <sub>4</sub> /m-Bi <sub>2</sub> O <sub>4</sub>	Hydrothermal	<i>E. coli</i>	300 W Xe lamp Cut off $\lambda < 400$ nm	$0.4 \text{ g L}^{-1}$	$10^6 \text{ CFU mL}^{-1}$	1.5 h	100%	(2017) <sup>125</sup>
Ni <sub>2</sub> P/g-C <sub>3</sub> N <sub>4</sub>	Hydrothermal	<i>E. coli</i>	300 W Xe lamp Cut off $\lambda > 420$ nm	$1 \text{ mg mL}^{-1}$	$10^7 \text{ CFU mL}^{-1}$	4 h	100%	(2017) <sup>8</sup>
u-g-C <sub>3</sub> N <sub>4</sub>	Thermal polymerization	<i>E. coli</i> <i>S. aureus</i>	300 W Xe lamp Cut off $\lambda > 426$ nm	$1 \text{ mg mL}^{-1}$	$10^6 \text{ CFU mL}^{-1}$		95.5%	(2017) <sup>126</sup>
GO/ g-C <sub>3</sub> N <sub>4</sub>	Sonication	<i>E. coli</i>	300 W Xe lamp Cut off $\lambda < 420$ nm	100 $\mu\text{g mL}^{-1}$	$10^7 \text{ CFU mL}^{-1}$	120 min	97.9%	(2017) <sup>71</sup>
Fullerene (C <sub>60</sub> & C <sub>70</sub> )/ g-C <sub>3</sub> N <sub>4</sub>	Hydrothermal	<i>E. coli</i>	300 W Xe lamp Cut off $\lambda > 420$ nm		$10^8 \text{ CFU mL}^{-1}$	4 h	C <sub>60</sub> /C <sub>3</sub> N <sub>4</sub> -86% C <sub>70</sub> /C <sub>3</sub> N <sub>4</sub> - 100%	(2017) <sup>63</sup>

Photocatalyst	Synthesis method	Target microorganism/Organic solvent	Operational Conditions			Inactivation/ Degradation efficiency		Year (Ref.)
			Light source	Catalyst loading	Initial Concentration	Time	Reduction/ Degradation	
Bi <sub>2</sub> MoO <sub>6</sub> / g-C <sub>3</sub> N <sub>4</sub>	Solvothermal	<i>E. coli</i>	300 W Xe lamp Cut off $\lambda > 420$ nm	0.1 mg mL <sup>-1</sup>	2.5*10 <sup>7</sup> CFU mL <sup>-1</sup>	3 h	100%	(2017) <sup>72</sup>
ns- g-C <sub>3</sub> N <sub>4</sub>	Thermal polymerization & sonication	<i>E. coli</i> <i>S. aureus</i>	270 W Xe lamp Cut off $\lambda = 400$ nm	1 mg mL <sup>-1</sup>	10 <sup>6</sup> CFU mL <sup>-1</sup>	2 h	<i>E. coli</i> – 97.2% <i>S. aureus</i> – 93.7%	(2016) <sup>127</sup>
Ag (3%)/g-C <sub>3</sub> N <sub>4</sub>	Thermal polymerization & photo-assisted reduction	<i>E. coli</i>	300 W Xe lamp Cut off $\lambda < 420$ nm	4 mg mL <sup>-1</sup>	10 <sup>7</sup> CFU mL <sup>-1</sup>	75 min	10 <sup>4.73</sup> CFU/mL	(2016) <sup>41</sup>
g-C <sub>3</sub> N <sub>4</sub> /TiO <sub>2</sub>	Hydrothermal calcination	<i>E. coli</i>	300 W Xe lamp Cut off $\lambda > 420$ nm	30 mg/50 mL	10 <sup>7</sup> CFU mL <sup>-1</sup>	180 min	100%	(2015) <sup>128</sup>
Ag/ g-C <sub>3</sub> N <sub>4</sub>	Polymerization & Sonication	<i>E. coli</i> <i>S. aureus</i>	Visible light	50 $\mu$ g mL <sup>-1</sup>	10 <sup>6</sup> CFU mL <sup>-1</sup>	30 min	100%	(2015) <sup>129</sup>
SL g-C <sub>3</sub> N <sub>4</sub>	Thermal etching & Ultrasonic exfoliation	<i>E. coli</i>	500 W Xe lamp Cut off $\lambda > 400$ nm	0.1 g L <sup>-1</sup>	2*10 <sup>7</sup> CFU mL <sup>-1</sup>	4 h	100%	(2014) <sup>130</sup>
g-C <sub>3</sub> N <sub>4</sub>	Condensation	<i>E. coli</i>	Visible light	1 mg mL <sup>-1</sup>	2.5*10 <sup>6</sup> CFU mL <sup>-1</sup>	4 h	100%	(2014) <sup>60</sup>

Table 2.3: List of other reported photocatalysts for water remediation

Photocatalysts	Synthesis method	Target microorganism/organic pollutant	Operational Conditions			Inactivation/Degradation efficiency		Year (Ref.)
			Light source	Catalyst loading	Initial Concentration	Time	Reduction/Degradation	
SnS-Bi <sub>2</sub> WO <sub>6</sub>	Bath sonication	<i>E. coli</i>	300 W tungsten lamp Cut off ( $\lambda > 410$ nm)	0.1 g/100 mL	10 <sup>6</sup> CFU mL <sup>-1</sup>	60 min	68%	(2019) <sup>111</sup>
		Rhodamine B			10 ppm			
Ag/Fe, N-TiO <sub>2</sub> /Fe <sub>3</sub> O <sub>4</sub> @SiO <sub>2</sub>	Coprecipitation	<i>E. coli</i>	Eight CFL, 8W, (330 W/m <sup>2</sup> )	1 g L <sup>-1</sup>	10 <sup>6</sup> CFU mL <sup>-1</sup>	120 min	100%	(2019) <sup>131</sup>
		Bisphenol A			2 mg L <sup>-1</sup>			
CQDs decorated ZnSn(OH) <sub>6</sub>	Etching-second growth & facile hydrothermal	<i>Staphylococcus aureus</i>	300 W Xe lamp Cut off $\lambda > 420$ nm	80 mg/30 mL	10 <sup>8</sup> CFU mL <sup>-1</sup>	16 h	100%	(2019) <sup>106</sup>
		Rhodamine B		50 mg/100 ml	0.01 mM	8 h	70.4%	
GdVO <sub>4</sub> /FG24	Sonochemical exfoliation	<i>E. coli</i> , <i>B. subtilis</i> , <i>P. fluorescens</i> , <i>S. aureus</i> , and <i>S. enterica</i>	35 W LED lamp	2 mg mL <sup>-1</sup>		180 min	<i>E. coli</i> – 96%, <i>B. subtilis</i> -99%, <i>P. fluore</i> – 99%, <i>S. aureus</i> –100% <i>S. enterica</i> –100%	(2019) <sup>110</sup>
		Phenol, DNP		50 mg/100 mL	1*10 <sup>-4</sup> mol dm <sup>-3</sup>		Phenol- 98% DNP-95%	
meso-Ag/Al <sub>2</sub> O <sub>3</sub>	Hydrothermal	<i>E. coli</i> & <i>S. aureus</i>	Simulated visible light	8 mg L <sup>-1</sup>	10 <sup>6</sup> CFU mL <sup>-1</sup>	120 min	>99.999%	(2018) <sup>132</sup>
Ag/AgBr/ZnFe <sub>2</sub> O <sub>4</sub>	Hydrothermal	<i>E. coli</i>	300 W Xe lamp Cut off $\lambda < 420$ nm	0.1 mg mL <sup>-1</sup>	10 <sup>5.5</sup> CFU mL <sup>-1</sup>	120 min	100%	(2018) <sup>133</sup>
		Methyl orange		1 g L <sup>-1</sup>	10 mg L <sup>-1</sup>	6 min	93.2%	

Photocatalysts	Synthesis method	Target microorganism/or organic pollutant	Operational Conditions			Inactivation/ Degradation efficiency		Year (Ref.)
			Light source	Catalyst loading	Initial Concentration	Time	Reduction/ Degradation	
Fe-(ZnO/K)	Co-precipitation	Enteric MDR bacterium, Enterobacter sp.	160 W LED visible light	150 mg L <sup>-1</sup>	10 <sup>7</sup> CFU mL <sup>-1</sup>	120 min	100%	(2018) <sup>114</sup>
Fe <sub>3</sub> O <sub>4</sub> @BiOI@AgI	Multi step process (solvothermal, precipitation, ion exchange reaction)	Rhodamine B and Bisphenol A	300 W Xe lamp Cut off $\lambda \geq 420$ nm	0.5 mg mL <sup>-1</sup>	RhB - 5 mg/L BPA - 20 mg L <sup>-1</sup>	RhB- 60 min, BPA- 50 min	RhB- 92%, BPA- 70%	(2018) <sup>134</sup>
		<i>E. coli</i>		0.08 mg mL <sup>-1</sup>	3*10 <sup>7</sup> CFU mL <sup>-1</sup>	48 min	100%	
CeO <sub>2</sub> -SnO <sub>2</sub> :TM (TM= Co, Ni and Mn)	Sol-gel	Rhodamine B	UV -A Light (400 W)	2 mg L <sup>-1</sup>	40 mg L <sup>-1</sup>	120 min	50%	(2018) <sup>112</sup>
		<i>E. coli</i> <i>P. aeruginosa</i> <i>S. aureus</i>			1.5*10 <sup>8</sup> CFU mL <sup>-1</sup>			
Ag (2%)/CeO <sub>2</sub>	Impregnation and photo-assisted reduction	<i>E. coli</i>	300 W Xe lamp Cut off $\lambda < 420$ nm	4 mg mL <sup>-1</sup>	10 <sup>7</sup> CFU mL <sup>-1</sup>	150 min	100%	(2018) <sup>135</sup>
ZnO/AAO	Anodization and Hydrothermal	<i>E. coli</i>	UV light		10 <sup>8</sup> -10 <sup>9</sup> CFU mL <sup>-1</sup>		70%	(2018) <sup>136</sup>
CdSe (QDs)/graphene /TiO <sub>2</sub>	Precipitation & Hydrothermal	<i>E. coli</i>	350 W Xe lamp Cut off $\lambda \leq 420$ nm	20 mg/ 30 mL	10 <sup>7</sup> CFU mL <sup>-1</sup>	60 min	90%	(2018) <sup>137</sup>
		Methylene blue		2.5mg mL <sup>-1</sup>	2*10 <sup>-5</sup> M	60 min		

Photocatalysts	Synthesis method	Target microorganism/or organic pollutant	Operational Conditions			Inactivation/ Degradation efficiency		Year (Ref.)
			Light source	Catalyst loading	Initial Concentration	Time	Reduction/ Degradation	
Cu-TiO <sub>2</sub>	Electrospinning	Bacteriophage f2 & <i>E. coli</i>	300 W Xe lamp Cut off $\lambda > 400$ nm	75 mg/L	10*5 CFU mL <sup>-1</sup>	120 min	100%	(2018) <sup>138</sup>
VS <sub>4</sub> /CP	Hydrothermal	<i>E. coli</i>	300 W Xe lamp Cut off $\lambda > 420$ nm	0.1 g L <sup>-1</sup>	10 <sup>9</sup> CFU mL <sup>-1</sup>	30 min	9.7 log	(2018) <sup>113</sup>
		<i>S. aureus</i>					1.7 log	
Polyether sulfone (PES) fiber	Electrospinning technique	Methylene blue	Simulated visible light	3 cm*3 cm in 30 mL	10 $\mu$ M	180 min	80%	(2018) <sup>139</sup>
		<i>E. coli</i>				6 h	78%	
Ag/AgCl/ZnFe <sub>2</sub> O <sub>4</sub>	Hydrothermal	RhB BPA	300 W Xe lamp Cut off $\lambda > 400$ nm	1 mg mL <sup>-1</sup>	10 mg/L	RhB- 70 min BPA- 120 min	RhB- ~100% BPA- 66.8%	(2018) <sup>140</sup>
		<i>E. coli</i>				15 min	100%	
SmVO <sub>4</sub> /FG24	Sonochemical exfoliation	<i>E. coli</i> , <i>B. subtilis</i> , <i>P. fluorescens</i> , <i>S. aureus</i> , and <i>S. enterica</i>	35 W LED lamp	2 mg mL <sup>-1</sup>	10 <sup>6</sup> CFU mL <sup>-1</sup>	180 min	<i>E. coli</i> –95%, <i>B. subtilis</i> –98%, <i>P. fluore</i> – 90%, <i>S. aureus</i> –96%, <i>S. enterica</i> –100%	(2018) <sup>109</sup>
		Phenol DNP		50 mg/100 mL	1*10 <sup>-4</sup> mol dm <sup>-3</sup>		Phenol- 95% DNP-88 %	
N-doped TiO <sub>2</sub> -coated membrane	Sol-gel deposition	MS2 bacteriophage	300 W Xe lamp Cut off $\lambda > 400$ nm		10 <sup>6</sup> CFU mL <sup>-1</sup>	120 min	99.99%	(2018) <sup>141</sup>



Photocatalysts	Synthesis method	Target microorganism/organic pollutant	Operational Conditions			Inactivation/Degradation efficiency		Year (Ref.)
			Light source	Catalyst loading	Initial Concentration	Time	Reduction/Degradation	
EuVO <sub>4</sub> /FG24	Sonochemical exfoliation	<i>E. coli</i> , <i>B. subtilis</i> , <i>P. fluorescense</i> , <i>S. aureus</i> , and <i>S. enterica</i>	35 W LED lamp	2 mg mL <sup>-1</sup>	1*10 <sup>-4</sup> mol dm <sup>-3</sup>	180 min	<i>E. coli</i> – 89% <i>B. subtilis</i> – 95%, <i>P. fluore.</i> – 97%, <i>S. aureus</i> – 99%, <i>S. enterica</i> –100%	(2018) <sup>108</sup>
		Phenol DNP		50 mg/100 mL			Phenol- 95% DNP-88 %	
Ag-doped TiO <sub>2</sub> /SiO <sub>2</sub>		<i>B. subtilis</i>	Four 6W lamp (λ: 300-400 nm)		10 <sup>5</sup> CFU mL <sup>-1</sup>	180 min	0.053 min <sup>-1</sup>	(2017) <sup>142</sup>
TiO <sub>2</sub> and (C-dots) co-decorated reduced graphene oxide	Hydrothermal	<i>E. coli</i>	300 W Xe lamp 1.5 AM filter	3 mg/30 mL	1.5*10 <sup>3</sup> CFU mL <sup>-1</sup>	60 min	1.03 log	(2017) <sup>143</sup>
TiO <sub>2</sub> /rGO/WO <sub>3</sub>	hydrolysis-hydrothermal	<i>E. coli</i>	200 W Hg-Xe lamp 1.5 AM filter	3 mg/30 mL	2*10 <sup>3</sup> CFU mL <sup>-1</sup>	80 min	97.3±3.8%	(2017) <sup>107</sup>
Ag@MOF-5		<i>E. coli</i>	Visible light			70 min	>91%	(2017) <sup>144</sup>
Ag@TiO <sub>2</sub>	Hydrolysis	<i>E. coli</i>	Real sun (I <sub>avg</sub> =970*10 <sup>2</sup> lux)	0.4 g L <sup>-1</sup>	40*10 <sup>8</sup> CFU mL <sup>-1</sup>	15 min	100%	(2017) <sup>145</sup>

## 2.6 References

1. Kshetri, Y. K., Regmi, C., Kim, T.-H. & Lee, S. W. BiVO<sub>4</sub>, a ternary metal oxide as an efficient photocatalytic material. in *Current Developments in Photocatalysis and Photocatalytic Materials*, Elsevier, 2020, 245–266. (doi:10.1016/B978-0-12-819000-5.00016-3)
2. Byrne, J. A., Fernandez-Ibañez, P. A., Dunlop, P. S. M., Alrousan, D. M. A. & Hamilton, J. W. J. Photocatalytic enhancement for solar disinfection of water: A Review. *Int. J. Photoenergy*, 2011, **2011**, 1–12.
3. Byrne, J. A., Fernández-Ibañez, P., & Sharma P. K. Water scarcity in developing regions. in *Sustainable Water Management* (ed. Chen, D. H.), CRC Press, 2016, 227–248. (doi:10.1201/9781315373850)
4. Gogoi A., Mazumder P., Tyagi V. K., Tushara Chaminda G.G., An A.K., & Kumar M. Occurrence and fate of emerging contaminants in water environment: A review. *Groundw. Sustain. Dev.* 2018, **6**, 169–180.
5. Bethi, B., Sonawane, S. H., Bhanvase, B. A. & Gumfekar, S. P. Nanomaterials-based advanced oxidation processes for wastewater treatment: A review. *Chem. Eng. Process. - Process Intensif.* 2016, **109**, 178–189.
6. Fernandez-Ibañez, P., Byrne, J. A., López, M. I. P., Singh, A. McMichael, S., & Singhal, A. Photocatalytic inactivation of microorganisms in water. in *Nanostructured Photocatalysts*, Elsevier, 2020, **148**, 229–248.
7. Cao, S., Low, J., Yu, J. & Jaroniec, M. Polymeric Photocatalysts Based on Graphitic Carbon Nitride. *Adv. Mater.* 2015, **27**, 2150–2176.
8. Cui, Y., Yang, C., Tang, S., Zhao, Y. & Chen, F. Two dimension C<sub>3</sub>N<sub>4</sub>/MoS<sub>2</sub> nanocomposites with enhanced photocatalytic hydrogen evolution under visible light irradiation. *J. Wuhan Univ. Technol. Sci. Ed.* 2019, **34**, 23–29.
9. Zhao, H., Yu, H., Quan, X., Chen, S., Zhang, Y., Zhao, H., & Wang, H. Fabrication of atomic single layer graphitic-C<sub>3</sub>N<sub>4</sub> and its high performance of photocatalytic disinfection under visible light irradiation. *Appl. Catal. B Environ.* 2014, **152–153**, 46–50.
10. Masih, D., Ma, Y. & Rohani, S. Graphitic C<sub>3</sub>N<sub>4</sub> based noble-metal-free photocatalyst systems: A review. *Appl. Catal. B Environ.* 2017, **206**, 556–588.
11. Niu, P., Yin, L., Yang, Y., Liu, G. & Cheng, H. Increasing the visible light absorption of graphitic carbon nitride (melon) photocatalysts by homogeneous

- self-modification with nitrogen vacancies. *Adv. Mater.* 2014, **26**, 8046–8052.
12. Ong, W., Tan, L., Ng, Y. H., Yong, S. & Chai, S. Graphitic carbon nitride (g-C<sub>3</sub>N<sub>4</sub>)-based photocatalysts for artificial photosynthesis and environmental remediation: are we a step closer to achieving sustainability? *Chem. Rev.* 2016, **116**, 7159–7329.
  13. Rather, R. A., Mehta, A., Lu, Y., Valant, M., Fang, M., & Liu, W. Influence of exposed facets, morphology and hetero-interfaces of BiVO<sub>4</sub> on photocatalytic water oxidation: A review. *Int. J. Hydrogen Energy*, 2021, **46**, 21866–21888.
  14. A. M., J., M., Muthupandian, A. K., & Prabhakaran, A. A review on BiVO<sub>4</sub> photocatalyst: Activity enhancement methods for solar photocatalytic applications. *Appl. Catal. A Gen.* 2018, **555**, 47–74.
  15. Wang, X., Maeda, K., Thomas, A., Takanabe, K., Xin, G., Carlsson, J. M., Domen, K., & Antonietti, M. A metal-free polymeric photocatalyst for hydrogen production from water under visible light. *Nat. Mater.* 2009, **8**, 76–80.
  16. Zhang, C., Li, Y., Shuai, D., Shen, Y., Xiong, W., & Wang, L. Graphitic carbon nitride (g-C<sub>3</sub>N<sub>4</sub>)-based photocatalysts for water disinfection and microbial control: A review. *Chemosphere*, 2019, **214**, 462–479 (2019).
  17. Wang, X., Blechert, S. & Antonietti, M. Polymeric graphitic carbon nitride for heterogeneous photocatalysis. *ACS Catal.* 2012, **2**, 1596–1606.
  18. Semencha, A. V. & Blinov, L. N. Theoretical prerequisites, problems, and practical approaches to the preparation of carbon nitride: A Review. *Glas. Phys. Chem.* 2010, **36**, 199–208.
  19. Thomas, A., Fischer, A., Goettmann, F., Antonietti, M., Müller, J. O., Schlögl, R., & Carlsson, J. M. Graphitic carbon nitride materials: variation of structure and morphology and their use as metal-free catalysts. *J. Mater. Chem.* 2008, **18**, 4893.
  20. Kroke, E., Schwarz, M., Horath-Bordon, E., Kroll, P., Noll, B., & Norman, A. D. Tri-s-triazine derivatives. Part I. From trichloro-tri-s-triazine to graphitic C<sub>3</sub>N<sub>4</sub> structures Part II: Alkalicyamelurates M<sub>3</sub>[C<sub>6</sub>N<sub>7</sub>O<sub>3</sub>], M = Li, Na, K, Rb, Cs, manuscript in preparation. *New J. Chem.* 2002, **26**, 508–512.
  21. Matsumoto, S., Xie, E.-Q. & Izumi, F. On the validity of the formation of crystalline carbon nitrides, C<sub>3</sub>N<sub>4</sub>. *Diam. Relat. Mater.* 1999, **8**, 1175–1182.
  22. Justus Liebig. Über einige Stickstoff-Verbindungen. *Ann. der Pharm.* 1834, **10**,

- 1–47.
23. Franklin, E. C. The ammono carbonic acids. *J. Am. Chem. Soc.* 1922, **44**, 486–509.
  24. Pauling, L. & Sturdivant, J. H. The structure of cyameluric acid, hydromelonic acid and related substances. *Proc. Natl. Acad. Sci.* 1937, **23**, 615–620.
  25. Redemann, C. E. & Lucas, H. J. Some derivatives of cyameluric acid and probable structures of melam, melem and melon. *J. Am. Chem. Soc.* 1940, **62**, 842–846.
  26. Hosmane, R. S., Rossman, M. A. & Leonard, N. J. Synthesis and structure of tri-s-triazine. *J. Am. Chem. Soc.* 1982, **104**, 5497–5499.
  27. Goettmann, F., Fischer, A., Antonietti, M. & Thomas, A. Metal-free catalysis of sustainable Friedel–Crafts reactions: direct activation of benzene by carbon nitrides to avoid the use of metal chlorides and halogenated compounds. *Chem. Commun.* 2006, 4530–4532.
  28. Teter, D. M. & Hemley, R. J. Low-compressibility carbon nitrides. *Science*. 1996, **271**, 53–55.
  29. Xu, Y. & Gao, S. Band gap of C<sub>3</sub>N<sub>4</sub> in the GW approximation. *Int. J. Hydrogen Energy* 2012, **37**, 11072–11080.
  30. Lotsch, B. V & Schnick, W. From Triazines to Heptazines: novel nonmetal tricyanomelaminates as precursors for graphitic carbon nitride materials. *Chem. Mater.* 2006, **18**, 1891–1900.
  31. Ramacharyulu, P. V. R. K., Abbas, S. J. & Ke, S. Enhanced charge separation and photoactivity in heterostructured g-C<sub>3</sub>N<sub>4</sub>: a synergistic interaction in environmental friendly CaO/g-C<sub>3</sub>N<sub>4</sub>. *Catal. Sci. Technol.* 2017, **7**, 4940–4943.
  32. Mo, Z., She, X., Li, Y., Liu, L., Huang, L., Chen, Z., Zhang, Q., Xu, H., & Li, H. Synthesis of g-C<sub>3</sub>N<sub>4</sub> at different temperatures for superior visible/UV photocatalytic performance and photoelectrochemical sensing of MB solution. *RSC Adv.* 2015, **5**, 101552–101562.
  33. Papailias, I., Giannakopoulou, T., Todorova, N., Demotikali, D., Vaimakis, T., & Trapalis, C. Effect of processing temperature on structure and photocatalytic properties of g-C<sub>3</sub>N<sub>4</sub>. *Appl. Surf. Sci.* 2015, **358**, 278–286.
  34. Gao, J., Zhou, Y., Li, Z., Yan, S., Wang, N., & Zou, Z. High-yield synthesis of millimetre-long, semiconducting carbon nitride nanotubes with intense photoluminescence emission and reproducible photoconductivity. *Nanoscale*

- 2012, **4**, 3687.
35. Gao, Q., Hu, S., Du, Y. & Hu, Z. The origin of the enhanced photocatalytic activity of carbon nitride nanotubes: a first-principles study. *J. Mater. Chem. A* 2017, **5**, 4827–4834.
  36. Haque, E., Jun, J. W., Talapaneni, S. N., Vinu, A. & Jhung, S. H. Superior adsorption capacity of mesoporous carbon nitride with basic CN framework for phenol. *J. Mater. Chem.* 2010, **20**, 10801–10803.
  37. Wen, J., Xie, J., Chen, X. & Li, X. A review on g-C<sub>3</sub>N<sub>4</sub> -based photocatalysts. *Appl. Surf. Sci.* 2017, **391**, 72–123.
  38. Li, X., Sun, Q., Li, M., Yang, J., Chen, X., Yang, Y., Li, X., Hu, T., Sui, Y., & Wu, X. Photocatalytic properties of nano-structured carbon nitride: a comparison with bulk graphitic carbon nitride. *Int. J. Mater. Res.* 2018, **109**, 129–135.
  39. Jiang, J., Ou-Yang, L. Zhu, L., Zheng, A., Zou, J., Yi, X., & Tang, H. Dependence of electronic structure of g-C<sub>3</sub>N<sub>4</sub> on the layer number of its nanosheets: A study by Raman spectroscopy coupled with first-principles calculations. *Carbon N. Y.* 2014, **80**, 213–221.
  40. Xiang, Q., Yu, J. & Jaroniec, M. Preparation and enhanced visible-light photocatalytic H<sub>2</sub>-production activity of graphene/C<sub>3</sub>N<sub>4</sub> composites. *J. Phys. Chem. C* 2011, **115**, 7355–7363.
  41. Ma, S., Zhan, S., Jia, Y., Shi, Q. & Zhou, Q. Enhanced disinfection application of Ag-modified g-C<sub>3</sub>N<sub>4</sub> composite under visible light. *Appl. Catal. B Environ.* 2016, **186**, 77–87.
  42. Zhu, B., Xia, P., Ho, W. & Yu, J. Isoelectric point and adsorption activity of porous g-C<sub>3</sub>N<sub>4</sub>. *Appl. Surf. Sci.* 2015, **344**, 188–195.
  43. Thanh Truc, N. T. *et al.* The superior photocatalytic activity of Nb doped TiO<sub>2</sub>/g-C<sub>3</sub>N<sub>4</sub> direct Z-scheme system for efficient conversion of CO<sub>2</sub> into valuable fuels. *J. Colloid Interface Sci.* 2019, **540**, 1–8.
  44. Huang, L. *et al.* Visible-light-induced WO<sub>3</sub>/g-C<sub>3</sub>N<sub>4</sub> composites with enhanced photocatalytic activity. *Dalt. Trans.* 2013, **42**, 8606–8616.
  45. Liu, J., Zhang, T., Wang, Z., Dawson, G. & Chen, W. Simple pyrolysis of urea into graphitic carbon nitride with recyclable adsorption and photocatalytic activity. *J. Mater. Chem.* 2011, **21**, 14398.
  46. Wei, X., Qiu, Y., Duan, W. & Liu, Z. Cathodic and anodic photocurrents

- generation from melem and its derivatives. *RSC Adv.* 2015, **5**, 26675–26679.
47. Chu, S., Wang, Y., Guo, Y., Feng, J., Wang, C., Luo, W., Fan, X., & Zou, Z. Band structure engineering of carbon nitride: in search of a polymer photocatalyst with high photooxidation property. *ACS Catal.* 2013, **3**, 912–919.
  48. Armstrong, D. A. *et al.* Standard electrode potentials involving radicals in aqueous solution: inorganic radicals (IUPAC Technical Report). *Pure Appl. Chem.* 2015, **87**, 1139–1150.
  49. Armstrong, D. A., Huie, R. E., Lyman, S., Koppenol, W. H., Merényi, G., Neta, P., Stanbury, D. M., Steenken, S., & Wardman, P. Standard electrode potentials involving radicals in aqueous solution: inorganic radicals. *Bioinorg. React. Mech.* 2013, **9**, 59–61.
  50. Cheng, C., Huang, Y., Tian, X., Zheng, B., Li, Y., Yuan, H., Xiao, D., Xie, S., & Choi, M. M. F. Electrogenerated chemiluminescence behavior of graphite-like carbon nitride and its application in selective sensing  $\text{Cu}^{2+}$ . *Anal. Chem.* 2012, **84**, 4754–4759.
  51. Hwang, S., Lee, S. & Yu, J. Template-directed synthesis of highly ordered nanoporous graphitic carbon nitride through polymerization of cyanamide. *Appl. Surf. Sci.* 2007, **253**, 5656–5659.
  52. Zhai, H., Cao, L. & Xia, X. Synthesis of graphitic carbon nitride through pyrolysis of melamine and its electrocatalysis for oxygen reduction reaction. *Chinese Chem. Lett.* 2013, **24**, 103–106.
  53. Yang, F., Lublow, M., Orthmann, S., Merschjann, C., Tyborski, T., Rusu, M., Kubala, S., Thomas, A., Arrigo, R., Hävecker, M., & Schedel-Niedrig, T. Metal-free photocatalytic graphitic carbon nitride on p-type chalcopyrite as a composite photocathode for light-induced hydrogen evolution. *ChemSusChem*, 2012, **5**, 1227–1232.
  54. Zhang, G., Zhang, J., Zhang, M. & Wang, X. Polycondensation of thiourea into carbon nitride semiconductors as visible light photocatalysts. *J. Mater. Chem.* 2012, **22**, 8083.
  55. Cui, Y., Zhang, J., Zhang, G., Huang, J., Liu, P., Antonietti, M., & Wang, X. Synthesis of bulk and nanoporous carbon nitride polymers from ammonium thiocyanate for photocatalytic hydrogen evolution. *J. Mater. Chem.* 2011, **21**, 13032.
  56. Lee, S. C., Lintang, H. O. & Yuliati, L. A urea precursor to synthesize carbon

- nitride with mesoporosity for enhanced activity in the photocatalytic removal of phenol. *Chem. - An Asian J.* 2012, **7**, 2139–2144.
57. Zhang, W., Zhang, Q., Dong, F. & Zhao, Z. The multiple effects of precursors on the properties of polymeric carbon nitride. *Int. J. Photoenergy* 2013, **2013**, 1–9.
  58. Theerthagiri, J., Senthil, R. A., Madhavan, J. & Neppolian, B. A comparative study on the role of precursors of graphitic carbon nitrides for the photocatalytic degradation of direct red 81. *Mater. Sci. Forum* 2014, **807**, 101–113.
  59. Devthade, V., Kulhari, D. & Umare, S. S. Role of precursors on photocatalytic behavior of graphitic carbon nitride. *Mater. Today Proc.* 2018, **5**, 9203–9210.
  60. Huang, J., Ho, W. & Wang, X. Metal-free disinfection effects induced by graphitic carbon nitride polymers under visible light illumination. *Chem. Commun.* 2014, **50**, 4338.
  61. Kang, S., Zhang, L., He, M., Zheng, Y., Cui, L., Sun, D., & Hu, B. ‘Alternated cooling and heating’ strategy enables rapid fabrication of highly-crystalline g-C<sub>3</sub>N<sub>4</sub> nanosheets for efficient photocatalytic water purification under visible light irradiation. *Carbon N. Y.* 2018, **137**, 19–30.
  62. Cui, Y., Li, M., Wang, H., Yang, C., Meng, S., & Chen, F. In-situ synthesis of sulfur doped carbon nitride microsphere for outstanding visible light photocatalytic Cr(VI) reduction. *Sep. Purif. Technol.* 2018, **199**, 251–259.
  63. Ouyang, K., Dai, K., Chen, H., Huang, Q., Gao, C., & Cai, P. Metal-free inactivation of *E. coli* O157:H7 by fullerene/C<sub>3</sub>N<sub>4</sub> hybrid under visible light irradiation. *Ecotoxicol. Environ. Saf.* 2017, **136**, 40–45.
  64. Gao, J., Wang, J., Qian, X., Dong, Y., Xu, H., Song, R., Yan, C., Zhu, H., Zhong, Q., Qian, G., & Yao, J. One-pot synthesis of copper-doped graphitic carbon nitride nanosheet by heating Cu–melamine supramolecular network and its enhanced visible-light-driven photocatalysis. *J. Solid State Chem.* 2015, **228**, 60–64.
  65. Xu, J., Gao, Q., Bai, X., Wang, Z. & Zhu, Y. Enhanced visible-light-induced photocatalytic degradation and disinfection activities of oxidized porous g-C<sub>3</sub>N<sub>4</sub> by loading Ag nanoparticles. *Catal. Today* 2019, **332**, 227–235.
  66. Jourshabani, M., Shariatnia, Z. & Badiei, A. Sulfur-doped mesoporous carbon nitride decorated with Cu particles for efficient photocatalytic degradation under visible-light irradiation. *J. Phys. Chem. C* 2017, **121**, 19239–19253.

67. Barbero, N. & Vione, D. Why Dyes Should Not Be Used to Test the Photocatalytic Activity of Semiconductor Oxides. *Environ. Sci. Technol.* 2016, **50**, 2130–2131.
68. Rochkind, M., Pasternak, S. & Paz, Y. Using dyes for evaluating photocatalytic properties: A critical review. *Molecules* 2015, **20**, 88–110.
69. Reza, K. M., Kurny, A. & Gulshan, F. Parameters affecting the photocatalytic degradation of dyes using TiO<sub>2</sub>: a review. *Appl. Water Sci.* 2017, **7**, 1569–1578.
70. Liu, Y., Zeng, X., Hu, X., Hu, J., Wang, Z., Yin, Y., Sun, C., & Zhang, X. Two-dimensional g-C<sub>3</sub>N<sub>4</sub>/TiO<sub>2</sub> nanocomposites as vertical Z-scheme heterojunction for improved photocatalytic water disinfection. *Catal. Today* 2019, **335**, 243–251.
71. Sun, L., Du, T., Hu, C., Chen, J., Lu, J., Lu, Z., & Han, H. Antibacterial activity of graphene oxide/g-C<sub>3</sub>N<sub>4</sub> composite through photocatalytic disinfection under visible light. *ACS Sustain. Chem. Eng.* 2017, **5**, 8693–8701.
72. Li, J., Yin, Y., Liu, E., Ma, Y., Wan, J., Fan, J., & Hu, X. In situ growing Bi<sub>2</sub>MoO<sub>6</sub> on g-C<sub>3</sub>N<sub>4</sub> nanosheets with enhanced photocatalytic hydrogen evolution and disinfection of bacteria under visible light irradiation. *J. Hazard. Mater.* 2017, **321**, 183–192.
73. Li, Y., Li, Y., Ma, S., Wang, P., Hou, Q., Han, J., & Zhan, S. Efficient water disinfection with Ag<sub>2</sub>WO<sub>4</sub> -doped mesoporous g-C<sub>3</sub>N<sub>4</sub> under visible light. *J. Hazard. Mater.* 2017, **338**, 33–46.
74. Faraji, M., Mohaghegh, N. & Abedini, A. Ternary composite of TiO<sub>2</sub> nanotubes/Ti plates modified by g-C<sub>3</sub>N<sub>4</sub> and SnO<sub>2</sub> with enhanced photocatalytic activity for enhancing antibacterial and photocatalytic activity. *J. Photochem. Photobiol. B Biol.* 2018, **178**, 124–132.
75. Ganeshbabu, M., Kannan, N., Venkatesh, P. S., Paulraj, G., Jeganathan, K., & MubarakAli, D. Synthesis and characterization of BiVO<sub>4</sub> nanoparticles for environmental applications. *RSC Adv.* 2020, **10**, 18315–18322.
76. Kudo, A., Omori, K. & Kato, H. A novel aqueous process for preparation of crystal form-controlled and highly crystalline BiVO<sub>4</sub> powder from layered vanadates at room temperature and its photocatalytic and photophysical properties. *J. Am. Chem. Soc.* 1999, **121**, 11459–11467.
77. Zhou, L., Wang, W., Zhang, L., Xu, H. & Zhu, W. Single-crystalline BiVO<sub>4</sub> microtubes with square cross-sections: microstructure, growth mechanism, and



- photocatalytic property. *J. Phys. Chem. C* 2007, **111**, 13659–13664.
78. Li, J.-Q., Guo, Z.-Y., Wang, D.-F., Lui, H., Du, J., & Zhu, Z.-F. Effects of pH value on the surface morphology of BiVO<sub>4</sub> microspheres and removal of methylene blue under visible light. *J. Exp. Nanosci.* 2014, **9**, 616–624.
79. Tokunaga, S., Kato, H. & Kudo, A. Selective preparation of monoclinic and tetragonal BiVO<sub>4</sub> with scheelite structure and their photocatalytic properties. *Chem. Mater.* 2001, **13**, 4624–4628.
80. Choi, M. Photocatalytic and photoelectrochemical activities of strained BiVO<sub>4</sub>. *Appl. Phys. Lett.* 2021, **118**, 161901.
81. Lardhi, S., Cavallo, L. & Harb, M. Significant impact of exposed facets on the BiVO<sub>4</sub> material performance for photocatalytic water splitting reactions. *J. Phys. Chem. Lett.* 2020, **11**, 5497–5503.
82. Huang, J. G., Wang, B., Pang, S., Zhang, X. Y., Yang, X. Y., Guo, X. T., & Wang, X. S. Effects of pH value and hydrothermal time on the structure and photocatalytic activity of monoclinic-scheelite BiVO<sub>4</sub>. *Optoelectron. Adv. Mater. Rapid Commun.* 2015, **9**, 1273–1279.
83. Walsh, A., Yan, Y., Huda, M. N., Al-Jassim, M. M. & Wei, S.-H. Band Edge Electronic Structure of BiVO<sub>4</sub>: Elucidating the role of the Bi s and V d orbitals. *Chem. Mater.* 2009, **21**, 547–551.
84. Cooper, J. K., Gul, S., Toma, F. M., Chen, L., Liu, Y.-S., Guo, J., Ager, J. W., Yano, J., & Sharp, I. D. Indirect bandgap and optical properties of monoclinic bismuth vanadate. *J. Phys. Chem. C* 2015, **119**, 2969–2974.
85. Wan, Y., Wang, S., Luo, W. & Zhao, L. Impact of preparative pH on the morphology and photocatalytic activity of BiVO<sub>4</sub>. *Int. J. Photoenergy* 2012, **2012**, 1–7.
86. Wang, X., Liu, H., Wang, J., Chang, L., Song, N., Yan, Z., & Wan, X. Additive-free solvothermal preparation, characterization, and photocatalytic activity of 3D butterfly-like BiVO<sub>4</sub>. *Res. Chem. Intermed.* 2015, **41**, 2465–2477.
87. Tan, G., Zhang, L., Ren, H., Wei, S., Huang, J., & Xia, A. Effects of pH on the hierarchical structures and photocatalytic performance of BiVO<sub>4</sub> Powders prepared via the microwave hydrothermal method. *ACS Appl. Mater. Interfaces* 2013, **5**, 5186–5193.
88. Cao, X., Gu, Y., Tian, H., Fang, Y., Johnson, D., Ren, Z., Chen, C., & Huang, Y. Microemulsion synthesis of ms/tz-BiVO<sub>4</sub> composites: The effect of pH on

- crystal structure and photocatalytic performance. *Ceram. Int.* 2020, **46**, 20788–20797.
89. Sun, M., Guo, P., Wang, M. & Ren, F. The effect of pH on the photocatalytic performance of BiVO<sub>4</sub> for phenol mine sewage degradation under visible light. *Optik (Stuttg)*. 2019, **179**, 672–679.
90. Wu, M., Jing, Q., Feng, X. & Chen, L. BiVO<sub>4</sub> microstructures with various morphologies: Synthesis and characterization. *Appl. Surf. Sci.* 2018, **427**, 525–532.
91. Shen, Y., Wang, X., Zuo, G., Li, F. & Meng, Y. Influence of heat treatment on photocatalytic performance of BiVO<sub>4</sub> synthesized by hydrothermal method. *High Temp. Mater. Process.* 2016, **35**, 853–856.
92. Chen, Q., Zhou, M., Ma, D. & Jing, D. Effect of preparation parameters on photoactivity of BiVO<sub>4</sub> by hydrothermal method. *J. Nanomater.* 2012, **2012**, 1–6.
93. Ke, D., Peng, T., Ma, L., Cai, P. & Dai, K. Effects of hydrothermal temperature on the microstructures of BiVO<sub>4</sub> and its photocatalytic O<sub>2</sub> evolution activity under visible light. *Inorg. Chem.* 2009, **48**, 4685–4691.
94. Qi, Y., Wang, M., Zhang, Y. & Zhu, T. Effect of calcination temperature on the structure and photocatalytic performance of BiVO<sub>4</sub> prepared via an improved solution combustion method. *Micro Nano Lett.* 2018, **13**, 1017–1020.
95. Shi, L., Zhuo, S., Abulikemu, M., Mettela, G., Palaniselvam, T., Rasul, S., Tang, B., Yan, B., Saleh, N. B., & Wang, P. Annealing temperature effects on photoelectrochemical performance of bismuth vanadate thin film photoelectrodes. *RSC Adv.* 2018, **8**, 29179–29188.
96. Li, D., Chen, R., Wang, P., Li, Z., Zhu, J., Fan, F., Shi, J., & Li, Can. Effect of facet-selective assembly of cocatalyst on BiVO<sub>4</sub> photoanode for solar water oxidation. *ChemCatChem* 2019, **11**, 3763–3769.
97. Kamble, G. S. & Ling, Y.-C. Solvothermal synthesis of facet-dependent BiVO<sub>4</sub> photocatalyst with enhanced visible-light-driven photocatalytic degradation of organic pollutant: assessment of toxicity by zebrafish embryo. *Sci. Rep.* 2020, **10**, 12993.
98. Li, R., Zhang, F., Wang, D., Yang, J., Li, M., Zhu, J., Zhou, X., Han, H., & Li, C. Spatial separation of photogenerated electrons and holes among {010} and {110} crystal facets of BiVO<sub>4</sub>. *Nat. Commun.* 2013, **4**, 1432.

99. Wang, D., Jiang, H., Zong, X., Xu, Q., Ma, Y., Li, G., & Li, C. Crystal Facet Dependence of Water Oxidation on BiVO<sub>4</sub> Sheets under Visible Light Irradiation. *Chem. - A Eur. J.* 2011, **17**, 1275–1282.
100. Han, H. S., Shin, S., Kim, D. H., Park, I. J., Kim, J. S., Huang, P.-S., Lee, J.-K., Cho, I. S., & Zheng, X. Boosting the solar water oxidation performance of a BiVO<sub>4</sub> photoanode by crystallographic orientation control. *Energy Environ. Sci.* 2018, **11**, 1299–1306.
101. Zhang, L., Chen, D. & Jiao, X. Monoclinic structured BiVO<sub>4</sub> nanosheets: hydrothermal preparation, formation mechanism, and coloristic and photocatalytic properties. *J. Phys. Chem. B* 2006, **110**, 2668–2673.
102. Yang, J. W., Park, I. J., Lee, S. A., Lee, M. G., Lee, T. H., Park, H., Kim, C., Park, J., Moon, J., Kim, J. Y., & Jang, Ho W. Near-complete charge separation in tailored BiVO<sub>4</sub>-based heterostructure photoanodes toward artificial leaf. *Appl. Catal. B Environ.* 2021, **293**, 120217.
103. Dehdar, A., Asgari, G., Leili, M., Madrakian, T. & Seid-mohammadi, A. Step-scheme BiVO<sub>4</sub>/WO<sub>3</sub> heterojunction photocatalyst under visible LED light irradiation removing 4-chlorophenol in aqueous solutions. *J. Environ. Manage.* 2021, **297**, 113338.
104. Rathi, V., Panneerselvam, A. & Sathiyapriya, R. A novel hydrothermal induced BiVO<sub>4</sub>/g-C<sub>3</sub>N<sub>4</sub> heterojunctions visible-light photocatalyst for effective elimination of aqueous organic pollutants. *Vacuum* 2020, **180**, 109458.
105. Zou, Y., Lu, M., Jiang, Z., Xu, L., Liu, C., Zhang, L., & Chen, Y. Hydrothermal synthesis of Zn-doped BiVO<sub>4</sub> with mixed crystal phase for enhanced photocatalytic activity. *Opt. Mater. (Amst)*. 2021, **119**, 111398.
106. Zhang, Y., Wang, L., Yang, M., Wang, J. & Shi, J. Carbon quantum dots sensitized ZnSn(OH)<sub>6</sub> for visible light-driven photocatalytic water purification. *Appl. Surf. Sci.* 2019, **466**, 515–524.
107. Zeng, X., Wang, Z., Meng, N., McCarthy, D. T., Deletic, A., Pan, J.-h., & Zhang, X. Highly dispersed TiO<sub>2</sub> nanocrystals and WO<sub>3</sub> nanorods on reduced graphene oxide: Z-scheme photocatalysis system for accelerated photocatalytic water disinfection. *Appl. Catal. B Environ.* 2017, **218**, 163–173.
108. Shandilya, P., Mittal, D., Soni, M., Raizada, P., Lim, J.-H., Jeong, D. Y., Dewedi, R. P., Saini, A. K. & Singh, P. Islanding of EuVO<sub>4</sub> on high-dispersed fluorine doped few layered graphene sheets for efficient photocatalytic

- mineralization of phenolic compounds and bacterial disinfection. *J. Taiwan Inst. Chem. Eng.* 2018, **93**, 528–542.
109. Shandilya, P., Mittal, D., Soni, M., Raizada, P., Hosseini-Bandegharai, A., Saini, A. K., & Singh, P. Fabrication of fluorine doped graphene and  $\text{SmVO}_4$  based dispersed and adsorptive photocatalyst for abatement of phenolic compounds from water and bacterial disinfection. *J. Clean. Prod.* 2018, **203**, 386–399.
110. Shandilya, P., Mittal, D., Sudhaik, A., Soni, M., Raizada, P., Saini, A. K. & Singh, P.  $\text{GdVO}_4$  modified fluorine doped graphene nanosheets as dispersed photocatalyst for mitigation of phenolic compounds in aqueous environment and bacterial disinfection. *Sep. Purif. Technol.* 2019, **210**, 804–816.
111. Li, Z., Meng, X. & Zhang, Z. Hexagonal  $\text{SnS}$  nanoplates assembled onto hierarchical  $\text{Bi}_2\text{WO}_6$  with enhanced photocatalytic activity in detoxification and disinfection. *J. Colloid Interface Sci.* 2019, **537**, 345–357.
112. Mazloom, J. & Zamani, H. Photocatalytic and photo-induced disinfection activities of sol-gel synthesized  $\text{CeO}_2$ – $\text{SnO}_2$ :TM (TM= Co, Ni and Mn) nanocomposites: Relation between physical properties and their performance. *J. Alloys Compd.* 2018, **754**, 238–246.
113. Zhang, B., Zou, S., Cai, R., Li, M. & He, Z. Highly-efficient photocatalytic disinfection of *Escherichia coli* under visible light using carbon supported Vanadium Tetrasulfide nanocomposites. *Appl. Catal. B Environ.* 2018, **224**, 383–393.
114. Misra, A. J., Das, S., Habeeb Rahman, A. P., Das, B., Jayabalan, R., Behera, S. K., Suar, M., Tamhankar, A. J., Mishra, A., Lundborg, C. S., & Tripathy, S. K. Doped  $\text{ZnO}$  nanoparticles impregnated on Kaolinite (Clay): A reusable nanocomposite for photocatalytic disinfection of multidrug resistant *Enterobacter* sp. under visible light. *J. Colloid Interface Sci.* 2018, **530**, 610–623.
115. Kisch, H. & Bahnemann, D. Best Practice in Photocatalysis: Comparing Rates or Apparent Quantum Yields? *J. Phys. Chem. Lett.* 2015, **6**, 1907–1910.
116. Vignolo-González, H. A., Laha, S., Jiménez-Solano, A., Oshima, T., Duppel, V., Schützendübe, P., & Lotsch, B. V. Toward Standardized Photocatalytic Oxygen Evolution Rates Using  $\text{RuO}_2$ @ $\text{TiO}_2$  as a Benchmark. *Matter* **3**, 464–486 (2020).

117. Xu, J., Li, Y., Zhou, X., Li, Y., Gao, Z. D., Song, Y. Y., & Schmuki, P. Graphitic C<sub>3</sub>N<sub>4</sub>-Sensitized TiO<sub>2</sub> Nanotube Layers: A Visible-Light Activated Efficient Metal-Free Antimicrobial Platform. *Chem. - A Eur. J.* 2016, **22**, 3947–3951.
118. Kang, S., Huang, W., Zhang, L., He, M., Xu, S., Sun, D., & Jiang, X. Moderate Bacterial Etching Allows Scalable and Clean Delamination of g-C<sub>3</sub>N<sub>4</sub> with Enriched Unpaired Electrons for Highly Improved Photocatalytic Water Disinfection. *ACS Appl. Mater. Interfaces* 2018, **10**, 13796–13804.
119. Zhang, C., Li, Y., Shuai, D., Zhang, W., Niu, L., Wang, L., & Zhang, H. Visible-light-driven, water-surface-floating antimicrobials developed from graphitic carbon nitride and expanded perlite for water disinfection. *Chemosphere* 2018, **208**, 84–92.
120. Wang, R., Kong, X., Zhang, W., Zhu, W., Huang, L., Wang, J., Zhang, X., Liu, X., Hu, N., Suo, Y., & Wang, J. Mechanism insight into rapid photocatalytic disinfection of Salmonella based on vanadate QDs-interspersed g-C<sub>3</sub>N<sub>4</sub> heterostructures. *Appl. Catal. B Environ.* 2018, **225**, 228–237.
121. Lin, T., Song, Z., Wu, Y., Chen, L., Wang, S., Fu, F., & Guo, L. Boron- and phenyl-codoped graphitic carbon nitride with greatly enhanced light responsive range for photocatalytic disinfection. *J. Hazard. Mater.* 2018, **358**, 62–68.
122. Maddigpu, P. R., Sawant, B., Wanjari, S., Goel, M. D., Vione, D., Dhodapkar, R. S., & Rayalu, S. Carbon nanoparticles for solar disinfection of water. *J. Hazard. Mater.* 2018, **343**, 157–165.
123. Xu, J., Gao, Q., Bai, X., Wang, Z. & Zhu, Y. Enhanced visible-light-induced photocatalytic degradation and disinfection activities of oxidized porous g-C<sub>3</sub>N<sub>4</sub> by loading Ag nanoparticles. *Catal. Today* 2019, **332**, 227–235.
124. Deng, J., Liang, J., Li, M. & Tong, M. Enhanced visible-light-driven photocatalytic bacteria disinfection by g-C<sub>3</sub>N<sub>4</sub>-AgBr. *Colloids Surfaces B Biointerfaces* 2017, **152**, 49–57.
125. Xia, D., Wang, W., Yin, R., Jiang, Z., An, T., Li, G., Zhao, H., & Wong, P. K. Enhanced photocatalytic inactivation of *Escherichia coli* by a novel Z-scheme g-C<sub>3</sub>N<sub>4</sub>/m-Bi<sub>2</sub>O<sub>4</sub> hybrid photocatalyst under visible light: The role of reactive oxygen species. *Appl. Catal. B Environ.* 2017, **214**, 23–33.
126. Thurston, J. H., Hunter, N. M., Wayment, L. J. & Cornell, K. A. Urea-derived graphitic carbon nitride (u-g-C<sub>3</sub>N<sub>4</sub>) films with highly enhanced antimicrobial

- and sporicidal activity. *J. Colloid Interface Sci.* 2017, **505**, 910–918.
127. Thurston, J. H., Hunter, N. M. & Cornell, K. A. Preparation and characterization of photoactive antimicrobial graphitic carbon nitride (g-C<sub>3</sub>N<sub>4</sub>) films. *RSC Adv.* 2016, **6**, 42240–42248.
  128. Li, G., Nie, X., Chen, J., Jiang, Q., An, T., Wong, P. K., Zhang, H., Zhao, H., & Yamashita, H. Enhanced visible-light-driven photocatalytic inactivation of *Escherichia coli* using g-C<sub>3</sub>N<sub>4</sub>/TiO<sub>2</sub> hybrid photocatalyst synthesized using a hydrothermal-calcination approach. *Water Res.* 2015, **86**, 17–24.
  129. Bing, W., Chen, Z., Sun, H., Shi, P., Gao, N., Ren, J., & Qu, X. Visible-light-driven enhanced antibacterial and biofilm elimination activity of graphitic carbon nitride by embedded Ag nanoparticles. *Nano Res.* 2015, **8**, 1648–1658.
  130. Zhao, H., Yu, H., Quan, X., Chen, S., Zhang, Y., Zhao, H., & Wang, H. Fabrication of atomic single layer graphitic-C<sub>3</sub>N<sub>4</sub> and its high performance of photocatalytic disinfection under visible light irradiation. *Appl. Catal. B Environ.* 2014, **152–153**, 46–50.
  131. He, J., Zeng, X., Lan, S. & Lo, I. M. C. Reusable magnetic Ag/Fe, N-TiO<sub>2</sub>/Fe<sub>3</sub>O<sub>4</sub>@SiO<sub>2</sub> composite for simultaneous photocatalytic disinfection of *E. coli* and degradation of bisphenol A in sewage under visible light. *Chemosphere* 2019, **217**, 869–878.
  132. Chen, H., Tian, W. & Ding, W. Preparation of meso-Ag/Al<sub>2</sub>O<sub>3</sub> and synergistic water disinfection of metallic silver and ROS under visible light. *Sol. Energy* 2018, **173**, 1065–1072.
  133. Xu, Y., Liu, Q., Liu, C., Zhai, Y., Xie, M., Huang, L., Xu, H., Li, H., & Jing, J. Visible-light-driven Ag/AgBr/ZnFe<sub>2</sub>O<sub>4</sub> composites with excellent photocatalytic activity for *E. coli* disinfection and organic pollutant degradation. *J. Colloid Interface Sci.* 2018, **512**, 555–566.
  134. Liang, J., Liu, F., Li, M., Liu, W. & Tong, M. Facile synthesis of magnetic Fe<sub>3</sub>O<sub>4</sub>@BiOI@AgI for water decontamination with visible light irradiation: Different mechanisms for different organic pollutants degradation and bacterial disinfection. *Water Res.* 2018, **137**, 120–129.
  135. Zhou, Q., Ma, S. & Zhan, S. Superior photocatalytic disinfection effect of Ag-3D ordered mesoporous CeO<sub>2</sub> under visible light. *Appl. Catal. B Environ.* 2018, **224**, 27–37.
  136. Najma, B., Kasi, A. K., Khan Kasi, J., Akbar, A., Bokhari, S. M. A., & Stroe,

- I. R. ZnO/AAO photocatalytic membranes for efficient water disinfection: Synthesis, characterization and antibacterial assay. *Appl. Surf. Sci.* 2018, **448**, 104–114.
137. Ma, X., Xiang, Q., Liao, Y., Wen, T. & Zhang, H. Visible-light-driven CdSe quantum dots/graphene/TiO<sub>2</sub> nanosheets composite with excellent photocatalytic activity for *E. coli* disinfection and organic pollutant degradation. *Appl. Surf. Sci.* 2018, **457**, 846–855.
138. Zheng, X., Shen, Z.-p., Cheng, C., Shi, L., Cheng, R., & Yuan, D.-h. Photocatalytic disinfection performance in virus and virus/bacteria system by Cu-TiO<sub>2</sub> nanofibers under visible light. *Environ. Pollut.* 2018, **237**, 452–459.
139. Al-Ghafri, B., Bora, T., Sathe, P., Dobrestov, S. & Al-Abri, M. Photocatalytic microbial removal and degradation of organic contaminants of water using PES fibers. *Appl. Catal. B Environ.* 2018, **233**, 136–142.
140. Liu, Q., Xu, Y., Wang, J., Xie, M., Wei, W., Huang, L., Xu, H., Song, Y., & Li, H. Fabrication of Ag/AgCl/ZnFe<sub>2</sub>O<sub>4</sub> composites with enhanced photocatalytic activity for pollutant degradation and *E. coli* disinfection. *Colloids Surfaces A Physicochem. Eng. Asp.* 2018, **553**, 114–124.
141. Horovitz, I., Avisar, D., Luster, E., Lozzi, L., Luxbacher, T., & Mamane, H. MS2 bacteriophage inactivation using a N-doped TiO<sub>2</sub>-coated photocatalytic membrane reactor: Influence of water-quality parameters. *Chem. Eng. J.* 2018, **354**, 995–1006.
142. Obuchi, E., Furusho, T., Katoh, K., Soejima, T. & Nakano, K. Photocatalytic disinfection of sporulating *Bacillus subtilis* using silver-doped TiO<sub>2</sub>/SiO<sub>2</sub>. *J. Water Process Eng.* 2019, **30**, 100511.
143. Zeng, X., Wang, Z., Meng, N., McCarthy, D. T., Deletic, A., Pan, J.-h., & Zhang, X. Highly dispersed TiO<sub>2</sub> nanocrystals and carbon dots on reduced graphene oxide: Ternary nanocomposites for accelerated photocatalytic water disinfection. *Appl. Catal. B Environ.* 2017, **202**, 33–41.
144. Thakare, S. R. & Ramteke, S. M. Fast and regenerative photocatalyst material for the disinfection of *E. coli* from water: Silver nano particle anchor on MOF-5. *Catal. Commun.* 2017, **102**, 21–25.
145. Sreeja, S. & Shetty K, V. Photocatalytic water disinfection under solar irradiation by Ag@TiO<sub>2</sub> core-shell structured nanoparticles. *Sol. Energy* 2017, **157**, 236–243.

## Chapter 3 - Materials and methods

This chapter presents the raw materials, preparative procedures, equipment, and instruments used and followed throughout this research work. This incorporates the details of all the preparative methods of photocatalytic materials used in this whole study. A summary of all the analytical techniques used to characterise photocatalytic materials are also provided. The experimental set up used to test the efficacy of photocatalysts is also presented. Unless otherwise stated, all experiments were carried out by the author at NIBEC. The help and support of others is explicitly cited in the acknowledgement section.

### 3.1 Materials

#### 3.1.1 List of chemicals, materials, source, and purity

All the chemicals used throughout this research were of analytical grade and used in experiments without any further purification. All the utilized chemicals and other materials are alphabetically listed below in Table 3.1 along with their molecular formula, source of purchase and purity grade.

**Table 3.1** List of chemicals with their molecular formula, source, and purity

Name	Molecular Formula	Source	Purity*
Absolute ethanol	C <sub>2</sub> H <sub>5</sub> OH	Sigma-Aldrich	≥99.5%
Acetic acid		Fisher scientific	
Ammonium vanadate	NH <sub>4</sub> VO <sub>3</sub>	Aldrich	99.99%
Bismuth nitrate pentahydrate	Bi(NO <sub>3</sub> ) <sub>3</sub> ·5H <sub>2</sub> O	Aldrich	98%
Citric acid	C <sub>6</sub> H <sub>8</sub> O <sub>7</sub>	Sigma-Aldrich	99.5%
Conductive Epoxy CW 2400		Circuit works	



Name	Molecular Formula	Source	Purity*
Decon 90		Decon Laboratories Ltd	
De-ionized water	Millipore H <sub>2</sub> O	ELGA Pure Lab	15 MΩ.cm <sup>-1</sup>
Durapore Membrane Filter	PVDF	Merck Millipore	Hydrophilic, 0.22μm, 25 mm
Ethanolamine		Sigma-Aldrich	98%
Formic acid	CH <sub>2</sub> O <sub>2</sub>	Merck	98-100%
Hydrochloric acid	HCl	Merck	37%
Isopropanol	(CH <sub>3</sub> ) <sub>2</sub> CHOH	Sigma-Aldrich	≥99.5%
Kapton tape		Amazon	Heat resistant ≤ 300°C
Melamine	C <sub>3</sub> H <sub>6</sub> N <sub>6</sub>	Sigma-Aldrich	99%
Methanol (For HPLC)	CH <sub>3</sub> OH	Sigma-Aldrich	≥99.9%
Nitric acid	HNO <sub>3</sub>	Sigma-Aldrich	≥65%
Nitrogen (Oxygen-free)	OFN	BOC	≥ 99.99%
N, N-Dimethyl-4-nitrosoaniline (RNO)	ONC <sub>6</sub> H <sub>4</sub> N(CH <sub>3</sub> ) <sub>2</sub>	Sigma-Aldrich	97%
Phenol	C <sub>6</sub> H <sub>6</sub> O	VWR, BDH, PROLAB	AnalaR Normapur
Polyvinyl alcohol		Aldrich	99%
Potassium perchlorate	KClO <sub>4</sub>		
Ringer's solution ¼ strength tablets		Fluka Analytical	For microbiology
Sodium bicarbonate	NaHCO <sub>3</sub>	Aldrich	99%
Sodium chloride	NaCl	Sigma-Aldrich	≥99.8%
Sodium Hydroxide	NaOH	Sigma-Aldrich	≥98.0%
SU8 photoresist		MicroChem	
Thiourea		Merck	98%
Titanium dioxide (P25)	TiO <sub>2</sub>	Evonik aeroxide	≥ 99.5%
Tryptone agar	(C <sub>12</sub> H <sub>18</sub> O <sub>9</sub> ) <sub>n</sub>	Sigma-Aldrich	For microbiology
Tryptone soya broth		Fulka-analytical	For microbiology
urea		Fluka	99.5%

*\*Information provided by the suppliers*

## 3.2 Synthesis methods of photocatalysts

After the detailed literature assessment, graphitic carbon nitride (g-C<sub>3</sub>N<sub>4</sub>) and bismuth vanadate (BiVO<sub>4</sub>) were chosen to explore their photocatalytic and physicochemical properties. Both photocatalysts were synthesised in lab under controlled reaction conditions with taking care of all the safety measures. Synthesis methods and corresponding reaction parameters are discussed here.

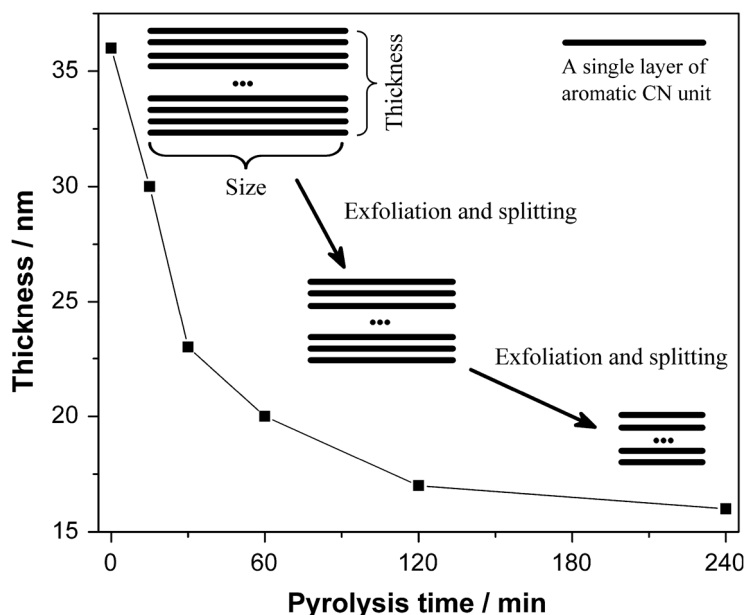
### 3.2.1 Thermal polymerization of g-C<sub>3</sub>N<sub>4</sub>

Thermal polymerisation is a process that uses thermal energy to convert a monomer into a polymer in a chain or step reaction. In this study, thermal polymerization method was employed to synthesize graphitic carbon nitride (g-C<sub>3</sub>N<sub>4</sub>) using different precursors (monomer) such as melamine, urea, thiourea and dicyandiamide. The synthesis process of g-C<sub>3</sub>N<sub>4</sub> through thermal polymerization is a combination of polyaddition and polycondensation pathways.<sup>1</sup>

In this study, g-C<sub>3</sub>N<sub>4</sub> was synthesised at varied thermal polymerization conditions to analyse the effect of precursors and reactions conditions on its properties, thus detailed reaction conditions are provided in the respective sections of chapter-4. However, in a typical synthesis process, adapted from the literature, a certain amount of precursor was loaded into a covered alumina crucible, then it was heated to the desired temperature and time with up and down heating ramp of 5°C min<sup>-1</sup> in a muffle furnace. The obtained yellow colour product was collected and ground into a fine powder using a mortar and pestle before further characterization and that is termed as bulk g-C<sub>3</sub>N<sub>4</sub>. Following the same procedure, all bulk g-C<sub>3</sub>N<sub>4</sub> samples were prepared using melamine, urea, thiourea and dicyandiamide with the respective reaction parameters.

### 3.2.2 Thermal exfoliation of g-C<sub>3</sub>N<sub>4</sub>

The g-C<sub>3</sub>N<sub>4</sub> stacking layers comprise the hydrogen bonding and the Van der Waals interactions between strands of polymeric melon units with NH/NH<sub>2</sub> group.<sup>2</sup> The layers of g-C<sub>3</sub>N<sub>4</sub> can gradually vanish and oxidise throughout the thermal annealing process by a layer-by-layer exfoliation pathway because hydrogen bonds are not sufficiently robust against thermal oxidation in air. Simultaneously, the large size of stacked g-C<sub>3</sub>N<sub>4</sub> is split up into thin layers after a longer pyrolysis time.<sup>3</sup> Fig. 3.1 explains a layered exfoliation and splitting mechanism.<sup>4</sup>



**Fig. 3.1.** The illustration for the layer exfoliation and splitting mechanism of g-C<sub>3</sub>N<sub>4</sub> with the correlation between layer thickness of g-C<sub>3</sub>N<sub>4</sub> and the pyrolysis time. [Reproduced from Dong *et al. J. Colloid Interface Sci.* 2013, 401, 70–79]<sup>4</sup>

Thus, thermal exfoliation may produce near to complete, exfoliated single layer graphitic carbon nitride. Although thermal exfoliation process significantly reduces the yield of the end-product. Since formation of polymeric g-C<sub>3</sub>N<sub>4</sub> occurred about 500°C, to produce exfoliated g-C<sub>3</sub>N<sub>4</sub> in this study, bulk g-C<sub>3</sub>N<sub>4</sub> samples were further heated at 500°C in an open crucible with heating ramp up and down of 2°C min<sup>-1</sup>.

### 3.2.3 Hydrothermal synthesis of $\text{BiVO}_4$

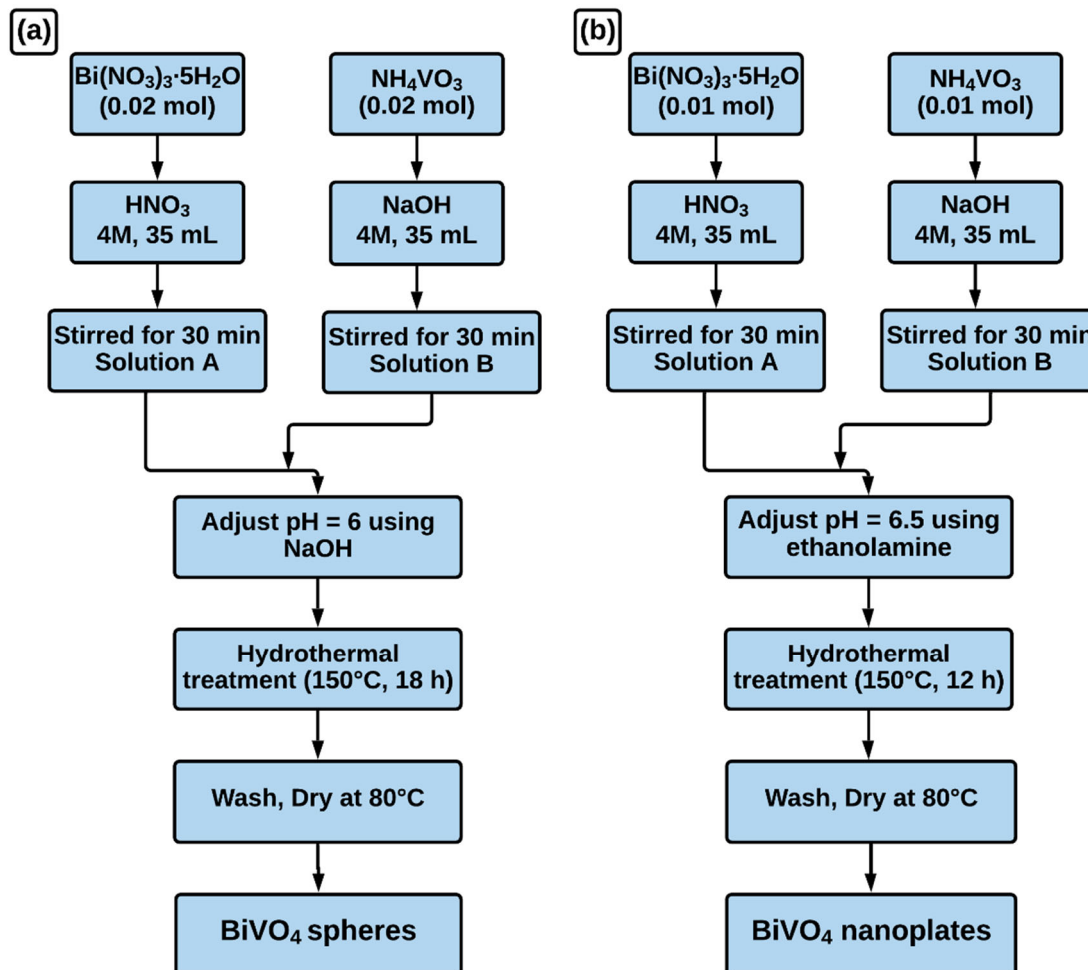
Hydrothermal synthesis refers to a heterogenous chemical reaction that occurs in the presence of aqueous solvents under self-generated pressure and high temperature in a closed system. This high pressure and temperature conditions causes the dissolution and recrystallisation of the materials which are relatively insoluble under normal conditions.<sup>5</sup> This method has been used to prepare different materials having various morphologies, crystal structure, sub-micron to nanoparticles with a narrow size distribution using simple equipment and size.



**Fig. 3.2.** Hydrothermal Parr reactor (Parr Instruments) used for  $\text{BiVO}_4$  synthesis

A typical hydrothermal set up consists of a closed stainless-steel vessel (also called a Parr reactor vessel) incorporating inputs for temperature sensor probe and pressure gauge. Along with high pressure and temperature, hydrothermal methods may require highly acidic or alkaline conditions which are subject to corrosion. To avoid this, reactions are executed in Teflon vessel which is placed inside stainless-steel vessel. Hydrothermal setup used in this study is shown in Fig. 3.2. This simple experimental setup for hydrothermal synthesis has been used to prepare high purity and homogenous product with different morphologies, crystal structure, sub-micron

to nanoparticles size and narrow particle size distributions, thus considered suitable for scale-up. However, it all depends on reaction parameters such as precursor, temperature, time, pH, chelating agent, *etc.*

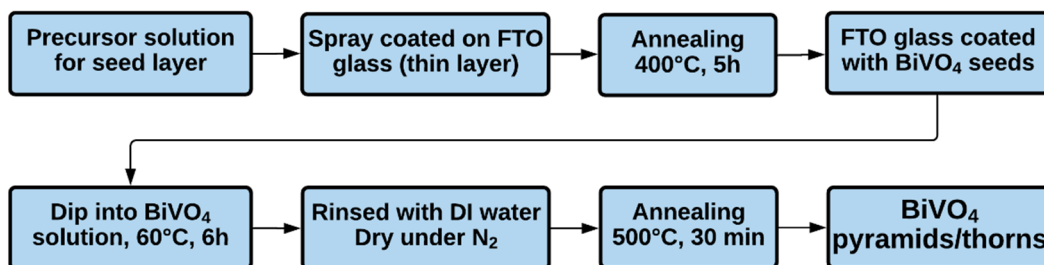


**Fig. 3.3.** Flowchart for the hydrothermal synthesis of (a)  $\text{BiVO}_4$  spheres and (b)  $\text{BiVO}_4$  nanoplates

In this study, a hydrothermal method was used to prepare bismuth vanadate ( $\text{BiVO}_4$ ) spheres and nanoplates. Bismuth vanadate having spherical shape particles were synthesized by adapting the method reported by Zhao *et al.*<sup>6</sup> while  $\text{BiVO}_4$  nanoplates were produced by adapting the method reported by Xi *et al.*<sup>7</sup> A flowchart for the hydrothermal synthesis of  $\text{BiVO}_4$  spheres and nanoplates are given in Fig. 3.3. The detailed synthesis procedures are provided in chapter 6.

### 3.2.4 Nucleation/seed mediated synthesis of BiVO<sub>4</sub>

Seed mediated method (SMM) is a wet chemistry method used to prepare different shapes of nanoparticles such as spheres, cubes, rods, *etc.* Seed mediated method is also known as nucleation method. Nucleation refers to the process whereby nuclei (seeds) act as templates for crystal growth. Thanh *et. al* has reported the various nucleation and growth mechanisms those can occur within solution such as LaMer nucleation, Ostwald ripening, digestive ripening, Finke-Watzky two step mechanism, coalescence and orientated attachment, and intraparticle growth.<sup>8</sup>



**Fig. 3.4.** Flowchart for the seed mediated synthesis of BiVO<sub>4</sub> pyramids/thorns

In this study, a seed mediated synthesis method was used to prepare pyramid/thorn shape bismuth vanadate by adapting the method reported by Su *et al.*<sup>9</sup> with some modification. Flowchart for seed mediated synthesis of BiVO<sub>4</sub> pyramids/thorns is given in Fig. 3.4. The detailed synthesis procedure is provided in chapter 6.

### 3.3 Electrode preparation

To test photoelectrochemical properties of prepared materials, they were coated on electrically conductive substrate to form electrode. Procedure to prepare a working electrode is given below.

### 3.3.1 Substrate and its cleaning

FTO (Fluorine-doped Tin Oxide) coated glasses (300 mm × 300 mm × 2.2 mm, surface resistivity  $\sim 7 \Omega/\text{sq}$ ) were purchased from Sigma-Aldrich, which were further cut into pieces (20 mm × 15 mm) to use as an electrically conductive substrate for photoelectrodes. Before further processing, these FTO substrates were cleaned by bath sonication firstly with Decon 90 (5%) which is a surface-active cleaning agent, followed by sequential sonication with distilled water and ethanol. The cleaned FTO glasses were then dried under oxygen-free nitrogen stream.

### 3.3.2 Spray coating on FTO substrates

The synthesized samples were immobilized on pre cleaned FTO substrates by spray coating method. These FTO substrates were masked with Kapton tape (heat resistant up to 300°C) to leave an unexposed area (5 mm × 15 mm) by spray coating for making electrical contacts and placed on a hot plate. 1 wt.% homogenous suspension of each sample prepared in methanol, was uniformly spray-coated on the exposed area of FTO coated glass using a lab spray gun (air brush) maintaining the catalyst loading of  $0.5 \text{ mg}\cdot\text{cm}^{-2}$  for each sample which was ensured by measuring the dry weight of the FTO coated glass pre and post spray-coating. The spray coated FTO glass were annealed at 400°C in the muffle furnace for 1 h (ramp up =  $2^\circ\text{C}\cdot\text{min}^{-1}$ ; ramp down =  $2^\circ\text{C}\cdot\text{min}^{-1}$ ) to sinter particles and improve adhesion of the sample to the substrate.

### 3.3.3 Electrical contact on FTO substrates

A copper wire was used to make electrical contact with the FTO glass. An abrasive sanding sponge block was used to clean the copper wire before the contact

was made. Conductive silver epoxy (CircuitWorks CW2400) was used to make the connection between FTO substrate and Cu wire, which was allowed to cure at 120°C for 60 min. The contact and area uncoated with photocatalyst were insulated with SU8 photoresist (MicroChem), followed by two slots of UV exposure for 5 min both sides (twice) and then hard baking at 160°C for 30 min. The UV exposure step was repeated two times to ensure proper curing of the photoresist. Thus, A working electrode with a photoactive area of 15 mm × 15 mm was obtained.

### **3.4 Materials characterization**

Various analytical techniques were employed to characterize physicochemical properties of synthesized materials which includes X-ray diffraction (XRD) to determine crystal structure of the materials, field emission scanning electron microscopy (FESEM) to determine the morphology, Fourier transform infrared spectroscopy (FTIR) to obtain chemical composition, Raman spectroscopy to acquire the information about chemical structure, X-ray/UV photoelectron spectroscopy (XPS/UPS) to perform elemental analysis and valence band position of the semiconductor, ultraviolet-visible spectroscopy and diffuse reflectance analysis to investigate optical properties and BET Measurement to analyse the surface area and porosity of synthesized materials. A brief description is provided here for all these analytical techniques.

#### **3.4.1 X-ray diffraction (XRD)**

XRD analysis was carried out on PANalytical X'PERT ProMPD (Malvern Panalytical Empyrean 3<sup>rd</sup> generation XRD system) equipped with a Cu K $\alpha$  X-ray source ( $\lambda = 1.54 \text{ \AA}$ ) in  $2\theta$  range of 5-50° and 10-70° for g-C<sub>3</sub>N<sub>4</sub> and BiVO<sub>4</sub>,



respectively, with step size 0.03 and scan speed 25 s/step. The applied voltage and current of the x-ray tube were 40 kV and 40 mA, respectively. The diffraction patterns of the samples were compared to the standard JCPDS files available in the inorganic crystal structure database (ICSD).

### **3.4.2 Field emission scanning electron microscopy (FESEM)**

A Hitachi SU5000 FESEM was used for morphological analysis. The FESEM was operated in an accelerating voltage of 10 kV, under high vacuum of  $\sim 10^{-8}$  bar and at a 5 mm of working distance. The images were recorded using the secondary electron (SE) detector. Energy dispersive x-ray analyser (EDX/EDS) was also attached with FESEM which were used to determine the bulk elemental composition of the as-prepared samples. EDX Images were captured with a backscattered secondary electron (BSE) detector, and Aztec software was used for EDS analysis.

### **3.4.3 Fourier transform infrared spectroscopy (FTIR)**

A Varian 640-IR FTIR spectrometer was used to record the interferograms the range of  $4000\text{--}500\text{ cm}^{-1}$ . KBr was used as a carrier for the samples since it is optically transparent in the IR range of measurements. It possesses 100 % transmittance in the range of wave number ( $400\text{--}4000\text{ cm}^{-1}$ ), hence there is no absorption interference. Each sample (1-2%) was mixed with KBr thoroughly in a mortar while grinding with the pestle and pressed into a pellet within a disc.

### **3.4.4 Raman spectroscopy**

Because carbon materials have a high polarizability, they are Raman active, hence Raman is generally favoured over FTIR. Raman spectra was collected at room

temperature using a Raman spectrometer (Renishaw inVia) equipped with laser 532 nm and 785 nm Lasers are used as a photon source due to their highly monochromatic nature, and high beam fluxes. Lasers in the visible region (e.g., 532 nm) offer high Raman scattering but also provide high fluorescence background, while near infra-red lasers (e.g., 785 nm) provide low fluorescence background while maintaining high Raman intensity. In this study, a 532 nm laser was used for the BVO<sub>4</sub> samples, and a 785 nm laser was used for the g-C<sub>3</sub>N<sub>4</sub> samples because fluorescence suppression was required.

Using a spatula, a little amount of powdered sample was mounted on a glass slide. The spectrometer was focused on the powder sample through the objective lens using the associated microscope and camera. For each sample, the scan was recorded with 10 acquisitions, 0.1% of laser power for 10 s exposure time in the range of 1600–100 cm<sup>-1</sup>.

#### **3.4.5 X-ray and ultraviolet photoelectron spectroscopy (XPS/UPS)**

X-ray photoelectron spectroscopy was carried out on an ESCALAB XI<sup>+</sup> instrument (ThermoFisher) with Al K $\alpha$  anode as X-ray source ( $h\nu = 1486.68$  eV) operated at approximately 15 kV and 15 mA. For XPS analysis, the as-prepared samples were spray coated on Si substrates for uniformity. A typical XPS analysis includes a wide energy survey scan (WESS) and a high-resolution scan for each element possibly available in the material. All the scans were performed at minimum three different sites to reduce the error in determining the elemental proportion. The CasaXPS software was used to analyse the XPS spectra. All the spectra were calibrated for charge correction with respect to adventitious carbon peak (C 1s at 284.8

eV). XPS spectra were further quantified after performing the Tougaard background correction.

Valance band XPS (VBXPS) and ultraviolet photoelectron spectroscopy (UPS) were also employed to explore the band edge energies and work function of g-C<sub>3</sub>N<sub>4</sub> samples. A He I emission UV source (21.22 eV) was used to collect UPS spectra of carbon nitride.

### 3.4.6 Ultraviolet-visible diffuse reflectance spectroscopy

A UV-Vis spectrophotometer (Perkin Elmer Lambda 365) equipped with integrating sphere (50 nm) was employed to determine the optical bandgap of prepared materials by measuring diffuse reflected light. The diffuse reflectance spectra (DRS) were recorded in 200-800 nm range.

The Tauc plot is a widely used method for determining band gap using optical absorption spectra that employs the following relational expression (equation 3.1) proposed by Tauc, Davis, and Mott.<sup>10,11</sup>

$$(\alpha \cdot h\nu)^{1/n} = B(h\nu - E_g) \quad (3.1)$$

Where,  $\alpha$  is the absorption coefficient,  $h$  is the Planck constant,  $\nu$  is the photon's frequency,  $E_g$  is the band gap energy,  $B$  is a constant and the factor 'n' depends on the nature of the electron transition and is equal to 1/2 or 2 for the direct and indirect transition band gap semiconductors, respectively.

To calculate the band gap energy by diffuse reflectance spectroscopy, the acquired reflectance spectra was converted to the corresponding absorption spectra using Kubelka-Munk ( $K-M$ ) function (equation 3.2) according to the theory presented by Kubelka and Munk in 1931.<sup>12</sup>

$$F(R) = \frac{K}{S} = \frac{(1-R)^2}{2R} \quad (3.2)$$

Where  $R$  is the reflectance, while  $K$  and  $S$  are the absorption and scattering coefficients, respectively.  $F(R)$  is the  $K$ - $M$  function which is proportional to the absorption coefficient. Thus  $\alpha$  in the Tauc equation (3.1) can be substituted with  $F(R)$ , which yields the equation 3.3

$$(F(R) \cdot h\nu)^{1/n} = B(h\nu - E_g) \quad (3.3)$$

Further,  $(F(R) \cdot h\nu)^{1/n}$  was plotted against the photon energy ( $h\nu$ ) where the x-axis intersection point of the linear fit of the Tauc plot provides approximate bandgap.<sup>13</sup>

The UV-Vis spectrophotometer was also used to record absorption spectra for p-nitrosodimethylaniline (RNO) at 440 nm, to detect the hydroxyl ( $\cdot\text{OH}$ ) radicals.

#### 3.4.7 BET surface area analysis (BET)

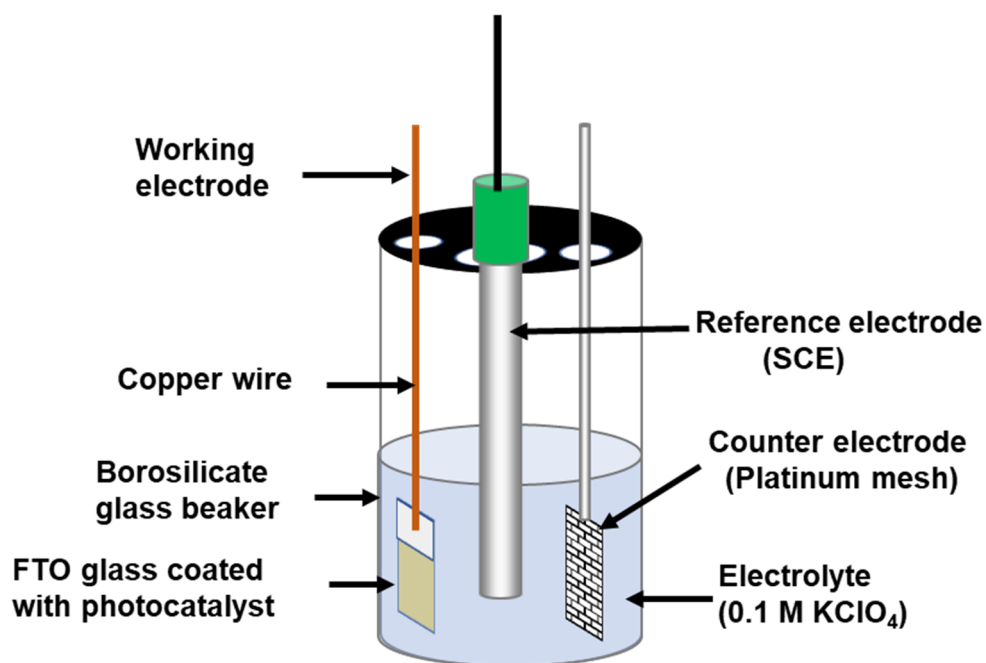
Surface area analysis of prepared photocatalyst was performed on Quantachrome Autosorb-1 system. Specific surface area, pore size distribution and pore volume were examined from obtained  $\text{N}_2$  adsorption - desorption isotherms. The known weight of each sample was outgassed under a flow of dry and inert gas (Helium) at  $250^\circ\text{C}$  for 3 h to remove any water/organic vapours present of the surface of the sample. A sample cell of 12 mm outer diameter without rod was used for all measurements. According to IUPAC six types of nitrogen adsorption isotherms (type I to type VI) and four types of hysteresis shapes of adsorption isotherms (type H1 to type H4) has been distinguished.<sup>14</sup>

### 3.5 Photoelectrochemical measurements

#### 3.5.1 Photoelectrochemical cell

Photoelectrochemical measurements were performed using a three-electrode system in a borosilicate beaker (Fig. 3.5). This three-electrode set up consists of a

reference electrode (saturated calomel electrode, Hanna instruments), a counter electrode (platinum mesh paddle (5.9 cm<sup>2</sup>)) and a working electrode (photocatalyst deposited on FTO coated glass). These electrodes are immersed in an electrolyte to prevent migration of charged reactants and products and allowing only diffusion to transport electroactive species to and from the electrode surface. Herein, 0.1 M KClO<sub>4</sub> solution (pH = 6) was used as an electrolyte. All photoelectrochemical measurements were performed in a Faraday cage (Metrohm) to protect electrochemical cell setup from electro-magnetic interference from external sources such as computer monitors, power lines or other instruments in the lab.



**Fig. 3.5.** A schematic representation of photoelectrochemical cell used for PEC measurements

A computer controlled electrochemical workstation (AUTOLAB PGSTAT 30, Metrohm) was used for potentiostatic or galvanostatic control during the measurements and 450 W Xe lamp (Jobin Yvon FL-1039/40) equipped with an IR water filter was used as a light source to illuminate the working electrode. A spectral radiometer (FLAME-S-UV-VIS-ES, Ocean Optics B.V, Netherlands) was used to

measure the incident light intensity of 450 W Xe lamp. The spectral emission of the light source is shown in Fig. 3.6. The incident light intensity on the reactor window was measured as  $240 \text{ W m}^{-2}$  in the UV-visible region (280-800 nm) and the UV portion (280-400) of the spectrum was  $13.8 \text{ W m}^{-2}$ . Chopped irradiation measurements were employed using an optical shutter (Uniblitz, WMM-T1). All electrode potentials in this study potentials are given with respect to the saturated calomel electrode (SCE) unless stated otherwise. The potential and current measurements were done using the General-Purpose Electrochemical Software (GPES) included with the AUTOLAB workstation.

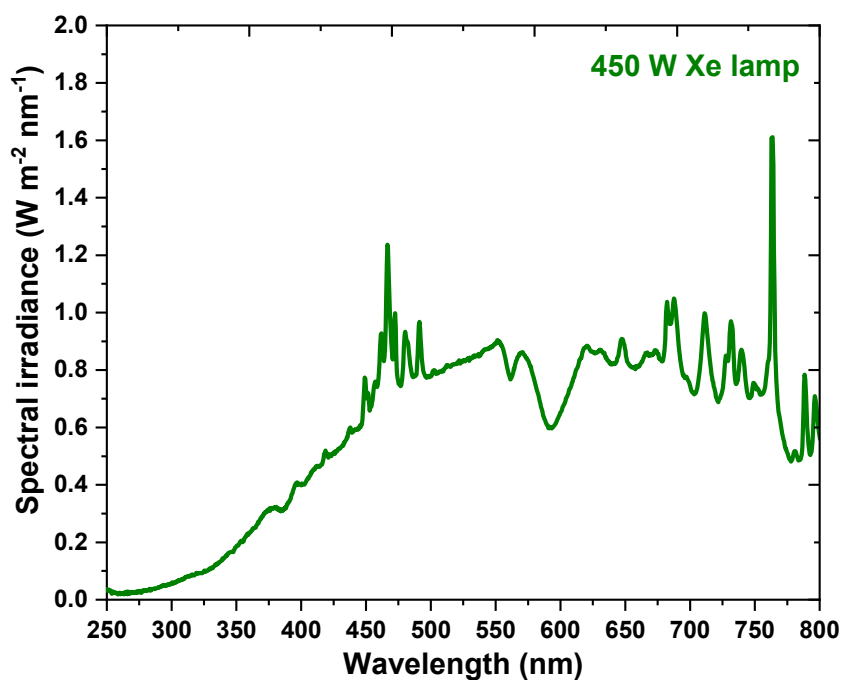


Fig. 3.6 – Spectral emission of the 450 W Xe lamp (250 – 800 nm)

## 3.5.2 Photoelectrochemical methods

### 3.5.2.1 Linear sweep voltammetry (LSV)

Linear sweep voltammetry (LSV) is the commonly used voltametric technique for investigating redox reactions of both organic and inorganic compounds. For LSV measurements, potential of working electrode is swept linearly with time from

potential  $V_i$  to  $V_i$  and the resulting output current is recorded which is represented as current vs applied potential (I-V) curve or current density vs applied potential ( $J$ -V curve), known as voltammogram. The photocurrent is defined as the difference between light and dark current which can be measured through LSV measurement under irradiation.

LSV measurements were performed from -1.0 V to +1.0V (anodic sweeps) and +1.0 V to -1.0 V (cathodic sweeps) at a constant scan rate ( $5 \text{ mV s}^{-1}$ ). Chopped LSV measurements were recorded by chopping the irradiation source at every 10 second interval.

### **3.5.2.2 Chronoamperometry**

Chronoamperometry is another widely used method in photoelectrochemistry which refers to the measurement of current between the working and counter electrodes at a fixed potential applied between the working and reference electrodes. The resulting current–time response is monitored and recorded in chopped irradiation. Irradiation was chopped ON/OFF once current achieved a steady state at the applied potential. In this study, a number of current-time response were performed at various potentials in between -1.0 to +1.0 V potential range to determine onset potential.

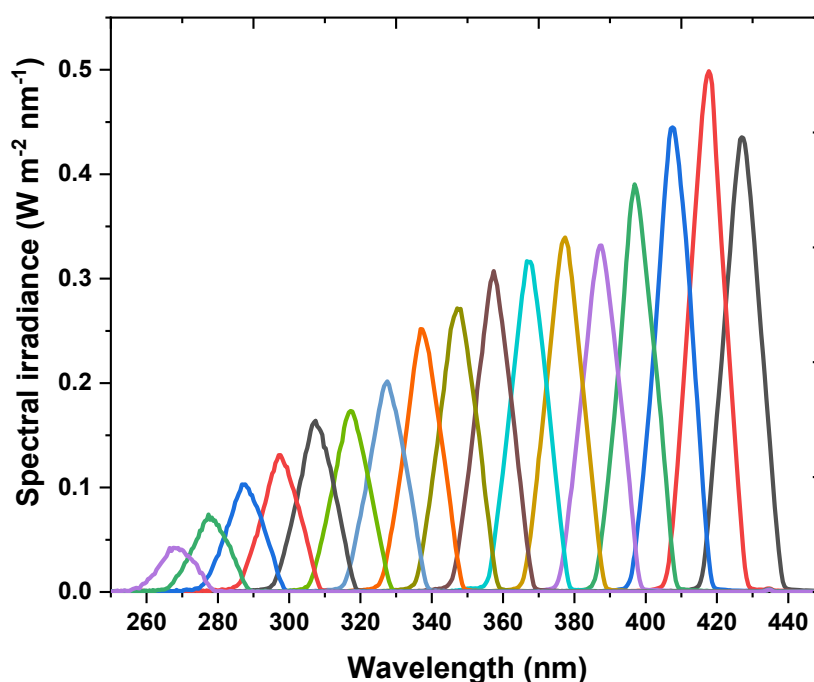
### **3.5.2.3 Spectral photocurrent response**

Spectral photocurrent was determined by measuring photocurrent at fixed potential under monochromatic light at various wavelengths. The spectral photocurrent response was recorded at applied voltage of +1.0 V (SCE) and 0 V (SCE) while varying the wavelength of the incident irradiation from 280 to 450 nm at 10 nm periods. The intensity output was measured at every 10 nm interval in the range of

250-500 nm, as shown in Fig. 3.7. The resulting spectral wavelength versus photocurrent data can be used to calculate the incident photon-to-current conversion efficiency (IPCE) using following equation 3.4.<sup>15-17</sup>

$$\text{IPCE}(\%) = \frac{hc}{e} \left( \frac{J_{ph}(\lambda)}{\lambda \cdot P(\lambda)} \right) \times 100 \quad (3.4)$$

where,  $h$  = the Plank's constant ( $6.626 \times 10^{-34}$  J s),  $c$  = speed of light ( $3 \times 10^8$  m s<sup>-1</sup>),  $e$  = charge of one electron ( $1.6 \times 10^{-19}$  C),  $J_{ph}(\lambda)$  = output current density (A cm<sup>-2</sup>) at wavelength  $\lambda$  (m) and  $P(\lambda)$  = incident spectral intensity (W cm<sup>-2</sup>).



**Fig. 3.7** Monochromatic spectral intensity for 450 W Xe lamp from 270-430 nm at 10 nm intervals.

#### 3.5.2.4 Open-circuit potential and open circuit photopotential

The open circuit potential (OCP), also known as the rest potential of an electrode, is the potential of an electrode that is not electrically connected to any other conducting materials, thus there is no net current at OCP conditions. In other words, the OCP is the measure of electrolyte redox potential or Fermi level in the equilibrium. When an electrode is irradiated at the open-circuit potential, there is a change in



potential due to electron-hole pairs generation which continues until the rates of hole and electron transfer equalize, this new equilibrium upon illumination is referred to as quasi-Fermi level. Upon irradiation, OCP is shifted to more negative and more positive for n-type and p-type materials, respectively. The difference between illuminated quasi-Fermi level and dark Fermi level is named as open circuit photopotential.<sup>18</sup>

Before taking measurements, the electrolyte was sparged with inter gas ( $O_2$  free  $N_2$ ) for 30 min to avoid interference from dissolved oxygen.<sup>19</sup> The AUTOLAB workstation was operated in potentiometric mode to perform open circuit photopotential measurements.

#### **3.5.2.5 Electrochemical impedance spectroscopy**

Electrochemical impedance spectroscopy (EIS) is a very useful method for studying the influence of mass transfer and reaction kinetics. The EIS measurements were carried out on OCP as set potential, 10 mV AC amplitude, the frequency range of 10 mHz to 100 kHz, a logarithmic frequency step and a single sine wave type. The Nyquist and Bode plots were obtained which are the 3D representations of the experimental results. In a typical Nyquist plot, imaginary part of impedance ( $-Z''$ ) is plotted against the real part of impedance ( $Z'$ ) while in a typical Bode plot, the phase angle ( $\phi$ ) and modulus ( $|Z|$ ) are plotted as a function of frequency.

An electrochemical equivalent circuit was obtained after fit and simulation of Nyquist plot using Nova software (version 1.11) which is a combination of electrical (resistance, capacitance) and electrochemical (faradaic) impedances.<sup>20</sup> The electrochemical impedance measurements were carried out in both dark and light conditions.

### 3.5.2.6 Mott Schottky analysis

Mott-Schottky (M-S) analysis is a widely adapted method for determining the flat band potential of a semiconductor electrode.<sup>20</sup> The flat band potential ( $U_{FB}$ ) helps in the estimation of band edge energies of a semiconductor material.  $U_{FB}$  of a semiconductor photoanode can be estimated by measuring the capacitance as a function of potential.<sup>18,21</sup> An FRA potential scan was carried out on OCP as set potential, in the range of -1.0 to +1.0 V with step potential of 0.02 V at a frequency where Bode phase angle was maximum, with single sinusoidal 10 mV AC voltage as the root mean square (RMS) value. The Mott–Schottky equation is used to evaluate the semiconductor capacitance ( $C_{sc}$ ) as given in equation 3.5.<sup>21,22</sup>

$$\frac{1}{C_{sc}^2} = \frac{2}{\epsilon\epsilon_0eN} \left( U - U_{FB} - \frac{k_B T}{e} \right) \quad (3.5)$$

where  $\epsilon$  is dielectric constant,  $\epsilon_0$  is vacuum permittivity,  $e$  is electronic charge,  $N$  is  $N_d$  (donor concentration for an n-type materials) or  $N_a$  (acceptor concentration for an p-type materials),  $k_B$  is the Boltzmann constant,  $U$  is applied potential (*vs.* reference electrode),  $U_{FB}$  is flat band potential (*vs.* reference electrode) and  $T$  is the temperature.

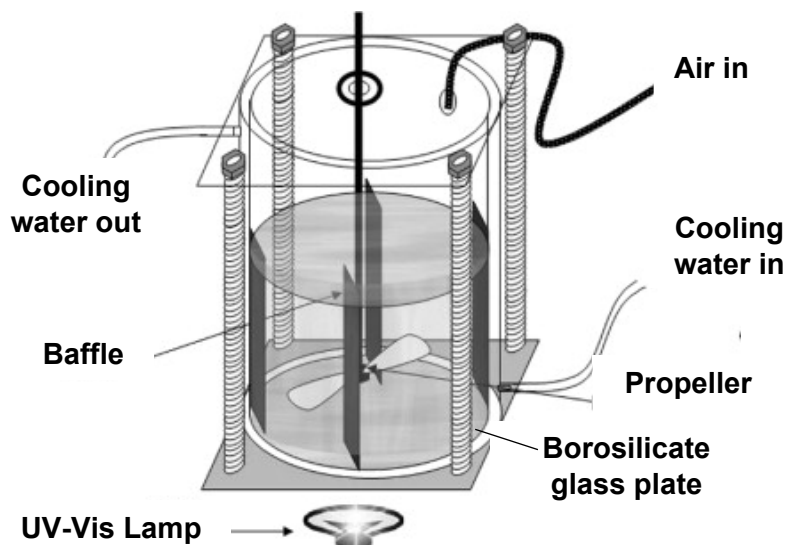
A graph of  $1/C^2$  as a function of applied potential gives a Mott-Schottky plot. The flat band potential was computed from the intercept of liner part of the Rs-Cp/Rp Mott-Schottky plot to the potential axis.

## 3.6 Photocatalysis experiments

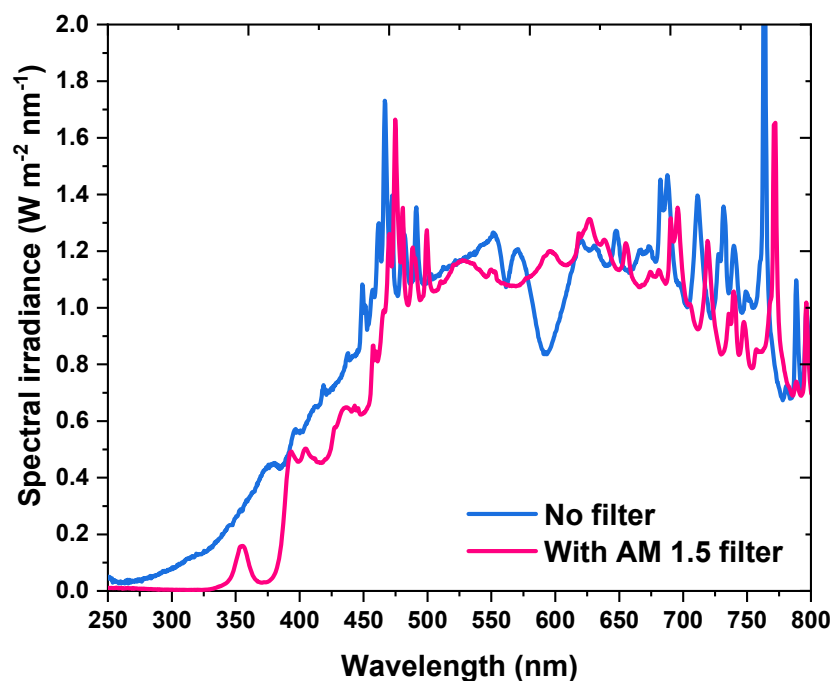
### 3.6.1 Experimental setup for photocatalytic testing

All photocatalytic experiments were carried out in a custom-built stirred tank reactor which has been previously reported by McMurray *et al.*<sup>23</sup> and Alrousan *et al.*<sup>24</sup> The reactor has a cylindrical vessel with inner diameter of 7 cm, and a working volume of 200 mL. A stainless-steel propeller (500 rpm) and baffle were used to give effective

mixing in the reactor. Dissolved oxygen was maintained in the solution through continuous air sparging. The lab set up for photocatalytic experiments is shown in Fig. 3.8.



**Fig. 3.8.** Schematic of stirred tank reactor used for photocatalytic experiments (Adapted from Alrousan *et al.* water research, 2009, 43, 47–54)<sup>24</sup>



**Fig. 3.9.** Spectral irradiance for the 1 kW Xe lamp for UV-Vis irradiation (250–800 nm) with and without AM 1.5 filter.

The photocatalytic activities for *E. coli* disinfection and phenol degradation were evaluated under UV-visible light irradiation which was provided by a 1 kW xenon lamp (LoT-QuantumDesign) equipped with AM 1.5 filter. The incident irradiance was measured using a spectroradiometer (FLAME-S-UV-VIS-ES, Ocean Optics B.V, Netherlands) at bottom of the reactor at different points. The average spectral emission of the light source in the range of 250-800 nm is shown in Fig. 3.9. The constant temperature ( $20 \pm 2^\circ\text{C}$ ) was maintained in the reactor through water circulation in outer jacket during the photocatalytic experiments. Before starting of each experiment, the lamp was allowed to warm up for at least 30 min.

### **3.6.2 Photocatalytic degradation of organic pollutants**

The photocatalytic activities of synthesized materials and P25-TiO<sub>2</sub> were evaluated by the degradation of phenol under UV-visible irradiation (AM 1.5 filter was used). Phenol (200 mL of 0.1 mM) solution containing as synthesized photocatalyst ( $100 \text{ mg L}^{-1}$ ) were placed in stirred tank reactor. Before irradiation, the suspension was stirred in the dark for 60 min to ensure the equilibrium adsorption state between the photocatalyst and the organic solution. At certain time intervals (-60, 0, 60, 120, 180, 240, 300 min), 3 mL of the suspension was taken out for analysis which was filtered using syringe filter (membrane filter,  $0.22 \mu\text{m}$ , 25 mm) to remove the particles.

### **3.6.3 Phenol analysis by high performance liquid chromatography (HPLC)**

HPLC is a qualitative and quantitative technique that is used for the identification and quantification of compounds in a various application such as pharmaceutical applications, environmental applications, forensics, clinical, food and flavour, *etc.* A typical HPLC system includes, a column that holds stationary phase, a

pump that moves the mobile phase (s) through the column and a detector that displays the retention time of the molecules.<sup>25</sup>

In our study, HPLC technique was employed to detect and quantify the change in phenol concentration during photocatalytic experiments. A series of experiments were performed to degrade phenol using synthesized photocatalysts and analysed using HPLC system (Agilent technologies 1200 series) equipped with UV detector and C18 column (Phenomenex guard, 22.0 mm x 4.0 mm, 5 $\mu$ m). The mobile phase solution was a mixture of methanol (100 %) and formic acid (1000 ppm) in the ratio of 40:60 (v/v). The flow rate of mobile phase was maintained at 1 mL/min and 20  $\mu$ L of the sample was injected by inbuilt autosampler in HPLC and analysed at 270 nm wavelength.

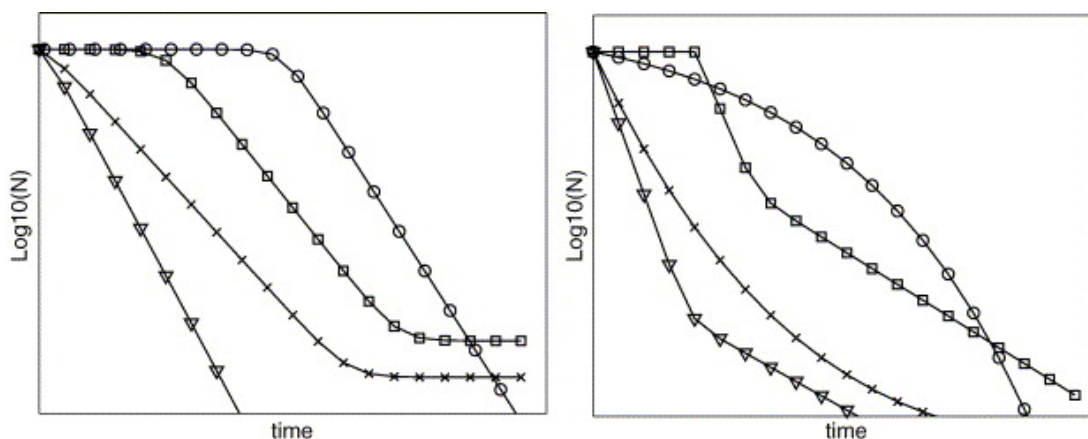
#### **3.6.4 Photocatalytic disinfection**

In this study, *E. coli* K-12 was selected as a model micro-organism for investigating the performance of photocatalyst for water disinfection. Fresh stock of *E. coli* K-12 (CTEC 4624) was cultured in tryptone soya broth (30 g L<sup>-1</sup>) and incubated at 37°C in aerobic conditions for 21 h, yielding a concentration of 10<sup>9</sup> CFU mL<sup>-1</sup>. Prepared *E. coli* culture (200  $\mu$ L) was spiked into 200 mL saline water (9 g L<sup>-1</sup> NaCl) to obtain an initial bacterial concentration of 10<sup>6</sup> CFU mL<sup>-1</sup>. The photocatalytic activities for water disinfection experiments were performed in stirred tank reactor under UV-visible irradiation (AM 1.5 filter was used) in the absence and presence of carbon nitride. Air was sparged into the suspension during the reaction to provide oxygen as an electron acceptor. The catalyst loading was kept constant 100 mg L<sup>-1</sup> for each sample tested for water disinfection. Each experiment was run for 5 h and about 500  $\mu$ L sample was collected from reactor at 0, 30, 60, 120, 180, 240 and 300 min and

a serial 10-fold dilution in Ringer's solution was made up to  $10^3$  CFU mL<sup>-1</sup>. Further, both drop plate method and plate spreading technique were used with aliquots of 10–100  $\mu$ L according to the expected *E. coli* concentrations to reach a detection limit of 2 CFU mL<sup>-1</sup>. Colony forming units were counted using the standard plated counting method after incubation of 24 h at 37°C.<sup>26,27</sup>

### 3.6.5 GInaFiT modelling tool for disinfection kinetics

In order to understand photocatalytic disinfection process, appropriate fitting models should be used to simulate the disinfection kinetics. GInaFIT tool (Geeraerd and Van Impe Inactivation Model Fitting Tool, version 1.6) can serve this purpose which was developed by Geeraerd *et al.*<sup>28</sup> It is a free tool and used as an add-in to Microsoft Excel. It can predict the model of the microbial population evolution over time among nine model types available in the tool. These nine model types cover all eight shapes of survival curves illustrated in Fig. 3.10.



**Fig. 3.10.** Eight types of inactivation curves included in GInaFiT modelling tool. Left plot: linear ( $\nabla$ , shape I), linear with tailing ( $\times$ , shape II), sigmoidal-like ( $\square$ , shape III), linear with a preceding shoulder ( $\circ$ , shape IV). Right plot: biphasic ( $\nabla$ , shape V), concave ( $\times$ , shape VI), biphasic with a shoulder ( $\square$ , shape VII), and convex ( $\circ$ , shape VIII). [Reproduced from Geeraerd *et al. Int. J. Food Microbiol.*, 2005, **102**, 95–105]<sup>28</sup>

This model has previously been used to fit experimental data from photocatalytic<sup>29-31</sup> and solar disinfection<sup>32,33</sup> studies. Each data set was fitted for all nine models and out of nine inactivation models, best fit model is selected based on sum of squared errors (SSE), root mean sum of squared errors (RMSE), the coefficient of determination ( $R^2$ ) and other parameters.

### 3.7 References

1. Thomas, A., Fischer, A., Goettmann, F., Antonietti, M., Müller, J. O., Schlögl, R., & Carlsson, J. M. Graphitic carbon nitride materials: variation of structure and morphology and their use as metal-free catalysts. *J. Mater. Chem.* 2008, **18**, 4893.
2. Xu, J., Zhang, L., Shi, R. & Zhu, Y. Chemical exfoliation of graphitic carbon nitride for efficient heterogeneous photocatalysis. *J. Mater. Chem. A* 2013, **1**, 14766–14772.
3. Niu, P., Zhang, L., Liu, G. & Cheng, H. M. Graphene-like carbon nitride nanosheets for improved photocatalytic activities. *Adv. Funct. Mater.* 2012, **22**, 4763–4770.
4. Dong, F., Wang, Z., Sun, Y., Ho, W. K. & Zhang, H. Engineering the nanoarchitecture and texture of polymeric carbon nitride semiconductor for enhanced visible light photocatalytic activity. *J. Colloid Interface Sci.* 2013, **401**, 70–79.
5. Byrappa, K. & Adschiri, T. Hydrothermal technology for nanotechnology. *Prog. Cryst. Growth Charact. Mater.* 2007, **53**, 117–166.
6. Zhao, J., Yan, J., Jia, H., Zhong, S., Zhang, X., & Xu, L. BiVO<sub>4</sub>/g-C<sub>3</sub>N<sub>4</sub> composite visible-light photocatalyst for effective elimination of aqueous organic pollutants. *J. Mol. Catal. A Chem.* 2016, **424**, 162–170.
7. Xi, G. & Ye, J. Synthesis of bismuth vanadate nanoplates with exposed {001} facets and enhanced visible-light photocatalytic properties. *Chem. Commun.* 2010, **46**, 1893–1895.
8. Thanh, N. T. K., Maclean, N. & Mahiddine, S. Mechanisms of nucleation and growth of nanoparticles in solution. *Chem. Rev.* 2014, **114**, 7610–7630.

9. Su, J., Guo, L., Yoriya, S. & Grimes, C. A. Aqueous growth of pyramidal-shaped BiVO<sub>4</sub> nanowire arrays and structural characterization: application to photoelectrochemical water splitting. *Cryst. Growth Des.* 2010, **10**, 856–861.
10. Tauc, J., Grigorovici, R. & Vancu, A. Optical Properties and Electronic Structure of Amorphous Germanium. *Phys. stat. sol.* 1966, **15**, 627–637.
11. Davis, E. A. & Mott, N. F. Conduction in non-crystalline systems V. Conductivity, optical absorption and photoconductivity in amorphous semiconductors. *Philos. Mag.* 1970, **22**, 0903–0922.
12. Kubelka, P. and Munk, F. A contribution to the optics of pigments. *Z. Tech. Phys.* 1931, **12**, 593-601.
13. Makuła, P., Pacia, M. & Macyk, W. How To Correctly Determine the Band Gap Energy of Modified Semiconductor Photocatalysts Based on UV-Vis Spectra. *J. Phys. Chem. Lett.* 2018, **9**, 6814–6817.
14. Leofanti, G., Padovan, M., Tozzola, G. & Venturelli, B. Surface area and pore texture of catalysts. *Catal. Today* 1998, **41**, 207–219.
15. Chen, Z., Jaramillo, T. F., Deutsch, T. G., Kleiman-Shwarsstein, A., Forman, A. J., Gaillard, N., Garland, R., Takanabe, K., Heske, C., Sunkara, M., McFarland, E. W., Domen, K., Miller, E. L., Turner, J. A. & Dinh, H. N. Accelerating materials development for photoelectrochemical hydrogen production: Standards for methods, definitions, and reporting protocols. *J. Mater. Res.* 2010, **25**, 3–16.
16. Kalamaras, E., Maroto-Valer, M. M., Shao, M., Xuan, J. & Wang, H. Solar carbon fuel via photoelectrochemistry. *Catal. Today* 2018, **317**, 56–75.
17. Cortes, M. A. L. R. M., McMichael, S., Hamilton, J. W.J., Sharma, P. K., Brown, A. & Byrne, J. A. Photoelectrochemical reduction of CO<sub>2</sub> with TiNT. *Mater. Sci. Semicond. Process.* 2020, **108**, 104900.
18. Basic theories of semiconductor electrochemistry. in *electrochemistry of silicon and its oxide*. Springer, 2004, 1–43. (doi:10.1007/0-306-47921-4\_1)
19. Elgrishi, N., Rountree, K. J., McCarthy, B. D., Rountree, E. S., Eisenhart, T. T., & Dempsey, J. L. A practical beginner's guide to cyclic voltammetry. *J. Chem. Educ.* 2018, **95**, 197–206.
20. Nishi, N. Electrochemical impedance spectroscopy. *Nat. Rev. Methods Prim.* 2021, **1**, 42.
21. Hankin, A., Bedoya-Lora, F. E., Alexander, J. C., Regoutz, A. & Kelsall, G. H.



- Flat band potential determination: avoiding the pitfalls. *J. Mater. Chem. A* 2019, **7**, 26162–26176.
22. Sivula, K. Mott–Schottky analysis of photoelectrodes: sanity checks are needed. *ACS Energy Lett.* 2021, **6**, 2549–2551.
  23. McMurray, T.A. Byrne, J.A., Dunlop, P.S.M., Winkelman, J.G.M., Eggins, B.R. & McAdams, E.T. Intrinsic kinetics of photocatalytic oxidation of formic and oxalic acid on immobilised TiO<sub>2</sub> films, *Applied Catalysis A: General.* 2004, **262**, 105-110.
  24. Alrousan, D. M. A., Dunlop, P. S. M., McMurray, T. A. & Byrne, J. A. Photocatalytic inactivation of *E. coli* in surface water using immobilised nanoparticle TiO<sub>2</sub> films. *Water Res.* 2009, **43**, 47–54.
  25. Malviya R, Bansal V, P. O. P. and S. P. K. High performance liquid chromatography: a short review. *J. Glob. Pharma Technol.* 2010, **5**, 22–26.
  26. Niemela, S. Statistical evaluation of Results from Quantitative microbiological Examinations. 2. NMKL Rapport (Sweden). *Nordisk Metodik-Kommitte foer Livsmedel. no. 1.* 1983.
  27. Tomasiewicz, D. M., Hotchkiss, D. K., Reinbold, G. W., Read, R. B. & Hartman, P. A. The Most Suitable Number of Colonies on Plates for Counting I. *J. Food Prot.* 1980, **43**, 282–286.
  28. Geeraerd, A. H., Valdramidis, V. P. & Van Impe, J. F. GInaFiT, a freeware tool to assess non-log-linear microbial survivor curves. *Int. J. Food Microbiol.* 2005, **102**, 95–105.
  29. Fernández-Ibáñez, P., Polo-López, M.I., Malato, S., Wadhwa, S., Hamilton, J. W. J., Dunlop, P. S. M., D'Sa, R., Magee, E., O'Shea, K., Dionysiou, D. D., & Byrne, J. A. Solar photocatalytic disinfection of water using titanium dioxide graphene composites. *Chem. Eng. J.* 2015, **261**, 36–44.
  30. Cruz-Ortiz, B. R., Hamilton, J. W. J., Pablos, C., Díaz-Jiménez, L., Cortés-Hernández, D. A., Sharma, P. K., Castro-Alfárez, M., Fernández-Ibáñez, P., Dunlop, P. S. M., & Byrne, J. A. Mechanism of photocatalytic disinfection using titania-graphene composites under UV and visible irradiation. *Chem. Eng. J.* 2017, **316**, 179–186.
  31. Makwana, N. M., Hazael, R., McMillan, P. F. & Darr, J. A. Photocatalytic water disinfection by simple and low-cost monolithic and heterojunction ceramic wafers. *Photochem. Photobiol. Sci.* 2015, **14**, 1190–1196.

32. Ubomba-Jaswa, E., Navntoft, C., Polo-López, M. I., Fernandez-Ibáñez, P. & McGuigan, K. G. Solar disinfection of drinking water (SODIS): an investigation of the effect of UV-A dose on inactivation efficiency. *Photochem. Photobiol. Sci.* 2009, **8**, 587.
33. Boyle, M., Sichel, C., Fernández-Ibáñez, P., Arias-Quiroz, G. B., Iriarte-Puña, M., Mercado, A., Ubomba-Jaswa, E., & McGuigan, K. G. Bactericidal effect of solar water disinfection under real sunlight conditions. *Appl. Environ. Microbiol.* 2008, **74**, 2997–3001.

## **Chapter 4 - The effect of precursors and synthesis parameters on the physicochemical properties and photocatalytic activity of g-C<sub>3</sub>N<sub>4</sub>**

### **4.1 Aim and objectives**

**4.1.1 Aim:** This chapter aims to study the effect of different precursors and reaction parameters on the physicochemical properties and photocatalytic activity of g-C<sub>3</sub>N<sub>4</sub>.

### **4.1.2 Objectives**

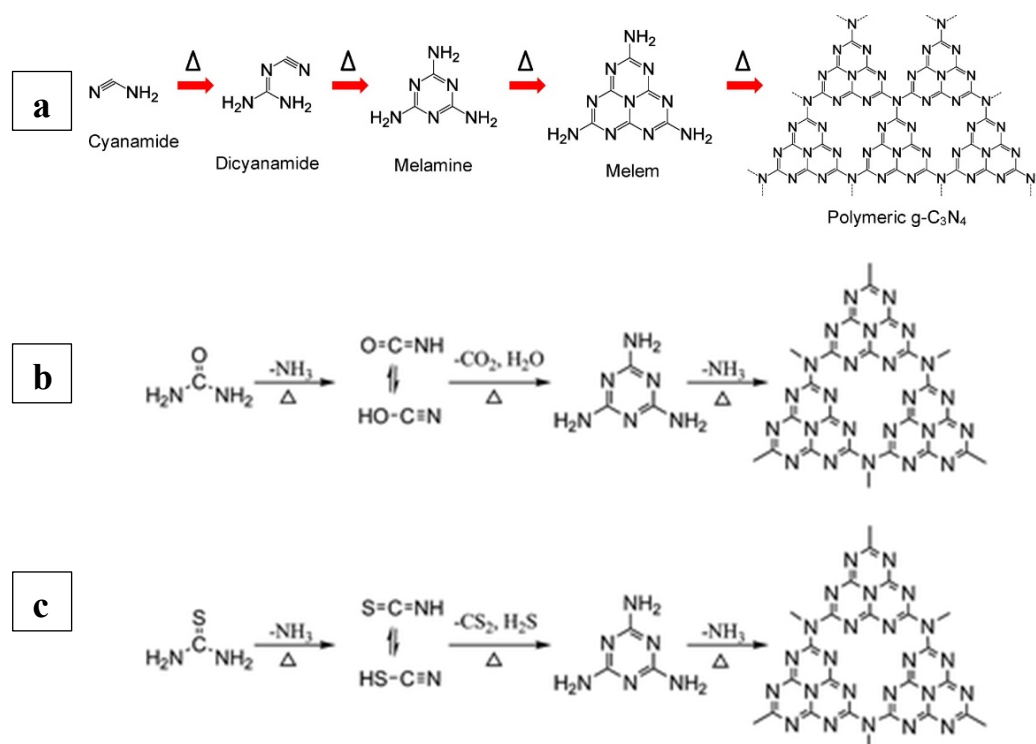
1. To synthesize graphitic carbon nitride (g-C<sub>3</sub>N<sub>4</sub>) and exfoliated g-C<sub>3</sub>N<sub>4</sub> using different precursors and reactions conditions in a thermal polymerization route.
2. To determine the effect of reaction temperature on physicochemical properties of g-C<sub>3</sub>N<sub>4</sub> using XRD, FTIR, Raman, BET and DRS.
3. To determine the effect of synthesis reaction time on physicochemical properties of g-C<sub>3</sub>N<sub>4</sub> using XRD, FTIR, Raman, BET and DRS.
4. To determine the effect of different synthesis precursors on the physicochemical properties of g-C<sub>3</sub>N<sub>4</sub> using XRD, FTIR, Raman, BET and DRS.
5. To study the impact of thermal exfoliation of g-C<sub>3</sub>N<sub>4</sub> on its physicochemical properties using XRD, FTIR, Raman, BET, DRS and FESEM.
6. To study the effect of precursors and synthesis parameters on photocatalytic activity of g-C<sub>3</sub>N<sub>4</sub> for water disinfection and organic chemical degradation under UV-visible irradiation and compare it against P25-TiO<sub>2</sub>.

## 4.2 Introduction

Graphitic carbon nitride (g-C<sub>3</sub>N<sub>4</sub>) has been reported to be an n-type narrow band gap semiconductor (~2.7 eV), physically and chemically stable, and earth abundant in nature.<sup>1,2</sup> It was first time synthesized by Berzelius and labelled as “melon” by Liebig in 1834.<sup>3</sup> Carbon nitride has possessed seven different phases named as  $\alpha$ -C<sub>3</sub>N<sub>4</sub>,  $\beta$ -C<sub>3</sub>N<sub>4</sub>, cubic C<sub>3</sub>N<sub>4</sub>, pseudo cubic C<sub>3</sub>N<sub>4</sub>, g-h-triazine, g-o-triazine and g-h-heptazine (has been discussed in detail in chapter 2).<sup>4,5</sup> Among these phases, g-h-heptazine unit which is also known as tri-s-triazine unit has been widely accepted as the most stable phase and as the elementary structure of layered g-C<sub>3</sub>N<sub>4</sub> which is composed of covalently crosslinked *sp*<sup>2</sup>-hybridized alternative C and N atoms.<sup>6,7</sup> Wang *et al.* was the first to report the photocatalytic behaviour of g-C<sub>3</sub>N<sub>4</sub> for H<sub>2</sub> evolution in 2009.<sup>8</sup> Since then, it has been explored for different photocatalytic applications such as organic pollutant degradation in water,<sup>9</sup> bacterial inactivation,<sup>10</sup> CO<sub>2</sub> reduction,<sup>11</sup> and H<sub>2</sub> evolution, *etc.*<sup>12</sup>

g-C<sub>3</sub>N<sub>4</sub> can be easily synthesized by thermal polymerization of various precursors such as cyanamide,<sup>13</sup> melamine,<sup>3</sup> dicyandiamide,<sup>14</sup> thiourea,<sup>15</sup> ammonium thiocyanate,<sup>16</sup> urea,<sup>17</sup> *etc.* The whole synthesis process is a combination of polyaddition and polycondensation where cyanamide, dicyandiamide, or melamine produces a melon polymer made up from melon units followed by ammonia elimination to get final product as carbon nitride. A difference in products was also observed if condensation is performed in closed and open crucibles. Melamine based products were found up to 350°C, further heating to 390°C derived in the development of tri-s-triazine units via melamine rearrangements. Additional heating lead to condensation of tri-s-triazine units in to polymers and final polymerization of g-C<sub>3</sub>N<sub>4</sub> occurs at temperature above 500°C and heating above 700°C resulted in the

disappearance of material due to formation of nitrogen and cyano fragments.<sup>6,18</sup> Urea and thiourea are oxygen and sulfur containing precursors respectively, thus they have some different intermediate species and additional elimination gases. A possible mechanism of the reaction pathways of polymeric carbon nitride formation using different precursors are shown in Fig. 4.1 a-c.<sup>15,19,20</sup>



**Fig. 4.1.** Possible mechanisms of the reaction pathways of polymeric carbon nitride formation using (a) Cyanamide [Reproduced from Ong *et al.* Chem. Rev. 2016, 116, 7159–7329],<sup>20</sup> (b) Urea, and (c) Thiourea, as precursor [Reproduced from Zhang *et al.* J. Mater. Chem. 2012, 22, 8083]<sup>15</sup>

Precursors and reactions conditions have a significant effect on the chemical and physical properties of final product which may affect its photocatalytic performance. Any change in reaction parameters such as condensation temperature, time and heating rate also affect the optical and electronic properties of g-C<sub>3</sub>N<sub>4</sub>. A precursor is judged based on cost, toxicity, yield and its impact on properties and applications of end product.<sup>21</sup> Comparative studies on the role of precursors<sup>21–23</sup> and condensation

temperature<sup>24-26</sup> on photocatalytic properties of g-C<sub>3</sub>N<sub>4</sub> have previously been reported. For instance, Vidyasagar *et al.* investigated the role of precursors on photocatalytic performance of g-C<sub>3</sub>N<sub>4</sub> for degradation of acid violet 7 dye AV 7 under visible light. Their results revealed the negative photocatalytic performance of thiourea derived g-C<sub>3</sub>N<sub>4</sub> while urea-based g-C<sub>3</sub>N<sub>4</sub> was reported to be an efficient photocatalyst.<sup>22</sup> In another study by Papailias *et al.*, g-C<sub>3</sub>N<sub>4</sub> was prepared using melamine precursor at different temperatures and photocatalytic activity was evaluated by NO oxidation under UV and visible light irradiation.<sup>25</sup>

The photocatalytic efficiency of the bulk g-C<sub>3</sub>N<sub>4</sub> is reported to be very low owing to fast recombination of photogenerated charge carriers (e<sup>-</sup> & h<sup>+</sup>), low electrical conductivity, small surface area, less active sites and the inability of absorption above 460 nm.<sup>27,28</sup> In general, higher surface area and higher crystallinity could improve photocatalytic performance of a material. However, in most of the cases both surface area and crystallinity are contradictory and hard to achieve at the same time because the particle size increases as the crystallisation progresses, hence the specific surface area decreases. Improvement in crystallinity also reduces the defects in crystal structure which prevent the e<sup>-</sup> - h<sup>+</sup> recombination while a material with higher surface area may provide more reactive sites for adsorption.<sup>29</sup> Therefore, optimization of synthesis parameters is essential to balance good crystallinity and high specific surface area to obtain a good catalyst.

The aim of this chapter is to analyze the effect of different precursors and reaction parameters on the physiochemical properties of g-C<sub>3</sub>N<sub>4</sub> *i.e.*, porosity, morphology, crystal structure, *etc.* and photocatalytic performance for organic degradation and bacterial inactivation. In this study, we used phenol as a model organic pollutant and

*Escherichia coli* as a model microorganism. The photocatalytic activity of g-C<sub>3</sub>N<sub>4</sub> were investigated under UV-visible irradiation and compare against P25-TiO<sub>2</sub>.

## 4.3 Experimental Section

### 4.3.1 Materials

All the chemicals, melamine (Sigma Aldrich, 99 %), urea (Fluka, 99.5 %), thiourea (Merck, 98 %), TiO<sub>2</sub> (Evonik Aeroxide P25) were of analytical grade and used in experiments without any further purification.

### 4.3.2 Synthesis of bulk g-C<sub>3</sub>N<sub>4</sub>

The g-C<sub>3</sub>N<sub>4</sub> was synthesized by direct heating using four different precursors (melamine, dicyandiamide, urea and thiourea). In a typical synthesis, 8 g melamine was loaded into a covered alumina crucible, then heated it in a muffle furnace at desired temperature and time with heating ramp up and down of 5°C min<sup>-1</sup>. Finally, the obtained yellow colour product was collected and ground into fine powder using mortar and pestle before further characterization and is referred to as bulk g-C<sub>3</sub>N<sub>4</sub>. Following the same procedure, all g-C<sub>3</sub>N<sub>4</sub> samples were prepared using melamine, dicyandiamide, urea, and thiourea with respective synthesis conditions as shown in Table 4.1. The different g-C<sub>3</sub>N<sub>4</sub> samples were given abbreviated names with temp and time indicated *i.e.*, melamine (MCN-temp-time), urea (UCN-temp-time), and thiourea (TCN-temp-time).

### 4.3.3 Thermal exfoliation of g-C<sub>3</sub>N<sub>4</sub>

Bulk g-C<sub>3</sub>N<sub>4</sub> samples were further heated at 500°C for 4 h in an open crucible to get exfoliated g-C<sub>3</sub>N<sub>4</sub>. Samples treated previously at 545°C for 4 h were used to

determine exfoliation impact on its physiochemical properties and photocatalytic performance.

**Table 4.1.** Summary of all the prepared g-C<sub>3</sub>N<sub>4</sub> samples with their reaction parameters

Parameters	Temperature effect	Time effect	Precursor effect	Exfoliation effect
Precursor	Melamine	Melamine	Melamine, thiourea, dicyandiamide, urea	Melamine, thiourea, urea
Temperature (°C)	450, 510, 545, 580, 650	545	545	545
Time (h)	4	1, 2, 3, 4, 5	4	4
Exfoliation	-	-	-	Thermal (500°C, 4h)

#### 4.3.4 Characterizations

The synthesized g-C<sub>3</sub>N<sub>4</sub> samples were characterized by X-ray diffraction (XRD) in the 2θ range of 5–50°, Fourier-Transform Infrared spectroscopy (FTIR) in the range of 4000–500 cm<sup>-1</sup> and Raman spectroscopy in the range of 1600-400 cm<sup>-1</sup>. The Brunauer–Emmett–Teller (BET) method was used to measure specific surface area of g-C<sub>3</sub>N<sub>4</sub> samples. Optical properties were analysed using diffuse reflectance spectroscopy (DRS). The morphology of the resultant product was examined by a field emission scanning electron microscope (FESEM). The details of all the characterization techniques are provided in chapter 3.

#### 4.3.5 Photocatalysis experiments

##### 4.3.5.1 Water disinfection

###### 4.3.5.1.1 Preparation of bacterial culture

In this study, *E. coli* K-12 was selected as a model micro-organism for investigating the performance of photocatalyst for water disinfection. Fresh stock of



*E. coli* K-12 (CTEC 4624) was cultured in tryptone soya broth ( $30 \text{ g L}^{-1}$ ) and incubated at  $37^\circ\text{C}$  in aerobic conditions for 21 h, yielding a concentration of  $10^9 \text{ CFU mL}^{-1}$ .

#### 4.3.5.1.2 Inactivation of *E. coli*

200  $\mu\text{L}$  of prepared *E. coli* culture was spiked into 200 mL saline water ( $9 \text{ g L}^{-1} \text{ NaCl}$ ) to obtain an initial bacterial concentration of  $10^6 \text{ CFU mL}^{-1}$ . The photocatalytic activities for water disinfection were evaluated in stirred tank reactor (see chapter 3) under UV-visible irradiation (AM 1.5 filter was used) in the absence and presence of carbon nitride. The catalyst loading was kept constant  $100 \text{ mg L}^{-1}$  for each sample tested for water disinfection. Each experiment was run for 5 h and about 500  $\mu\text{L}$  sample was collected from reactor at 0, 30, 60, 120, 180, 240 and 300 min and a serial 10-fold dilution in Ringer's solution was made up to  $10^3 \text{ CFU mL}^{-1}$ . Both the drop plate method and plate spreading technique were used with aliquots of 10–100  $\mu\text{L}$  according to the expected *E. coli* concentrations to reach a detection limit of 2  $\text{CFU mL}^{-1}$ . Colony forming units were counted using the standard plated counting method after incubation of 24 h at  $37^\circ\text{C}$ .

#### 4.3.5.2 Photocatalytic degradation of phenol

The photocatalytic activities of as prepared  $\text{g-C}_3\text{N}_4$  materials and P25- $\text{TiO}_2$  were also evaluated by the degradation of phenol under UV-visible irradiation (AM 1.5 filter was used). Phenol (200 mL of 0.1 mM) solution containing as synthesized photocatalyst ( $100 \text{ mg L}^{-1}$ ) were placed in stirred tank reactor. Before irradiation, the suspension was stirred in the dark for 1 h to ensure equilibrium between the photocatalyst and the organic solution. At certain time intervals (-60, 0, 60, 120, 180,

240, 300 min), 3 mL of the suspension was taken out for analysis which was filtered using syringe filter (membrane filter, 0.22  $\mu\text{m}$ , 25 mm) to remove the particles. The degradation of phenol was analysed using high performance liquid chromatography (HPLC) at 270 nm. More details are provided in chapter 3.

## 4.4 Results and Discussion

### 4.4.1 Physicochemical properties

#### 4.4.1.1 Effect of synthesis reaction temperature

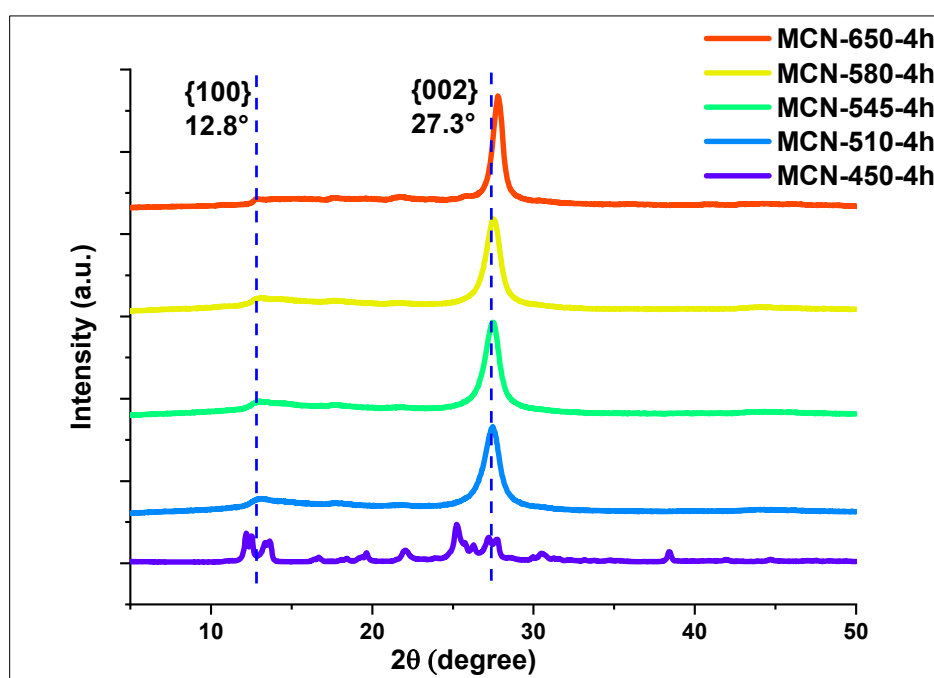
In this section, effect of synthesis temperature on the physicochemical properties (*i.e.*, crystal structure, chemical structure, surface area, bandgap, *etc.*) of g-C<sub>3</sub>N<sub>4</sub> is investigated through various characterization techniques such as XRD, FTIR, Raman, BET, and DRS, *etc.* Five different synthesis temperatures (450°C, 510°C, 545°C, 580°C, 650°C) were investigated. All prepared g-C<sub>3</sub>N<sub>4</sub> samples with reaction conditions and their abbreviated names are summarized in Table 4.2, also varying parameter marked in bold letters for easy understanding.

**Table 4.2.** Abbreviated names of synthesized samples with their reaction parameters

Precursor	<b>Temperature (°C)</b>	Time (h)	Abbreviation
Melamine	<b>450</b>	4	MCN-450-4h
Melamine	<b>510</b>	4	MCN-510-4h
Melamine	<b>545</b>	4	MCN-545-4h
Melamine	<b>580</b>	4	MCN-580-4h
Melamine	<b>650</b>	4	MCN-650-4h

XRD patterns of melamine calcinated in a closed crucible at various temperatures for similar time period, 4 h are shown in Fig. 4.2. The XRD pattern of melamine calcinated at 450°C for 4 h (MCN-450-4h) shows a series of diffraction

peaks which belongs to melem derivatives.<sup>30</sup> Interestingly, when the calcination temperature is increased above 500°C (MCN-510-4h, MCN-545-4h, MCN-580-4h and MCN-650-4h), the peaks at around 13° have almost disappeared whereas there is one strong peak at 27.3° and other weak intensity peak at 12.8° were observed which is melon characteristic signature, hence g-C<sub>3</sub>N<sub>4</sub>. This demonstrates that melamine could not be fully transformed from the melem phase to the melon phase until the calcination temperature was higher than 500°C.



**Fig. 4.2.** XRD patterns of g-C<sub>3</sub>N<sub>4</sub> samples synthesized at different temperatures using melamine as a precursor

It can also be observed in Fig. 4.2 that above 500°C, all the samples have XRD pattern similar to melon which is elementary unit of g-C<sub>3</sub>N<sub>4</sub>. However, the characteristic peak position of these patterns is not exactly same with each other, but there is a shift to higher angle (27.3° to 27.8°) while increasing the calcination temperature and therefore slightly lower interplanar distance, d-values (0.326 nm to 0.321 nm). This indicates a structural contraction along the layer stacking direction, probably as a result of a more prolonged condensation of the carbon nitride chains at

elevated temperature.<sup>25</sup> The interplanar distance ( $d$ ) or  $d$ -spacing was calculated using Bragg's law as given in equation 4.1.<sup>31</sup>

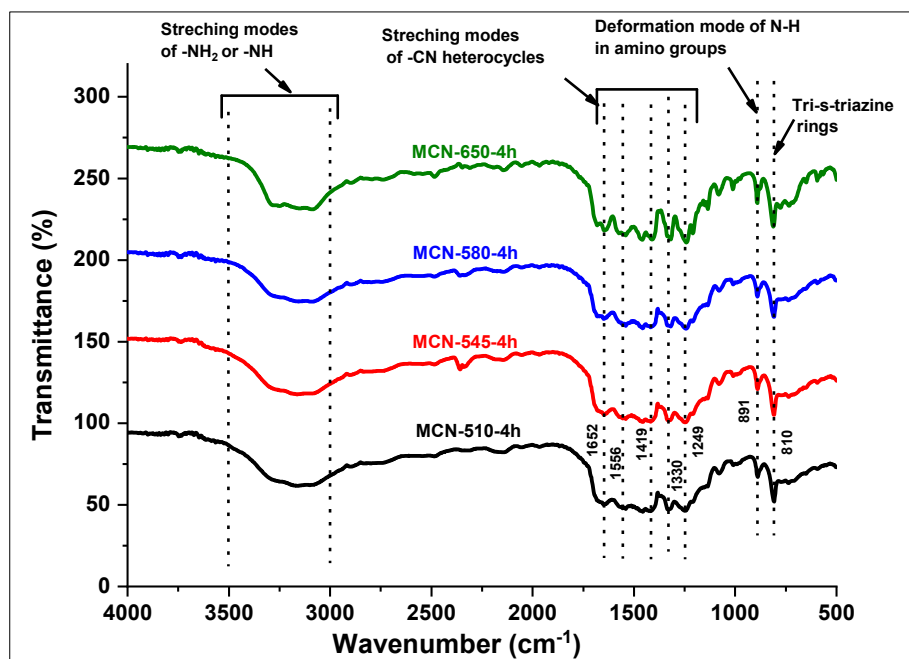
$$n\lambda = 2d\sin\theta \quad (4.1)$$

Where  $n = 1$  is a positive integer,  $\lambda$  is the wavelength of the incident X-ray beam (0.15406 nm), and  $\theta$  is the incident angle.

These two characteristic peaks (12.8° & 27.3°) of g-C<sub>3</sub>N<sub>4</sub> are associated with two different crystallographic planes, (100) and (002), respectively and are in good agreement with JCPDS 87-1526.<sup>32</sup> The weak intensity peak at 12.8° ( $d = 0.691$  nm) represents the structural heptazine (tri-s-triazine) unit of g-C<sub>3</sub>N<sub>4</sub> whereas the strong diffraction peak at 27.3° ( $d = 0.326$  nm) corresponds to the characteristic interlayer stacking structure as graphite.<sup>8</sup>

Further, g-C<sub>3</sub>N<sub>4</sub> may contain several basic groups such as -NH-, =N-, -NH<sub>2</sub> and -N-C= on its surface which are favourable for the removal of acidic pollutants. Fourier transform infrared spectroscopy (FTIR) can be used to identify these functional groups and C-N bonding information. In Fig. 4.3, FTIR spectra of g-C<sub>3</sub>N<sub>4</sub> samples synthesized at different temperatures using melamine are shown for the range of 4000-500 cm<sup>-1</sup>. The main characteristic peaks were observed in three regions in the spectra: 800-900 cm<sup>-1</sup>, 1200-1650 cm<sup>-1</sup> and 3000-3600 cm<sup>-1</sup>. The sharp absorption peak nearby 810 cm<sup>-1</sup> advocates the existence of heptazine/tri-s-triazine rings. The absorption peak at 891 cm<sup>-1</sup> indicates the presence of the deformation mode of N-H in amino groups. Various strong bands (1249, 1330, 1419, 1556, and 1652 cm<sup>-1</sup>) found in the region between 1200 and 1650 cm<sup>-1</sup> suggests the presence of typical stretching modes of CN heterocycles (C-NH-C or C-N(-C)-C), which can be inferred for the polymeric material. The broad peaks between 3000 and 3500 cm<sup>-1</sup> were related to the stretching modes of terminal -NH<sub>2</sub> or -NH groups at the defect sites of the aromatic

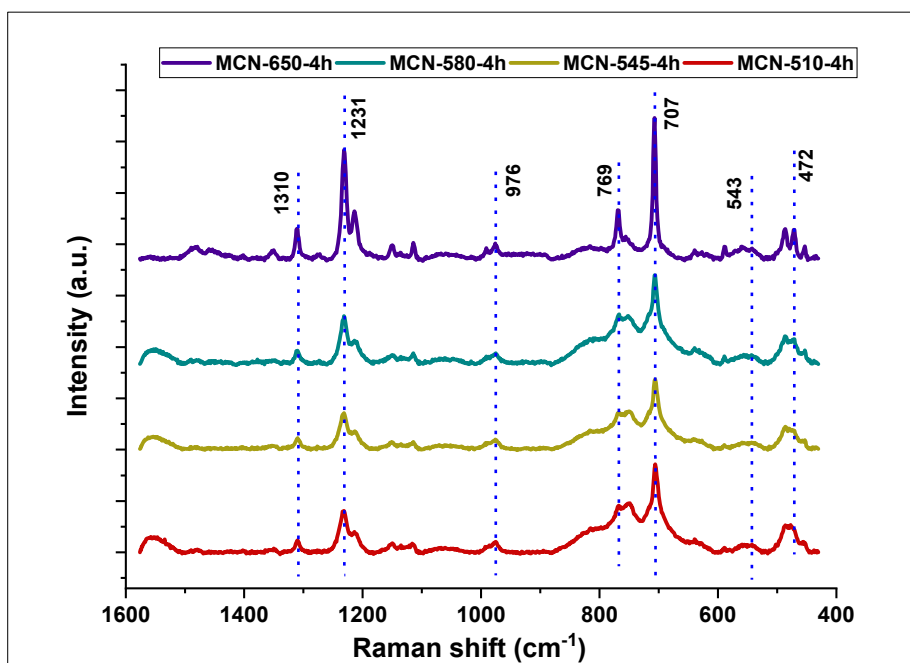
rings.<sup>33</sup> Here is no noticeable difference in FTIR spectra of g-C<sub>3</sub>N<sub>4</sub> samples with increasing calcination temperature above 500°C indicating the presence of all characteristic stretching vibrations in the spectra of g-C<sub>3</sub>N<sub>4</sub> samples synthesized at different temperatures using melamine which ensure the existence of uninterrupted g-C<sub>3</sub>N<sub>4</sub> framework in all the prepared samples.



**Fig. 4.3.** FTIR spectra of g-C<sub>3</sub>N<sub>4</sub> samples synthesized at different temperatures using melamine as a precursor

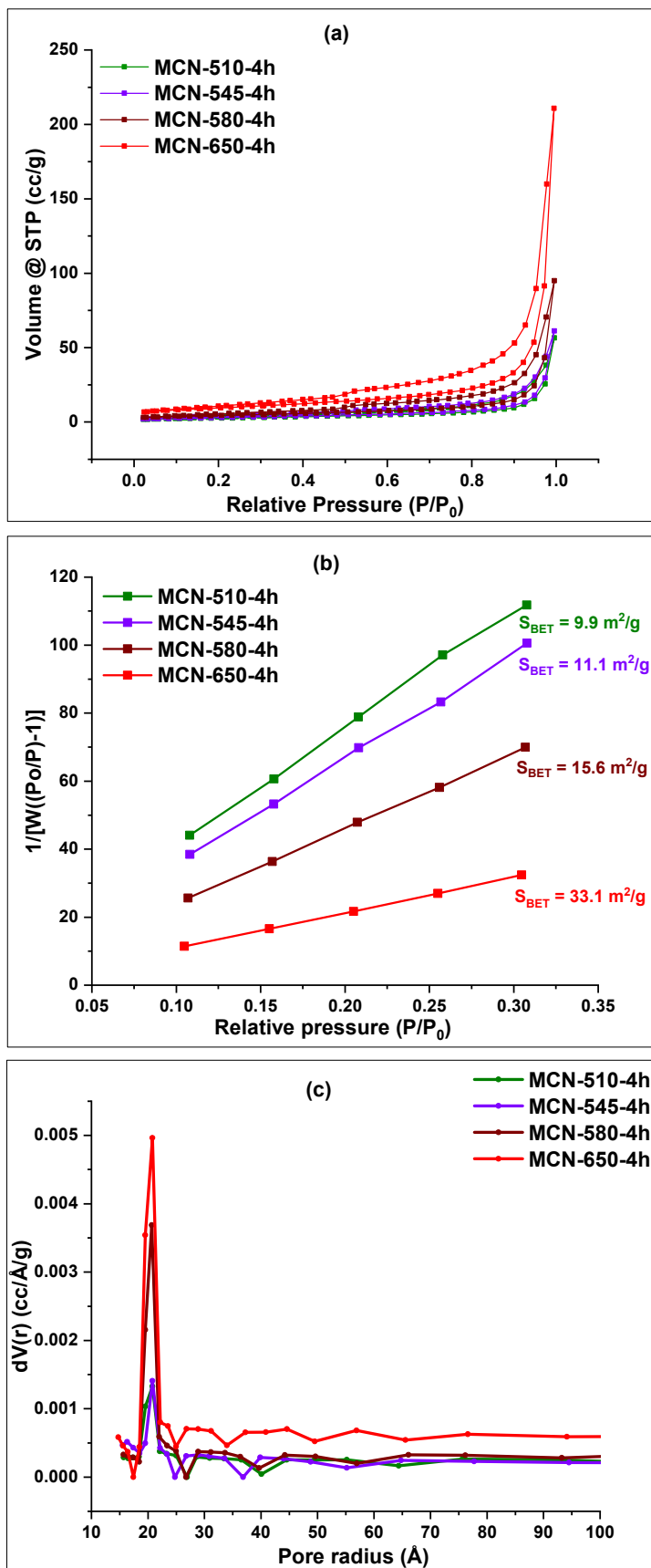
All prepared g-C<sub>3</sub>N<sub>4</sub> samples were also characterized by Raman spectroscopy. As shown in Fig. 4.4, all g-C<sub>3</sub>N<sub>4</sub> samples have multiple characteristic peaks in the 1600-400 cm<sup>-1</sup> spectral range. This spectral region is attributed to the skeletal vibrations of nitrogen aromatic rings. The major peaks are located at 1310, 1231, 976, 769, 707, 543, and 472 cm<sup>-1</sup> and can be seen in all the samples. Each peak can be assigned to the specific vibration modes. The strong peak located at 707 cm<sup>-1</sup> is indexed to heptazine ring, the weak peak at 976 cm<sup>-1</sup> is attributed to the triazine skeletal vibration and the bands at 1231, 1310 cm<sup>-1</sup> are assigned to characteristic stretching vibration modes of C=N and C-N heterocycles. The peaks at 707, 976, 1231,

and  $1310\text{ cm}^{-1}$  are the typical peaks for  $\text{g-C}_3\text{N}_4$  and intensifying with increasing calcination temperature from  $510^\circ\text{C}$  to  $650^\circ\text{C}$ , highest intensity was observed at  $650^\circ\text{C}$  which highlights the change in composition of  $\text{g-C}_3\text{N}_4$  samples during thermal polymerization. These findings are in agreement with earlier reports by Praus *et al.*<sup>34</sup> and Yuan *et al.*<sup>35</sup>



**Fig. 4.4.** Raman spectra of  $\text{g-C}_3\text{N}_4$  samples synthesized at different temperatures using melamine

In order to determine the impact of calcination temperature on specific surface area of  $\text{g-C}_3\text{N}_4$ , BET measurements for samples MCN-545-4h, MCN-580-4h and MCN-650-4h were performed. Fig. 4.5a-c show nitrogen adsorption-desorption isotherms and corresponding pore size distribution curve altogether five-point BET surface area graph, corresponding values are tabulated in Table 4.3.



**Fig. 4.5.** (a) Nitrogen adsorption-desorption isotherms, (b) Specific surface area by five-point BET, and (c) corresponding pore size distribution curves for g-C<sub>3</sub>N<sub>4</sub> samples synthesized at different temperatures using melamine

Based on the IUPAC classification, all prepared samples followed type IV isotherm and type H3 hysteresis loop indicating the presence of nonuniform mesopores (mesopores have pore diameter between 2 and 50 nm).<sup>36</sup> It can be depicted from isotherm (Fig. 4.5a) that sample calcinated at higher temperature adsorbs more nitrogen than sample calcinated at lower temperature which turns into the high surface area. For specific surface area calculation, five points (0.10, 0.15, 0.20, 0.25 and 0.30) were considered between relative pressure range, 0.1-0.3. Fig. 4.5b clearly reveals the three times increment (*i.e.*, 11.1 m<sup>2</sup> g<sup>-1</sup> to 33.1 m<sup>2</sup> g<sup>-1</sup>) in specific surface area of MCN-650-4h than for MCN-545-4h supporting the more active sites available for reaction. Average pore-size and average pore volume distribution was determined by the BJH (Barrett–Joyner–Halenda) method. Pore volume distribution curves (Fig. 4.5c) shows the sharp peak at 20 Å (in terms of pore radius) conforming the mesoporous structures. Remarkably, sample MCN-650-4h shows a wide distribution of pores than other samples since it contains larger size mesopores and some macropores. One might expect that a high surface area and large pore size are favourable for better photocatalytic properties, as a result of better adsorption and more active sites.<sup>25</sup>

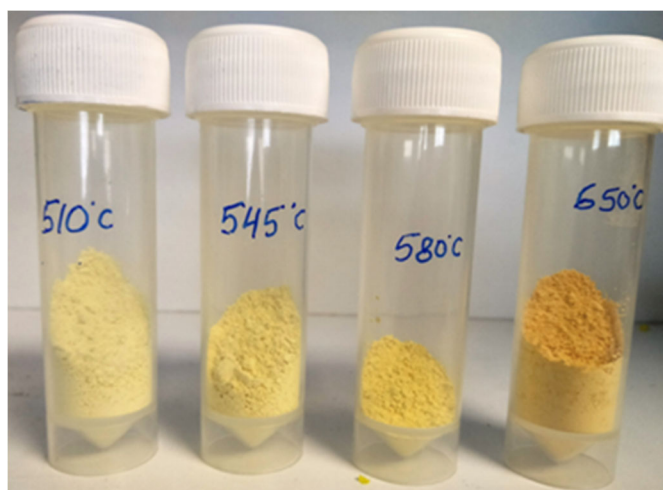
**Table 4.3.** Effect of calcination temperature of g-C<sub>3</sub>N<sub>4</sub> on BET parameters and band gap energy

Sample Name	S <sub>BET</sub> <sup>a</sup> (m <sup>2</sup> g <sup>-1</sup> )	P <sub>r</sub> <sup>b</sup> (Å)	P <sub>v</sub> <sup>c</sup> (cc g <sup>-1</sup> )	E <sub>g</sub> <sup>d</sup> (eV)	Mass yield (%)
MCN-510-4h	9.9	20.8	0.088	2.75	51.1
MCN-545-4h	11.1	20.8	0.094	2.69	50.2
MCN-580-4h	15.6	20.7	0.148	2.65	39.1
MCN-650-4h	33.1	20.8	0.329	2.54	37.2

[a] Specific surface area (S<sub>BET</sub>) was determined by the BET equation. [b] Mode of pore radius (P<sub>r</sub>) was determined by the BJH method. [c] Average pore volume (P<sub>v</sub>) was determined by the BJH method. [d] Band gap energy (E<sub>g</sub>) calculated from Tauc plots

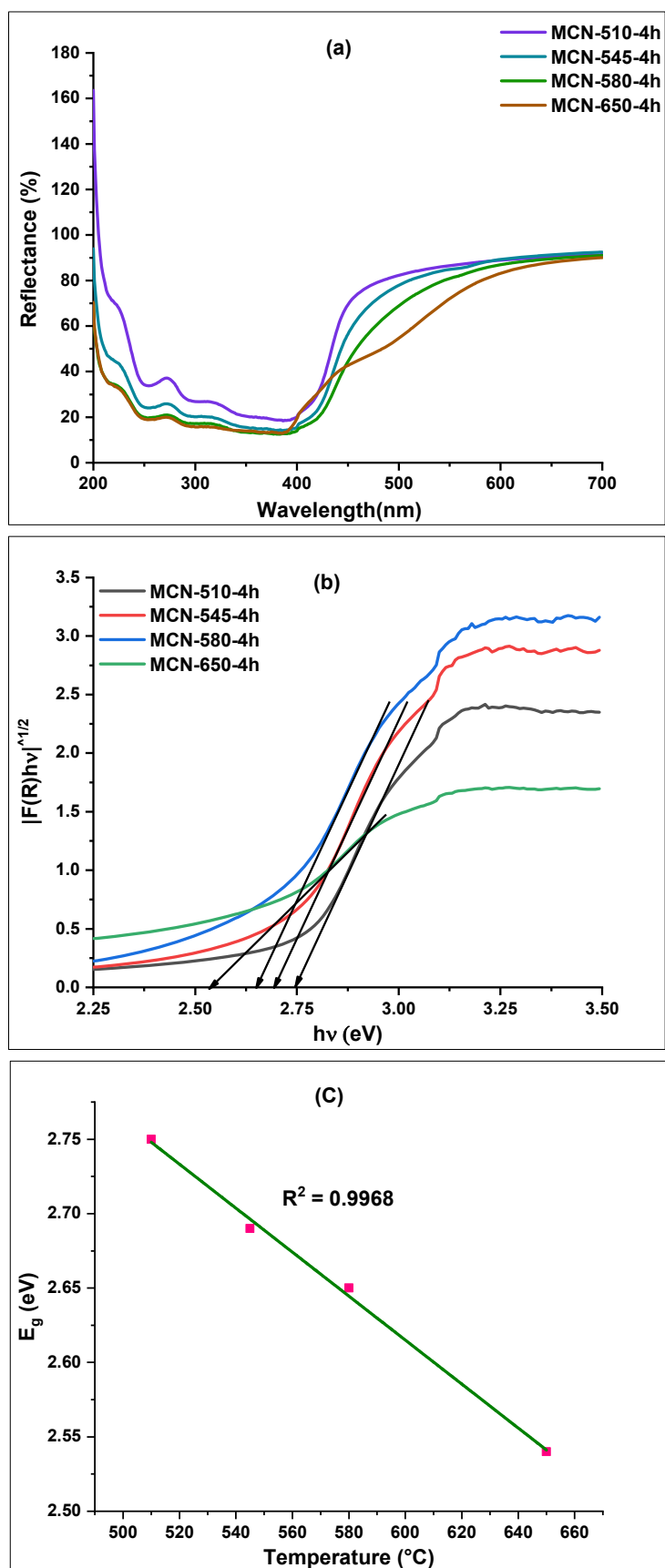


A digital photograph of melamine derived g-C<sub>3</sub>N<sub>4</sub> samples is shown in Fig. 4.6 which depicts the colour change from light yellow to dark yellow with increasing synthesis temperature suggesting improved absorption in the visible light region. It was also found that mass yield of the final product also decreases as temperature rises which is due to the accelerated degree of polymerization and condensation. The mass yield for final product was found 51.1% (at 510°C), 50.2% (at 545°C), 39.1% (at 580°C) and 37.2% (at 650°C). The rapid weight loss at 580°C compared to 545°C suggests that the degree of polymerization and condensation increases rapidly when the temperature is raised from 545°C to 580°C.



**Fig. 4.6.** Digital photograph of melamine derived g-C<sub>3</sub>N<sub>4</sub> samples at different temperatures

The optical absorption of melamine derived g-C<sub>3</sub>N<sub>4</sub> samples synthesized at different temperatures were studied by UV-Visible diffused reflectance spectroscopy. Variation in absorption edge can be noticed in Fig. 4.7a that sample MCN-650-4h exhibited highest absorption in visible region estimated up to 500 nm compared to other g-C<sub>3</sub>N<sub>4</sub> samples whereas MCN-510-4h sample has the lowest absorption in visible region estimated up to 450 nm which means with increase in temperature there is a red shift in absorption edge.



**Fig. 4.7.** (a) UV-Vis diffuse reflectance spectra, (b) Tauc plots for the band gap energy calculation, of melamine derived g-C<sub>3</sub>N<sub>4</sub> samples synthesized at different temperatures, and (c) Correlation between bandgap and calcination temperature

To calculate the band gap energy of g-C<sub>3</sub>N<sub>4</sub> samples the Kubelka-Munk (K-M) function was used. The intercept of the tangents to the Tauc plots of  $(F(R).hv)^{1/n}$  vs. photon energy ( $hv$ ) can provide approximate bandgap as shown in Fig. 4.7b. Where  $F(R)$ -Kubelka-Munk function,  $\nu$ -frequency,  $n=2$  as g-C<sub>3</sub>N<sub>4</sub> follows indirect absorption.<sup>37</sup> More details about Kubelka-Munk function and Tauc plots are provided in chapter-3. The obtained values of band gap energies are listed in Table 4.3 which reveals that with increase in calcination temperature, band gap energies decrease from 2.75 eV to 2.54 eV hence increase in the light absorption. Theoretically, improved light absorption ability should also improve the photocatalytic activity of g-C<sub>3</sub>N<sub>4</sub> degree.

An approximate linear relationship may also be established (Fig. 4.7c) between temperature and band gap energy of g-C<sub>3</sub>N<sub>4</sub> as equation 4.2. which is very close to the findings of Liu *et al.*<sup>37</sup>

$$E_g(T) = 3.5016 - 0.0015T \quad (4.2)$$

where T is in degrees Celsius.

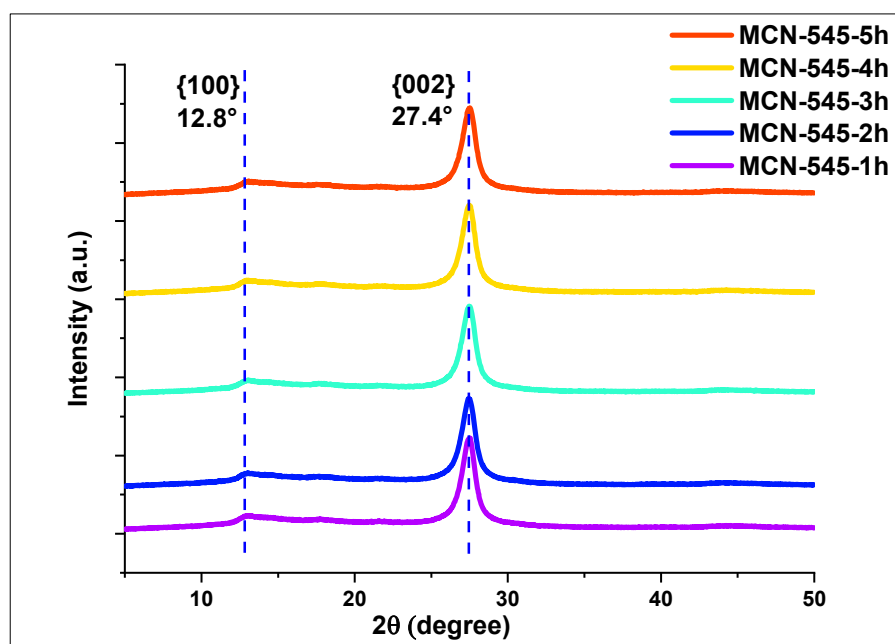
#### 4.4.1.2 Effect of reaction time

The effect of calcination time on the physiochemical properties (*i.e.*, crystal structure, chemical structure, surface area, band gap, *etc.*) of g-C<sub>3</sub>N<sub>4</sub> was investigated through XRD, FTIR, Raman, BET, and DRS, *etc.* The melamine was calcined for five different time periods (1 h, 2 h, 3 h, 4 h, 5 h) following the protocol discussed in section 4.3.2 and obtained powder samples were further characterized. All prepared g-C<sub>3</sub>N<sub>4</sub> samples with their reaction conditions and abbreviated names are summarized in Table 4.4, also varying parameter marked in bold letters for easy understanding.

**Table 4.4.** Abbreviated names of synthesized samples with their reaction parameters

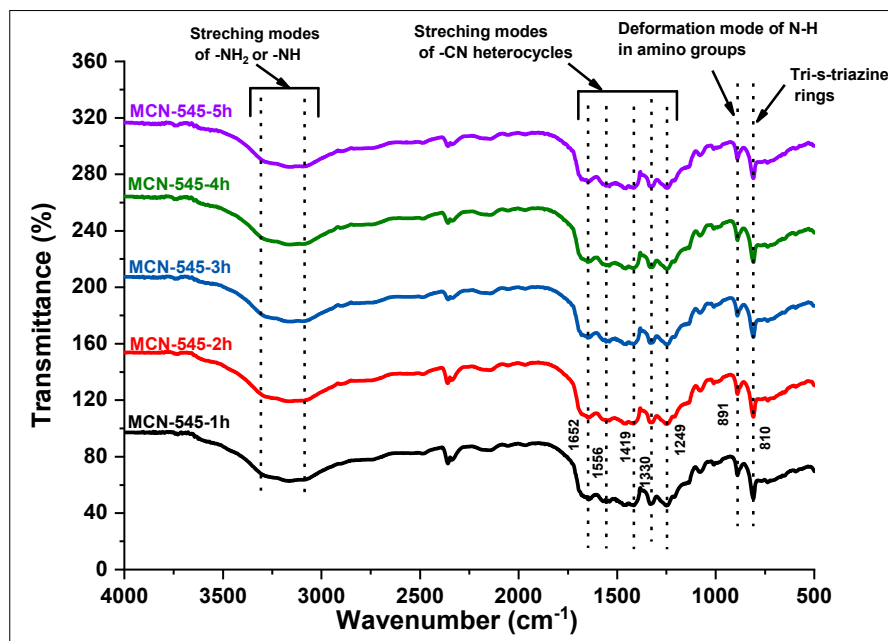
Precursor	Temperature (°C)	Time (h)	Abbreviation
Melamine	545	1	MCN-545-1h
Melamine	545	2	MCN-545-2h
Melamine	545	3	MCN-545-3h
Melamine	545	4	MCN-545-4h
Melamine	545	5	MCN-545-5h

XRD pattern of melamine derived g-C<sub>3</sub>N<sub>4</sub> samples calcinated in a closed crucible at 545°C for varying time period are shown in Fig. 4.8. It can be observed that there is no change in characteristic peak position in XRD pattern with changing in calcination time however, all the samples have both characteristic peaks at 12.8° & 27.4° and their d-values are 0.691 nm & 0.325 nm respectively.

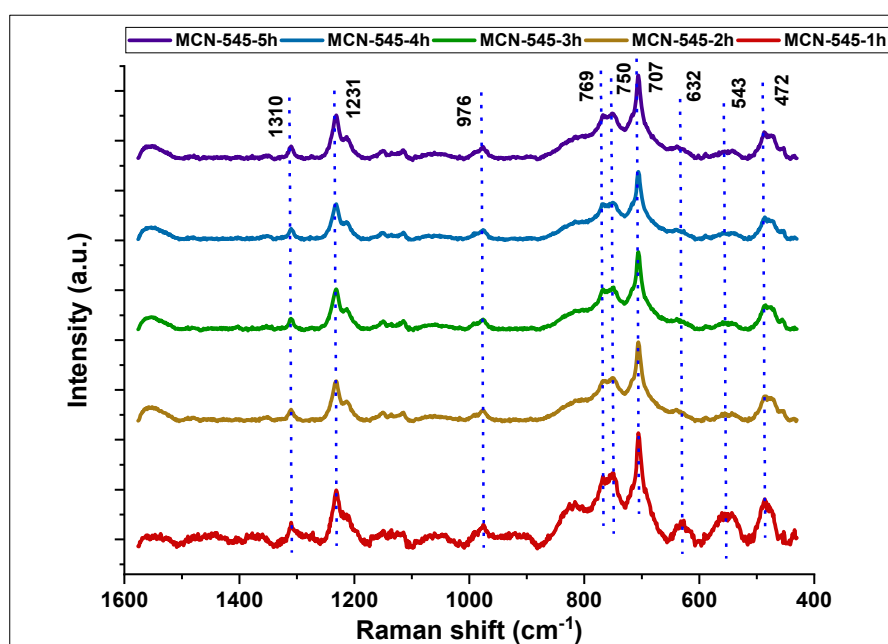
**Fig. 4.8.** XRD patterns of melamine derived g-C<sub>3</sub>N<sub>4</sub> samples calcinated for different time period

FTIR spectra of melamine derived g-C<sub>3</sub>N<sub>4</sub> samples calcinated for different time period are shown in Fig. 4.9 indicating the presence of all characteristics

stretching vibrations discussed earlier. Although there couldn't be seen significant impact of variation in calcination time period on the FTIR spectra of melamine derived  $g\text{-C}_3\text{N}_4$  samples which supports the XRD data and again ensure the existence of uninterrupted  $g\text{-C}_3\text{N}_4$  framework in all the prepared samples.



**Fig. 4.9.** FTIR-spectra of melamine derived  $g\text{-C}_3\text{N}_4$  samples calcinated for different time period



**Fig. 4.10.** Raman spectra of melamine derived  $g\text{-C}_3\text{N}_4$  samples calcinated for different time period

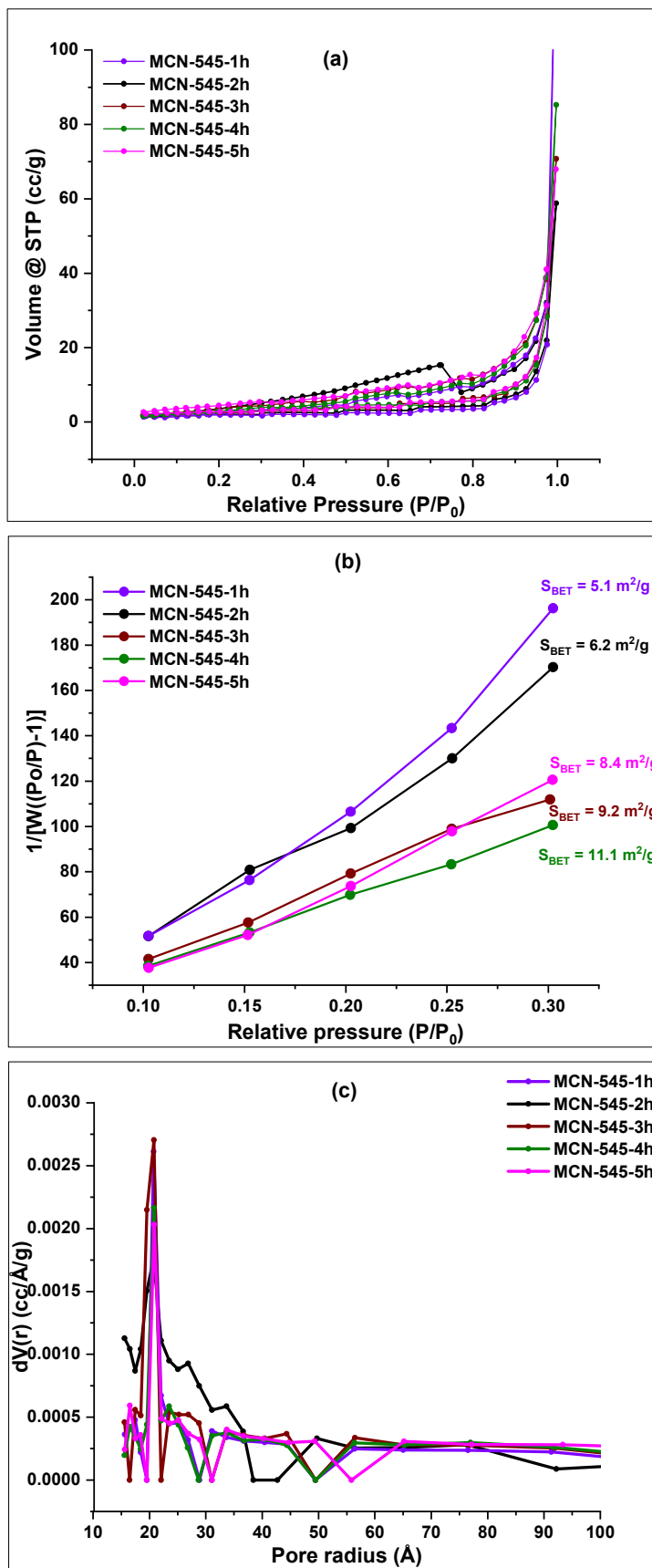
Raman spectra of all prepared g-C<sub>3</sub>N<sub>4</sub> samples are compared in Fig. 4.10. All the g-C<sub>3</sub>N<sub>4</sub> samples have several characteristic peaks at 1310, 1231, 976, 750, 707, 632, 543, and 472 cm<sup>-1</sup> which are indexed to vibration modes of CN heterocycles and are intact in all the samples with increasing calcination time from 1 h to 5 h except some peaks at 632, 543 cm<sup>-1</sup>, their intensity is reduced after 1h calcination time.

**Table 4.5.** Effect of calcination time of g-C<sub>3</sub>N<sub>4</sub> on BET parameters and band gap energy

Sample Name	S <sub>BET</sub> <sup>a</sup> (m <sup>2</sup> g <sup>-1</sup> )	P <sub>r</sub> <sup>b</sup> (Å)	P <sub>v</sub> <sup>c</sup> (cc g <sup>-1</sup> )	E <sub>g</sub> <sup>d</sup> (eV)
MCN-545-1h	5.1	20.7	0.221	2.74
MCN-545-2h	6.2	20.8	0.115	2.70
MCN-545-3h	9.2	20.8	0.106	2.70
MCN-545-4h	11.1	20.8	0.094	2.69
MCN-545-5h	8.4	20.9	0.107	2.69

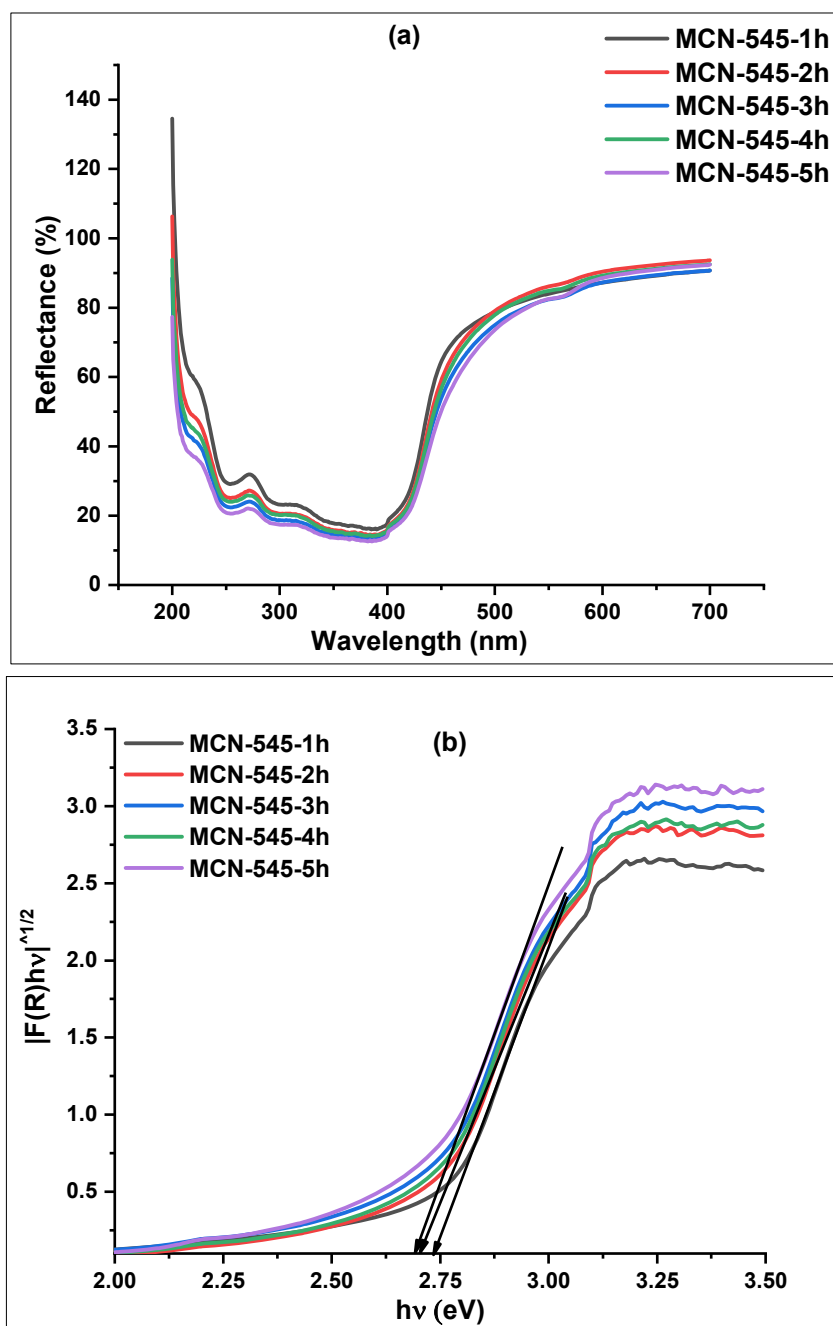
[a] Specific surface area (S<sub>BET</sub>) was determined by the BET equation. [b] Mode of pore radius (P<sub>r</sub>) was determined by the BJH method. [c] Average pore volume (P<sub>v</sub>) was determined by the BJH method. [d] Band gap energy (E<sub>g</sub>) calculated from Tauc plots

In order to determine the impact of calcination time on specific surface area of g-C<sub>3</sub>N<sub>4</sub>, BET measurements for samples MCN-545-1h, MCN-545-2h, MCN-545-3h, MCN-545-4h and MCN-545-5h were performed. Fig. 4.11a-c shows nitrogen adsorption-desorption isotherms and corresponding pore size distribution curve altogether five-point BET surface area graph, corresponding values are tabulated in Table 4.5.



**Fig. 4.11.** (a) Nitrogen adsorption-desorption isotherms, (b) Specific surface area by five-point BET, and (c) corresponding pore size distribution curves for g-C<sub>3</sub>N<sub>4</sub> samples synthesized at different temperatures using melamine

The optical responses of melamine derived g-C<sub>3</sub>N<sub>4</sub> samples calcinated for 1 h to 5 h at 545°C temperature examined by UV-Visible diffused reflectance spectroscopy are shown in Fig. 4.12a and b which reveals that there is no significant change in absorption edge could be noticed with varying calcination duration. All g-C<sub>3</sub>N<sub>4</sub> samples has the absorption in visible region estimated up to 450 nm and band gap energies about 2.7 eV (Table 4.5).



**Fig. 4.12.** (a) UV-Vis diffuse reflectance spectra, and (b) Tauc plots for the band gap energy calculation, of melamine derived g-C<sub>3</sub>N<sub>4</sub> samples calcinated for different time period.



#### 4.4.1.3 Effect of precursors

The effect of the different precursors a on the physiochemical properties (*i.e.*, crystal structure, chemical structure, morphology, surface area, *etc.*) was investigated through XRD, FTIR, Raman, BET, DRS, and so on. For instance, four different precursors (Melamine, Thiourea, Dicyandiamide, Urea) were taken into consideration. All prepared g-C<sub>3</sub>N<sub>4</sub> samples with their reaction conditions and abbreviated names are summarized in Table 4.6, also varying parameter is marked in bold letters for easy understanding.

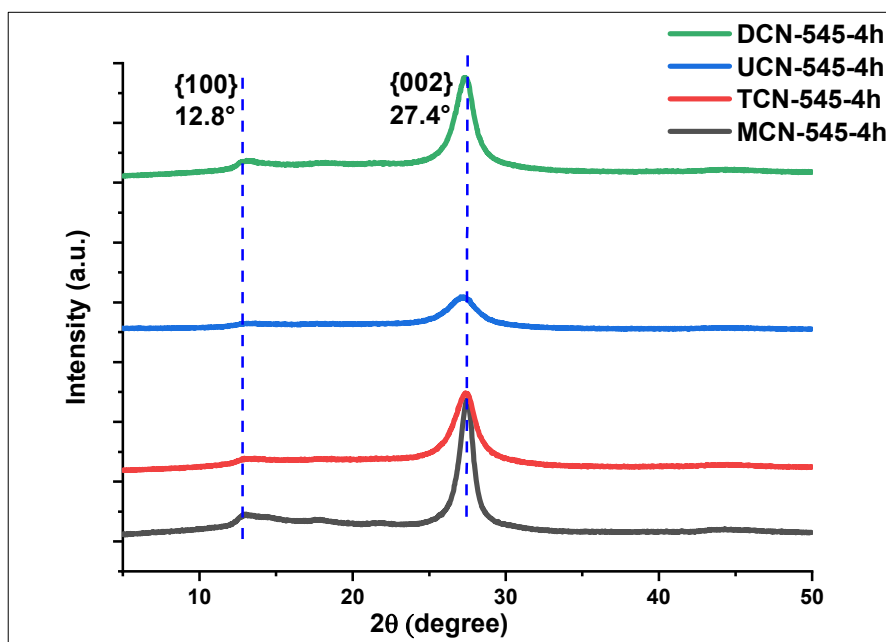
**Table 4.6.** Abbreviated names of synthesized samples with their reaction parameters

<b>Precursor</b>	Temperature (°C)	Time (h)	Abbreviation
<b>Melamine</b>	545	4	MCN-545-4h
<b>Thiourea</b>	545	4	TCN-545-4h
<b>Dicyandiamide</b>	545	4	DCN-545-4h
<b>Urea</b>	545	4	UCN-545-4h

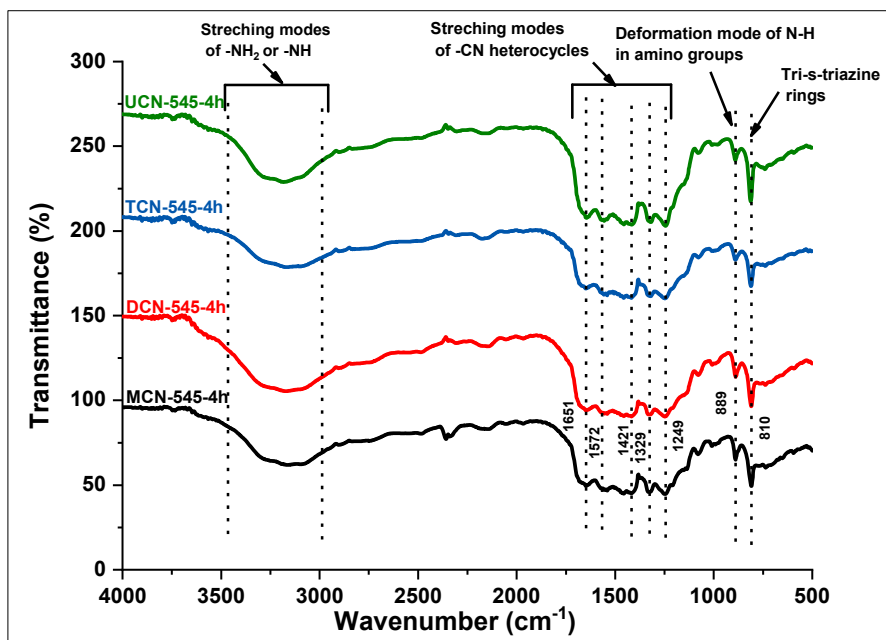
XRD pattern of g-C<sub>3</sub>N<sub>4</sub> samples prepared from four different precursors for same reaction conditions are shown in Fig. 4.13. However, all the samples have both characteristic peaks near to 12.8° and 27.4° but urea derived g-C<sub>3</sub>N<sub>4</sub> (UCN-545-4h) has shown a small deviation in (002) peak position from 27.4° to 27.2° (d=0.328 nm), also it shows the peak broadening than its counterparts. Reduction in sheet thickness of urea derived g-C<sub>3</sub>N<sub>4</sub> might be the reason behind this peak broadening which can also be justified with FESEM image (Fig. 4.28).

FTIR spectra of g-C<sub>3</sub>N<sub>4</sub> samples synthesized from different precursors are shown in Fig. 4.14. All characteristic stretching vibrations discussed earlier are present and similar with each other which confirm the presence of uninterrupted g-C<sub>3</sub>N<sub>4</sub> structure in all the prepared samples. Sample UCN-545-4h has the intense peak at 810

$\text{cm}^{-1}$  than others and that is the confirmation of formation of tri-s-triazine rings in more numbers which also supports the XRD data.

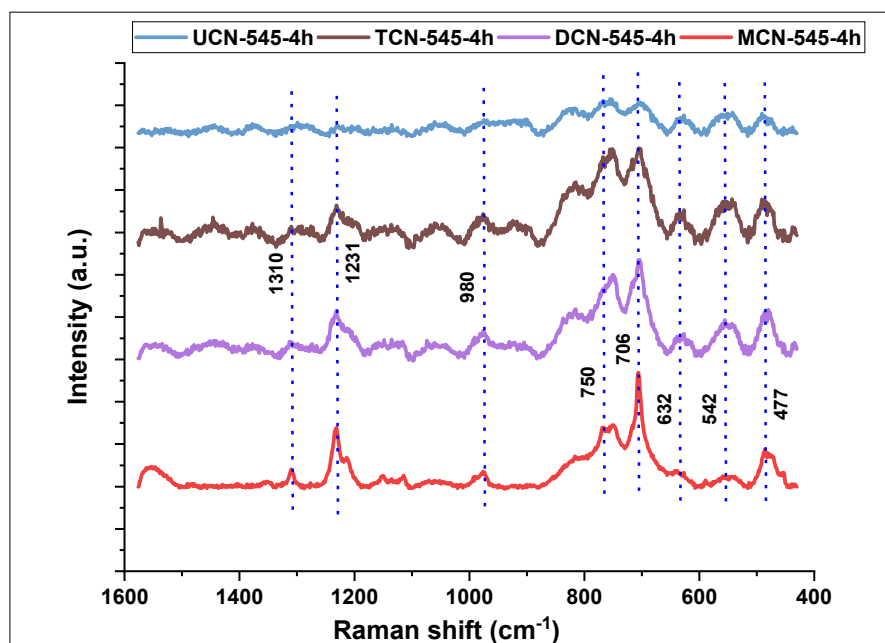


**Fig. 4.13.** XRD patterns of  $\text{g-C}_3\text{N}_4$  prepared using different precursors for same reaction conditions



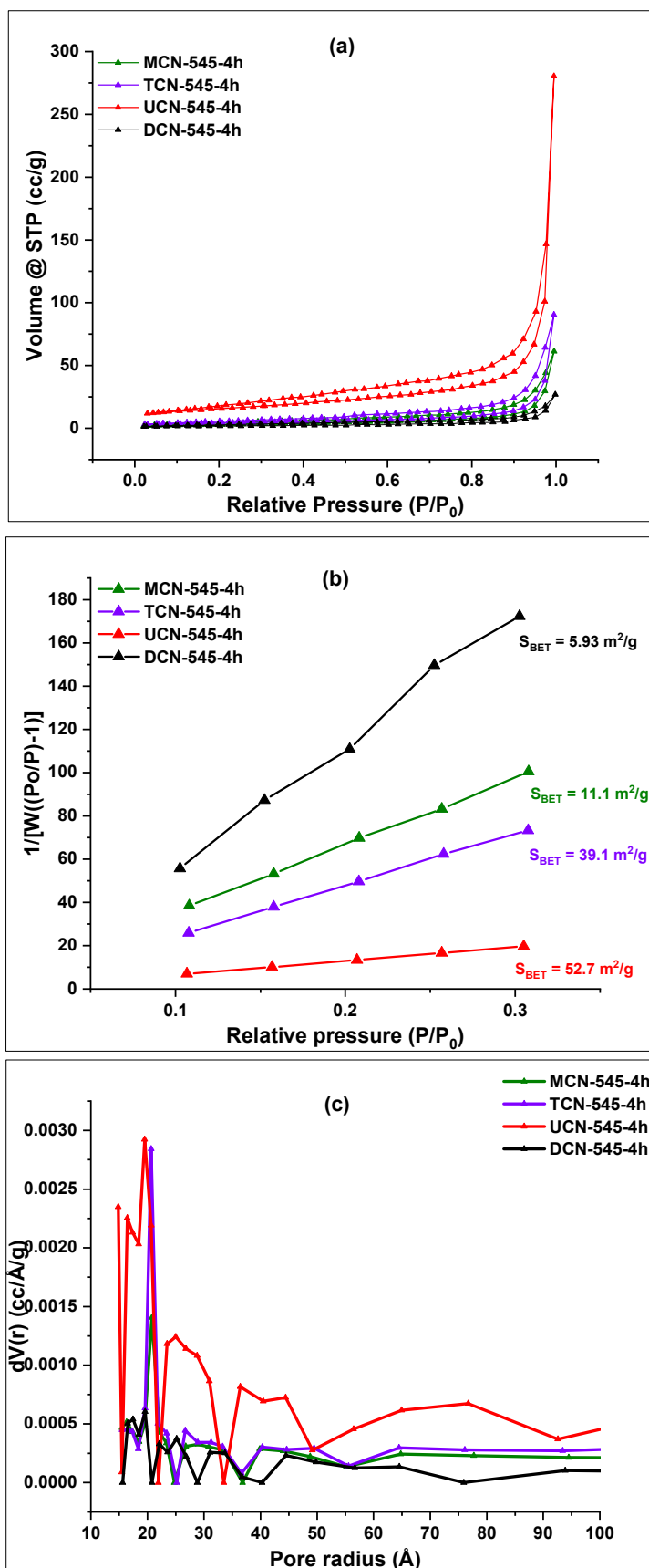
**Fig. 4.14.** FTIR-spectra of  $\text{g-C}_3\text{N}_4$  prepared using different precursors for same reaction conditions

Raman spectra of all prepared g-C<sub>3</sub>N<sub>4</sub> samples are presented in Fig. 4.15. All the g-C<sub>3</sub>N<sub>4</sub> samples have several characteristic peaks at 1310, 1231, 980, 750, 706, 632, 542, and 477 cm<sup>-1</sup> which are indexed to vibration modes of CN heterocycles however, peak pattern and peak intensity are different in these samples which can also be correlate with number of triazine rings.



**Fig. 4.15.** Raman spectra of melamine derived g-C<sub>3</sub>N<sub>4</sub> samples prepared using different precursors for same reaction conditions

In order to determine the impact of precursors on specific surface area of g-C<sub>3</sub>N<sub>4</sub>, BET measurements for samples MCN-545-4h, TCN-545-4h, DCN-545-4h and UCN-545-4h were performed. Fig. 4.16a-c shows nitrogen adsorption-desorption isotherms and corresponding pore size distribution curve altogether five-point BET surface area graph, corresponding values are tabulated in Table 4.7.



**Fig. 4.16.** (a) Nitrogen adsorption-desorption isotherms, (b) Specific surface area by five-point BET, and (c) corresponding pore size distribution curves for  $g\text{-C}_3\text{N}_4$  samples synthesized using different precursors

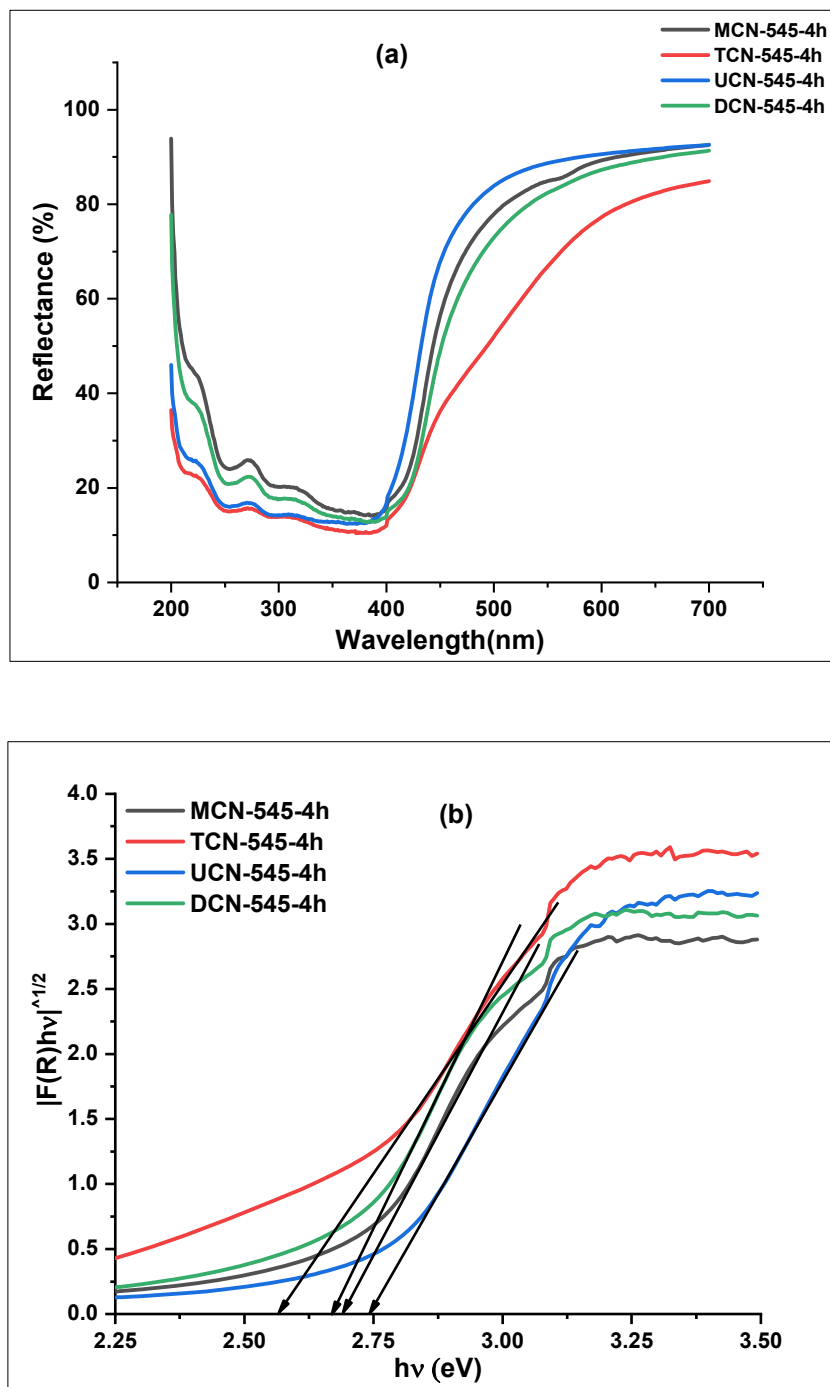
**Table 4.7.** Role of precursors on BET parameters and band gap energy

Sample Name	$S_{\text{BET}}^{\text{a}}$ ( $\text{m}^2 \text{g}^{-1}$ )	$P_r^{\text{b}}$ ( $\text{\AA}$ )	$P_v^{\text{c}}$ ( $\text{cc g}^{-1}$ )	$E_g^{\text{d}}$ (eV)
MCN-545-4h	11.1	20.8	0.094	2.69
TCN-545-4h	39.1	20.7	0.140	2.56
DCN-545-4h	5.93	19.6	0.042	2.67
UCN-545-4h	52.7	19.5	0.424	2.74

[a] Specific surface area ( $S_{\text{BET}}$ ) was determined by the BET equation. [b] Mode of pore radius ( $P_r$ ) was determined by the BJH method. [c] Average pore volume ( $P_v$ ) was determined by the BJH method. [d] Band gap energy ( $E_g$ ) calculated from Tauc plots

Based on the IUPAC classification, all prepared samples followed type IV isotherm and type H3 hysteresis loop indicating the presence of nonuniform mesopores. It can be depicted from isotherm (Fig. 4.16a) that UCN-545-4h adsorbs more nitrogen than other precursor's mediated g-C<sub>3</sub>N<sub>4</sub> samples which turns into the high surface area for urea derived g-C<sub>3</sub>N<sub>4</sub> *i.e.*, 52.7 m<sup>2</sup> g<sup>-1</sup> because of improved porosity due to high evolution of ammonia and CO<sub>2</sub> gas during pyrolysis. Pore volume distribution curves (Fig. 4.5c) shows the sharp peak at 20 Å conforming the mesoporous structures. Noticeably, urea derived g-C<sub>3</sub>N<sub>4</sub> has the smallest pore size (mode) than others, however, UCN-545-4h also shows a wide distribution of pores than other samples since it contains larger size mesopores and some macropores similar to MCN-650-4h sample which is discussed in previous section. It is said that high surface area and large pore size are favourable for better photocatalytic properties, as a result of better adsorption and more active sites. If we consider the v/w ratio, urea holds the highest v/w ratio (Urea>Thiourea>Melamine), however it possesses the lowest mass yield among the three precursors (Melamine>Thiourea>Urea). For thermal polymerization at 545°C for 4 h, the efficiency or mass yield of precursor to g-C<sub>3</sub>N<sub>4</sub> conversion was found to be 47.5% (melamine), 33.3% (thiourea), and 4.7% (urea). Very low mass yield for urea is due

to the rapid degree of polymerization and condensation. Moreover, above 550°C there was no product found in case of urea as it decomposed completely above this temperature.



**Fig. 4.17.** (a) UV-Vis diffuse reflectance spectra, and (b) Tauc plots for the band gap energy calculation, for g-C<sub>3</sub>N<sub>4</sub> samples synthesized using different precursors

The optical responses of g-C<sub>3</sub>N<sub>4</sub> samples synthesized from different precursors studied by UV-Visible diffused reflectance spectroscopy are shown in Fig. 4.17a in which only small variation in adsorption edge can be seen. Their transformed Tauc plots using Kubelka-Munk (K-M) function is shown in Fig. 4.17b and the obtained value of band gap energies are listed in Table 4.7. Sample TCN-545-4h shows lowest band gap *i.e.*, 2.56 eV means the approximate absorption up to 485 nm.

#### 4.4.1.4 Effect of exfoliation

For this study, bulk g-C<sub>3</sub>N<sub>4</sub> was synthesized using different precursors as previously discussed and then further heat treated to get exfoliated g-C<sub>3</sub>N<sub>4</sub>. Combined impact of precursor and exfoliation on physiochemical properties (*i.e.*, crystal structure, chemical structure, morphology, surface area, *etc.*) was investigated through XRD, FTIR, Raman, BET, DRS, FESEM and so on. For instance, four different precursors (Melamine, Thiourea, Dicyandiamide, Urea) were taken into consideration and further exfoliated at 500°C for 4h. All prepared g-C<sub>3</sub>N<sub>4</sub> samples with their reaction conditions and abbreviated names are summarized in Table 4.8, also varying parameter marked in bold letters for easy understanding.

**Table 4.8.** Abbreviated names of synthesized samples with their reaction parameters

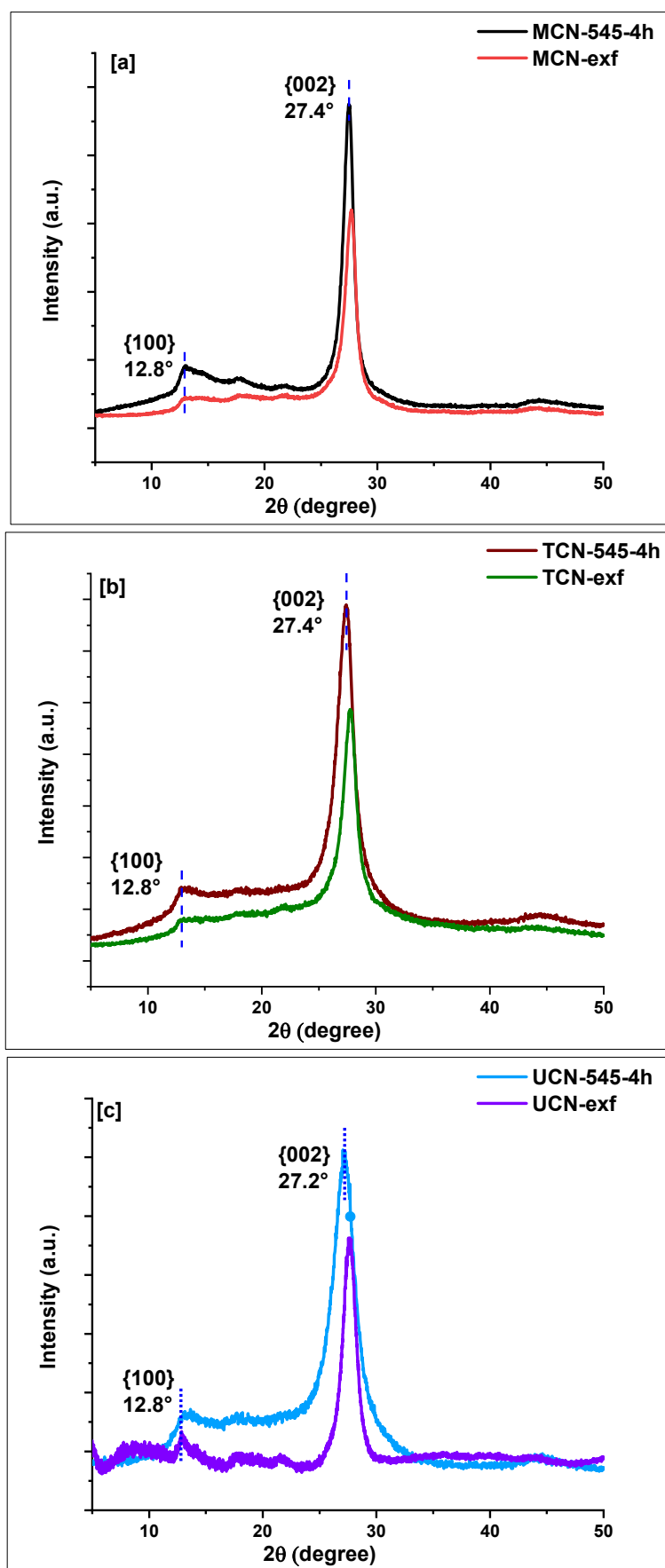
<b>Precursor</b>	Temperature (°C)	Time (h)	Exfoliation	Abbreviation
<b>Melamine</b>	545	4	500°C, 4h	MCN-exf
<b>Thiourea</b>	545	4		TCN-exf
<b>Urea</b>	545	4		UCN-exf

In Fig. 4.18a-c, XRD pattern of exfoliated g-C<sub>3</sub>N<sub>4</sub> synthesized with melamine, thiourea & urea, is compared with their respective partner in bulk form. However, each sample has both characteristic peaks near to 12.8° and 27.4° but there could be seen a

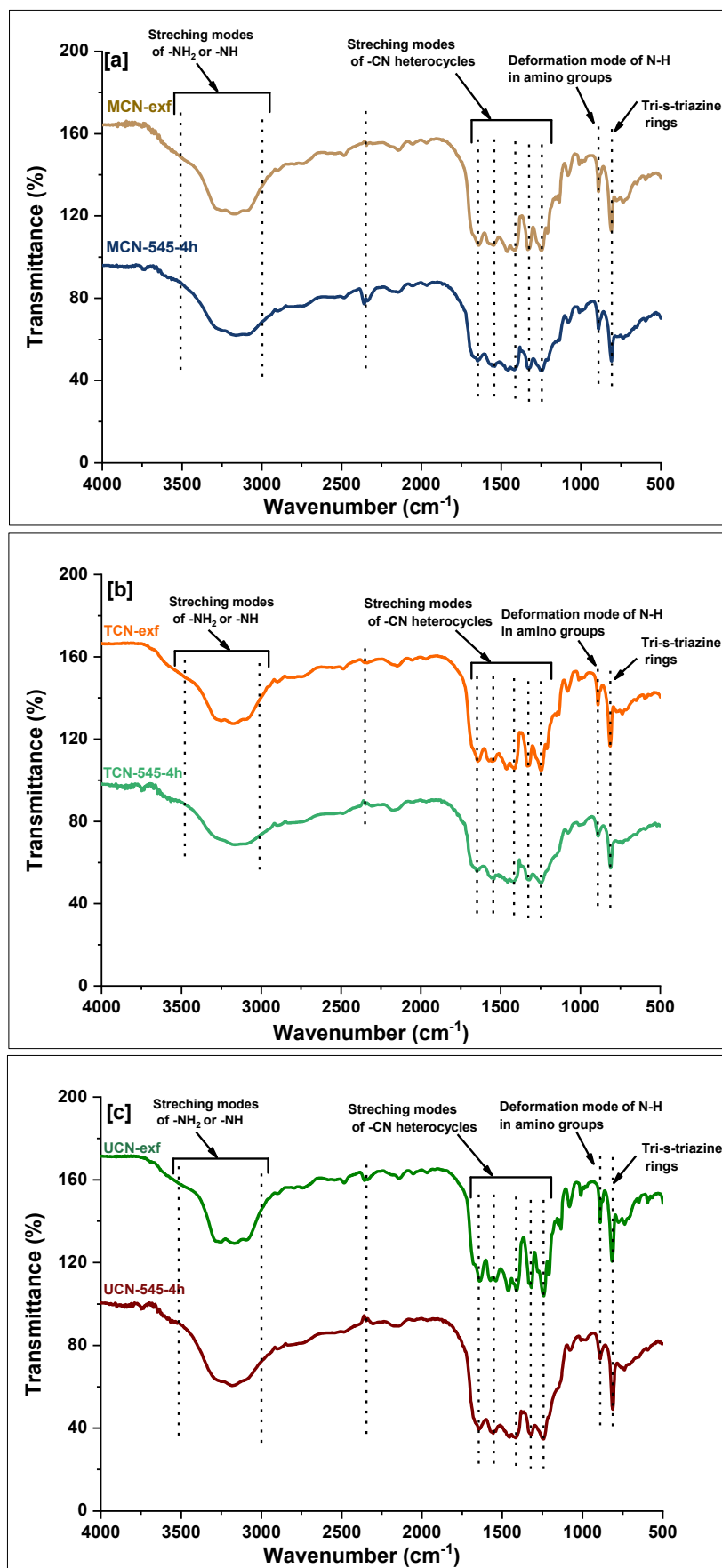
shift in peak position towards higher angle ( $27.4^\circ$  to  $27.8^\circ$ ) when we compare exfoliate  $g\text{-C}_3\text{N}_4$  samples with their bulk counterpart which indicates a structural contraction along the layer stacking direction due to more prolonged condensation of the carbon nitride chains. Also, after exfoliation, the intensity of this peak (002) significantly decreases, indicating the successful exfoliation of bulk  $g\text{-C}_3\text{N}_4$ .<sup>38</sup> FTIR spectra of exfoliated  $g\text{-C}_3\text{N}_4$  samples synthesized from different precursors are shown in Fig. 4.19a-c. All characteristic stretching vibrations discussed earlier are present and similar with each other which confirm the presence of same chemical structure as their parent bulk  $g\text{-C}_3\text{N}_4$ .

Raman spectra of all prepared  $g\text{-C}_3\text{N}_4$  samples are presented in Fig. 4.20. All the  $g\text{-C}_3\text{N}_4$  samples have characteristic peaks which are indexed to vibration modes of CN heterocycles however, peak pattern and peak intensity are different in these samples which can be correlate with number of triazine rings. Moreover, this is similar to that of bulk  $g\text{-C}_3\text{N}_4$ , suggesting that the structure of  $g\text{-C}_3\text{N}_4$  nanosheets is well kept during our exfoliation process.

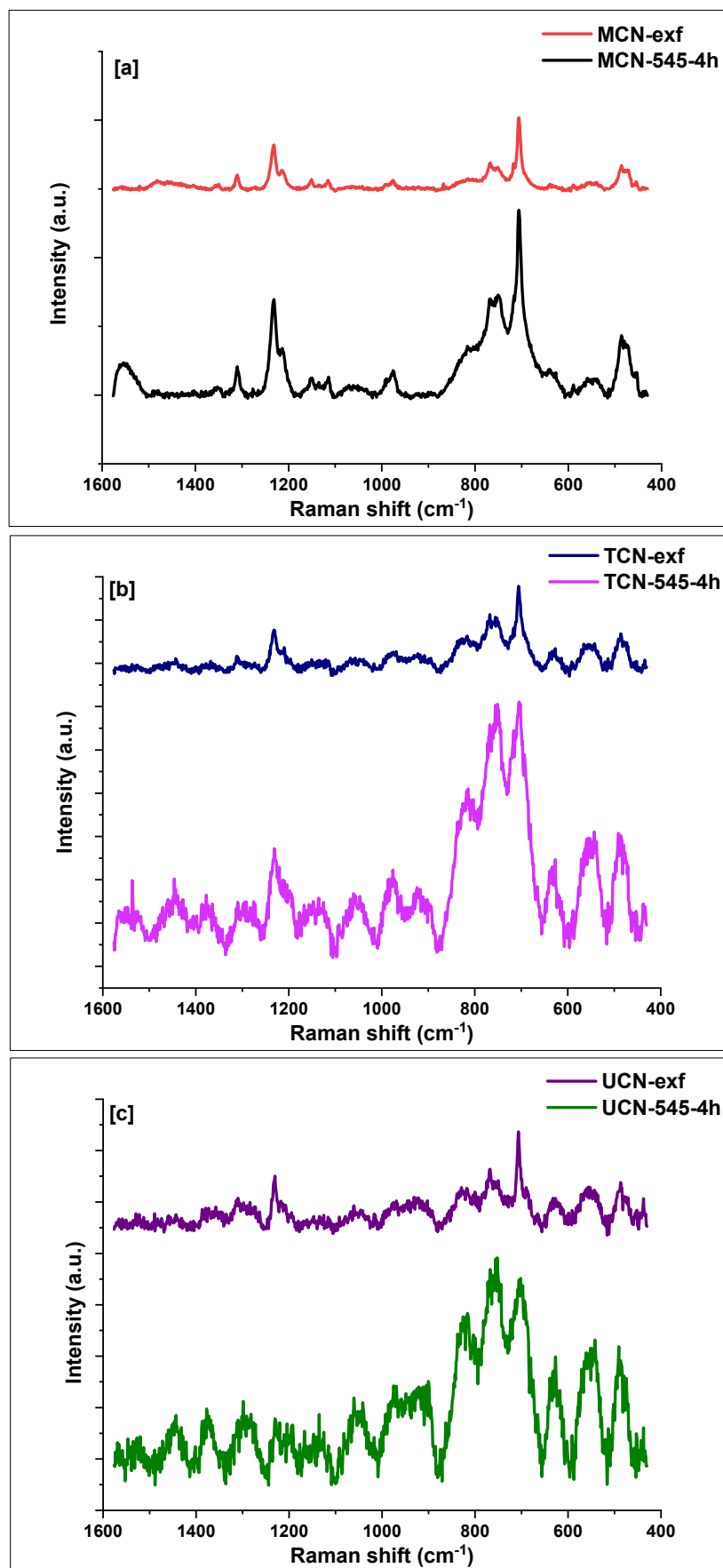




**Fig. 4.18.** XRD patterns of bulk and exfoliated  $g\text{-C}_3\text{N}_4$  samples prepared using (a) melamine, (b) thiourea, and (c) urea as precursor



**Fig. 4.19.** FTIR spectra of bulk and exfoliated  $g\text{-C}_3\text{N}_4$  samples prepared using (a) melamine, (b) thiourea, and (c) urea as precursor



**Fig. 4.20.** Raman spectra of bulk and exfoliated  $g\text{-C}_3\text{N}_4$  samples prepared using (a) melamine, (b) thiourea, and (c) urea as precursor

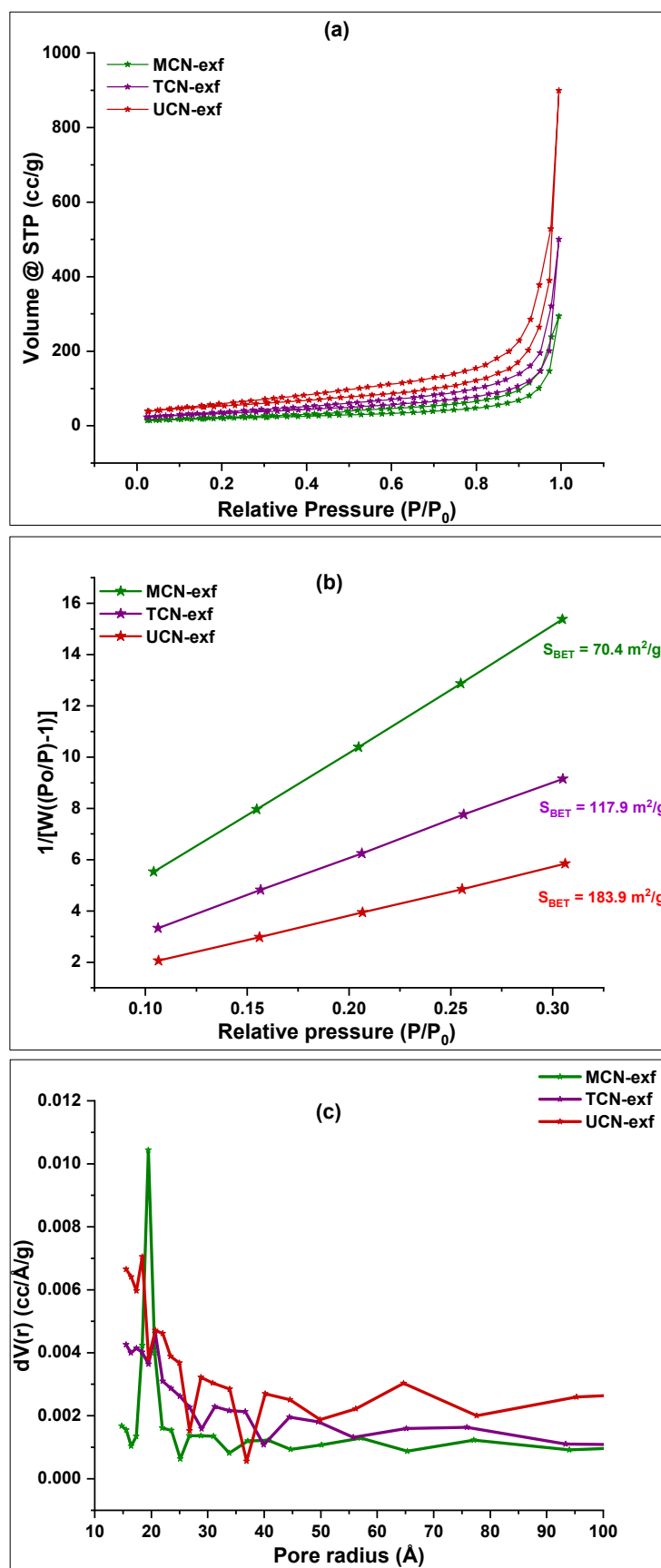
In order to determine the effect of exfoliation on specific surface area of g-C<sub>3</sub>N<sub>4</sub>, BET measurements for samples MCN-exf, TCN-exf and UCN-exf were performed and analyzed in detail. Fig. 4.21a-c shows nitrogen adsorption-desorption isotherms and corresponding pore size distribution curve altogether five-point BET surface area graph, corresponding values are tabulated in Table 4.9.

**Table 4.9.** Combined impact of precursor and exfoliation on BET parameters and band gap energy

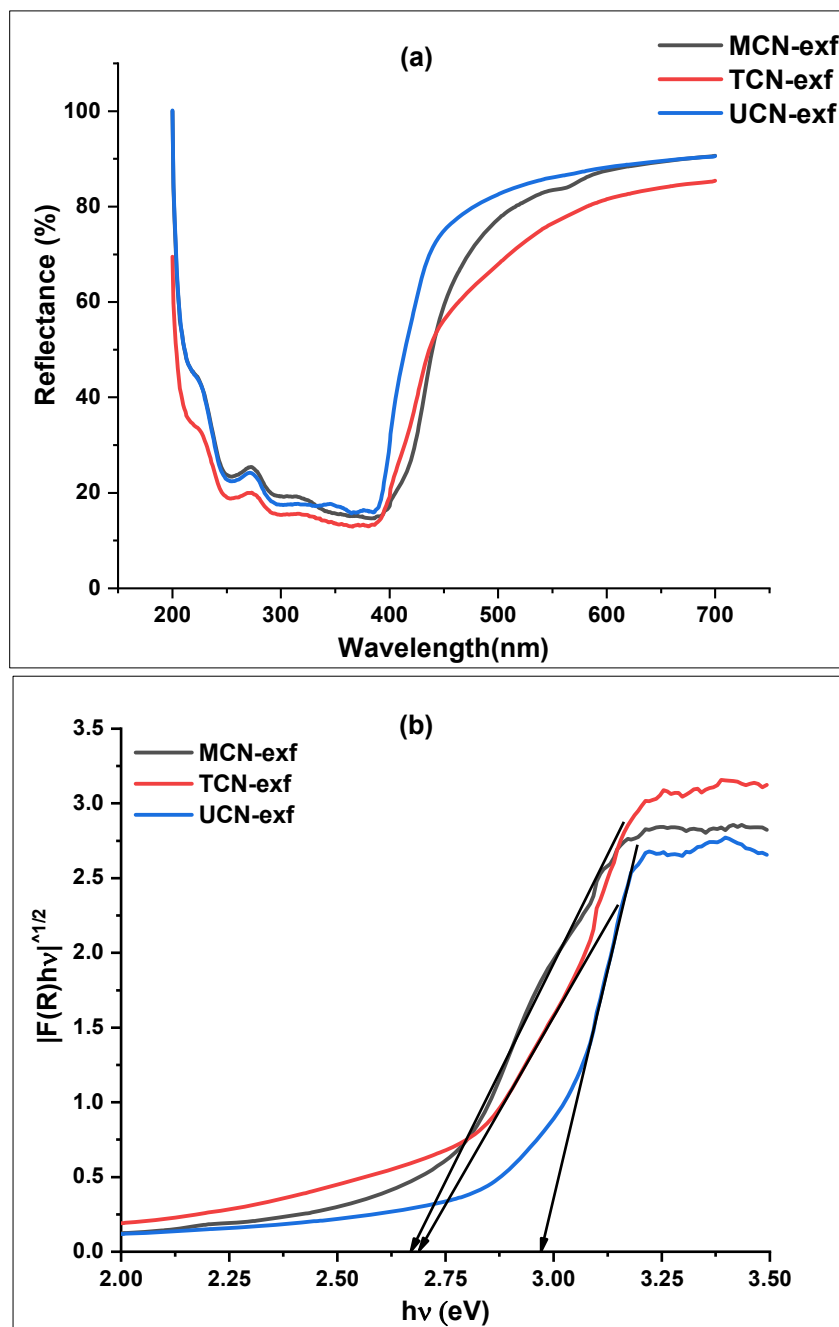
Sample Name	S <sub>BET</sub> <sup>a</sup> (m <sup>2</sup> g <sup>-1</sup> )	P <sub>r</sub> <sup>b</sup> (Å)	P <sub>v</sub> <sup>c</sup> (cc g <sup>-1</sup> )	E <sub>g</sub> <sup>d</sup> (eV)
MCN-exf	70.4	19.5	0.454	2.70
TCN-exf	117.9	20.7	0.756	2.69
UCN-exf	183.9	18.4	1.364	2.98

[a] Specific surface area (S<sub>BET</sub>) was determined by the BET equation. [b] Mode of pore radius (P<sub>r</sub>) was determined by the BJH method. [c] Average pore volume (P<sub>v</sub>) was determined by the BJH method. [d] Band gap energy (E<sub>g</sub>) calculated from Tauc plots

Based on the IUPAC classification, all prepared samples followed type IV isotherm and type H3 hysteresis loop indicating the presence of nonuniform mesopores. It can be depicted from isotherm (Fig. 4.21a) that UCN-exf adsorbs more nitrogen than other exfoliated g-C<sub>3</sub>N<sub>4</sub> samples which turns into the high surface area for it *i.e.*, 183.9 m<sup>2</sup> g<sup>-1</sup>. If we compare surface area of bulk g-C<sub>3</sub>N<sub>4</sub> (Table 4.7) with exfoliated g-C<sub>3</sub>N<sub>4</sub> (Table 4.9), we can see the clear effect of exfoliation on surface area since it improved the porosity due to more evolution of ammonia and CO<sub>2</sub> gas during pyrolysis. Pore volume distribution curves (Fig. 4.21c) shows that after exfoliation, number of larger sizes mesopores and macropores has been increased in sample UCN-exf and TCN-exf. Although major number of pores are still near to 20 Å in all samples even after exfoliation. Increasing surface area and large pore size theoretically result in better photocatalytic properties, as a result of better adsorption and more active sites.



**Fig. 4.21.** (a) Nitrogen adsorption-desorption isotherms, (b) Specific surface area by five-point BET, and (c) corresponding pore size distribution curves for exfoliated  $g\text{-C}_3\text{N}_4$  samples synthesized using different precursors

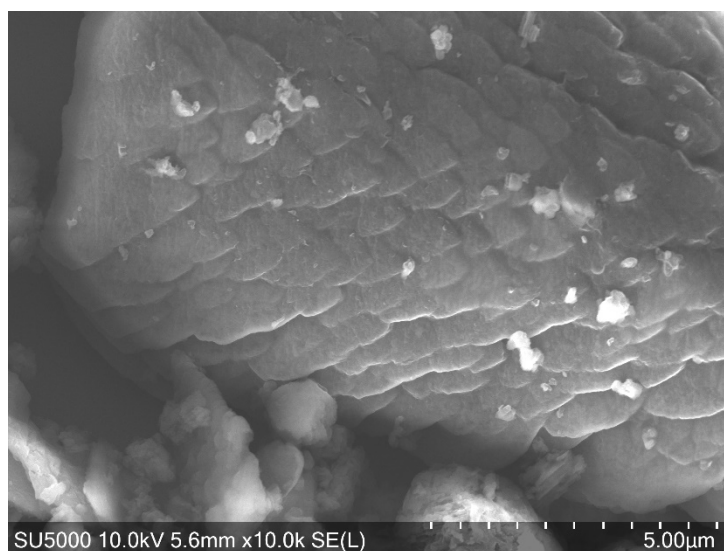


**Fig. 4.22.** (a) UV-Vis diffuse reflectance spectra, and (b) Tauc plots for the band gap energy calculation, for exfoliated  $g\text{-C}_3\text{N}_4$  samples synthesized using different precursors

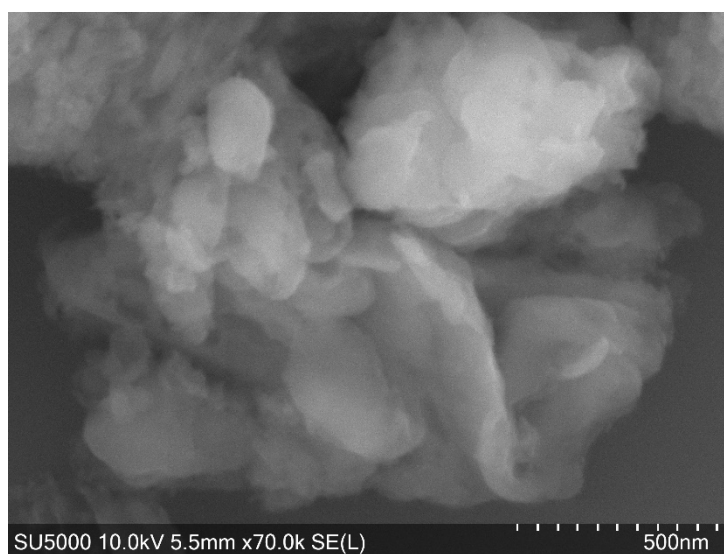
The optical responses of exfoliated  $g\text{-C}_3\text{N}_4$  samples synthesized from different precursors studied by UV-Visible diffused reflectance spectroscopy are shown in Fig. 4.22a in which significant variation in adsorption edge can be seen. Their transformed Tauc plots using Kubelka-Munk (K-M) function are shown in Fig. 4.21b and the

obtained value of band gap energies are listed in Table 4.9. After exfoliation bandgap energy is increased compared to their parent bulk  $g\text{-C}_3\text{N}_4$  listed in Table 4.7.

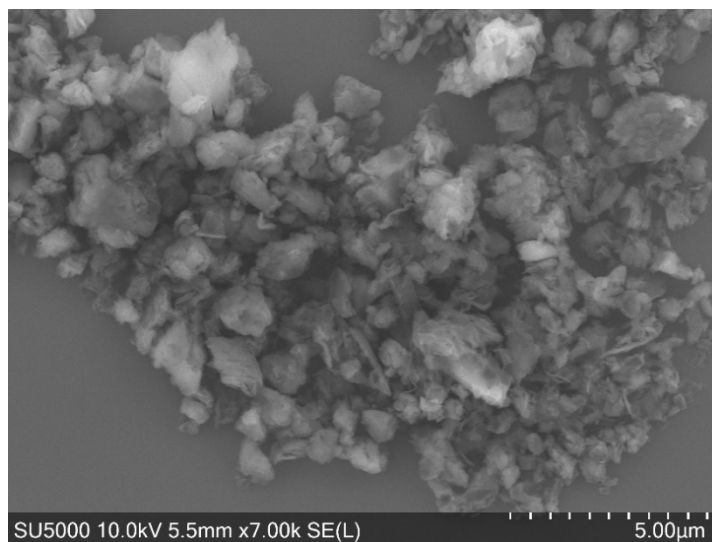
The morphology of prepared  $g\text{-C}_3\text{N}_4$  samples were characterized by FESEM. The  $g\text{-C}_3\text{N}_4$  appeared as flake/sheet like structure with multiple layers as shown in Fig. 4.23-4.28. The lateral size of the bulk  $g\text{-C}_3\text{N}_4$  flakes is about 400-700 nm, which supports the hypothesis of multiple layered structure of  $g\text{-C}_3\text{N}_4$ . Layers/sheet thickness can be reduced by increasing polymerization temperature and exfoliation process.



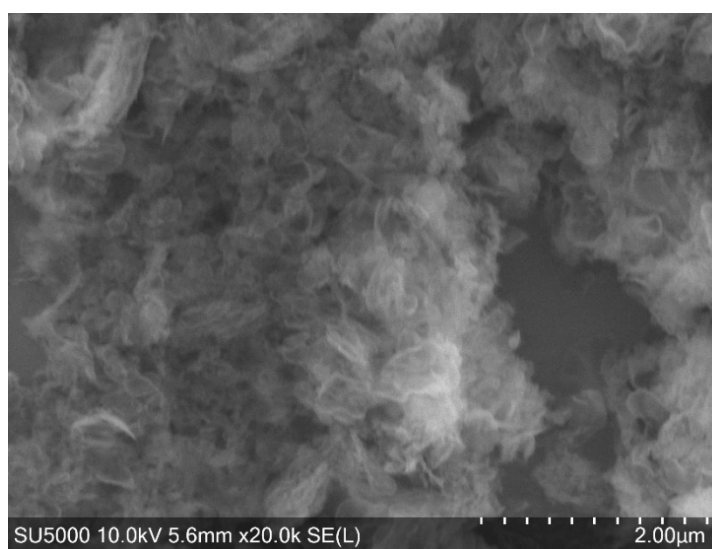
**Fig. 4.23.** FESEM micrograph of melamine derived bulk  $g\text{-C}_3\text{N}_4$  sample (MCN-545-4h)



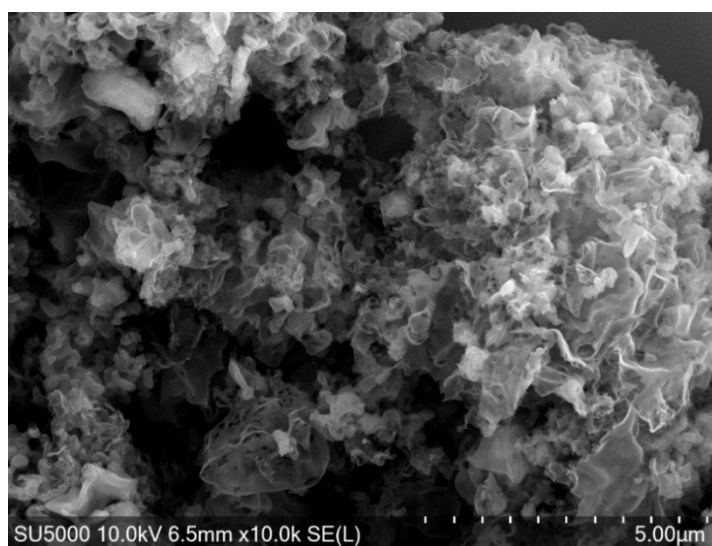
**Fig. 4.24.** FESEM micrograph of melamine derived exfoliated  $g\text{-C}_3\text{N}_4$  sample (MCN-xf)



**Fig. 4.25.** FESEM micrograph of thiourea derived bulk g-C<sub>3</sub>N<sub>4</sub> sample (TCN-545-4h)

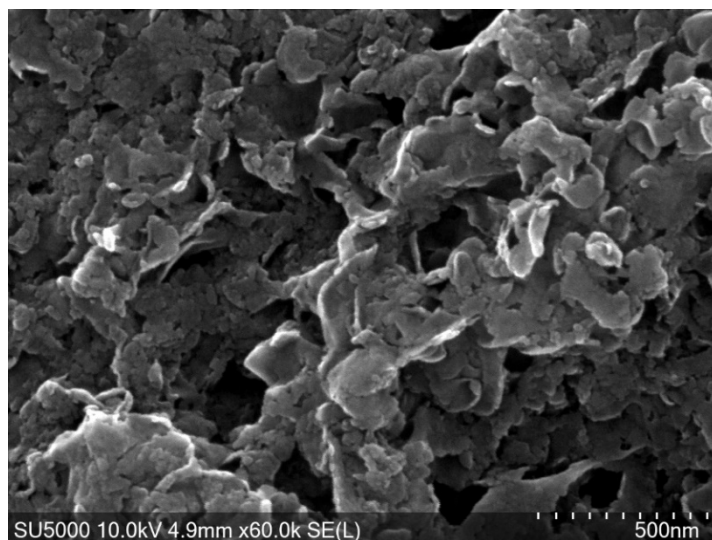


**Fig. 4.26.** FESEM micrograph of thiourea derived exfoliated g-C<sub>3</sub>N<sub>4</sub> sample (TCN-xf)



**Fig. 4.27.** FESEM micrograph of urea derived bulk g-C<sub>3</sub>N<sub>4</sub> sample (UCN-545-4h)





**Fig. 4.28.** FESEM micrographs of urea derived exfoliated  $g\text{-C}_3\text{N}_4$  sample (UCN-exf)

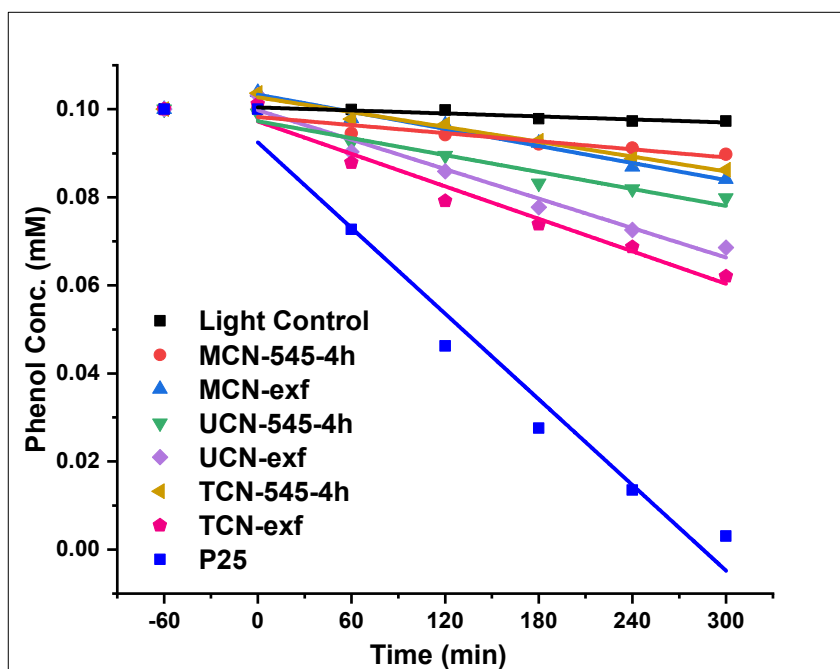
#### 4.4.2 Photocatalytic activity

This section focuses on the photocatalytic activity of  $g\text{-C}_3\text{N}_4$ . Samples were selected for photocatalytic testing based upon favourable physicochemical parameters.

##### 4.4.2.1 Phenol degradation

The prepared  $g\text{-C}_3\text{N}_4$  samples were explored to evaluate their photocatalytic efficacy for the photocatalytic degradation of phenol as a model organic pollutant, under UV-Vis irradiation. Results shown in Fig. 4.29 reveals that exfoliated  $g\text{-C}_3\text{N}_4$  samples perform better than their counterpart (bulk form) owing to higher surface area. The experimental data of phenol degradation were observed follow pseudo-zero order kinetics. For each sample, initial rate in first two light hours was considered as rate of reaction or rate constant for pseudo-zero order reaction. The rate of reaction and linear fitting regression coefficients shown by all tested samples are tabulated in Table 4.10. Exfoliated samples of  $g\text{-C}_3\text{N}_4$  prepared by thiourea and urea performed well among all the tested  $g\text{-C}_3\text{N}_4$  samples, with reaction rates (rate constants) of  $1.83 \times 10^{-7} \text{ mol L}^{-1} \text{ min}^{-1}$  (TCN-exf) and  $2.14 \times 10^{-7} \text{ mol L}^{-1} \text{ min}^{-1}$  (UCN-exf) while other samples showed

very slow degradation rate. However, the photocatalytic efficiency for phenol degradation achieved by exfoliated g-C<sub>3</sub>N<sub>4</sub> is still far behind the photocatalytic efficiency of P25-TiO<sub>2</sub>, *i.e.*, complete degradation in phenol concentration with initial rate of  $4.48 \times 10^{-7} \text{ mol L}^{-1} \text{ min}^{-1}$  in 5 h of UV-Vis irradiation.



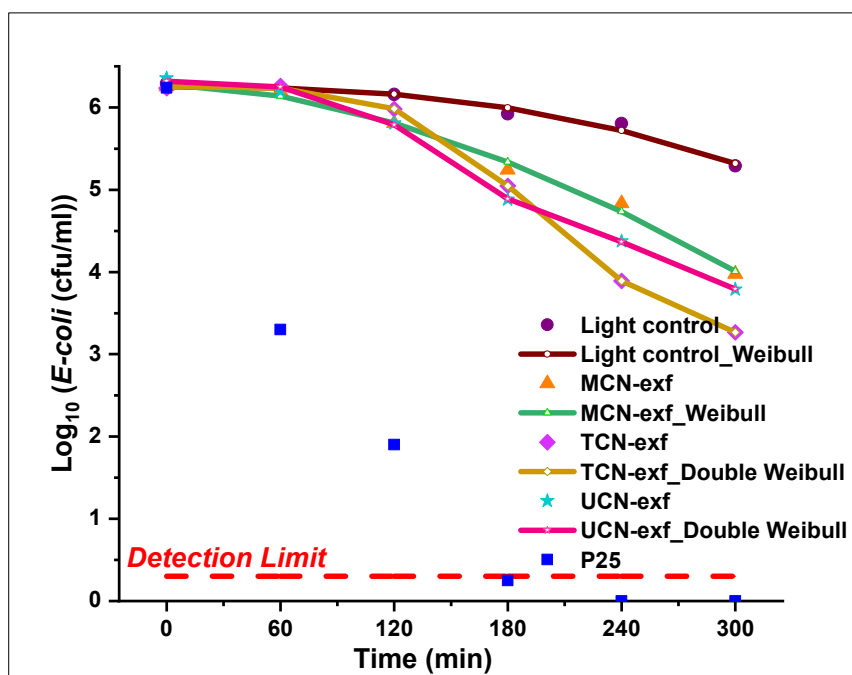
**Fig. 4.29.** Photolytic and photocatalytic phenol degradation using different g-C<sub>3</sub>N<sub>4</sub> samples and P25-TiO<sub>2</sub> under UV-Vis irradiation. Initial phenol concentration: 0.1 mM, Photocatalyst: 100 mg L<sup>-1</sup> (Markers are experimental data, while lines represented the trendline based upon regression analysis)

**Table 4.10:** Initial rate of zero order reaction (*k*), coefficient of regression (*R*<sup>2</sup>) shown by g-C<sub>3</sub>N<sub>4</sub> samples in phenol degradation

Sample Name	<i>k</i> (mol L <sup>-1</sup> min <sup>-1</sup> )	<i>R</i> <sup>2</sup>
Light Control	$2.34 \times 10^{-9}$	0.8625
MCN-545-4h	$4.96 \times 10^{-8}$	0.8768
TCN-545-4h	$5.93 \times 10^{-8}$	0.9796
UCN-545-4h	$8.04 \times 10^{-8}$	0.9479
MCN-exf	$6.16 \times 10^{-8}$	0.9816
TCN-exf	$1.83 \times 10^{-7}$	0.9636
UCN-exf	$2.14 \times 10^{-7}$	0.9646
P25-TiO <sub>2</sub>	$4.48 \times 10^{-7}$	0.9685

#### 4.4.2.2 Bacterial inactivation

Similar to organic degradation, synthesized  $g\text{-C}_3\text{N}_4$  samples were also explored to evaluate their photocatalytic efficacy for bacterial inactivation of a modal bacteria, *E. coli* under UV-Vis irradiation. As seen in the results of phenol degradation, mainly exfoliated samples exhibit significant photocatalytic efficacy, thus only exfoliated samples were evaluated for *E. coli* disinfection. Each sample was plated for the multiple dilution ( $10^3$ ,  $10^4$  &  $10^5$ ) and in triplicate to get more accurate counts, and the results were averaged correspondingly. Control experiment (photolysis) was also conducted in the absence of any photocatalyst. Images of *E. coli* colonies on solid culture medium showing photocatalytic disinfection performance by exfoliated  $g\text{-C}_3\text{N}_4$  samples are summarized in Table 4.11 for  $10^3$  dilution and the results, fitted with Glnafit tool, are shown in Fig. 4.30.



**Fig. 4.30** *E. coli* disinfection shown by exfoliated  $g\text{-C}_3\text{N}_4$  samples synthesized using different precursors and P25-TiO<sub>2</sub> at 100 mg L<sup>-1</sup> concentration. Detection limit = 2 CFU mL<sup>-1</sup>. (Markers are experimental data, while lines represented the best fitted data using GlnaFiT models)

In the photolysis of *E. coli*, only 1-log reduction of *E. coli* was observed in 5 h of UV-Vis irradiation. Like phenol degradation, sample TCN-exf outpaced than others with 3-log reduction in 5 h of irradiation, followed by UCN-exf and MCN-exf showing 2.6 and 2.3 *E. coli* log reduction, respectively. However, again P25-TiO<sub>2</sub> outperformed with total *E. coli* inactivation within 180 min.


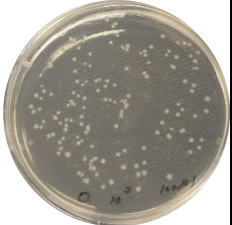
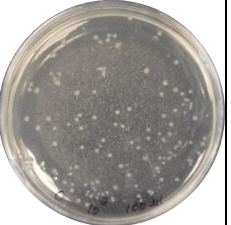
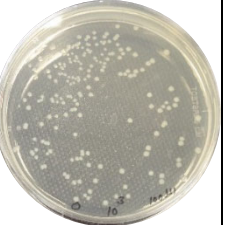
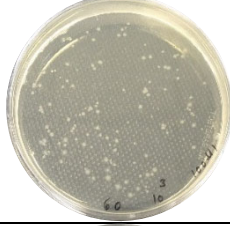
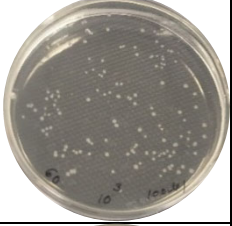
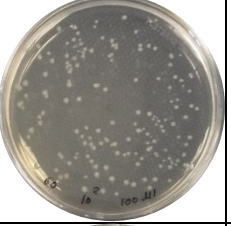
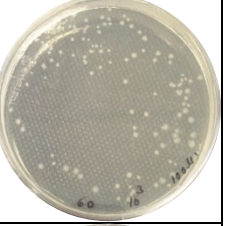
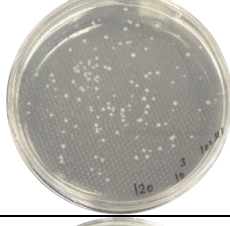
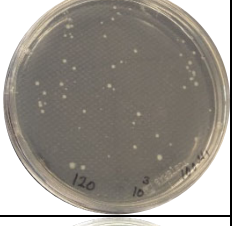
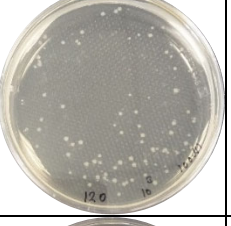
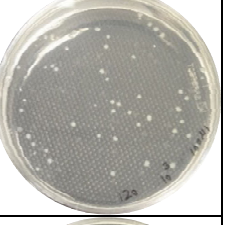
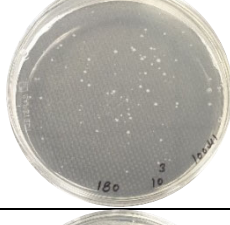
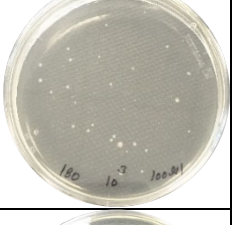
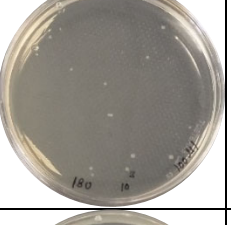
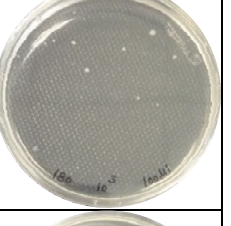
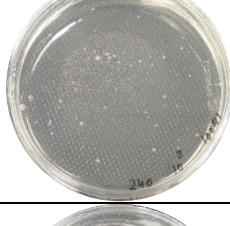
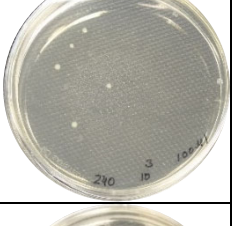
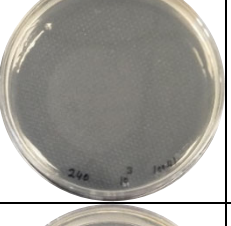
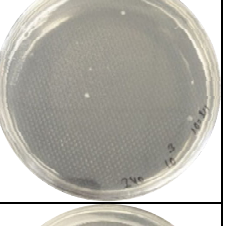

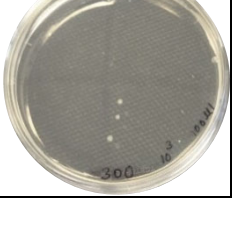
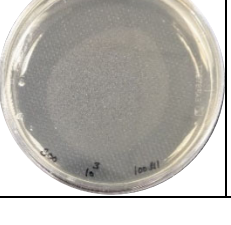
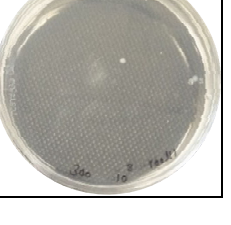
Further, the experimental data of *E. coli* inactivation by each g-C<sub>3</sub>N<sub>4</sub> sample were fitted with nine models of the GInaFiT tool (Geeraerd and Van Impe Inactivation Model Fitting Tool, version 1.6).<sup>39</sup> The details of GInaFiT tool are in chapter 3. To compare the results of the nine models, sum of squared errors (SSE), root mean sum of squared errors (RMSE), the coefficient of determination (R<sup>2</sup>), and other obtained parameters are reported in Table 4.12-4.15 for photolysis, MCN-exf, TCN-exf and UCN-exf, respectively. Out of nine inactivation models, best fit model is selected for each sample and kept in bold for easy understanding.

It can be seen in Table 4.12-4.15 that most of the fitting models gives unrealistic high standard errors, represented as non-significant (n.s.) in tables which means those models are unfit for particular data set. Simple log-linear model is also not suitable for these data sets due to low value of R<sup>2</sup>. For models with tailing (Log-linear + tail, Log-linear + shoulder + tail, and Weibull + tail), program warns, “Log<sub>10</sub>(N<sub>res</sub>) is less than the minimal measured value. Model with tailing is unlikely for these data.” thus a model without tailing should be selected. For the biphasic model fit, the program gave warning as “The parameter estimate for  $k_{max1}$  is exactly equal to  $k_{max2}$ . This indicates that the biphasic model is unlikely for these data”. Considering all the parameters, only Log-linear + shoulder and Weibull models look feasible for the data set of light control and MCN-exf for *E. coli* disinfection but if we compare both of these models, Weibull model gives low SSE, low RMSE and higher R<sup>2</sup> value

which makes it the best fitting model for experimental data set of light control and MCN-exf. Similarly considering same parameters, double Weibull model becomes the best fitting model for data set of TCN-exf and UCN-exf.

The best fitting model and obtained parameter values for each experimental data set of *E. coli* disinfection by exfoliated g-C<sub>3</sub>N<sub>4</sub> samples are filtered and summarized in Table 4.16. *E. coli* inactivation model is usually described in three stages, (i) duration of initial decay, termed as "shoulder" which is denoted by  $\delta$  or  $\delta_1$  in models of GInaFiT tool. This refers to the time taken for the first log reduction in *E. coli* cells which depends on generation of reactive oxygen species (ROS), (ii) "a log-linear region", here rapid inactivation occurs, it covers the most part of reaction, but some cells show higher resistance than others which can be compared by another scale parameter,  $\delta_2$  mentioned in double Weibull model, (iii) "Tail", a deceleration of the phase.<sup>40</sup> Now if one evaluates the Table 4.16, we can see that light control experiment (photolysis of *E. coli*) had its first log reduction ( $\delta_1$ ) of *E. coli* in 308.0±10.4 min while exfoliated g-C<sub>3</sub>N<sub>4</sub> samples (MCN-exf, TCN-exf and UCN-exf) took 186.1±11.7, 169.0±2.1, 145.1±6.8 min to deliver first log reduction of *E. coli*, respectively. Thus, it reveals that urea derived g-C<sub>3</sub>N<sub>4</sub> sample was faster in doing first log reduction than other exfoliated samples (U<T<M). if we consider error factor, time taken to inactivate more resistant bacterial cells ( $\delta_2$ ) is almost similar for UCN-exf (283.3±15.9 min) and TCN-exf (294.9±6.9 min) although TCN-exf sample was better in inactivating *E. coli* in 5 h of UV-Vis irradiation with 3 log reductions.

**Table 4.11** Images of *E. coli* colonies on solid culture medium showing photocatalytic disinfection performance by exfoliated g-C<sub>3</sub>N<sub>4</sub> samples (MCN-exf, TCN-exf and UCN-exf) under 5 h of UV-Vis irradiation. (Sampling- 100  $\mu$ l of 10<sup>3</sup> dilution)

Time	Light Control	MCN-exf	TCN-exf	UCN-exf
<b>0 min</b>				
<b>60 min</b>				
<b>120 min</b>				
<b>180 min</b>				
<b>240 min</b>				
<b>300 min</b>				

**Table 4.12** Statistical measures and parameter values obtained when applying nine models available in GInaFiT Version 1.6 on the experimental data set of light control

Model Type	SSE	Log <sub>10</sub> (N <sub>0</sub> ) [cfu mL <sup>-1</sup> ]	RMSE	R <sup>2</sup>	Log <sub>10</sub> (N <sub>res</sub> ) [cfu mL <sup>-1</sup> ]	SI/ δ1/ δ2 [min]	$k_{max} / k_{max1} / k_{max2}$ [min <sup>-1</sup> ]
Log-linear regression	0.09	6.41±0.11	0.1494	0.8703			$k_{max}=0.01±0.00$
Log-linear + shoulder	0.02	6.26±0.05	0.0734	0.9765		SI=187.4±22.9	$k_{max}=0.02±0.00$
Log-linear + tail	0.09	6.41±0.15	0.1725	0.8703	0.46 <sup>n.s.</sup>		$k_{max}=0.01±0.01$
Log-linear + shoulder + tail	0.02	6.26±n.s.	0.0899	0.9765	-189.4 <sup>n.s.</sup>	SI=187.4±n.s.	$k_{ma}=0.02±n.s.$
<b>Weibull</b>	<b>0.01</b>	<b>6.25±0.05</b>	<b>0.0693</b>	<b>0.9791</b>		<b>δ=308.0±10.4</b>	
Weibull + tail	0.01	6.25±0.07	0.0849	0.9791	-1.21 <sup>n.s.</sup>	δ=308±n.s.	
Double Weibull	0.01	6.25±0.11	0.0849	0.9791		δ1=307.9±n.s. δ2=308.3±n.s.	
Biphasic model	0.09	6.41±0.21	0.2113	0.8703			$k_{max1}=0.01±n.s.$ $k_{max2}=0.01±n.s.$
Biphasic + shoulder	0.02	6.26±0.13	0.1271	0.9765		SI=187.4±n.s.	$k_{max1}=0.02±0.05$ $k_{max2}=0.02±n.s.$

**Table 4.13** Statistical measures and parameter values obtained when applying nine models available in GInaFiT Version 1.6 on the experimental data set of MCN-exf

Model Type	SSE	Log <sub>10</sub> (N <sub>0</sub> ) [cfu mL <sup>-1</sup> ]	RMSE	R <sup>2</sup>	Log <sub>10</sub> (N <sub>res</sub> ) [cfu mL <sup>-1</sup> ]	SI/ δ1/ δ2 [min]	$k_{max} / k_{max1} / k_{max2}$ [min <sup>-1</sup> ]
Log-linear regression	0.23	6.53±0.17	0.2375	0.9423			$k_{max}=0.02±0.00$
Log-linear + shoulder	0.03	6.27±0.09	0.1039	0.9917		SI=96.3±18.7	$k_{max}=0.03±0.00$
Log-linear + tail	0.23	6.53±0.22	0.2743	0.9423	-0.86 <sup>n.s.</sup>		$k_{max}=0.02±0.00$
Log-linear + shoulder + tail	0.03	6.27±0.11	0.1273	0.9917	-5.28 <sup>n.s.</sup>	SI=96.3±29.2	$k_{max}=0.03±0.01$
<b>Weibull</b>	<b>0.02</b>	<b>6.28±0.08</b>	<b>0.0904</b>	<b>0.9937</b>		<b>δ=186.1±11.7</b>	
Weibull + tail	0.02	6.28±0.10	0.1107	0.9937	-1.11 <sup>n.s.</sup>	δ=186.1±14.3	
Double Weibull	0.02	6.28±0.16	0.1107	0.9937		δ1=186.1±n.s. δ2=192.7±n.s.	
Biphasic model	0.23	6.53±0.27	0.3359	0.9423			$k_{max1}=0.02±n.s.$ $k_{max2}=0.02±n.s.$
Biphasic + shoulder	0.03	6.27±0.17	0.1800	0.9917		SI=96.3±n.s.	$k_{max1}=0.03±0.09$ $k_{max2}=0.03±n.s.$

**Table 4.14** Statistical measures and parameter values obtained when applying nine models available in GInaFiT Version 1.6 on the experimental data set of TCN-exf

Model Type	SSE	Log <sub>10</sub> (N <sub>0</sub> ) [cfu mL <sup>-1</sup> ]	RMSE	R <sup>2</sup>	Log <sub>10</sub> (N <sub>res</sub> ) [cfu mL <sup>-1</sup> ]	SI/ δ1/ δ2 [min]	k <sub>max</sub> / k <sub>max1</sub> / k <sub>max2</sub> [min <sup>-1</sup> ]
Log-linear regression	0.75	6.75±0.31	0.4335	0.9087			k <sub>max</sub> =0.03±0.00
Log-linear + shoulder	0.08	6.30±0.13	0.1651	0.9901		SI=105.4±17.5	k <sub>max</sub> =0.04±0.00
Log-linear + tail	0.75	6.75±0.40	0.5006	0.9087	-1.45 <sup>n.s.</sup>		k <sub>max</sub> =0.03±0.01
Log-linear + shoulder + tail	0.08	6.30±0.16	0.2023	0.9901	-10.2 <sup>n.s.</sup>	SI=105.4±26.3	k <sub>ma</sub> =0.04±0.01
Weibull	0.19	6.38±0.21	0.2529	0.9767		δ=154.6±24.5	
Weibull + tail	0.02	6.29±0.07	0.0929	0.9979	3.3±0.1	δ=169.4±7.4	
<b>Double Weibull</b>	<b>0.00</b>	<b>6.26±0.03</b>	<b>0.0228</b>	<b>0.9999</b>		<b>δ1=169.0±2.1</b> <b>δ2=294.9±6.9</b>	
Biphasic model	0.75	6.75±0.48	0.6131	0.9087			k <sub>max1</sub> =0.03±n.s. k <sub>max2</sub> =0.03±n.s.
Biphasic + shoulder	0.02	6.31±0.10	0.1237	0.9981		SI=110.8±16.9	k <sub>max1</sub> =0.04±0.01 k <sub>max2</sub> =0.00±0.10

**Table 4.15** Statistical measures and parameter values obtained when applying nine models available in GInaFiT Version 1.6 on the experimental data set of UCN-exf

Model Type	SSE	Log <sub>10</sub> (N <sub>0</sub> ) [cfu mL <sup>-1</sup> ]	RMSE	R <sup>2</sup>	Log <sub>10</sub> (N <sub>res</sub> ) [cfu mL <sup>-1</sup> ]	SI/ δ1/ δ2 [min]	k <sub>max</sub> / k <sub>max1</sub> / k <sub>max2</sub> [min <sup>-1</sup> ]
Log-linear regression	0.18	6.61±0.16	0.2143	0.9664			k <sub>max</sub> =0.02±0.00
Log-linear + shoulder	0.06	6.40±0.13	0.1372	0.9897		SI=63.3±22.9	k <sub>max</sub> =0.03±0.00
Log-linear + tail	0.18	6.61±0.20	0.2475	0.9664	-1.07 <sup>n.s.</sup>		k <sub>max</sub> =0.02±0.00
Log-linear + shoulder + tail	0.06	6.40±0.16	0.1680	0.9897	-10.9 <sup>n.s.</sup>	SI=63.3±35.1	k <sub>ma</sub> =0.03±0.01
Weibull	0.08	6.43±0.15	0.1648	0.9851		δ=143.3±20.7	
Weibull + tail	0.04	6.39±0.14	0.1490	0.9919	3.7±0.2	δ=149.1±17.0	
<b>Double Weibull</b>	<b>0.00</b>	<b>6.32±0.06</b>	<b>0.0468</b>	<b>0.9992</b>		<b>δ1=145.1±6.8</b> <b>δ2=283.3±16</b>	
Biphasic model	0.18	6.61±0.22	0.3031	0.9664			k <sub>max1</sub> =0.02±n.s. k <sub>max2</sub> =0.02±n.s.
Biphasic + shoulder	0.02	6.37±0.14	0.1467	0.9961		SI=80.4±25.2	k <sub>max1</sub> =0.04±0.03 k <sub>max2</sub> =0.02±0.02



**Table 4.16** The best fitting model and obtained parameter values on the experimental data set of *E. coli* disinfection

Sample	Model Type	SSE	Log <sub>10</sub> (N <sub>0</sub> ) [cfu mL <sup>-1</sup> ]	RMSE	R <sup>2</sup>	SI/ δ1/ δ2 [min]
Light Control	Weibull	0.01	6.25±0.05	0.0693	0.9791	δ=308.0±10.4
MCN-exf	Weibull	0.02	6.28±0.08	0.0904	0.9937	δ=186.1±11.7
TCN-exf	Double Weibull	0.00	6.26±0.03	0.0228	0.9999	δ1=169.0±2.1 δ2=294.9±6.9
UCN-exf	Double Weibull	0.00	6.32±0.06	0.0468	0.9992	δ1=145.1±6.8 δ2=283.3±15.9

Despite achieving similar or even better physiochemical properties for g-C<sub>3</sub>N<sub>4</sub> to prior studies, we did not achieve as much photocatalytic activity of g-C<sub>3</sub>N<sub>4</sub> as many others have claimed in literature.<sup>9,17–19,21–25</sup> Although the majority of these research employed dyes as a model pollutant to evaluate photocatalytic efficiency of g-C<sub>3</sub>N<sub>4</sub>, which is not recommended because most dyes are photosensitive.<sup>41,42</sup> For instance, Devthade *et al.*<sup>22</sup> claimed the excellent photocatalytic performance of urea-derived g-C<sub>3</sub>N<sub>4</sub> (specific surface area of 55.1 m<sup>2</sup>g<sup>-1</sup> and a bandgap of 2.69 eV) by achieving 100 % degradation of acid violet 7 (AV7) dye after 30 minutes of visible light exposure. However, some researchers also used the typical contaminants other than sensitized dyes and microbes to evaluate photocatalytic efficiency of g-C<sub>3</sub>N<sub>4</sub>. For example, Ge<sup>26</sup> reported 92.5% phenol degradation by the g-C<sub>3</sub>N<sub>4</sub> samples heated at 520 °C for 4 h. Likewise Kang *et al.*<sup>9</sup> achieved a specific surface area of 14.48 m<sup>2</sup>g<sup>-1</sup> for bulk g-C<sub>3</sub>N<sub>4</sub> and 89.59 m<sup>2</sup>g<sup>-1</sup> for exfoliated g-C<sub>3</sub>N<sub>4</sub> using melamine as a precursor, and for the latter one, they claimed for 7-log reduction of *E. coli* in 120 min and 65% degradation (k=0.01) of humic acid after 70 min of visible-light irradiation, which sounds unrealistic because they did not show any specific argument behind this enhanced photocatalytic performance. However, in our study we observed limited photocatalytic

activities shown by exfoliated samples of g-C<sub>3</sub>N<sub>4</sub> prepared from melamine, thiourea and urea with reaction rates of  $4.96 \times 10^{-8}$  (MCN-exf),  $1.83 \times 10^{-7}$  (TCN-exf) and  $2.14 \times 10^{-7}$  mol L<sup>-1</sup> min<sup>-1</sup> (UCN-exf) for phenol degradation and ~2-3 log reduction in *E. coli* colonies after 5 h of UV-Vis irradiation.

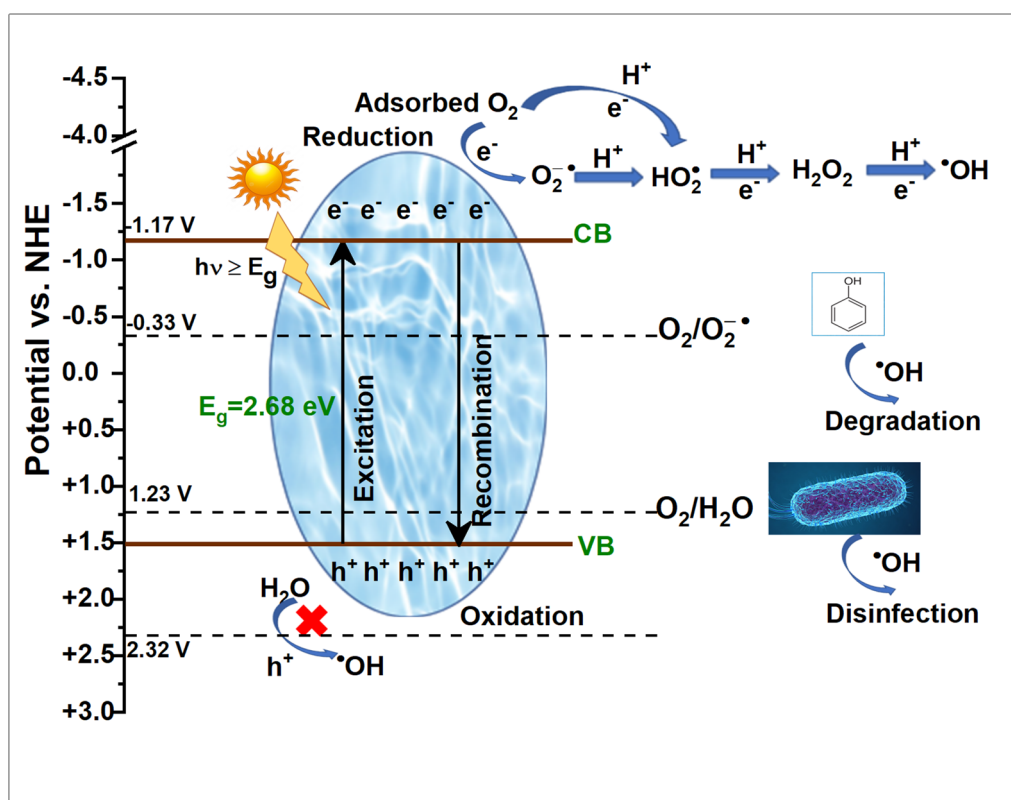
#### 4.5 The possible photocatalytic mechanism of g-C<sub>3</sub>N<sub>4</sub>

The photocatalytic processes leading to the disinfection and organic degradation usually involve the formation of various reactive oxygen species (ROS) such as hydroxyl radicals ( $\cdot\text{OH}$ ), superoxide anion radicals ( $\text{O}_2^{\cdot-}$ ), and hydrogen peroxide ( $\text{H}_2\text{O}_2$ ). Although hydroxyl radical is considered the primary ROS leading to photocatalytic disinfection and organic degradation. A photocatalyst should possess suitable band edge potentials for the formation of these ROS *i.e.*, to reduce molecular O<sub>2</sub> to generate superoxide ( $\text{O}_2^{\cdot-}$ ) radicals ( $E_0 = -0.33$  V (NHE)) and to oxidise water to produce hydroxyl radicals ( $\cdot\text{OH}$ ) ( $E_0 = +2.32$  V (NHE)) at pH 7.

TiO<sub>2</sub> fulfils the above criterion because its CB potential (-0.51 V) and the VB potential (+2.69V) are aligned with the required band edge potentials thus it can easily produce hydroxyl radicals hence can disinfect *E. coli* and degrade phenol. On the other hand, the VB and CB potential of g-C<sub>3</sub>N<sub>4</sub> is estimated to be situated around +1.51 V and -1.17 V (NHE), respectively (see chapter 4). Although the VB potential of g-C<sub>3</sub>N<sub>4</sub> is insufficient for the water oxidation which is the primary mechanism to produce  $\cdot\text{OH}$  radicals. Thus g-C<sub>3</sub>N<sub>4</sub> may utilize different process to generate OH radicals. The CB potential of g-C<sub>3</sub>N<sub>4</sub> is negative enough for the generation of other ROS such as  $\text{O}_2^{\cdot-}$  by reduction of adsorbed O<sub>2</sub> that may further produce H<sub>2</sub>O<sub>2</sub> or  $\cdot\text{OH}$  radicals by multiple reduction reactions of O<sub>2</sub> (equation 4.3-4.7).<sup>43,44</sup>



$\text{O}_2^{\bullet -}$  and  $\cdot\text{OH}$  radicals are the oxidants, which may oxidise phenol and disinfect *E. coli*.<sup>45–47</sup> The schematic of possible photocatalytic mechanism of g-C<sub>3</sub>N<sub>4</sub> explicating degradation of phenol and *E. coli* disinfection is given in Fig. 4.31.



**Fig. 4.31.** The schematic of possible photocatalytic mechanism of g-C<sub>3</sub>N<sub>4</sub> explicating degradation of phenol and *E. coli* disinfection

## 4.6 Conclusions

In summary, bulk g-C<sub>3</sub>N<sub>4</sub> samples were prepared by a simple thermal polymerization of various precursors *i.e.*, thiourea, dicyandiamide, melamine, and

urea at different combinations of reaction conditions. Further heat treatment was given to bulk g-C<sub>3</sub>N<sub>4</sub> samples to get exfoliated g-C<sub>3</sub>N<sub>4</sub> samples. All the obtained samples exhibited physicochemical properties of graphitic carbon nitride as confirmed by wide characterisation techniques such as XRD, FTIR, Raman, BET and DRS. All the prepared samples were compared with each other for their structural, optical, and morphological properties. The systematic result analysis confirmed that the precursors and reaction parameters have significant effect on the surface area, pore size, pore volume, band gap, morphology, and photocatalytic activity of g-C<sub>3</sub>N<sub>4</sub>. Considering the v/w ratio, urea derived g-C<sub>3</sub>N<sub>4</sub> holds the highest v/w ratio (U>T>M), however it possesses the lowest yield among the three precursors (M>T>U). Above 550°C there was no product found in case of urea as it decomposed completely above this temperature. Increase in calcination temperature led to increase in surface area and decrease in band gap energies hence more available active sites and increased light absorption which may improve the photocatalytic activity of g-C<sub>3</sub>N<sub>4</sub>. The urea derived samples displayed high specific surface area than all the other samples which could be linked to an increase in photocatalytic active sites. When compared to their bulk counterpart, surface area and bandgap energy of exfoliated g-C<sub>3</sub>N<sub>4</sub> samples increases after exfoliation. Samples having favourable physicochemical properties have been tested for their photocatalytic performance by degradation organic pollutant, phenol, and *E. coli* inactivation under UV-Vis irradiation. The thiourea and urea derived exfoliated g-C<sub>3</sub>N<sub>4</sub> samples exhibited better phenol degradation and *E. coli* disinfection performance than all the other samples due to their high specific surface area which could be correlated with an increase in the available active sites for photocatalytic reactions. GInaFiT (Geeraerd and Van Impe Inactivation Model Fitting Tool) was used to get suitable fit for experimental data sets of *E. coli* disinfection. After the

comparison of obtained parameters, Weibull model becomes the best suit for light control and MCN-exf sample while double Weibull model is for TCN-exf and UCN-exf samples. Urea derived g-C<sub>3</sub>N<sub>4</sub> sample shows faster first log reduction than other exfoliated samples (U<T<M). However, the photocatalytic efficiency demonstrated by all the g-C<sub>3</sub>N<sub>4</sub> is still much lower than the photocatalytic efficiency of P25-TiO<sub>2</sub> tested for phenol degradation and *E. coli* inactivation. The study provides the detailed insights into appropriate selection of precursors and reaction conditions for g-C<sub>3</sub>N<sub>4</sub> synthesis and their effect on physicochemical and photocatalytic performance of graphitic carbon nitride and photocatalytic efficiency comparison for water treatment against P25-TiO<sub>2</sub>.

#### 4.7 References

1. Masih, D., Ma, Y. & Rohani, S. Graphitic C<sub>3</sub>N<sub>4</sub> based noble-metal-free photocatalyst systems: A review. *Appl. Catal. B Environ.* 2017, **206**, 556–588.
2. Niu, P., Yin, L., Yang, Y., Liu, G. & Cheng, H. Increasing the visible light absorption of graphitic carbon nitride (melon) photocatalysts by homogeneous self-modification with nitrogen vacancies. *Adv. Mater.* 2014, **26**, 8046–8052.
3. Zhai, H., Cao, L. & Xia, X. Synthesis of graphitic carbon nitride through pyrolysis of melamine and its electrocatalysis for oxygen reduction reaction. *Chinese Chem. Lett.* 2013, **24**, 103–106.
4. Teter, D. M. & Hemley, R. J. Low-compressibility carbon nitrides. *Science.* 1996, **271**, 53–55.
5. Xu, Y. & Gao, S. Band gap of C<sub>3</sub>N<sub>4</sub> in the GW approximation. *Int. J. Hydrogen Energy* 2012, **37**, 11072–11080.
6. Lotsch, B. V & Schnick, W. From triazines to heptazines: novel nonmetal tricyanomelaminates as precursors for graphitic carbon nitride materials. *Chem. Mater.* 2006, **18**, 1891–1900.
7. Kroke, E., Schwarz, M., Horath-Bordon, E., Kroll, P., Noll, B., & Norman, A. D. Tri-s-triazine derivatives. Part I. From trichloro-tri-s-triazine to graphitic

- C<sub>3</sub>N<sub>4</sub> structures Part II: Alkalicyamelurates M<sub>3</sub>[C<sub>6</sub>N<sub>7</sub>O<sub>3</sub>], M = Li, Na, K, Rb, Cs, manuscript in preparation. *New J. Chem.* 2002, **26**, 508–512.
8. Wang, X., Maeda, K., Thomas, A., Takanabe, K., Xin, G., Carlsson, J. M., Domen, K., & Antonietti, M. A metal-free polymeric photocatalyst for hydrogen production from water under visible light. *Nat. Mater.* 2009, **8**, 76–80.
  9. Kang, S., Zhang, L., He, M., Zheng, Y., Cui, L., Sun, D., & Hu, B. ‘Alternated cooling and heating’ strategy enables rapid fabrication of highly-crystalline g-C<sub>3</sub>N<sub>4</sub> nanosheets for efficient photocatalytic water purification under visible light irradiation. *Carbon N. Y.* 2018, **137**, 19–30.
  10. Xu, J., Gao, Q., Bai, X., Wang, Z. & Zhu, Y. Enhanced visible-light-induced photocatalytic degradation and disinfection activities of oxidized porous g-C<sub>3</sub>N<sub>4</sub> by loading Ag nanoparticles. *Catal. Today* 2019, **332**, 227–235.
  11. Pomilla, F. R., Cortes, M. A. L. R.M. Hamilton, J. W. J., Molinari, R., Barbieri, G., Marci, G., Palmisano, L., Sharma, P. K., Brown, A., & Byrne, J. A. An Investigation into the stability of graphitic C<sub>3</sub>N<sub>4</sub> as a photocatalyst for CO<sub>2</sub> reduction. *J. Phys. Chem. C* 2018, **122**, 28727–28738.
  12. Hong, J., Xia, X., Wang, Y. & Xu, R. Mesoporous carbon nitride with in situ sulfur doping for enhanced photocatalytic hydrogen evolution from water under visible light. *J. Mater. Chem.* 2012, **22**, 15006.
  13. Hwang, S., Lee, S. & Yu, J. Template-directed synthesis of highly ordered nanoporous graphitic carbon nitride through polymerization of cyanamide. *Appl. Surf. Sci.* 2007, **253**, 5656–5659.
  14. Yang, F., Lublow, M., Orthmann, S., Merschjann, C., Tyborski, T., Rusu, M., Kubala, S., Thomas, A., Arrigo, R., Hävecker, M., & Schedel-Niedrig, T. Metal-free photocatalytic graphitic carbon nitride on p-type chalcopyrite as a composite photocathode for light-induced hydrogen evolution. *ChemSusChem* 2012, **5**, 1227–1232.
  15. Zhang, G., Zhang, J., Zhang, M. & Wang, X. Polycondensation of thiourea into carbon nitride semiconductors as visible light photocatalysts. *J. Mater. Chem.* 2012, **22**, 8083.
  16. Cui, Y., Zhang, J., Zhang, G., Huang, J., Liu, P., Antonietti, M., & Wang, X. Synthesis of bulk and nanoporous carbon nitride polymers from ammonium thiocyanate for photocatalytic hydrogen evolution. *J. Mater. Chem.* 2011, **21**,

- 13032.
17. Lee, S. C., Lintang, H. O. & Yuliati, L. A urea precursor to synthesize carbon nitride with mesoporosity for enhanced activity in the photocatalytic removal of phenol. *Chem. - An Asian J.* 2012, **7**, 2139–2144.
  18. Thomas, A., Fischer, A., Goettmann, F., Antonietti, M., Müller, J. O., Schlögl, R., & Carlsson, J. M. Graphitic carbon nitride materials: variation of structure and morphology and their use as metal-free catalysts. *J. Mater. Chem.* 2008, **18**, 4893.
  19. Zhang, Y., Liu, J., Wu, G. & Chen, W. Porous graphitic carbon nitride synthesized via direct polymerization of urea for efficient sunlight-driven photocatalytic hydrogen production. *Nanoscale* 2012, **4**, 5300.
  20. Ong, W., Tan, L., Ng, Y. H., Yong, S. & Chai, S. Graphitic carbon nitride (g-C<sub>3</sub>N<sub>4</sub>)-based photocatalysts for artificial photosynthesis and environmental remediation: are we a step closer to achieving sustainability? *Chem. Rev.* 2016, **116**, 7159–7329.
  21. Zhang, W., Zhang, Q., Dong, F. & Zhao, Z. The multiple effects of precursors on the properties of polymeric carbon nitride. *Int. J. Photoenergy* 2013, **2013**, 1–9.
  22. Devthade, V., Kulhari, D. & Umare, S. S. Role of precursors on photocatalytic behavior of graphitic carbon nitride. *Mater. Today Proc.* 2018, **5**, 9203–9210.
  23. Theerthagiri, J., Senthil, R. A., Madhavan, J. & Neppolian, B. A comparative study on the role of precursors of graphitic carbon nitrides for the photocatalytic degradation of direct red 81. *Mater. Sci. Forum* 2014, **807**, 101–113.
  24. Mo, Z., She, X., Li, Y., Liu, L., Huang, L., Chen, Z., Zhang, Q., Xu, & H., Li, Huaming Synthesis of g-C<sub>3</sub>N<sub>4</sub> at different temperatures for superior visible/UV photocatalytic performance and photoelectrochemical sensing of MB solution. *RSC Adv.* 2015, **5**, 101552–101562.
  25. Papailias, I., Giannakopoulou, T., Todorova, N., Demotikali, D., Vaimakis, T., & Trapalis, C. Effect of processing temperature on structure and photocatalytic properties of g- C<sub>3</sub>N<sub>4</sub>. *Appl. Surf. Sci.* 2015, **358**, 278–286.
  26. Ge, L. Synthesis and photocatalytic performance of novel metal-free g-C<sub>3</sub>N<sub>4</sub> photocatalysts. *Mater. Lett.* 2011, **65**, 2652–2654.
  27. Li, Y., Li, Y., Ma, S., Wang, P., Hou, Q., Han, J., & Zhan, S. Efficient water disinfection with Ag<sub>2</sub>WO<sub>4</sub>-doped mesoporous g-C<sub>3</sub>N<sub>4</sub> under visible light. *J.*

- Hazard. Mater.* 2017, **338**, 33–46.
28. Li, G., Nie, X., Chen, J., Jiang, Q., An, T., Wong, P. K., Zhang, H., Zhao, H., & Yamashita, H. Enhanced visible-light-driven photocatalytic inactivation of *Escherichia coli* using g-C<sub>3</sub>N<sub>4</sub>/TiO<sub>2</sub> hybrid photocatalyst synthesized using a hydrothermal-calcination approach. *Water Res.* 2015, **86**, 17–24.
  29. Dong, F., Ou, M., Jiang, Y., Guo, S. & Wu, Z. Efficient and durable visible light photocatalytic performance of porous carbon nitride nanosheets for air purification. *Ind. Eng. Chem. Res.* 2014, **53**, 2318–2330.
  30. Abdelhafeez, I. A., Yao, Q., Wang, C., Su, Y., Zhou, X., & Zhang, Y. Green synthesis of ultrathin edge-activated foam-like carbon nitride nanosheets for enhanced photocatalytic performance under visible light irradiation. *Sustain. Energy Fuels* 2019, **3**, 1764–1775.
  31. Bragg, W. H. & Bragg, W. . L. The reflection of X-rays by crystals. *Proc. R. Soc. London. Ser. A, Contain. Pap. a Math. Phys. Character* 1913, **88**, 428–438.
  32. Fernández-Ibáñez, P., Polo-López, M.I., Malato, S., Wadhwa, S., Hamilton, J. W. J., Dunlop, P. S. M., D'Sa, R., Magee, E., O'Shea, K., Dionysiou, D. D., & Byrne, J. A. Solar photocatalytic disinfection of water using titanium dioxide graphene composites. *Chem. Eng. J.* 2015, **261**, 36–44.
  33. Li, X., Sun, Q., Li, M., Yang, J., Chen, X., Yang, Y., Li, X., Hu, T., Sui, Y., & Wu, X. Photocatalytic properties of nano-structured carbon nitride: a comparison with bulk graphitic carbon nitride. *Int. J. Mater. Res.* 2018, **109**, 129–135.
  34. Praus, P., Svoboda, L., Ritz, M., Troppová, I., Šihor, M., & Kočí, K. Graphitic carbon nitride: Synthesis, characterization and photocatalytic decomposition of nitrous oxide. *Mater. Chem. Phys.* 2017, **193**, 438–446.
  35. Yuan, Y., Zhang, L., Xing, J., Utama, M. I. B., Lu, X., Du, K., Li, Y., Hu, X., Wang, S., Genç, A., Dunin-Borkowski, R., Arbiol, J., Xiong, Q. High-yield synthesis and optical properties of g-C<sub>3</sub>N<sub>4</sub>. *Nanoscale* 2015, **7**, 12343–12350.
  36. Leofanti, G., Padovan, M., Tozzola, G. & Venturelli, B. Surface area and pore texture of catalysts. *Catal. Today* 1998, **41**, 207–219.
  37. Wei, X., Qiu, Y., Duan, W. & Liu, Z. Cathodic and anodic photocurrents generation from melem and its derivatives. *RSC Adv.* 2015, **5**, 26675–26679.
  38. Yang, S., Gong, Y., Zhang, J., Zhan, L., Ma, L., Fang, Z., Vajtai, R., Wang, X.,



- & Ajayan, P. M. Exfoliated graphitic carbon nitride nanosheets as efficient catalysts for hydrogen evolution under visible light. *Adv. Mater.* 2013, **25**, 2452–2456.
39. Geeraerd, A. H., Valdramidis, V. P. & Van Impe, J. F. GInaFiT, a freeware tool to assess non-log-linear microbial survivor curves. *Int. J. Food Microbiol.* 2005, **102**, 95–105.
40. Marugán, J., van Grieken, R., Sordo, C. & Cruz, C. Kinetics of the photocatalytic disinfection of *Escherichia coli* suspensions. *Appl. Catal. B Environ.* 2008, **82**, 27–36.
41. Barbero, N. & Vione, D. Why dyes should not be used to test the photocatalytic activity of semiconductor oxides. *Environ. Sci. Technol.* 2016, **50**, 2130–2131.
42. Rochkind, M., Pasternak, S. & Paz, Y. Using dyes for evaluating photocatalytic properties: A critical review. *Molecules* 2015, **20**, 88–110.
43. Armstrong, D. A., Huie, R. E., Lyman, S., Koppenol, W. H., Merényi, G., Neta, P., Stanbury, D. M., Steenken, S., & Wardman, P. Standard electrode potentials involving radicals in aqueous solution: inorganic radicals. *Bioinorg. React. Mech.* 2013, **9**, 59–61.
44. Li, J., Jiang, M., Zhou, H., Jin, P., Cheung, K. M. C., Chu, P. K., & Yeung, K. W. K. Vanadium Dioxide Nanocoating Induces Tumor Cell Death through Mitochondrial Electron Transport Chain Interruption. *Glob. Challenges* 2019, **3**, 1800058.
45. Abdullah, A. M., Garcia-Pinilla, M. Á., Pillai, S. C. & O'Shea, K. UV and Visible Light-Driven Production of Hydroxyl Radicals by Reduced Forms of N, F, and P Codoped Titanium Dioxide. *Molecules* 2019, **24**, 2147.
46. Daneshvar, H., Zadeh, B. S., Tarighati, A. R. & Hosseini, S. F. Chemical engineering research and design photocatalytic activity of g-C<sub>3</sub>N<sub>4</sub>: An empirical kinetic model , optimization by neuro-genetic approach and identification of intermediates. *Chem. Eng. Res. Des.* 2017, **127**, 113–125.
47. Thakur, P., Raizada, P., Singh, P. & Kumar, A. Exploring recent advances in silver halides and graphitic carbon nitride-based photocatalyst for energy and environmental applications. *Arab. J. Chem.* 2020, **13**, 8271–8300.

## Chapter 5 - Photoelectrochemical properties of exfoliated graphitic carbon nitride (g-C<sub>3</sub>N<sub>4</sub>)

### 5.1 Aim and objectives

**5.1.1 Aim:** This chapter aims to examine the photoelectrochemical properties of exfoliated g-C<sub>3</sub>N<sub>4</sub> and correlate to other physicochemical properties.

### 5.1.2 Objectives

1. To synthesize exfoliated graphitic carbon nitride (g-C<sub>3</sub>N<sub>4</sub>) through thermal polymerisation method.
2. To estimate the C/N ratio through elemental mapping using EDX.
3. To determine the elemental composition and chemical states present in g-C<sub>3</sub>N<sub>4</sub> using XPS.
4. To determine the optical bandgap and band edge positions of g-C<sub>3</sub>N<sub>4</sub> using Tauc plots and valence band XPS.
5. To determine the work function of g-C<sub>3</sub>N<sub>4</sub> using UPS.
6. To prepare g-C<sub>3</sub>N<sub>4</sub> working electrode on FTO coated glass using spray coating.
7. To investigate photoelectrochemical properties of g-C<sub>3</sub>N<sub>4</sub>.
8. To determine the flat band potential of g-C<sub>3</sub>N<sub>4</sub> by electrochemical impedance spectroscopy (EIS)
9. To propose an energy band diagram of g-C<sub>3</sub>N<sub>4</sub> based on the obtained results.

## 5.2 Introduction

Graphitic carbon nitride (g-C<sub>3</sub>N<sub>4</sub>) has been widely reported as a promising material for various photocatalytic applications. The physiochemical properties and photocatalytic activities (phenol degradation, *E. coli* disinfection) of g-C<sub>3</sub>N<sub>4</sub> samples prepared from different precursors were discussed in chapter 3. However, the photocatalytic activity of this material was very poor as compared to P25. These findings are contradictory with the previous published work reported by Zhao *et al.* (2014),<sup>1</sup> Lee *et al.* (2012),<sup>2</sup> Huang *et al.* (2014),<sup>3</sup> Thurston *et al.* (2017),<sup>4</sup> Yang *et al.* (2021),<sup>5</sup> and many others<sup>6-9</sup> who have reported good photocatalytic activities for g-C<sub>3</sub>N<sub>4</sub>. It should be noted that there are also some reports of poor photocatalytic activity of bare g-C<sub>3</sub>N<sub>4</sub>.<sup>10,11</sup>

To understand the efficiency of photocatalytic processes of semiconductors, it is necessary to understand the thermodynamics and kinetics of charge transfer at the semiconductor/solution interface. A semiconductor photocatalyst should have appropriate band edge energies to generate reactive oxygen species (ROS) such as hydroxyl radical ( $\cdot\text{OH}$ ), superoxide anion radical ( $\text{O}_2^{\cdot-}$ ), singlet oxygen ( $^1\text{O}_2$ ) and hydrogen peroxide ( $\text{H}_2\text{O}_2$ ), *etc.*<sup>12</sup> However,  $\cdot\text{OH}$  and  $\text{O}_2^{\cdot-}$  are the leading ROS involved in photocatalytic organic degradation and microbial disinfection. Therefore, a good photocatalyst should have a VB edge potential to be more positive than the oxidation potential of water, *i.e.*, +2.73 V (*vs.* NHE), to form hydroxyl radicals ( $\cdot\text{OH}$ ) and the CB edge potential to be more negative than the reduction potential of oxygen, *i.e.*, -0.33 V (*vs.* NHE), to form superoxide anion radicals ( $\text{O}_2^{\cdot-}$ ). However, in order to absorb visible light photons, the bandgap of a semiconductor should be less than 3.1 eV.<sup>13</sup> Therefore, visible light active photocatalysts must present different reaction

pathways to form ROS. Table 5.1 provides the typical redox reaction pathways and their corresponding redox potentials to form reactive oxygen species.

**Table 5.1** Redox reactions, redox couples, and their corresponding redox potentials to form reactive oxygen species.

Half reactions	Redox couple	Redox potential (V vs. NHE) <sup>14-17</sup>
$O_2(g) + e^- \rightarrow O_2^{\cdot-}$	$O_2 / O_2^{\cdot-}$	-0.33
$O_2(g) + H^+ + e^- \rightarrow HO_2^{\cdot}$	$O_2 / HO_2^{\cdot}$	-0.07
$HO_2^{\cdot} + H^+ + e^- \rightarrow H_2O_2$	$HO_2^{\cdot} / H_2O_2$	+1.46
$O_2^{\cdot-} + 2H^+ + e^- \rightarrow H_2O_2$	$O_2^{\cdot-} / H_2O_2$	+0.89
$H_2O_2 + H^+ + e^- \rightarrow H_2O + \cdot OH$	$H_2O_2 / \cdot OH$	+0.38
$H_2O + h^+ \rightarrow H^+ + \cdot OH$	$H_2O / \cdot OH$	+2.32
$O_2 + 2H^+ + 2e^- \rightarrow H_2O_2$	$O_2 / H_2O_2$	+0.28
$O_2 + 4H^+ + 4e^- \rightarrow 2H_2O$	$O_2 / H_2O$	+1.23
${}^1O_2(g) + e^- \rightarrow O_2^{\cdot-}$	${}^1O_2 / O_2^{\cdot-}$	+0.64

The VB and CB potential of g-C<sub>3</sub>N<sub>4</sub> is reported to be around +1.4 V and -1.3 V (NHE) respectively.<sup>18</sup> Although the VB potential is not enough positive to produce OH radicals but the CB potential is negative enough for the reduction of H<sup>+</sup> ions into H<sub>2</sub> (0 V, NHE) and can generate other ROSs such as O<sub>2</sub><sup>·-</sup> (-0.33 V, NHE), H<sub>2</sub>O<sub>2</sub> (+0.89 V, NHE) or ·OH radicals by multiple reduction reactions of O<sub>2</sub>. Despite its ability to produce reactive oxygen species, the photocatalytic efficiency of g-C<sub>3</sub>N<sub>4</sub> is still inferior to those of TiO<sub>2</sub>, the benchmark commercial photocatalyst, owing to the low separation efficiency and rapid recombination of photogenerated electron-hole pairs and limited utilization of visible light.

In this work, to understand the relatively inefficient photocatalytic performance of g-C<sub>3</sub>N<sub>4</sub>, its electronic and photoelectrochemical properties were investigated by diffuse reflectance spectroscopy (DRS), X-ray and UV photoelectron

spectroscopy (XPS/UPS) and photoelectrochemical methods including linear sweep voltammetry (LSV), chronoamperometry, spectral response, electrochemical impedance spectroscopy (EIS) and photo-potential. The measurement of electrical variables such as current, potential as well as their correlation to chemical parameters, is the focus of electrochemical techniques. Several characteristics, obtained from photoelectrochemical methods and other techniques such as XPS/UPS, were calculated and correlated including onset potential, flat band potential, Fermi energy, work function, band edge positions, open circuit potential (OCP), and photo potential, allowing us to gain a better knowledge of the electronic band structure and photoelectrochemical behaviour of g-C<sub>3</sub>N<sub>4</sub>.

## **5.3 Experimental Section**

### **5.3.1 Synthesis of exfoliated g-C<sub>3</sub>N<sub>4</sub>**

Exfoliated g-C<sub>3</sub>N<sub>4</sub> samples were synthesized using melamine as a precursor in a two-step synthesis process as explained in section 4.3.3 of chapter 4. The prepared sample was named as MCN-exf.

### **5.3.2 Working electrode preparation**

To perform photoelectrochemical measurements, the working electrodes used in this study were fabricated following the protocol that was formerly discussed in detail in section 3.3 of Chapter 3. In brief, fabrication of a typical working electrode follows the three steps which includes cleaning of conductive substrate (FTO coated glass was used in our work), Spray coating of photocatalyst (g-C<sub>3</sub>N<sub>4</sub>) on cleaned substrate and making an electrical contact (using copper wire).

### 5.3.3 Analytical characterization

The exfoliated g-C<sub>3</sub>N<sub>4</sub> samples were characterized by X-ray diffraction spectroscopy (XRD), Fourier-Transform Infrared spectroscopy (FTIR), Raman spectroscopy, diffuse reflectance spectroscopy (DRS), field emission scanning electron microscope (FESEM) and BET surface area measurements. Details of all these characterization techniques are provided in chapter 3. Although outcome of these characterization techniques has previously been explained in section 4.4.1.4.

An FESEM equipped with a dispersive energy X-ray (EDX/EDS) analyser was used to determine the bulk elemental composition of the samples under low vacuum pressure of  $\sim 10^{-4}$  bar at working distance of 5 mm and an accelerating voltage of 10 kV. The resultant images were captured with a backscattered secondary electron (BSE) detector and the results obtained from EDX were analysed with the Aztec software that came with the instrument.

X-ray photoelectron spectroscopy (XPS) was performed to study the surface composition and chemical states of prepared sample. The binding energy was calibrated to the C 1s peak at 248.8 eV. The peaks were fitted using CasaXPS software after performing the U 2 Tougaard background correction before quantification. Valence band XPS (VBXPS) and ultraviolet photoelectron spectroscopy (UPS) were also employed to explore the band edge energies and work function of g-C<sub>3</sub>N<sub>4</sub>. Synthesized sample was spray coated on Si wafer for uniformity to carry out XPS/UPS analysis. A He I emission UV source (21.22 eV) was used to collect UPS spectra of carbon nitride. The further details of all these instruments have been provided in section 3.4.4.

### 5.3.4 Photoelectrochemical methods

The photoelectrochemical measurements were performed using a three-electrode system in a borosilicate glass beaker. This three-electrode configuration consisted of a platinum mesh paddle (5.9 cm<sup>2</sup>) as the counter electrode, saturated calomel electrode (Hanna instruments) as the reference electrode and earlier prepared photoelectrode as the working electrode. 0.1 M KClO<sub>4</sub> solution (pH = 6) was used as an electrolyte. 450 W Xe lamp was used as an irradiation source. All photoelectrochemical measurements were performed on an electrochemical workstation (AUTOLAB PGSTAT 30). More details of the irradiation source, photoelectrochemical cell and electrochemical workstation are given in chapter 3.

Linear sweep voltammetry (LSV) was used to determine the photocurrent-potential behaviour in the absence and presence of monochromatic irradiation sweeping from -1.0 to +1.0 V at a sweep rate of 5 mV s<sup>-1</sup>. The photocurrent-time response was also measured over a range of fixed potentials. The open-circuit potential vs. SCE was measured in the dark and under irradiation in potentiometric mode. Electrochemical impedance spectroscopy (EIS) was employed in the dark and under illumination using frequency response analyser (FRA) potential scan in the potential range of -1.0 to +1.0 V and frequency range of 10 mHz to 100 kHz to determine the flat band potential of the sample. More details are provided in chapter 3.

## 5.4 Results and discussion

### 5.4.1 Electronic properties

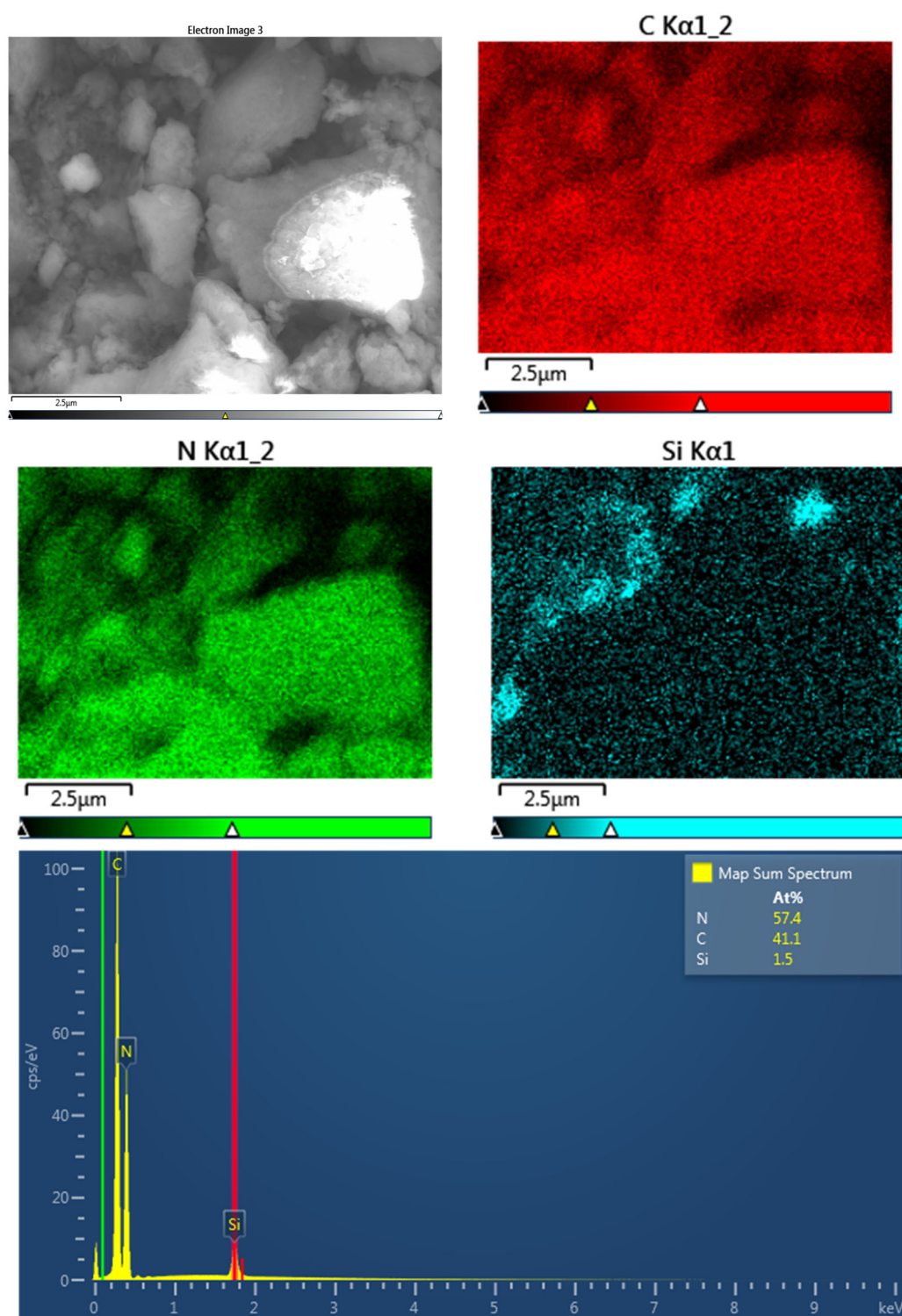
The physicochemical properties of exfoliated g-C<sub>3</sub>N<sub>4</sub> were investigated using EDX to determine the bulk elemental composition, UV-Visible diffuse reflectance spectroscopy to determine the bandgap, X-ray photoelectron spectroscopy (XPS) to

study the elemental composition and electronic states on the surface region, and UV photoelectron spectroscopy (UPS) was used to determine the binding energy of valance band maximum ( $E_{VBM}$ ) with respect to Fermi level and work function ( $\phi_s$ ) of carbon nitride.

#### 5.4.1.1 Elemental mapping by EDX

The elemental compositions of g-C<sub>3</sub>N<sub>4</sub> were explored using EDX and the results are shown in Fig. 5.1. Individual EDX elemental maps revealed a uniform distribution of nitrogen (N) and carbon (C), and no additional peak was found other than Si which came from the substrate, shows the purity of synthesized material. Quantitative analysis of exfoliated g-C<sub>3</sub>N<sub>4</sub> showed that atomic proportion of C and N in prepared sample were 41.4 and 57.4%, respectively which gives the C/N ratio of 0.72. Although true C/N ratio in g-C<sub>3</sub>N<sub>4</sub> is 0.75 which is subject to change with precursor types and reaction conditions.<sup>19</sup> The EDX results were further confirmed by XPS.

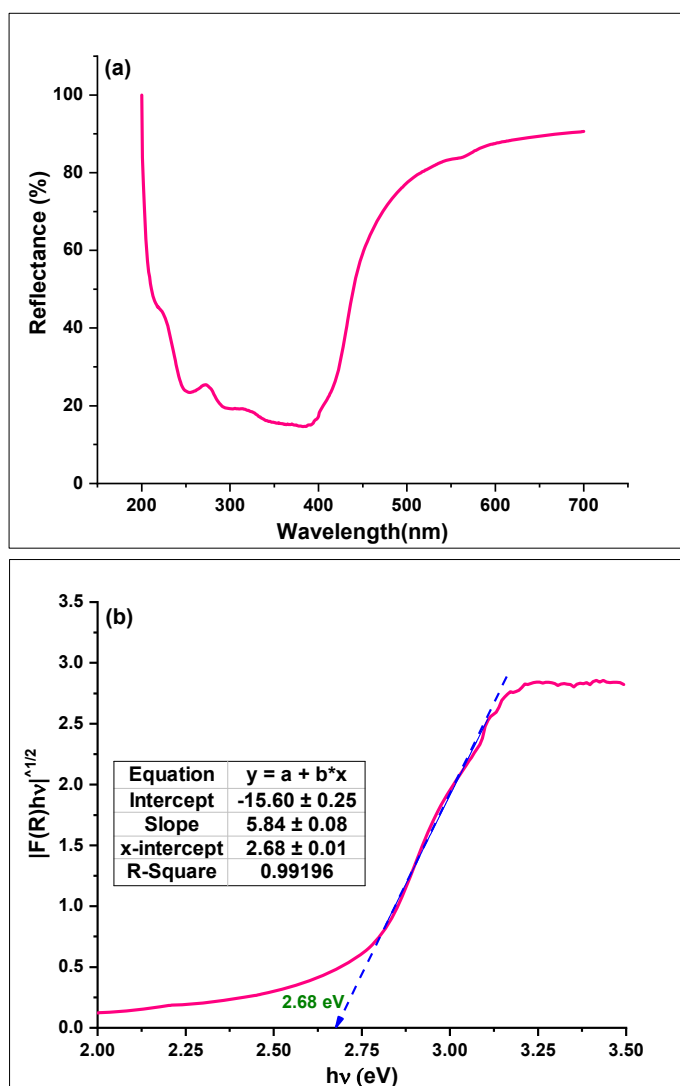




**Fig. 5.1.** (a) FESEM image of exfoliated g-C<sub>3</sub>N<sub>4</sub>, and corresponding EDX elemental mapping for (b) C, (c) N, (d) Si, and (e) EDX spectrum.

### 5.4.1.2 Optical bandgap determination

The optical properties of exfoliated g-C<sub>3</sub>N<sub>4</sub> was studied by UV-Visible diffuse reflectance spectroscopy. The obtained spectrum is shown in Fig. 5.2a and its transformed Tauc plot is shown in Fig. 5.2b. The optical bandgap of exfoliated g-C<sub>3</sub>N<sub>4</sub> was calculated using the K-M function which is used to plot  $(F(R)*hv)^{1/n}$  vs. photon energy ( $hv$ ) graph, where  $F(R)$  is Kubelka-Munk function,  $\nu$  is light frequency and  $n=2$  as g-C<sub>3</sub>N<sub>4</sub> follows indirect absorption. The intercept of the tangents to the plots of  $(F(R)*hv)^{1/n}$  vs. photon energy ( $hv$ ) provides the approximate bandgap of 2.68 eV which is in agreement with the reported literature.



**Fig. 5.2.** (a) UV-Vis diffuse reflectance spectra, and (b) Tauc plots for the band gap energy calculation, for melamine derived exfoliated g-C<sub>3</sub>N<sub>4</sub>

### 5.4.1.3 X-ray photoelectron spectroscopy analysis

The XPS analysis for exfoliated g-C<sub>3</sub>N<sub>4</sub> sample was carried out to examine the elemental composition and electronic states on the surface region. A typical XPS analysis includes a wide energy survey scan (WESS) and a high-resolution scan for each element possibly available in the material. All the scans were performed at minimum four different sites to reduce error in determining the elemental proportion. The typical wide energy survey scan of exfoliated g-C<sub>3</sub>N<sub>4</sub> is shown in Fig. 5.3. All the peaks were calibrated for charge correction with respect to adventitious carbon peak (C 1s at 284.8 eV). The survey spectrum of g-C<sub>3</sub>N<sub>4</sub> contains C 1s, N 1s and O 1s peaks. Atomic percentage of C 1s peak (ca. 43.62%) comprises the adventitious carbon peak at 284.8 eV as well as the other carbon bonding configurations present in g-C<sub>3</sub>N<sub>4</sub>.

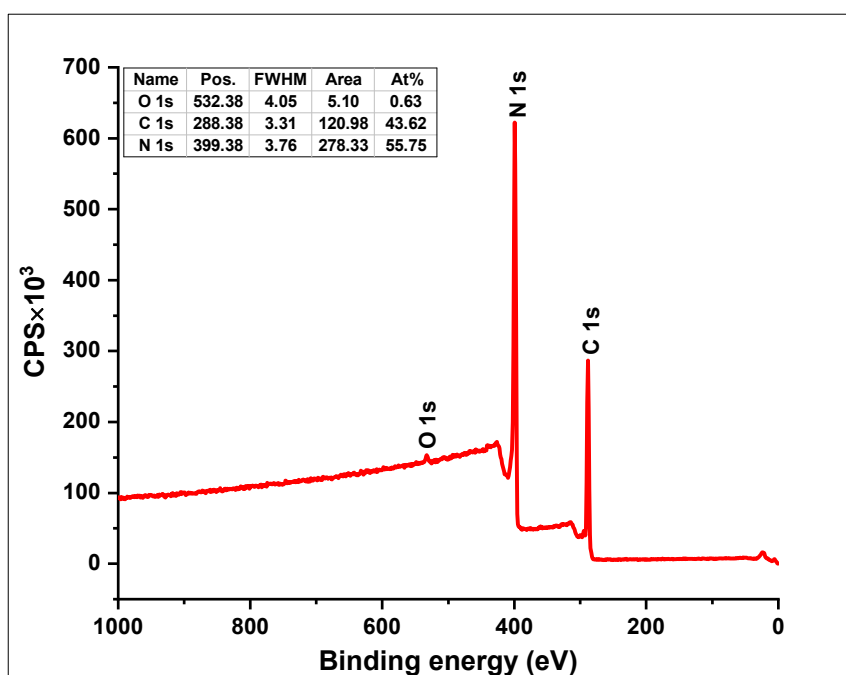
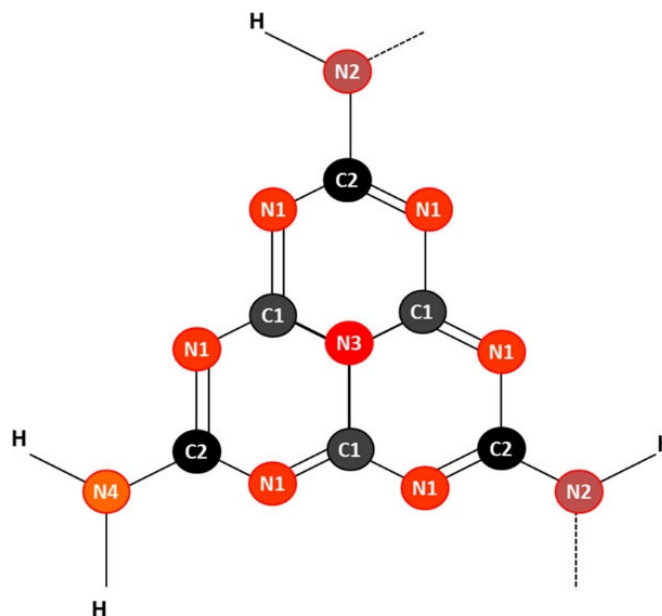


Fig. 5.3. XPS survey spectrum for exfoliated g-C<sub>3</sub>N<sub>4</sub>

Pomilla *et al.* (2018) has well reported the carbon - nitrogen bonding configurations present in g-C<sub>3</sub>N<sub>4</sub> structure. According to them g-C<sub>3</sub>N<sub>4</sub> framework has two bonding configurations for carbon (C1, C2) and four bonding configurations for nitrogen (N1, N2, N3 and N4) which can be represented as C-N1=C (sp<sup>2</sup> hybridized),

N2-H (edge group), N3-C<sub>3</sub> (sp<sup>3</sup> hybridized central nitrogen) and N4-H<sub>2</sub> (terminal group) as shown in Fig. 5.4.<sup>20</sup>



**Fig. 5.4.** Structure of the repeating heptazine carbon nitride unit with the corresponding atomic assignment according to XPS analysis. [Reproduced from Pomilla *et al.*, *J. Phys. Chem. C* 2018, **122**, 28727–28738]<sup>20</sup>

To investigate the above bonding configurations, present in the g-C<sub>3</sub>N<sub>4</sub>, high resolution spectra (also called narrow scan spectra) were obtained for elements C1s, N1s, and O1s in their specific energy regions. After deconvoluting the narrow scan spectrum for each element, the observed binding energy for each bond were at the anticipated positions and in good agreement with the values reported in the literature.<sup>20,21</sup> The high-resolution spectra of C 1s, N 1s and O 1s for exfoliated g-C<sub>3</sub>N<sub>4</sub> are shown in Fig. 5.5-5.7. The C 1s spectrum (Fig. 5.5) splits into four synthetic peaks at binding energies 284.9 eV, 288.1 eV, 288.8 eV, and 293.9 eV which corresponds to adventitious carbon contamination (C-C), C1, C2 and  $\pi$ - $\pi$  interactions, respectively. Similarly, the N 1s spectrum (Fig. 5.6) is incorporated into five peaks at 398.6 eV, 399.3 eV, 400.1 eV, 401.2 eV and 404.5 eV which were assigned to N1, N2, N3, N4 and  $\pi$ - $\pi$  transitions, respectively.

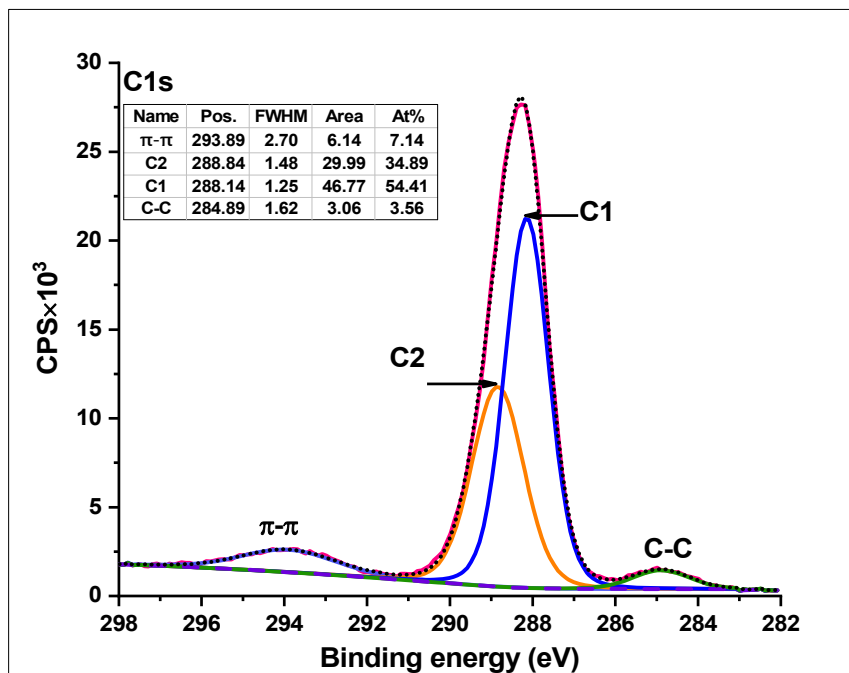


Fig. 5.5. High resolution C 1s spectrum of exfoliated g-C<sub>3</sub>N<sub>4</sub>

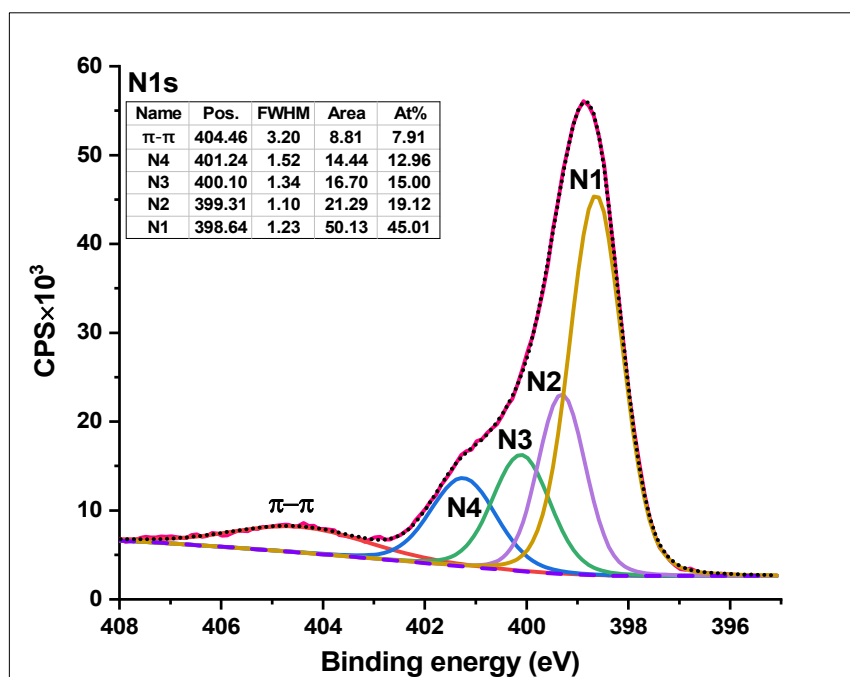


Fig. 5.6. High resolution N 1s spectrum of exfoliated g-C<sub>3</sub>N<sub>4</sub>

O 1s spectrum (Fig. 5.7) shows the presence of low oxygen quantity in sample which may correspond to the adsorbed contaminants such as H<sub>2</sub>O and CO<sub>2</sub>. The C/N ratio obtained by XPS is 0.78 which is little higher side than results obtained from EDX *i.e.*, 0.72 which may attribute to the surface contamination. A similar observation

was also spotted by Hellgren *et al.*<sup>22</sup> that XPS gives higher C/N ratio; 5-20%, than its actual value present in sample. Thus, EDX and XPS results can be justified as comparable with each other and confirm the existence of g-C<sub>3</sub>N<sub>4</sub>. Further details of peak fitting and their characteristic bond are provided in Table 5.2.

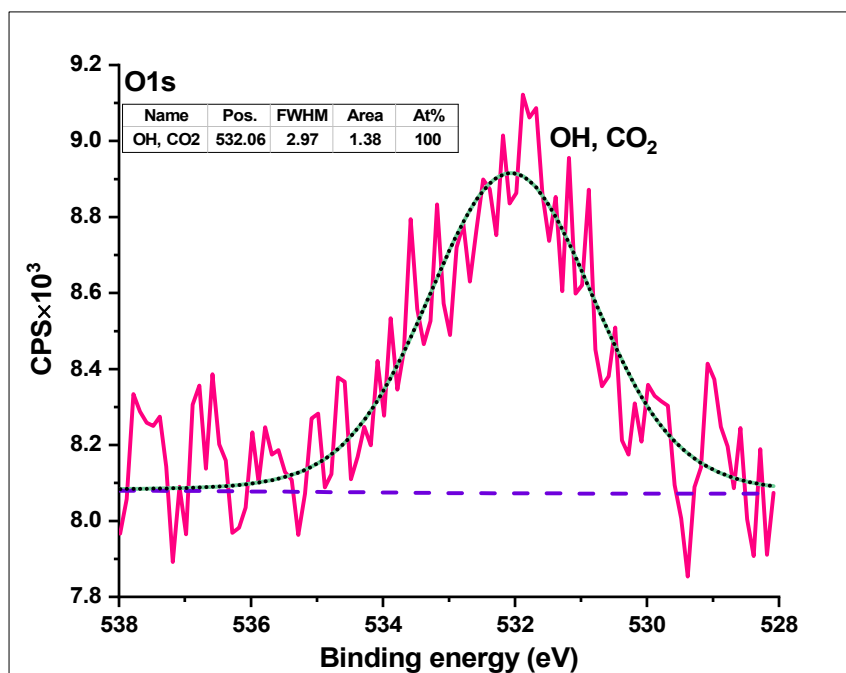


Fig. 5.7. High resolution O 1s spectrum of g-C<sub>3</sub>N<sub>4</sub>

Table 5.2. C, N and O bonding compositions and corresponding binding energies estimated from deconvolution of high-resolution spectrum obtained by XPS

Element state	Binding energies (eV)	Characteristic bond	FWHM	Area	At%
C 1s	293.89	C $\pi$ - $\pi$ transition	2.70	6.14	7.14
	288.84	C2 -heptazine ring	1.48	29.99	34.89
	288.14	C1 -heptazine ring	1.25	46.77	54.41
	284.89	C-C	1.62	3.06	3.56
N 1s	404.46	N $\pi$ - $\pi$ transition	3.20	8.81	7.91
	401.24	N4 (NH <sub>2</sub> )	1.52	14.44	12.96
	400.10	N3 (sp <sup>3</sup> ) N-C <sub>3</sub>	1.34	16.70	15.00
	399.31	N2 (N-H)	1.10	21.29	19.12
	398.64	N1 (C-N=C)	1.23	50.13	45.01
O 1s	532.06	-OH, CO <sub>2</sub>	2.97	1.38	100

#### 5.4.1.4 Band edge positions and work function determination

X-ray and UV photoelectron spectroscopy (XPS and UPS) were used to determine the binding energy of valance band maximum ( $E_{VBM}$ ) with respect to Fermi level and work function ( $\phi_s$ ) of carbon nitride. Fig. 5.8 depicts the valence band XPS spectrum of g-C<sub>3</sub>N<sub>4</sub> obtained from XPS which reveals the VBM position with reference to fermi level ( $E_F - E_{VBM}$ ) of g-C<sub>3</sub>N<sub>4</sub> to be  $1.81 \pm 0.06$  eV which can also be termed as electronic bandgap.<sup>20</sup> With the optical band gap of g-C<sub>3</sub>N<sub>4</sub> derived from DRS (*i.e.*,  $2.68 \pm 0.01$  eV) and the electronic bandgap obtained from XPS, the conduction band minima ( $E_F - E_{CBM}$ ) energy can be calculated using equation (5.1), which equals  $0.87 \pm 0.07$  eV.

$$(E_F - E_{CBM}) = E_g - (E_F - E_{VBM}) \quad (5.1)$$

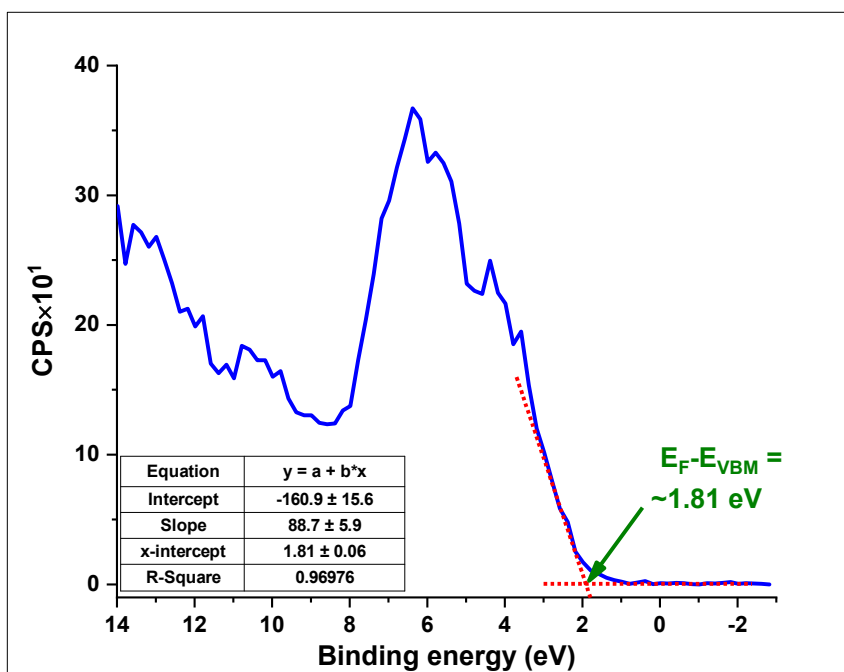


Fig. 5.8. Valence band XPS spectrum of exfoliated g-C<sub>3</sub>N<sub>4</sub>

The band edge energies can also be estimated using the work function. The work function ( $\phi_s$ ) can be defined as the energy barrier to free space that prevents an electron at the Fermi level from escaping the solid or the amount of energy required to escape an electron from the Fermi level into vacuum.<sup>23</sup> To determine the work

function of g-C<sub>3</sub>N<sub>4</sub>, its UPS spectra were collected using a He I emission UV source (21.22 eV). An obtained spectrum is shown in Fig. 5.9. A small bias of 10 V was applied to the sample surface to deconvolute the true work function of the surface from the spectrometer's internal work function.

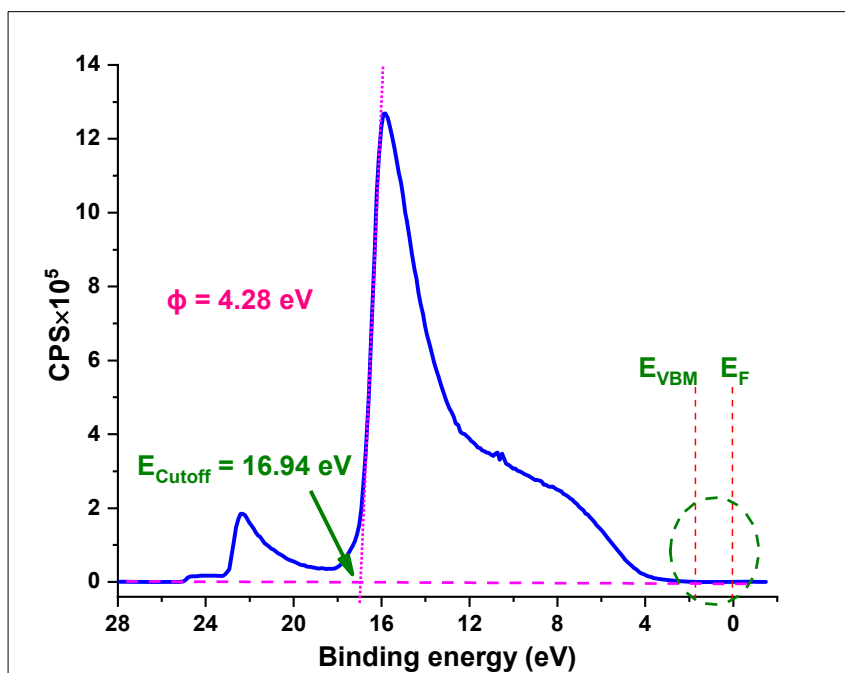


Fig. 5.9. UPS spectrum of exfoliated g-C<sub>3</sub>N<sub>4</sub>

The work function ( $\phi_s$ ) of the sample was calculated by subtracting the characteristic cut-off energy ( $E_{\text{cut-off}}$ ) from the UV source energy (equation 5.2).

$$\Phi_s = h\nu - E_{\text{cut-off}} \quad (5.2)$$

The secondary electron cut-off energy for g-C<sub>3</sub>N<sub>4</sub> is observed to be 16.94 eV derived from UPS spectrum, yielding a work function value of 4.28 eV which is close to reported values 4.0 eV by Mezzi *et al.*<sup>24</sup> and 4.34 eV by Rhimi *et al.*<sup>25</sup> and Liu *et al.*<sup>26</sup> Similar to XPS, the photoelectron intensity onset near the Fermi level, also known as valance band maxima energy ( $E_{\text{VBM}}$ ) with respect to fermi energy, can be determined using UPS measurement as the intersection point between the zero intensity constant backgrounds and a linear extrapolation of the valence band decay,



as shown in Fig. 5.10 and measured to be 1.73 eV which is quite close to the value of  $(E_F - E_{VBM})$  obtained from XPS. However, to avoid ambiguity only the results obtained from UPS analysis will be considered for further interpretation and calculation. As before, the value of  $(E_F - E_{CBM})$  can also be calculated using equation (5.1) which yields a value of 0.95 eV.

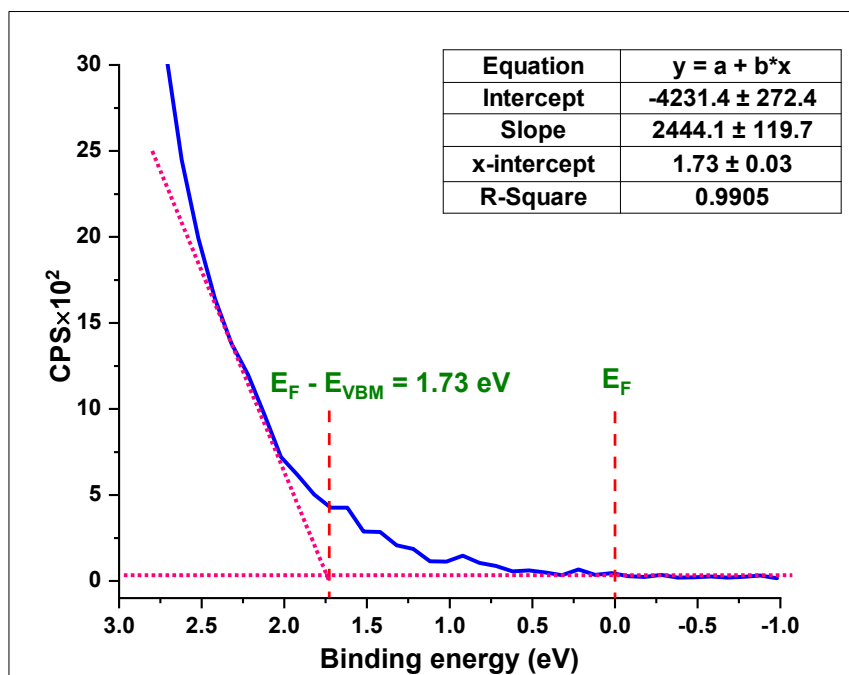


Fig. 5.10. Magnified UPS spectrum of exfoliated  $g\text{-C}_3\text{N}_4$  near valence band region

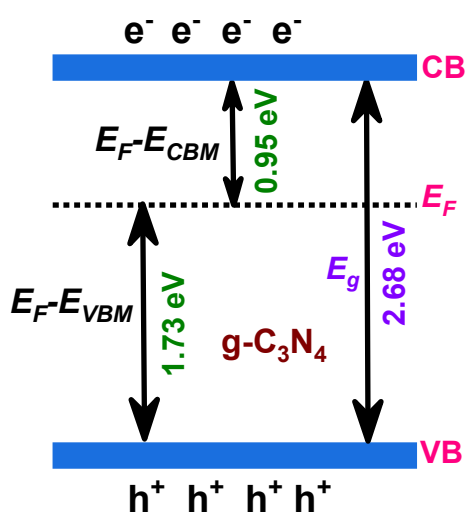


Fig. 5.11 Schematic band diagram for  $g\text{-C}_3\text{N}_4$  showing the position of its Fermi level

The energy difference ( $E_F - E_{VBM} = 1.73$  eV &  $E_F - E_{CBM} = 0.95$  eV) obtained for g-C<sub>3</sub>N<sub>4</sub> suggests that Fermi level for g-C<sub>3</sub>N<sub>4</sub> lies far below the conduction band and far away the valence band as shown in Fig. 5.11. Since the Fermi level is not close enough to either conduction band or valence band, it cannot be called a true either n-type or p-type semiconductor.

Furthermore, the position of  $E_{VBM}$  and  $E_{CBM}$  with respect to vacuum can be estimated with the help of work function using following equations (5.3 and 5.4):

$$E_{VBM} \text{ (vs. vacuum)} = -(\Phi_s + \text{onset}) \quad (5.3)$$

$$E_{CBM} \text{ (vs. vacuum)} = (E_{VBM} + E_g) \quad (5.4)$$

With reference to vacuum, the band edge energies of  $E_{VBM}$  and  $E_{CBM}$  calculated from equations (5.3 and 5.4) are -6.01 and -3.33 eV, respectively which can also be reported on the electrochemical scale relative to NHE which is approximately placed at -4.5 eV (at 298.15 K) with respect to the vacuum level.<sup>27,28</sup> Hence, potentials for g-C<sub>3</sub>N<sub>4</sub> on the NHE scale can be write as +1.51 V (VB edge) and -1.17 V (CB edge).

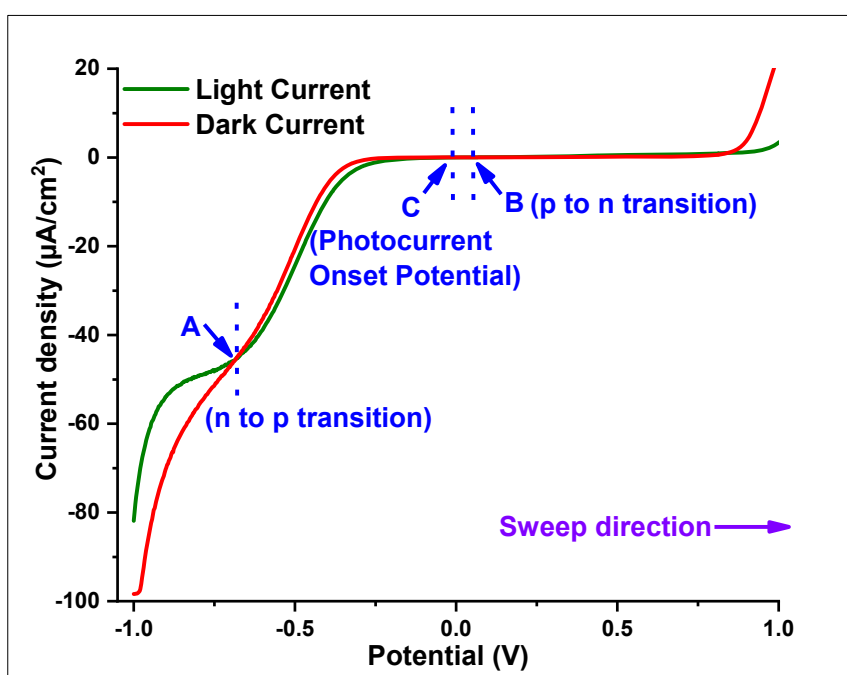
## 5.4.2 Photoelectrochemical measurements

In this section, photoelectrochemical properties of exfoliated g-C<sub>3</sub>N<sub>4</sub> (MCN-exf) sample were investigated by different photoelectrochemical methods to understand how its electronic structure changes when exposed to a redox electrolyte under the action of electromagnetic radiation.

### 5.4.2.1 Linear sweep voltammetry

Linear sweep voltammetry method was carried out in the dark and upon UV-Vis irradiation to measure the photocurrent (type, magnitude) and photocurrent onset potential for working electrode of exfoliated g-C<sub>3</sub>N<sub>4</sub> by varying the applied potential

in the range of -1.0 V to +1.0 V vs. SCE, the resulting current–potential curve, also known as voltammogram is shown in Figs. 5.12-5.16. Exfoliated g-C<sub>3</sub>N<sub>4</sub> electrode generated a very small photocurrent (<1  $\mu\text{A}\cdot\text{cm}^{-2}$ ). Along with the small photocurrent, peculiar behavior was observed in the current-potential response for g-C<sub>3</sub>N<sub>4</sub> electrodes. The photocurrent switching behavior was spotted in the applied potential range which is termed as the PEPS effect (photoelectrochemical photocurrent switching)<sup>29</sup>. It is defined as photocurrent polarity switching in response to changes in photoelectrode potential and/or incident light wavelength. In case of g-C<sub>3</sub>N<sub>4</sub>, we have observed the switching in photocurrent polarity in response to changes only in electrode potential. Some researchers have previously reported the photocurrent switching behavior for g-C<sub>3</sub>N<sub>4</sub>.<sup>30-32</sup>

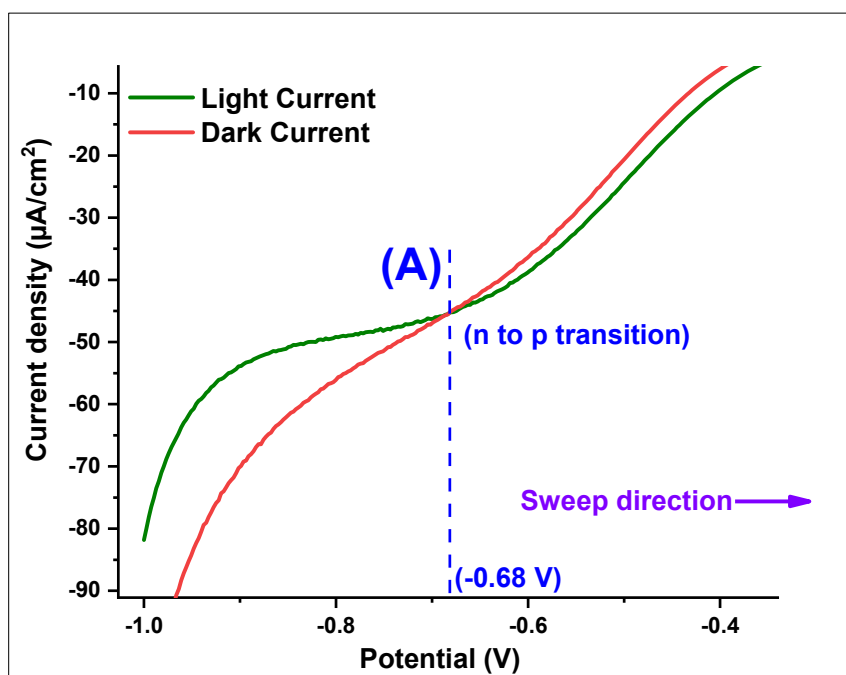


**Fig. 5.12.** LSV of exfoliated g-C<sub>3</sub>N<sub>4</sub> from -1.0 to +1.0 V, Electrolyte 0.1 M KClO<sub>4</sub>, irradiation source 450 W Xe lamp.

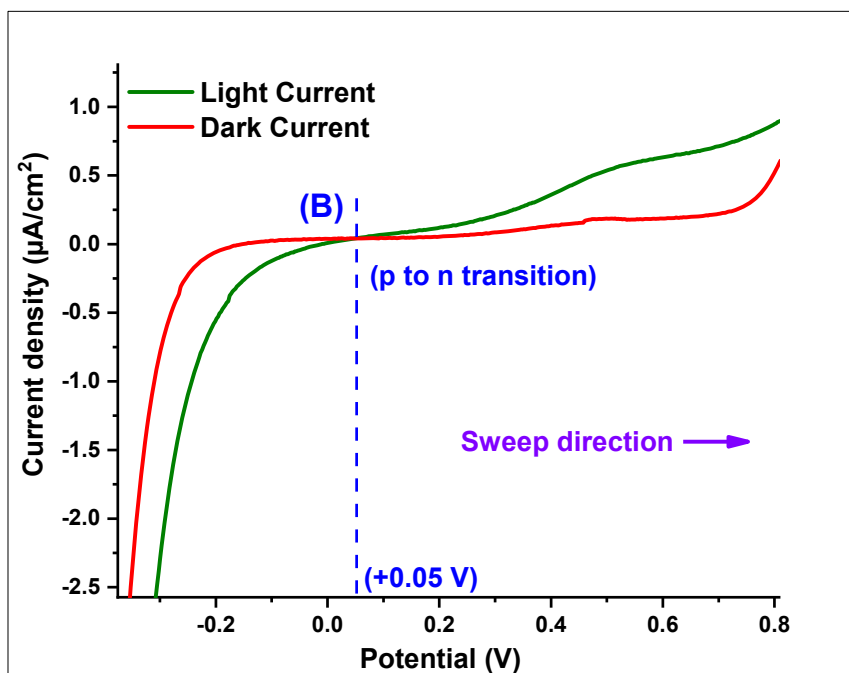
The g-C<sub>3</sub>N<sub>4</sub> photoelectrode showed either cathodic or anodic photocurrents at different range of electrode potential as shown in Fig. 5.12. It was observed that anodic (or positive) photocurrent switched to cathodic (or negative) photocurrent at -0.68 V

(vs. SCE) or  $-0.44$  V (vs. NHE) which again converted to anodic photocurrent at  $+0.05$  V (vs. SCE) or  $+0.29$  V (vs. NHE) with sweeping the bias from  $-1.0$  to  $+1.0$  V. Thus g-C<sub>3</sub>N<sub>4</sub> photoelectrode behaved as a p-type semiconductor in the potential range of  $-0.68$  V to  $+0.05$  V, beyond this region it behaved as n-type semiconductor. Cathodic to anodic photocurrent transition has also been observed by Jing *et al.*<sup>30</sup> at  $0.02$  V (vs. Ag/AgCl) or  $0.22$  V (vs. NHE) which is very close to the value obtained in this work.

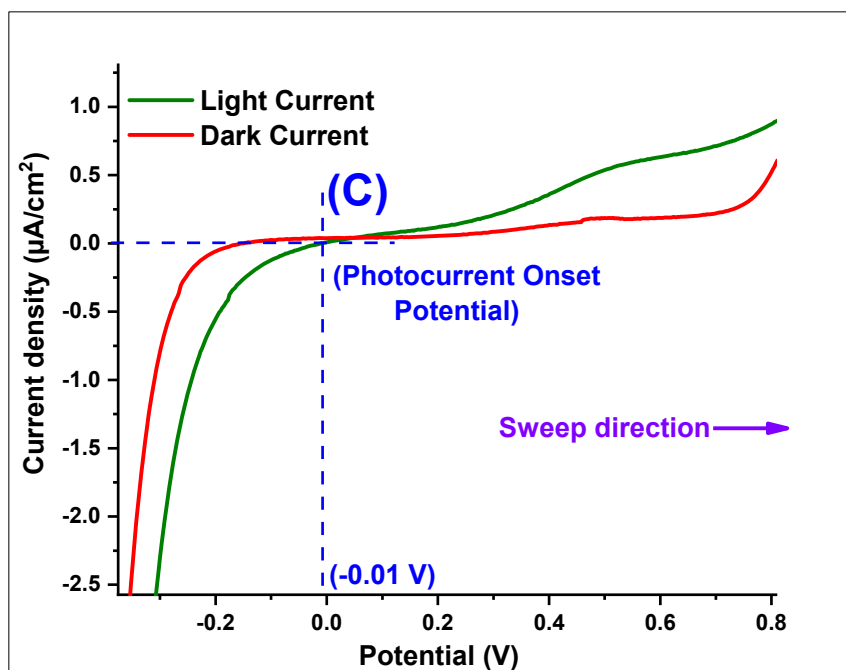
For a better demonstration of the photocurrent switching behavior of g-C<sub>3</sub>N<sub>4</sub>, corresponding regions (A and B) of the LSV plot are magnified in Figs. 5.13 and 5.14. The photocurrent onset potential, the potential beyond which positive current occurs under illumination, is monitored at about  $-0.01$  V (vs. SCE), or  $+0.23$  V (vs. NHE) with sweeping the bias from  $-1.0$  to  $+1.0$  V as demonstrated in Fig. 5.15 which is in close agreement with the value  $0.06$  V (vs. Ag/AgCl) or  $0.26$  V (vs. NHE) reported by Jin *et al.*<sup>33</sup> Fig. 5.16 depicts the recorded chopped voltammogram of g-C<sub>3</sub>N<sub>4</sub> as the applied potential is varied in the range of  $-1.0$  to  $+1.0$  V.



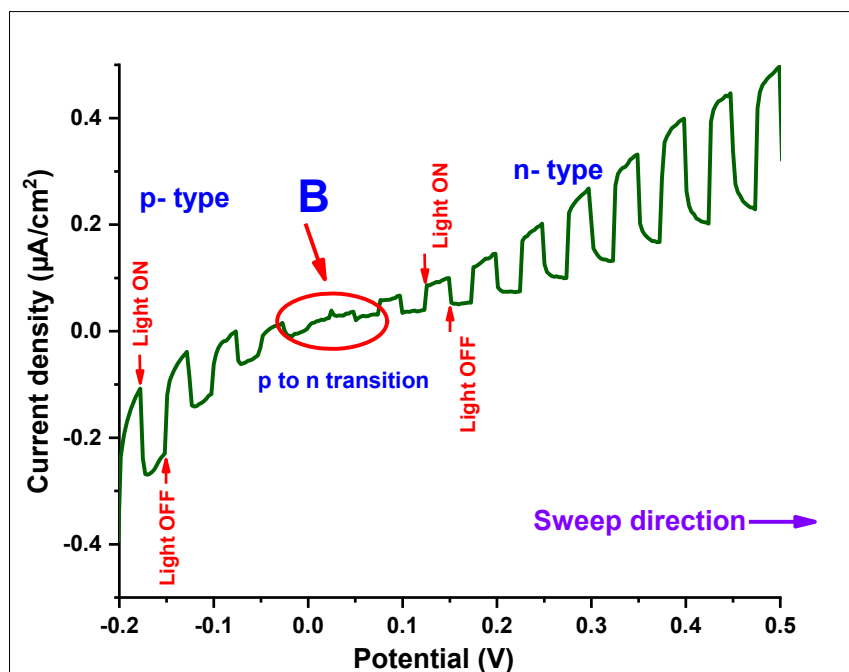
**Fig. 5.13.** Enlarged area A from LSV (Fig. 5.12) of exfoliated g-C<sub>3</sub>N<sub>4</sub>, showing anodic (n-type) to cathodic (p-type) photocurrent transition, Electrolyte  $0.1$  M KClO<sub>4</sub>, irradiation source  $450$  W Xe lamp.



**Fig. 5.14.** Enlarged area B from LSV (Fig. 5.12) of exfoliated  $\text{g-C}_3\text{N}_4$ , showing cathodic (p-type) to anodic (n-type) photocurrent transition, Electrolyte 0.1 M  $\text{KClO}_4$ , irradiation source 450 W Xe lamp.



**Fig. 5.15.** Enlarged area C from LSV (Fig. 5.12) of exfoliated  $\text{g-C}_3\text{N}_4$  showing photocurrent onset potential, Electrolyte 0.1 M  $\text{KClO}_4$ , irradiation source 450 W Xe lamp.

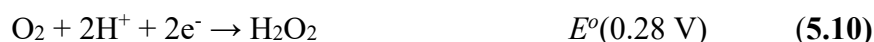
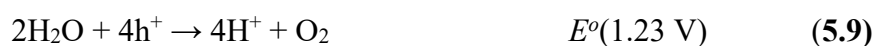
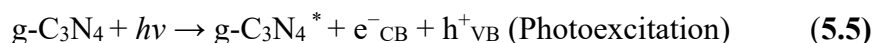


**Fig. 5.16.** Chopped LSV of g-C<sub>3</sub>N<sub>4</sub> (magnified in the range of -0.2 to +0.5 V). Point B showing cathodic (p-type) to anodic (n-type) photocurrent transition. Electrolyte 0.1 M KClO<sub>4</sub>, irradiation source 450 W Xe lamp.

The reasons for photocurrent switching in a photo-electrochemical setup may include several factors, including the band edge potential and redox properties of the semiconductor, the availability of donors and acceptors in the electrolyte, the applied potential, and the wavelength of the incident photon energy.<sup>34,35</sup> In our case, the unbiased Fermi level of g-C<sub>3</sub>N<sub>4</sub> located about in the middle of the forbidden gap (as shown in Fig. 5.11) was thought to be the cause of the dual photocurrent behaviour of g-C<sub>3</sub>N<sub>4</sub>. A photocurrent is produced when the semiconductor is photoexcited with an energy larger than the band gap. Although the direction of photocurrent is determined by the net result of the various redox processes. Anodic (positive) photocurrents are observed when the oxidation reactions predominate at the working electrode, whereas the cathodic (negative) photocurrents require efficient reduction reactions.

Photoexcitation of g-C<sub>3</sub>N<sub>4</sub> directs to a spatial charge separation between the electron in the CB and the hole in the VB. According to the density functional theory

(DFT) calculations revealed by Wang *et al.*,<sup>36</sup> the valence bands (VBs) are composed of nitrogen  $P_z$  orbitals while the conduction bands (CBs) are composed of carbon  $P_z$  orbitals. Therefore, nitrogen provides holes to act as oxidation reaction sites for  $H_2O$  to produce  $O_2$  (oxygen evolution reaction), and carbon offers electrons to work as reduction reaction sites for  $H^+$  to  $H_2$  (hydrogen evolution reaction). CB electrons can also reduce the oxygen into superoxide radicals that may further produce  $H_2O_2$  or  $\cdot OH$  radicals followed by multiple reduction reactions.<sup>36,37</sup> However, Pomilla *et al.*<sup>20</sup> has questioned the stability of  $C_3N_4$  as a photocatalyst. In their experiments, they found the modification of the  $C_3N_4$  structure (photo corrosion) due to the substitution of N with O. The authors suspected that instead of water splitting, photoexcitation causes the oxidation of  $C_3N_4$  itself because the valence band edge of g- $C_3N_4$  (+1.51 V) is close to the water oxidation potential (+1.23 V), and it has a limited overpotential to drive water oxidation reaction. This it may accumulate intermediate reactive oxygen species that could lead the oxidation of  $C_3N_4$  by substituting N with O. Based on VB and CB edge potentials, the following electrochemical or photoelectrochemical oxidation and reduction reactions may possibly undergone in this photoelectrochemical setup:



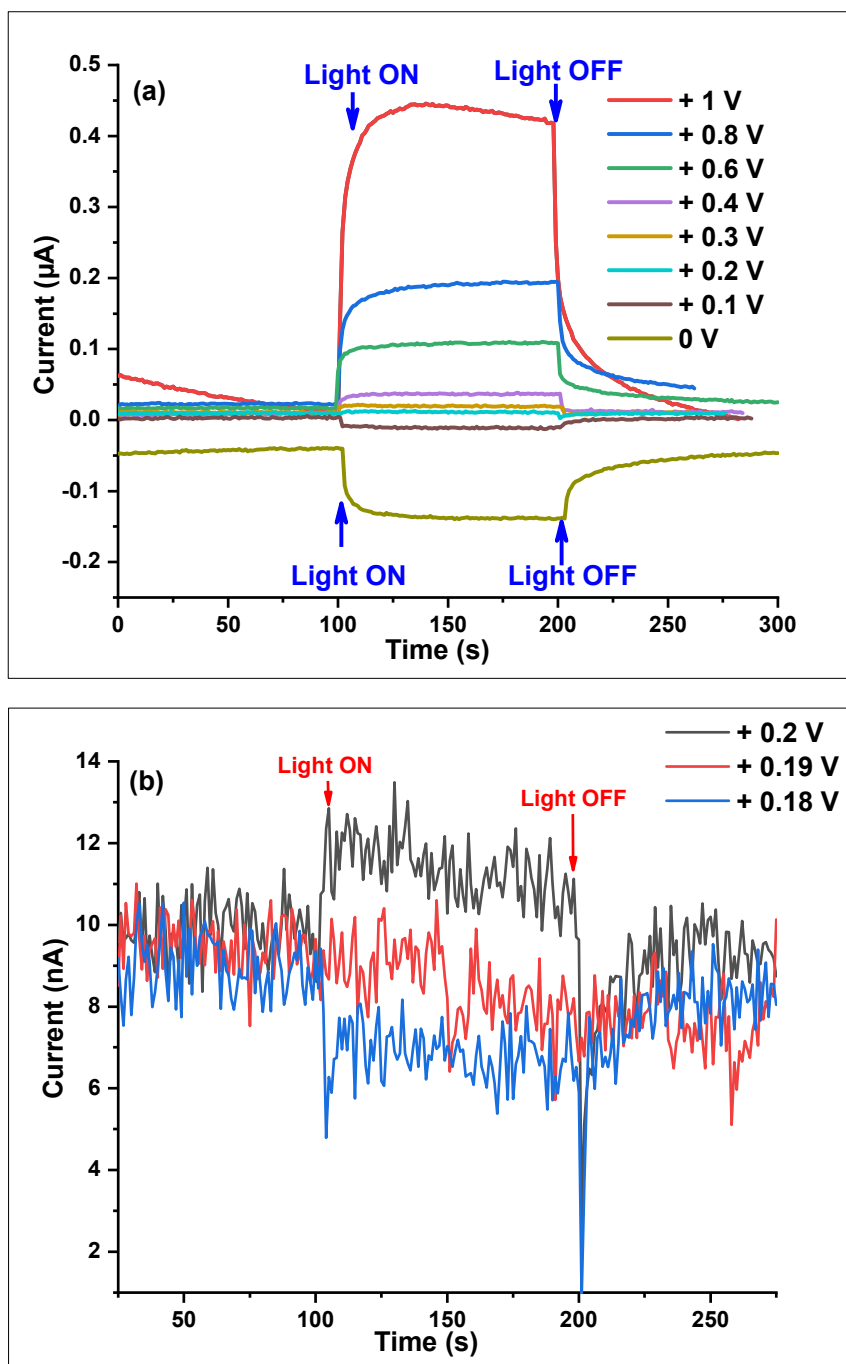
Linear sweep voltammetry is a quick way to determine the photocurrent component of materials. However, photocurrent measured by linear sweep voltammetry contains both Faradaic and capacitive components. As a result, chronoamperometry measurements (current-time responses at fixed potential) are required to separate capacitive and Faradaic components.

#### 5.4.2.2 Chronoamperometry

The photocurrent - time response was recorded on applying fixed potentials from the range of 0.0 V to +1.0 V and demonstrated in Fig. 5.17a and b.

The photocurrent was measured for 100 s at every applied potential. The anodic photocurrent was observed up to +0.2 V on applying fixed potential from the range of +1.0 to +0.2 V which is a characteristic of an n-type semiconductor while photocurrent switched to cathodic photocurrent at near +0.2 V (+0.18 V as shown in Fig. 5.17 b) which is a characteristic of a p-type semiconductor. These results are consistent with the outcomes obtained from linear sweep voltammetry and gives the double confirmation to the dual photocurrent behaviour of g-C<sub>3</sub>N<sub>4</sub> depending on potential range. Although the switching potential obtained from chronoamperometry (+0.18 V), is higher than the potential value obtained from LSV (+0.05 V).



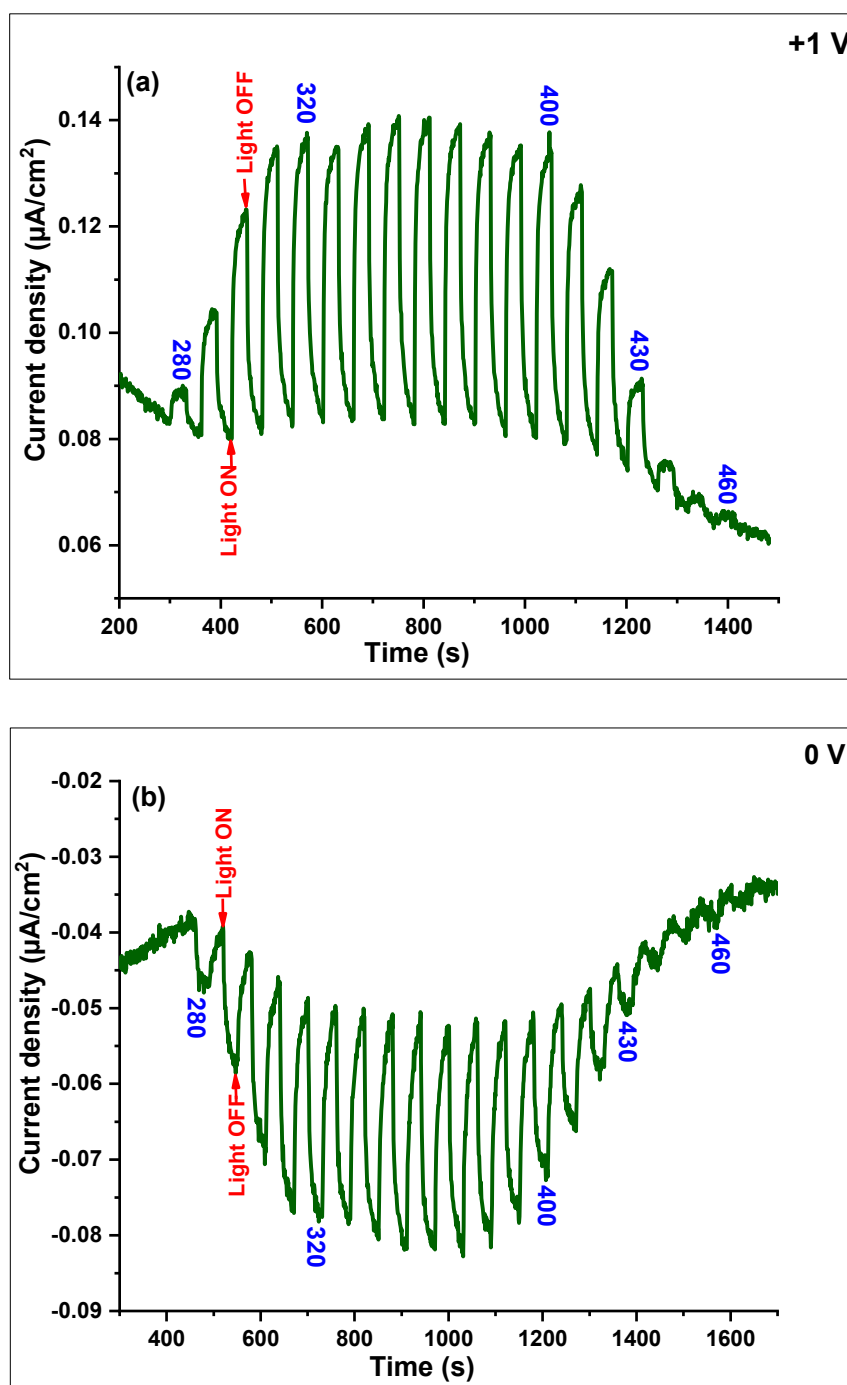


**Fig. 5.17.** Photocurrent response for exfoliated g-C<sub>3</sub>N<sub>4</sub> at various potentials (a) ranging from 0.0 V to 1.0 V, and (b) showing photocurrent transition potential. Electrolyte 0.1 M KClO<sub>4</sub>, irradiation source 450 W Xe lamp

### 5.4.2.3 Spectral photocurrent response

As stated earlier that photoelectrochemical photocurrent switching can be in response to changes in photoelectrode potential and/or incident light wavelength. To confirm this, the spectral response of g-C<sub>3</sub>N<sub>4</sub> were measured at applied voltage of +1.0

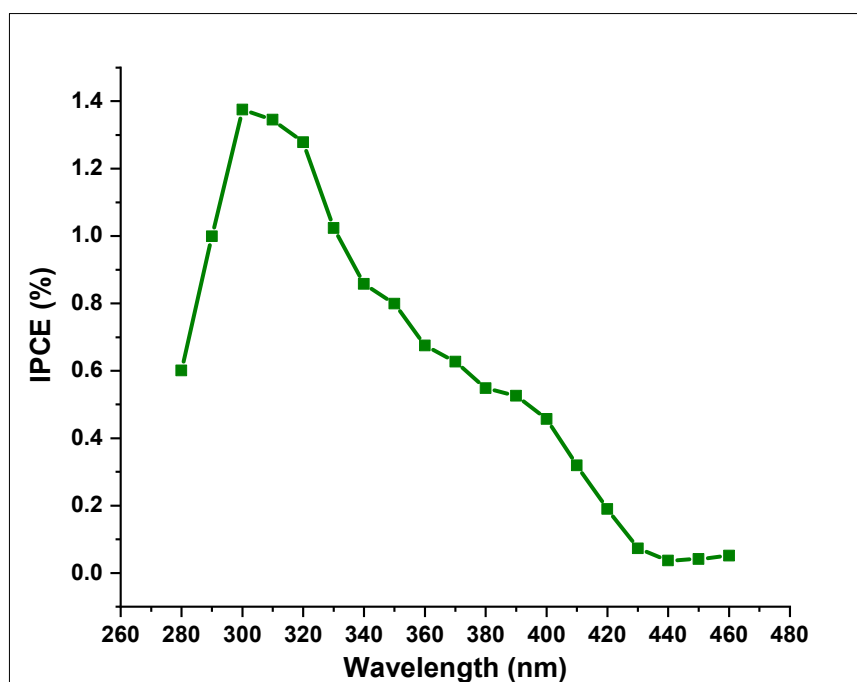
V (SCE) and 0.0 V (SCE) while varying the wavelength of the incident irradiation from 280 to 480 nm at 10 nm periods and obtained results are shown in Figs. 5.18a-b.



**Fig. 5.18.** Spectral response for exfoliated g-C<sub>3</sub>N<sub>4</sub> measured at (a) +1 V, and (b) 0 V varying the incident irradiation wavelength from 280 to 460 nm at 10 nm periods and 30 s exposure-delay cycle. The blue numbers indicate the wavelength of irradiation at which photocurrent is measured. Electrolyte 0.1 M KClO<sub>4</sub>, irradiation source 450 W Xe lamp.

It is clear from Fig. 5.18 that g-C<sub>3</sub>N<sub>4</sub> showed the switching in photocurrent polarity in response to changes only in electrode potential and that the switching was not dependent on the incident irradiation wavelength. The photocurrent response of g-C<sub>3</sub>N<sub>4</sub> photoelectrode was measurable up to 460 nm, which corresponds to an effective bandgap of 2.7 eV. Action spectra recorded anodic photocurrent at +1.0 V whereas at 0.0 V it was cathodic photocurrent which again approve the results obtained from LSV and chronoamperometry and gives the third confirmation to the dual photocurrent behaviour of g-C<sub>3</sub>N<sub>4</sub> in response to changes only in photoelectrode potential.

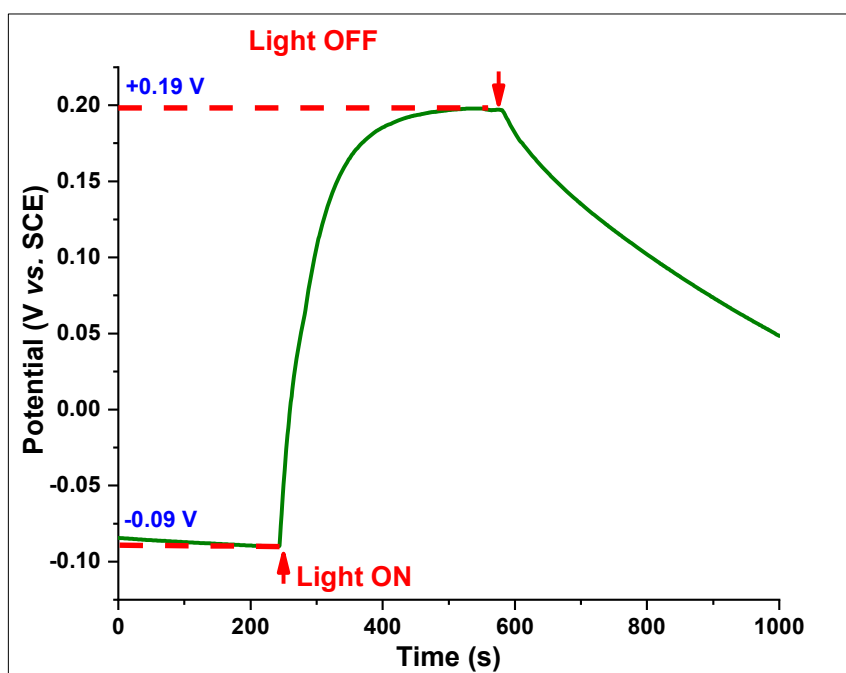
The obtained spectral wavelength versus photocurrent data at +1 V was used to calculate the incident photon-to-current conversion efficiency (IPCE) for C<sub>3</sub>N<sub>4</sub>. IPCE was calculated from spectral photocurrent response obtained in the wavelength range of 250-460 nm using equation 3.4. A plot of the incident spectral irradiances vs. wavelengths for 450 W Xe lamp is given chapter 3. Fig. 5.19 shows the IPCE plot as a function of wavelength.



**Fig. 5.19.** IPCE (%) for exfoliated g-C<sub>3</sub>N<sub>4</sub> plotted as a function of wavelength

#### 5.4.2.4 Open-circuit potential ( $E_{ocp}$ ) and Open circuit Photopotential ( $E_{oph}$ )

The open circuit potential (OCP), also known as the rest potential of an electrode, is the potential of an electrode that is not electrically connected to any other conducting materials, thus there is no net current at OCP conditions. In other words, the OCP is the measure of electrolyte redox potential or Fermi level in the equilibrium. When an electrode is irradiated at the open-circuit potential condition, there is a change in potential due to electron-hole pairs generation which continues until the rates of hole and electron transfer equalize, this new equilibrium upon illumination is referred to as quasi-Fermi level. The difference between illuminated quasi-Fermi level and dark Fermi level is named as open circuit photopotential<sup>38</sup>. Fig. 5.20 depicts the open-circuit potential for g-C<sub>3</sub>N<sub>4</sub> under dark and illumination.



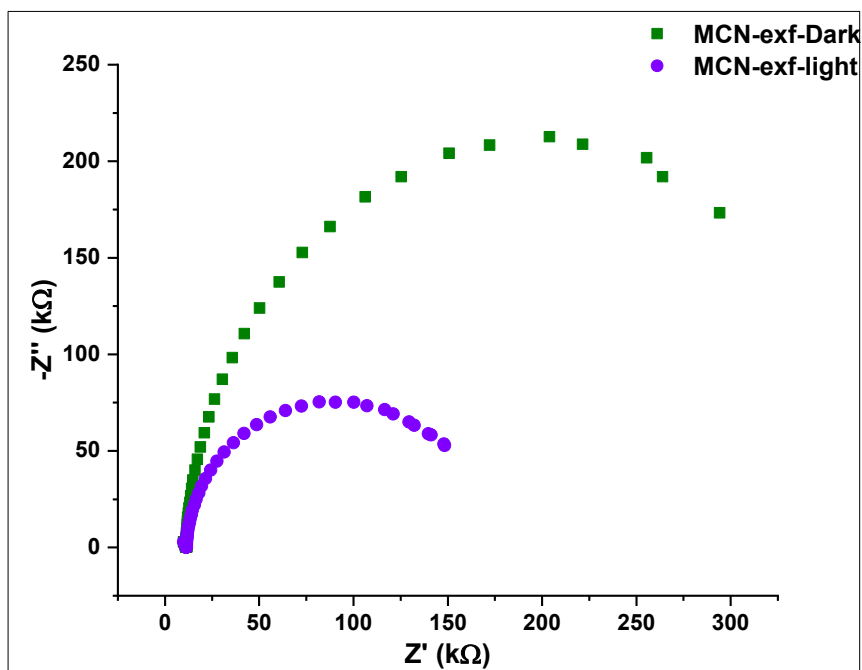
**Fig. 5.20.** Open circuit potential for exfoliated g-C<sub>3</sub>N<sub>4</sub> under dark and UV-vis irradiation. electrolyte 0.1 M KClO<sub>4</sub>, irradiation source 450 W Xe lamp.

In dark equilibrium, g-C<sub>3</sub>N<sub>4</sub> electrode has  $E_{ocp}$  value around -0.09 V (SCE). when the electrode was irradiated, the  $E_{ocp}$  value shifted towards positive values,

around +0.19 V (SCE), which indicated that the measured electrode is a p-type semiconductor. It has already been seen in the results of linear sweep voltammetry and chronoamperometry that g-C<sub>3</sub>N<sub>4</sub> behaves as a p-type semiconductor near potential of OCP value. The observed positive shift of 0.28 V is the result of electron-hole pairs generation upon irradiation, although it can be seen in Fig. 5.20 that change in open circuit potential is very slow which indicates the slow charge separation and high surface recombination which is the sufficient reason behind poor photocatalytic activity of g-C<sub>3</sub>N<sub>4</sub>.

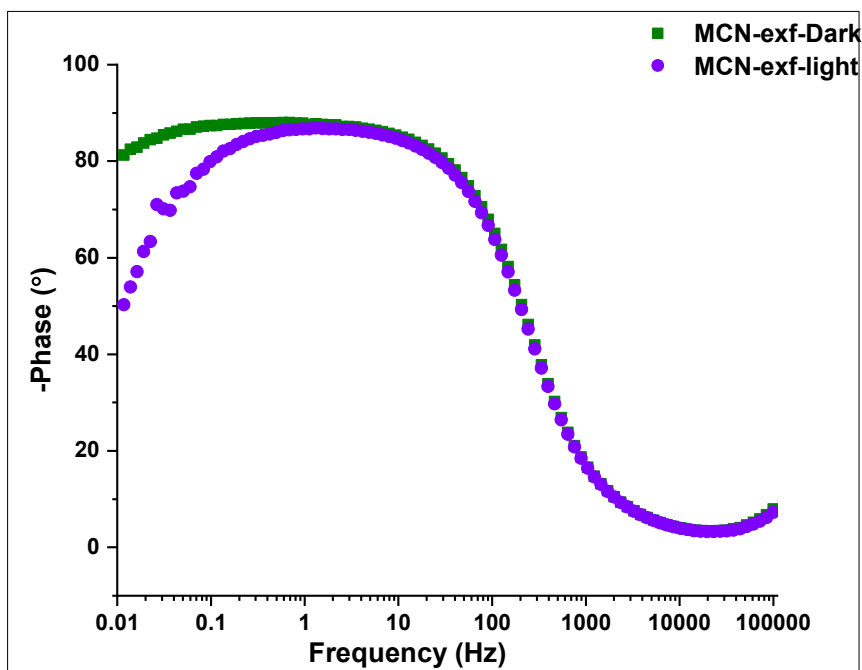
#### 5.4.2.5 Electrochemical impedance spectroscopy

To investigate the excitation and transfer of photogenerated charge carriers, electrochemical impedance spectroscopy (EIS) was performed on exfoliated g-C<sub>3</sub>N<sub>4</sub> photoelectrode. The EIS measurements were carried out at open circuit potential *i.e.*, -0.09 V (*vs.* SCE) as a set potential, 10 mV AC amplitude, the frequency range of 10 mHz to 100 kHz, a logarithmic frequency step and a single sine wave type. The obtained results can be represented as Nyquist plot (Fig. 5.21) and Bode plot (Fig. 5.22). A Nyquist plot gives information about the charge transfer resistance at the electrode/electrolyte interface which is equal to the diameter of the semi-circle in the Nyquist plot. Therefore, a smaller diameter represents less resistance implying more conductive material.<sup>39,40</sup> Fig. 5.21 demonstrates the Nyquist plot for the prepared exfoliated g-C<sub>3</sub>N<sub>4</sub> sample obtained under dark and UV-Vis irradiation conditions. It is evident that after irradiation, the resistance of the g-C<sub>3</sub>N<sub>4</sub> electrode is reduced (smaller diameter) compared to the resistance of dark condition (larger diameter) suggesting improved electron transfer process.<sup>41</sup>

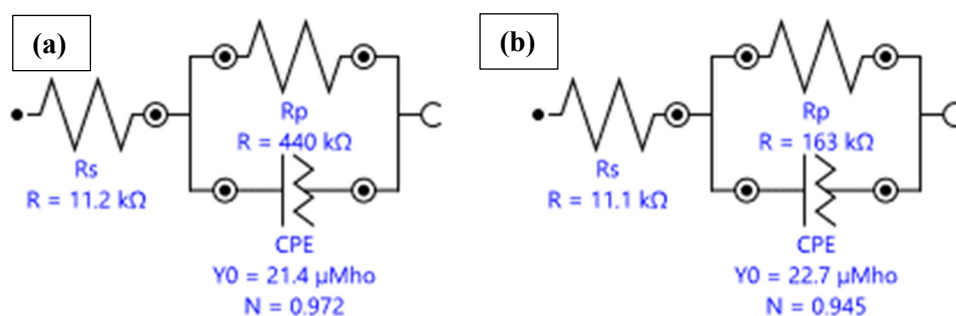


**Fig. 5.21.** The EIS Nyquist plot for exfoliated  $g\text{-C}_3\text{N}_4$  measured at OCP = -0.09 V under dark and UV-vis irradiation. AC amplitude = 10 mV, frequency range of 10 mHz to 100 kHz, electrolyte 0.1 M  $\text{KClO}_4$ , irradiation source 450 W Xe lamp.

Further, to calculate the value of resistance, the EIS Nyquist plot was fitted and simulated using Nova software (version 1.11) using  $[\text{R}(\text{RQ})]$  circuit model, which includes electrolyte solution resistance ( $R_s$ ), charge transfer resistance ( $R_{\text{ct}}$  or  $R_p$ ) and electrochemical double-layer capacitance ( $Q$ ).<sup>40,42</sup> The Nyquist plot was well fitted with  $[\text{R}(\text{RQ})]$  circuit model, indicating that it was a legitimate circuit model. The resulting electrochemical equivalent circuit is displayed in Fig. 5.23a and b, which reveals that upon light irradiation, the charge separation resistance of exfoliated  $g\text{-C}_3\text{N}_4$  electrode was reduced from 440  $\text{k}\Omega$  in the dark condition to 163  $\text{k}\Omega$  which leads to better separation of the  $e^-h^+$  pairs and improved interfacial charge transfer.<sup>39</sup> However even upon irradiation, the charge separation resistance is very high which restricts the separation and migration of charge carriers, resulting in small photocurrent and poor photocatalytic activity of  $g\text{-C}_3\text{N}_4$ .



**Fig. 5.22** The EIS Bode phase plot for exfoliated  $g\text{-C}_3\text{N}_4$  measured at OCP = -0.09 V under dark and UV-vis irradiation. AC amplitude = 10 mV, frequency range of 10 mHz to 100 kHz, electrolyte 0.1 M  $\text{KClO}_4$ , irradiation source 450 W Xe lamp.



**Fig. 5.23** The electrochemical equivalent circuit obtained after simulating impedance data for exfoliated  $g\text{-C}_3\text{N}_4$  (a) in dark, and (b) UV-Vis irradiation

Furthermore, the EIS Bode phase plot can be used to estimate the electron lifetime ( $\tau$ ) with the help of equation (5.12).<sup>39,41</sup>

$$\tau \approx \frac{1}{2\pi f} \quad (5.12)$$

where  $f$  is the characteristic peak frequency, Fig. 5.22 shows that the characteristic peak frequency for  $g\text{-C}_3\text{N}_4$  shifts from lower frequency (0.59 Hz) to higher frequency (1.56 Hz) upon irradiation. From the equation (5.5), the electron lifetime ( $\tau$ ) of the

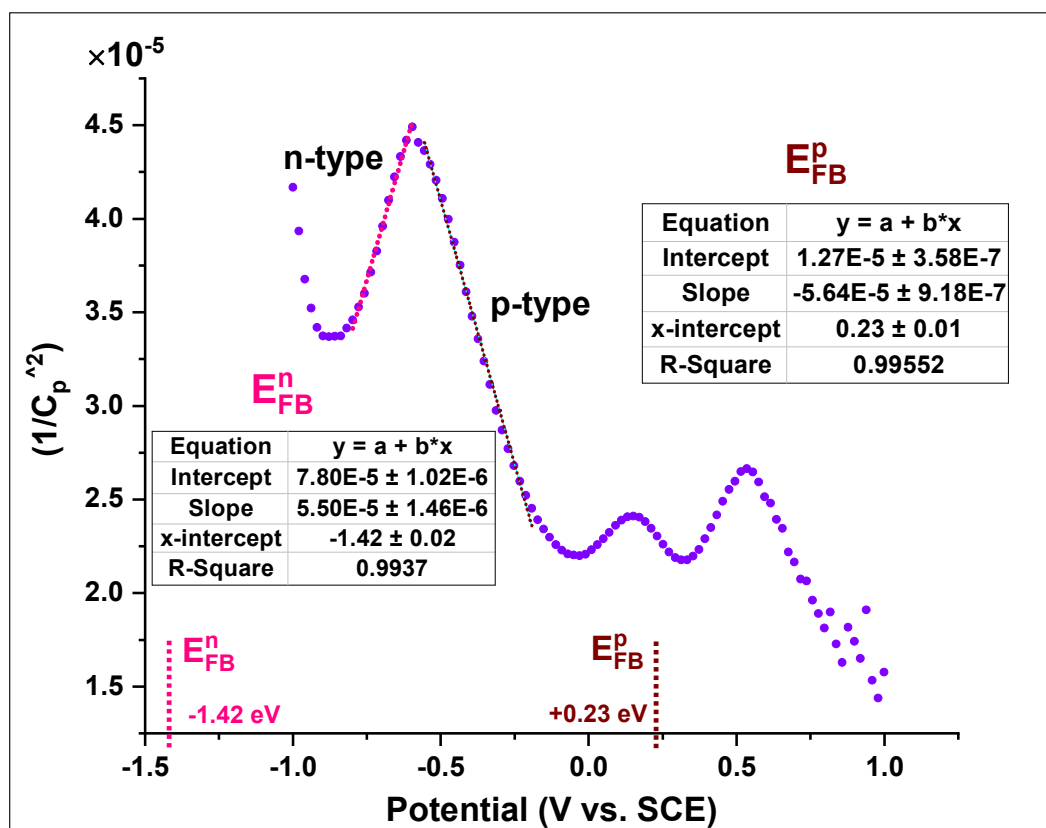
exfoliated g-C<sub>3</sub>N<sub>4</sub> was reduced to be 102 ms (in light) from 270 ms (in dark) indicating increase in charge recombination, hence poor photocatalytic activity. Thus, it can be concluded from EIS measurements that high charge transfer resistance and rapid recombination are the primary reason behind poor photocatalytic activity of g-C<sub>3</sub>N<sub>4</sub>.

#### 5.4.2.6 Mott-Schottky analysis

The Mott-Schottky analysis was employed to estimate the flat band potential and nature of exfoliated g-C<sub>3</sub>N<sub>4</sub>. The flat band potential provides the precise position of conduction band edge for a semiconductor. A frequency response analysis (FRA) potential scan was carried out in the dark at OCP = -0.09 V as the set potential, in the potential range of -1.0 to +1.0 V with step potential of 0.02 V at a frequency of 1 Hz and single sinusoidal 10 mV AC voltage as the root mean square (RMS) value to obtain Mott-Schottky (M-S) plot, as shown in Fig. 5.24. The flat band potential was computed from the intercept of linear part of the Rs-Cp/Rp Mott-Schottky plot to the potential axis. The M-S plot for exfoliated g-C<sub>3</sub>N<sub>4</sub> shows both positive and negative slope, confirming the amphoteric nature of g-C<sub>3</sub>N<sub>4</sub> which is consistent with the voltametric and chronoamperometric results.

Extrapolating the positive slope ( $1/C_p^2 = 0$ ) of the M-S plot returned a flat band potential ( $E_{FB}^n$ ) of -1.42 V (SCE) or -1.18 V (NHE) indicating that it is an n-type semiconductor, whereas extrapolating the negative slope ( $1/C_p^2 = 0$ ) of the M-S plot yielded a flat band potential ( $E_{FB}^p$ ) of +0.23 V (SCE) or +0.47 V (NHE) implies to be a p-type semiconductor. The obtained flat band potential ( $E_{FB}^n$ ), *i.e.*, -1.18 V (*vs.* NHE) from the M-S plot is similar to the CB edge, *i.e.*, -1.17 V (*vs.* NHE) obtained from XPS and UPS results.

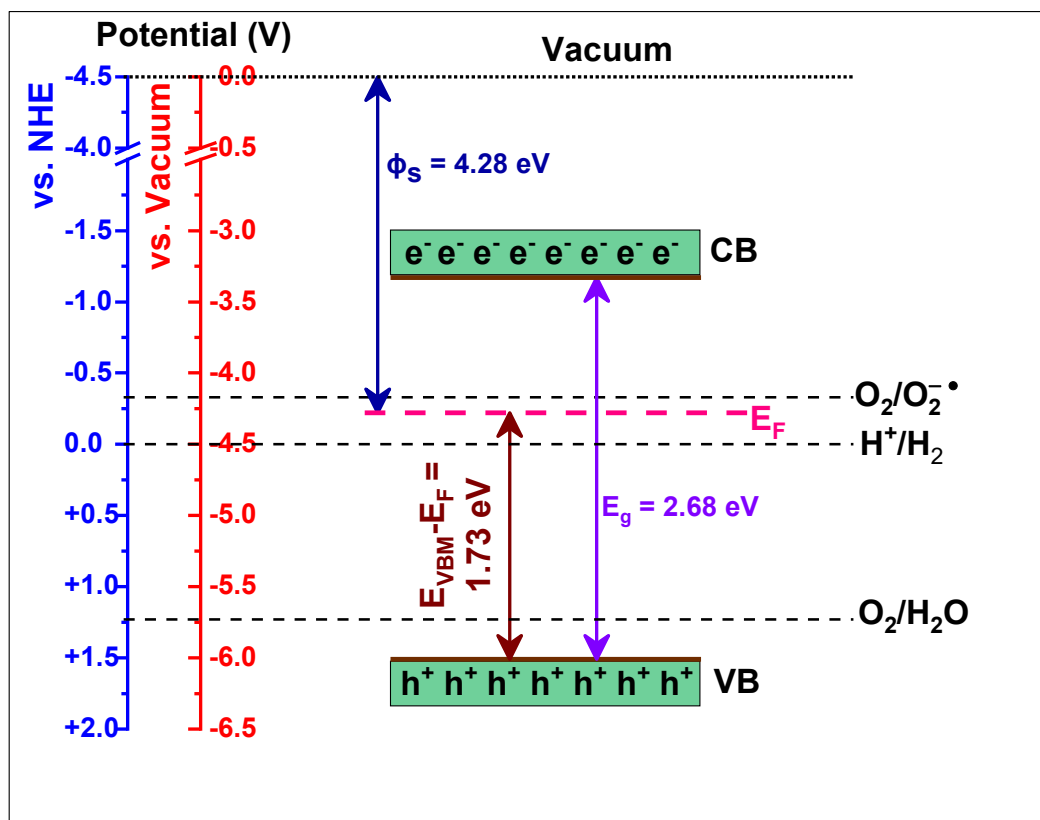




**Figure 5.24** Mott-Schottky plot for exfoliated g-C<sub>3</sub>N<sub>4</sub> sample in the potential range of -1.0 to +1.0 V, step potential 0.02V, Electrolyte 0.1 M KClO<sub>4</sub> (pH = 6)

### 5.4.3 A proposed energy band diagram

A schematic energy level diagram of the exfoliated g-C<sub>3</sub>N<sub>4</sub> based on obtained results from DRS, VBXPS, UPS and photoelectrochemical measurements is proposed here in Fig. 5.25 at vacuum and NHE scale. Optical bandgap of exfoliated g-C<sub>3</sub>N<sub>4</sub> was determined to be 2.68 eV by DRS and from the VBXPS and UPS results, we obtained band edge energies of g-C<sub>3</sub>N<sub>4</sub> as -6.01 eV ( $E_{VBM}$ ) and -3.33 eV ( $E_{CBM}$ ) with reference to vacuum which turns to +1.51 V (VB edge) and -1.17 V (CB edge) on the NHE scale. The flat band potential obtained from Mott-Schottky analysis also justifies these energy levels.



**Fig. 5.25.** Schematic energy band diagram of g-C<sub>3</sub>N<sub>4</sub> derived from DRS, VBXPS and UPS measurements

In a semiconductor, The Fermi level refers to the probability of occupying energy levels in the valence and conduction bands. An intrinsic semiconductor acts as a perfect insulator at absolute zero temperature (0 K). For an intrinsic semiconductor the Fermi level is positioned in the middle of forbidden band whereas for an n-type semiconductor, the Fermi level lies just below the conduction band and for p-type semiconductor, the Fermi level is just above the valence band.

However, in accordance with the UPS results obtained in our study, the energy difference ( $E_F - E_{VBM} = 1.73$  eV &  $E_F - E_{CBM} = 0.95$  eV) obtained for g-C<sub>3</sub>N<sub>4</sub> suggests that Fermi level for g-C<sub>3</sub>N<sub>4</sub> lies far below the conduction band and far away the valence band. Since the Fermi level is not close enough to either conduction band or valence band, it cannot be called a true either n-type or p-type semiconductor. However, g-C<sub>3</sub>N<sub>4</sub> is widely considered to be an n-type semiconductor because of

positive slope demonstrated in Mott Schottky plots<sup>43,44</sup>. In the present work, the Mott-Schottky plot also suggested the amphoteric behaviour of g-C<sub>3</sub>N<sub>4</sub> due to existence of both positive and negative slope. Therefore, it can be concluded that g-C<sub>3</sub>N<sub>4</sub> is behaving as an intrinsic semiconductor because its Fermi level is placed in approximately middle of the forbidden gap which results in poor photocatalytic activities.

## 5.5 Conclusions

In summary, the poor photocatalytic performance of exfoliated g-C<sub>3</sub>N<sub>4</sub> was investigated through its physiochemical properties, *i.e.*, bandgap energy, band edge positions, work function, photocurrent, open circuit photopotential, and flat band potential, *etc.* EDX analysis revealed the C/N ratio to be 0.72 in sample matrix and a uniform distribution of nitrogen (N) and carbon (C) also indicated the purity of synthesized material. Using the bandgap energy (2.68 eV) obtained from Tauc plot and the work function (4.28 eV) obtained from UPS study, the band edge energies for g-C<sub>3</sub>N<sub>4</sub> on the NHE scale was calculated to be +1.51 V (VB edge) and -1.17 V (CB edge). The analysis of UPS results also showed that Fermi level of g-C<sub>3</sub>N<sub>4</sub> is approximately in the middle of the forbidden gap, indicating that it behaves as an intrinsic semiconductor.

A very small photocurrent and photoelectrochemical photocurrent switching (PEPS) effect was observed in photoelectrochemical results. Although further research is needed to determine what is truly happening in this photoelectrochemical system and source of anodic and cathodic current. The very slow change in open circuit potential indicated the slow charge separation and high surface recombination. Electrochemical impedance spectroscopy (EIS) results exhibited the high charge

transfer resistance which inhibits the separation and migration of  $e^-$ - $h^+$  pairs. Existence of both positive and negative slope in the M-S plot confirms the amphoteric nature of g-C<sub>3</sub>N<sub>4</sub>. Hence, position of Fermi level, slow change in open circuit potential and high charge transfer resistance restricts the separation and migration of charge carriers, resulting in small photocurrent and poor photocatalytic activity of g-C<sub>3</sub>N<sub>4</sub>.

## 5.6 References

1. Zhao, H., Yu, H., Quan, X., Chen, S., Zhang, Y., Zhao, H., & Wang, H. Fabrication of atomic single layer graphitic-C<sub>3</sub>N<sub>4</sub> and its high performance of photocatalytic disinfection under visible light irradiation. *Appl. Catal. B Environ.* 2014, **152–153**, 46–50.
2. Lee, S. C., Lintang, H. O. & Yuliati, L. A Urea Precursor to Synthesize Carbon Nitride with Mesoporosity for Enhanced Activity in the Photocatalytic Removal of Phenol. *Chem. - An Asian J.* 2012, **7**, 2139–2144.
3. Huang, J., Ho, W. & Wang, X. Metal-free disinfection effects induced by graphitic carbon nitride polymers under visible light illumination. *Chem. Commun.* 2014, **50**, 4338.
4. Thurston, J. H., Hunter, N. M., Wayment, L. J. & Cornell, K. A. Urea-derived graphitic carbon nitride (u-g-C<sub>3</sub>N<sub>4</sub>) films with highly enhanced antimicrobial and sporicidal activity. *J. Colloid Interface Sci.* 2017, **505**, 910–918.
5. Yang, Z., Li, L., Yu, H., Liu, M., Chi, Y., Sha, J., & Xu, S. Facile synthesis of highly crystalline g-C<sub>3</sub>N<sub>4</sub> nanosheets with remarkable visible light photocatalytic activity for antibiotics removal. *Chemosphere* 2021, **271**, 129503.
6. Ma, L., Fan, H., Li, M., Tian, H., Fang, J., & Dong, G. A simple melamine-assisted exfoliation of polymeric graphitic carbon nitrides for highly efficient hydrogen production from water under visible light. *J. Mater. Chem. A* 2015, **3**, 22404–22412.
7. Sun, H., Zhou, X., Zhang, H. & Tu, W. An efficient exfoliation method to obtain graphitic carbon nitride nanosheets with superior visible-light photocatalytic activity. *Int. J. Hydrogen Energy* 2017, **42**, 7930–7937.

8. Xu, J., Zhang, L., Shi, R. & Zhu, Y. Chemical exfoliation of graphitic carbon nitride for efficient heterogeneous photocatalysis. *J. Mater. Chem. A* 2013, **1**, 14766.
9. Yang, S., Gong, Y., Zhang, J., Zhan, L., Ma, L., Fang, Z., Vajtai, R., Wang, X., & Ajayan, P. M. Exfoliated Graphitic Carbon Nitride Nanosheets as Efficient Catalysts for Hydrogen Evolution Under Visible Light. *Adv. Mater.* 2013, **25**, 2452–2456.
10. Wu, Y., Liu, L.-M., An, X. & Wei, T. New insights into interfacial photocharge transfer in TiO<sub>2</sub>/C<sub>3</sub>N<sub>4</sub> heterostructures: effects of facets and defects. *New J. Chem.* 2019, **43**, 4511–4517.
11. Li, Y., Li, Y., Ma, S., Wang, P., Hou, Q., Han, J., & Zhan, S. Efficient water disinfection with Ag<sub>2</sub>WO<sub>4</sub>-doped mesoporous g-C<sub>3</sub>N<sub>4</sub> under visible light. *J. Hazard. Mater.* 2017, **338**, 33–46.
12. Nosaka, Y. & Nosaka, A. Y. Generation and Detection of Reactive Oxygen Species in Photocatalysis. *Chem. Rev.* 2017, **117**, 11302–11336.
13. Abdullah, E. A. Band edge positions as a key parameter to a systematic design of heterogeneous photocatalyst. *Eur. J. Chem.* 2019, **10**, 82–94.
14. Sawyer, D. T. & Valentine, J. S. How super is superoxide? *Acc. Chem. Res.* 1981, **14**, 393–400.
15. Armstrong, D. A., Huie, R. E., Lyman, S., Koppenol, W. H., Merényi, G., Neta, P., Stanbury, D. M., Steenken, S., & Wardman, P. Standard electrode potentials involving radicals in aqueous solution: inorganic radicals. *Bioinorg. React. Mech.* 2013, **9**, 59–61.
16. Odling, G. & Robertson, N. Bridging the gap between laboratory and application in photocatalytic water purification. *Catal. Sci. Technol.* 2019, **9**, 533–545.
17. Li, J., Jiang, M., Zhou, H., Jin, P., Cheung, K. M. C., Chu, P. K., & Yeung, K. W. K. Vanadium Dioxide Nanocoating Induces Tumor Cell Death through Mitochondrial Electron Transport Chain Interruption. *Glob. Challenges* 2019, **3**, 1800058.
18. Wen, J., Xie, J., Chen, X. & Li, X. A review on g-C<sub>3</sub>N<sub>4</sub>-based photocatalysts. *Appl. Surf. Sci.* 2017, **391**, 72–123.
19. Yan, S. C., Li, Z. S. & Zou, Z. G. Photodegradation Performance of g-C<sub>3</sub>N<sub>4</sub> Fabricated by Directly Heating Melamine. *Langmuir* 2009, **25**, 10397–10401.

20. Pomilla, F. R., Cortes, M. A. L. R.M. Hamilton, J. W. J., Molinari, R., Barbieri, G., Marci, G., Palmisano, L., Sharma, P. K., Brown, A., & Byrne, J. A. An Investigation into the Stability of Graphitic C<sub>3</sub>N<sub>4</sub> as a Photocatalyst for CO<sub>2</sub> Reduction. *J. Phys. Chem. C* 2018, **122**, 28727–28738.
21. Dante, R. C., Sánchez-Arévalo, F. M., Chamorro-Posada, P., Vázquez-Cabo, J., Huerta, L., Lartundo-Rojas, L., Santoyo-Salazar, J., Solorza-Feria, O., Diaz-Barrios, A., Zoltan, T., Vargas, F., Valenzuela, T., Muñoz-Bisesti, F., & Quiroz-Chávez, F. J. Synthesis and characterization of Cu-doped polymeric carbon nitride. *Fullerenes, Nanotub. Carbon Nanostructures* 2016, **24**, 171–180.
22. Hellgren, N., Haasch, R. T., Schmidt, S., Hultman, L. & Petrov, I. Interpretation of X-ray photoelectron spectra of carbon-nitride thin films: New insights from in situ XPS. *Carbon N. Y.* 2016, **108**, 242–252.
23. Kahn, A. Fermi level, work function and vacuum level. *Mater. Horizons* 2016, **3**, 7–10.
24. Mezzi, A., Soltani, P., Kaciulis, S., Bellucci, A., Girolami, M., Mastellone, M., & Trucchi, D. M. Investigation of work function and chemical composition of thin films of borides and nitrides. *Surf. Interface Anal.* 2018, **50**, 1138–1144.
25. Rhimi, B., Wang, C. & Bahnemann, D. W. Latest progress in g-C<sub>3</sub>N<sub>4</sub> based heterojunctions for hydrogen production via photocatalytic water splitting: a mini review. *J. Phys. Energy* 2020, **2**, 042003.
26. Liu, J. Origin of High Photocatalytic Efficiency in Monolayer g-C<sub>3</sub>N<sub>4</sub>/CdS Heterostructure: A Hybrid DFT Study. *J. Phys. Chem. C* 2015, **119**, 28417–28423.
27. Beranek, R. (Photo)electrochemical Methods for the Determination of the Band Edge Positions of TiO<sub>2</sub> -Based Nanomaterials. *Adv. Phys. Chem.* **2011**, 1–20.
28. Wang, E., Ma, Z., Zhang, Z., Henriksson, P., Inganäs, O., Zhang, F., & Andersson, M. R. An isoindigo-based low band gap polymer for efficient polymer solar cells with high photo-voltage. *Chem. Commun.* 2011, **47**, 4908.
29. Szaciłowski, K. & Macyk, W. Photoelectrochemical Photocurrent Switching Effect: A New Platform for Molecular Logic Devices. *Chim. Int. J. Chem.* 2007, **61**, 831–834.
30. Jing, J., Chen, Z. & Feng, C. Dramatically enhanced photoelectrochemical properties and transformed p/n type of g-C<sub>3</sub>N<sub>4</sub> caused by K and I co-doping.

- Electrochim. Acta* 2019, **297**, 488–496.
31. Jin, Z., Zhang, Q., Chen, J., Huang, S., Hu, L., Zeng, Y. J., Zhang, H., Ruan, S., & Ohno, T. Hydrogen bonds in heterojunction photocatalysts for efficient charge transfer. *Appl. Catal. B Environ.* 2018, **234**, 198–205.
  32. Wang, Y., Zhang, J., Wang, X., Antonietti, M. & Li, H. Boron- and Fluorine-Containing Mesoporous Carbon Nitride Polymers: Metal-Free Catalysts for Cyclohexane Oxidation. *Angew. Chemie* 2010, **122**, 3428–3431.
  33. Chen, Q., Zhou, M., Ma, D. & Jing, D. Effect of Preparation Parameters on Photoactivity of BiVO<sub>4</sub> by Hydrothermal Method. *J. Nanomater.* **2012**, 1–6.
  34. Gawęda, S., Kowalik, R., Kwolek, P., MacYk, W., Mech, J., Oszejca, M., Podborska, A., Szaciłowski, & K. Nanoscale digital devices based on the photoelectrochemical photocurrent switching effect: Preparation, properties and applications. *Isr. J. Chem.* 2011, **51**, 36–55.
  35. Mukhokosi, E. P., Manohar, G. V. S., Nagao, T., Krupanidhi, S. B. & Nanda, K. K. Device architecture for visible and near-infrared photodetectors based on two-dimensional SnSe<sub>2</sub> and MoS<sub>2</sub>: A review. *Micromachines* 2020, **11**, 1–30.
  36. Wang, X., Maeda, K., Thomas, A., Takanabe, K., Xin, G., Carlsson, J. M., Domen, K., & Antonietti, M. A metal-free polymeric photocatalyst for hydrogen production from water under visible light. *Nat. Mater.* 2008, **8**, 76–80.
  37. Rahman, M. Z., Davey, K. & Mullins, C. B. Tuning the Intrinsic Properties of Carbon Nitride for High Quantum Yield Photocatalytic Hydrogen Production. *Adv. Sci.* 2018, **5**, 1800820.
  38. Basic Theories of Semiconductor Electrochemistry. in *Electrochemistry of Silicon and Its Oxide* 1–43 (Springer, Boston, MA, 2004). doi:10.1007/0-306-47921-4\_1
  39. Zhang, Z., Lin, S., Li, X., Li, H. & Cui, W. Metal free and efficient photoelectrocatalytic removal of organic contaminants over g-C<sub>3</sub>N<sub>4</sub> nanosheet films decorated with carbon quantum dots. *RSC Adv.* 2017, **7**, 56335–56343.
  40. Liu, C., Wang, F., Zhang, J., Wang, K., Qiu, Y., Liang, Q., & Chen, Z.. Efficient Photoelectrochemical Water Splitting by g-C<sub>3</sub>N<sub>4</sub>/TiO<sub>2</sub> Nanotube Array Heterostructures. *Nano-Micro Lett.* 2018, **10**, 37.
  41. Sun, S., Wang, W. & Zhang, L. Bi<sub>2</sub>WO<sub>6</sub> Quantum Dots Decorated Reduced Graphene Oxide: Improved Charge Separation and Enhanced Photoconversion

- Efficiency. *J. Phys. Chem. C* 2013, **117**, 9113–9120.
42. Murashkina, A. A., Bakiev, T. V., Artemev, Y. M., Rudakova, A. V., Emeline, A. V., & Bahnemann, D. W. Photoelectrochemical Behavior of the Ternary Heterostructured Systems CdS/WO<sub>3</sub>/TiO<sub>2</sub>. *Catalysts* 2019, **9**, 999.
  43. Liu, Y., Zheng, Z., Li, Y., Xi, K. & Mi, Y. PI/g-C<sub>3</sub>N<sub>4</sub> composite photocatalyst with enhanced activity of degrading pollutants under visible light. *J. Mater. Sci.* 2021, **56**, 9122–9133.
  44. Wang, H., Zhang, X., Xie, J., Zhang, J., Ma, P., Pan, B., & Xie, Y. Structural distortion in graphitic-C<sub>3</sub>N<sub>4</sub> realizing an efficient photoreactivity. *Nanoscale* 2015, **7**, 5152–5156.



## **Chapter 6 - Synthesis of BiVO<sub>4</sub> micro/nano structures with different morphologies: characterization and photocatalytic activities**

### **6.1 Aim and objectives**

**6.1.1 Aim:** This chapter aims to synthesize different morphologies of bismuth vanadate (BiVO<sub>4</sub>) and to investigate their physiochemical, electronic and photoelectrochemical properties and correlate to the photocatalytic activities.

#### **6.1.2 Objectives**

1. To synthesize BiVO<sub>4</sub> spheres using a hydrothermal method
2. To prepare BiVO<sub>4</sub> nanoplates using a hydrothermal method
3. To grow BiVO<sub>4</sub> pyramids/thorns on FTO coated glass using seed-mediated aqueous growth method
4. To study the crystalline properties of the synthesized samples using XRD
5. To study the morphology and elemental mapping of materials through FESEM-EDX
6. To determine the elemental composition and chemical states present in prepared BiVO<sub>4</sub> samples using XPS.
7. To explore photoelectrochemical properties of prepared BiVO<sub>4</sub> photoelectrodes
8. To investigate the photocatalytic activity of BiVO<sub>4</sub> for the degradation of a model organic pollutant under UV-Vis irradiation

## 6.2 Introduction

In recent years, researchers have been made great efforts to develop effective semiconductor photocatalysts to harness the visible spectrum of sunlight in photocatalytic applications. Bismuth vanadate ( $\text{BiVO}_4$ ) is a material which has gained worldwide research attention in the field of photocatalysis. Being an n-type semiconductor with narrow bandgap ( $\sim 2.4$  eV) and good photostability, it has been recognized as a potential visible light active photocatalyst.<sup>1</sup>  $\text{BiVO}_4$  is found in three crystal phases: monoclinic-scheelite (m-s), tetragonal-zircon (t-z), and tetragonal-scheelite (t-s).<sup>2,3</sup> Tetragonal-zircon phase absorbs predominantly UV light with a bandgap of 2.9 eV, whereas monoclinic-scheelite phase absorbs light from both the visible and UV regions of the solar spectrum with a bandgap of 2.4 eV. UV light absorption in monoclinic and tetragonal phase are associated with the band transition from O 2p to V 3d and visible region absorption is caused by the transition from a valence band formed by Bi 6s or a hybrid orbital (made by overlapping of O 2p and Bi 6s) to a conduction band of V 3d. Owing to distorted Bi-O band which increases the separation efficiency of the photo-induced electrons and holes, the monoclinic phase is believed to be most photoactive phase among the three crystal phases.<sup>4</sup>

$\text{BiVO}_4$  has been employed in various applications such as gas sensors, solid-state electrolytes, paints and batteries, and for photocatalytic applications such as water splitting and pollutant degradation.<sup>5</sup> Several methodologies have been used for the synthesis of  $\text{BiVO}_4$  including hydrothermal method, solid-state reactions, solvothermal method, sol-gel method, chemical bath deposition, electrospinning, microwave synthesis and solution combustion processes.<sup>1,6,7</sup> The hydrothermal method has been commonly used to prepare monoclinic  $\text{BiVO}_4$ . Numerous morphologies of  $\text{BiVO}_4$  have been developed using above mention methods such as

hollow nanosphere, micro ribbons, microtubes, spheres, peanut, dendrite, dumbbells, polyhedral, octahedral, nanoplates and many more.<sup>2</sup> The final morphology of BiVO<sub>4</sub> is strongly influenced by the preparation method and reaction conditions especially the initial pH of precursor solution.<sup>8</sup> It has been commonly stated that the crystal morphology plays an important role in the determination of their properties.<sup>6</sup>

In this study, a hydrothermal method and a seed-mediated method were used to prepare BiVO<sub>4</sub> particles with three different morphologies (spheres, nanoplates, and pyramids/thorns), adapted from methods reported in the literature by Zhao *et al.*,<sup>9</sup> Xi *et al.*,<sup>10</sup> and Su *et al.*,<sup>11</sup>. The materials were analysed for their morphology, structure, elemental composition, optical properties and photoelectrochemical properties. The as-synthesized BiVO<sub>4</sub> samples were also tested for their efficacy in photocatalytic phenol degradation under UV-vis irradiation.

## 6.3 Experimental Section

### 6.3.1 Materials

All the chemicals, Bi(NO<sub>3</sub>)<sub>3</sub>·5H<sub>2</sub>O (Aldrich, 98%), NH<sub>4</sub>VO<sub>3</sub> (Aldrich, 99.99%), HNO<sub>3</sub> (Sigma-Aldrich, 65%), NaOH (Sigma-Aldrich, 98%), ethanolamine (Sigma-Aldrich, 98%), citric acid (Sigma-Aldrich, 99.5%), polyvinyl alcohol (Aldrich, 99%), acetic acid (Fisher scientific), NaHCO<sub>3</sub> (Aldrich, 99 %) were of analytical grade and used in experiments without any further purification.

### 6.3.2 Synthesis of BiVO<sub>4</sub>

In this study, three different morphologies (spheres, nanoplates, and pyramids/thorns) of BiVO<sub>4</sub> were prepared using hydrothermal method and seed-mediated method.

### 6.3.2.1 Spheres: hydrothermal synthesis

Bismuth vanadate spheres were synthesized by adapting the method reported by Zhao *et al.*<sup>9</sup>. In a typical synthesis, 0.02 mol  $\text{Bi}(\text{NO}_3)_3 \cdot 5\text{H}_2\text{O}$  was dissolved in 35 mL of 4M  $\text{HNO}_3$  and stirred for 30 min in a glass beaker. This solution was named as solution A. Similarly, 0.02 mol  $\text{NH}_4\text{VO}_3$  was dissolved in 35 mL of 4M NaOH and stirred for 30 min in another glass beaker. This solution is called as solution B. Afterwards solution B was slowly added to solution A and the pH of this final mixture was adjusted to pH 6 using NaOH and stirred for 60 min.

This final suspension was transferred to a 100 mL sample container made of Teflon which was then placed inside a hydrothermal Parr reactor built with stainless-steel (Fig. 6.1a). The Parr reactor was tightly screwed and allowed to heat at 150°C for 18 h, raising the pressure to 5 bar. After 18 h of reaction, the reactor was allowed to cool down naturally at room temperature. After opening the Parr reactor, yellow precipitates were obtained which were collected by centrifugation at 5000 rpm and washed several times with distilled water to remove any insoluble acidic residue, until the pH of the solution became neutral. Finally, the precipitates were rinsed with ethanol to remove any organic impurities and dried overnight in a vacuum oven at 80°C. In the end, the obtained yellow colour product was collected and ground into fine powder using mortar and pestle before further characterization and that was called BiV-1. A flowchart for the hydrothermal synthesis of  $\text{BiVO}_4$  spheres is given in chapter 3 (section 3.2.3).

### 6.3.2.2 Nanoplates: hydrothermal synthesis

$\text{BiVO}_4$  nanoplates were synthesized via a hydrothermal route by adapting the method reported by Xi *et al.*<sup>10</sup>. Except for a few changes, all materials and steps were

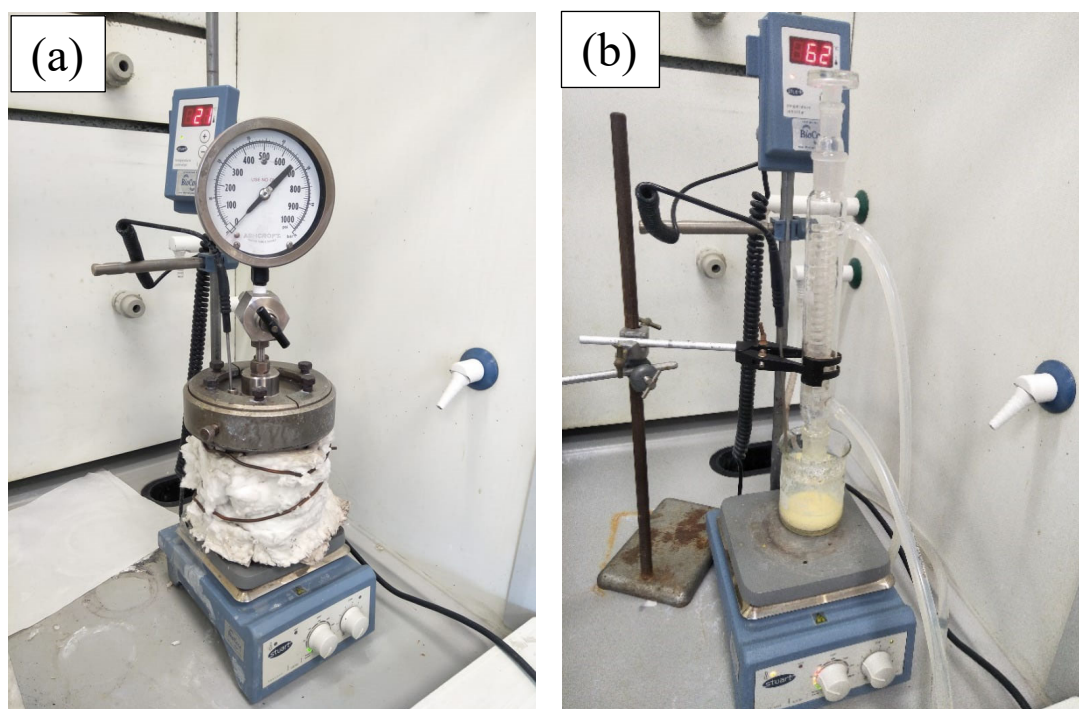
similar to the procedure followed for the preparation of BiV-1. Stoichiometry of precursors was reduced by half (0.01 mol) compared to that used to prepare BiV-1. Instead of NaOH, ethanolamine was used for pH adjustment of the precursor solution (pH = 6.5). In addition, hydrothermal treatment was given at the same temperature (150°C) for 12 h. The yellow colour product obtained was collected and ground into fine powder using mortar and pestle before further characterization and that was called BiV-2. Flowchart for the hydrothermal synthesis of BiVO<sub>4</sub> nanoplates is provided in chapter 3 (3.2.3).

### 6.3.2.3 Pyramids/thorns: Seed-mediated method

Bismuth vanadate pyramids/thorns were synthesized using a seed mediated method also known as nucleation method by adopting the procedure reported by Su *et al.*<sup>11</sup>. A typical synthesis process is as follows: These BiVO<sub>4</sub> structures were grown on pre cleaned FTO coated glass in a two step process. In first step, A thin layer of BiVO<sub>4</sub> seeds was deposited on FTO coated glass by spray coating of precursor solution using a lab spray gun (air brush). Precursor solution was prepared by dissolving 0.005 mol of Bi(NO<sub>3</sub>)<sub>3</sub>·5H<sub>2</sub>O, 0.005 mol of NH<sub>4</sub>VO<sub>3</sub>, and 0.01 mol of citric acid in 15 mL of 23.3% HNO<sub>3</sub> aqueous solution. The solution was stirred until it became a clear, blue coloured solution. After that, polyvinyl alcohol (0.08 g) and acetic acid (0.25 mL) were mixed into this blue-coloured solution and stirred well to get final precursor solution. The seed layer coated FTO glass was annealed in a muffle furnace at 400°C for 5 h.

In the second step of process, the seed layer coated FTO glass was immersed in an Erlenmeyer flask containing the BiVO<sub>4</sub> solution, with the seed layer facing up. This Erlenmeyer flask was then placed on a temperature-controlled water bath and

connected to a condenser as a part of reflux system (Fig. 6.1b). The seed layer coated FTO glass was positioned in such a way as to ensure reflux of  $\text{BiVO}_4$  solution with constant magnetic stirring for 6 h at  $60^\circ\text{C}$ . After 6 h, FTO glass was carefully taken out, rinsed with DI water, and dried under oxygen-free nitrogen stream. Finally, this  $\text{BiVO}_4$  coated FTO glass was annealed at  $500^\circ\text{C}$  for half hour. Annealed sample was named BiV-3. Flowchart for the seed mediated synthesis of  $\text{BiVO}_4$  pyramids/thorns is provided in chapter 3 (3.2.3)



**Fig. 6.1** Experimental setup for (a) Hydrothermal synthesis of spherical and plate shape  $\text{BiVO}_4$  particles, (b) Reflux set up for seed mediated synthesis of pyramid/thorn shape  $\text{BiVO}_4$  particles.

### 6.3.3 Electrode preparation

To perform photoelectrochemical measurements, the working electrodes used in this study were fabricated following the protocol that was formerly discussed in detail in section 3.3 of Chapter 3. In brief, fabrication of a typical working electrode follows the three steps which includes cleaning of conductive substrate (FTO coated),

spray coating of photocatalyst ( $\text{BiVO}_4$ ) on cleaned substrate and making an electrical contact (using copper wire).

#### 6.3.4 Analytical characterization

The resultant products were examined for their morphology by a field emission scanning electron microscope (FESEM). An energy dispersive X-ray (EDX/EDS) analyser attached to FESEM was used to determine the bulk elemental composition of the samples under low vacuum pressure of  $\sim 10^{-4}$  bar at working distance of 10 mm and an accelerating voltage of 10 kV. The synthesized  $\text{BiVO}_4$  samples were characterized by X-ray diffraction ( $2\theta$  range of  $5\text{--}70^\circ$ ), and Raman spectroscopy in the range of  $1200\text{--}100\text{ cm}^{-1}$ . Optical properties were analysed using UV diffuse reflectance spectroscopy (DRS). X-ray photoelectron spectroscopy (XPS) was performed to study the surface composition and chemical states of prepared sample. The binding energy was calibrated to the C 1s peak at 284.8 eV. The peaks were fitted using CasaXPS software after performing the Tougaard background correction before quantification. Valance band XPS (VBXPS) were also employed to determine the valance band edge energies of as-prepared samples. The details of all the characterization techniques are provided in chapter 3.

#### 6.3.5 Photoelectrochemical methods

The photoelectrochemical measurements were performed using a three-electrode system in a beaker. This three-electrode configuration consisted of a platinum mesh paddle ( $5.9\text{ cm}^2$ ) as the counter electrode, saturated calomel electrode (Hanna instruments) as the reference electrode and earlier prepared photoelectrode as the working electrode. 0.1 M  $\text{KClO}_4$  solution (pH 6) was used as an electrolyte. A 450 W Xe lamp was used as an irradiation source. All photoelectrochemical

measurements were performed on an electrochemical workstation (AUTOLAB PGSTAT 30). More details of the irradiation source, photoelectrochemical cell and electrochemical workstation are given in chapter 3.

The photocurrent-potential response was investigated using linear sweep voltammetry (LSV) in dark, continuous, and chopped irradiation sweeping from -1.0 to +1.0 V or +1.0 V to -1.0 V at a sweep rate of  $5 \text{ mV s}^{-1}$ . The photocurrent-time response was also measured over a range of fixed potentials. All potentials mentioned in the chapter were referenced to SCE electrode unless stated otherwise.

### **6.3.6 Photocatalysis experiment**

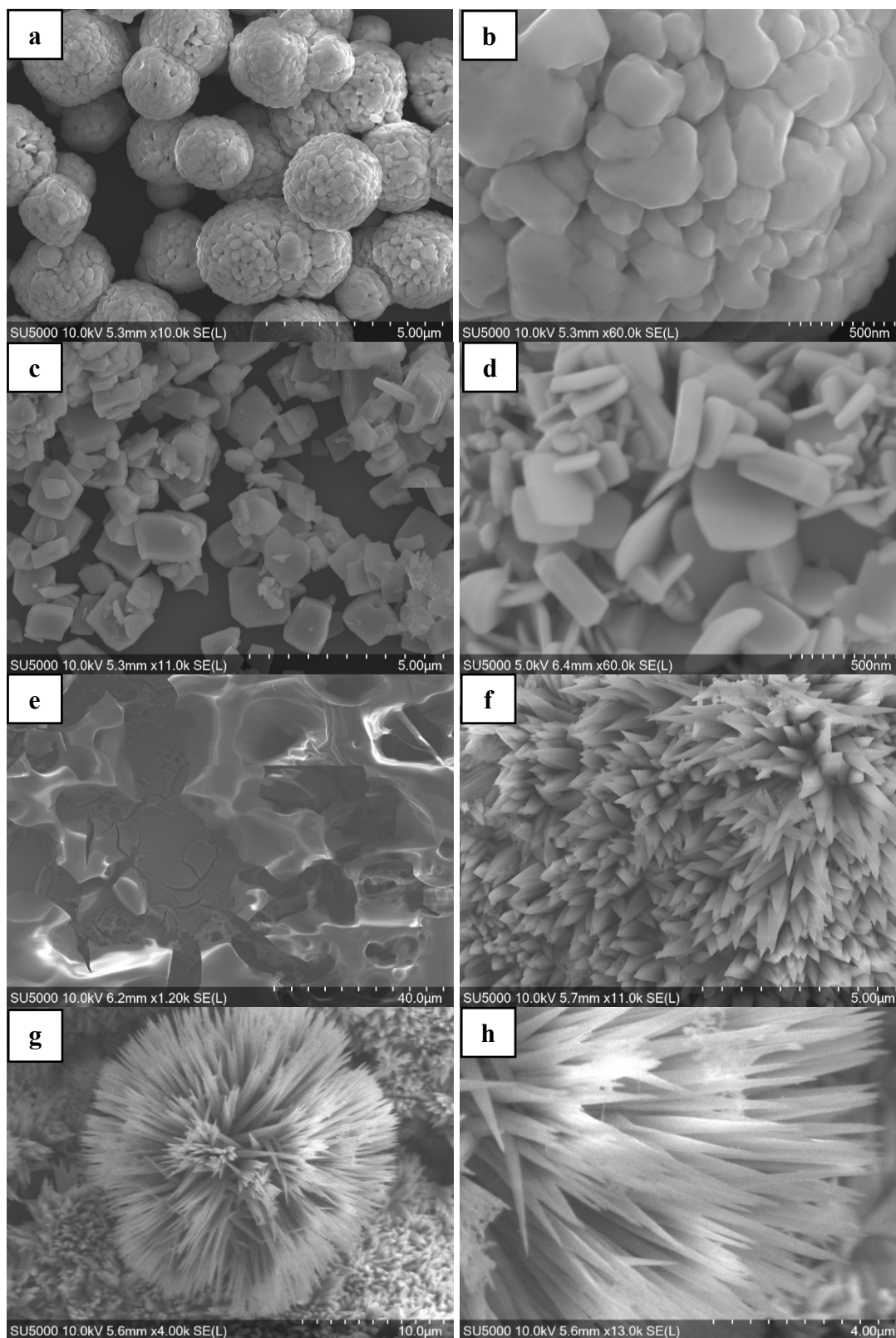
The photocatalytic activities of as prepared  $\text{BiVO}_4$  samples were evaluated for phenol degradation under UV-visible irradiation. The details about set up and conditions followed for photocatalysis experiment are provided in section 3.6.

## **6.4 Result and discussion**

### **6.4.1 Morphology and micro/nanostructures**

It is well known that initial pH and other reaction conditions have a significant impact on the final morphology of  $\text{BiVO}_4$  particles. The morphologies of the as-prepared  $\text{BiVO}_4$  samples were determined by field emission scanning electron microscopy (FESEM), and the obtained typical FESEM micrographs are shown in Fig. 6.2a-h, demonstrating that the synthesized products, BiV-1, BiV-2, and BiV-3, are composed of sphere-like (Fig. 6.2a and b), plate-like (Fig. 6.2c and d), and pyramid/thorn-like (Fig. 6.2f and h), micro/nano structures, which were prepared using different synthesis methods and reaction conditions.





**Fig. 6.2** FESEM images of  $\text{BiVO}_4$  samples synthesized by different methods: BiV-1 (a)  $\text{BiVO}_4$  Spheres, and (b)  $\text{BiVO}_4$  spheres at high magnification showing clusters of nano-size particles. BiV-2 (c)  $\text{BiVO}_4$  plates, and (d)  $\text{BiVO}_4$  plates at high magnification. BiV-3 (e) seed layer, (f)  $\text{BiVO}_4$  pyramids/thorns, (g) Sea urchin-like structures, and (h)  $\text{BiVO}_4$  pyramids/thorns at high magnification

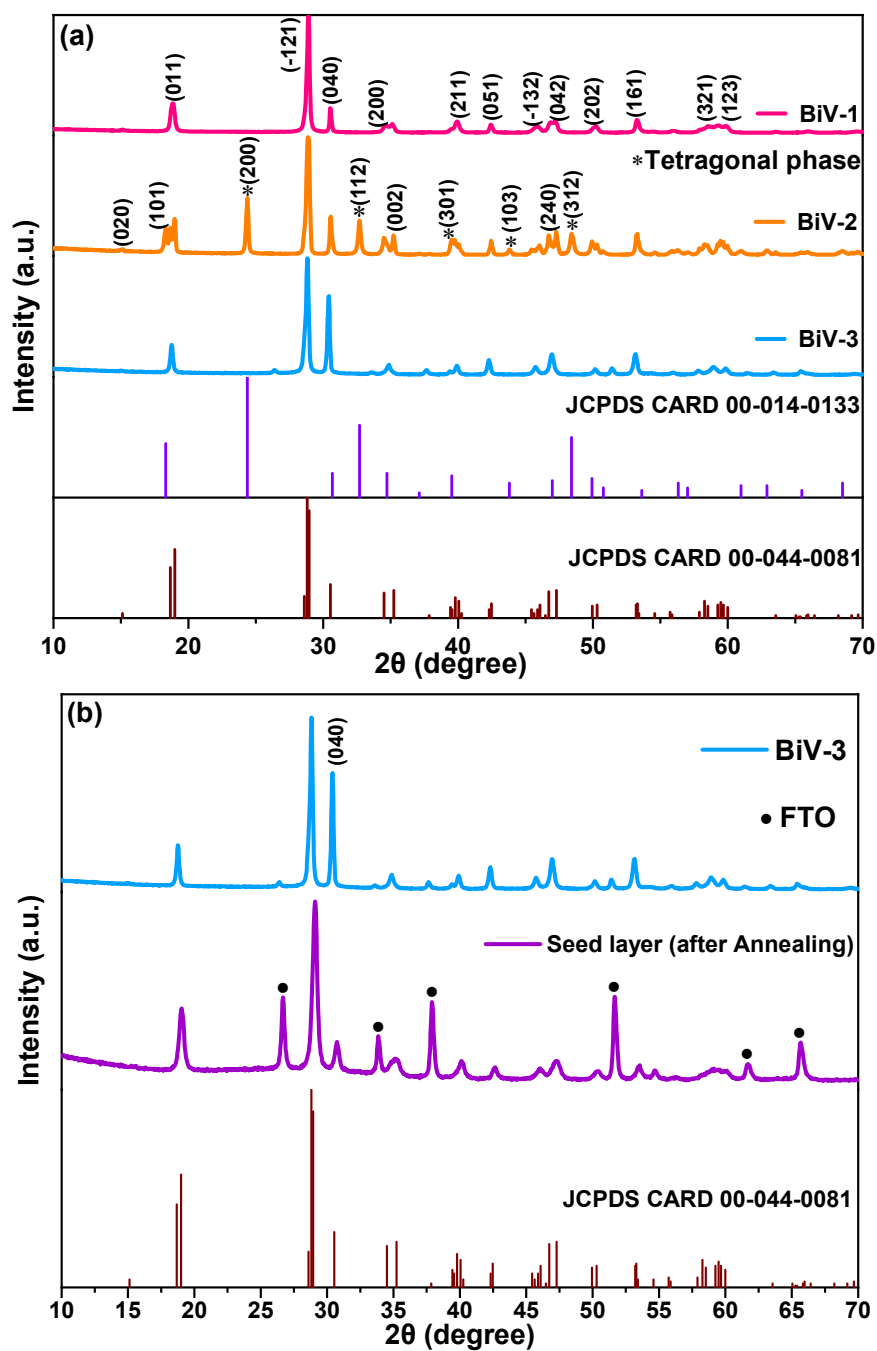
Spherical and plate shape particles were produced by hydrothermal method whereas pyramid/thorn shape particles were the end product of the seed mediated method. The low magnification FESEM image (Fig. 6.2a) gives the all-around view of BiV-1 sample and shows that most of the crystals have a solid spherical shape with an average diameter of about 2.5  $\mu\text{m}$ . Fig. 6.2b depicts a magnified view of a sphere, indicating that these spheres are clusters of numerous nano-size particles. The BiV-2 sample (Fig. 6.2c and d) contains plate-like  $\text{BiVO}_4$  particles with a thickness of 30-70 nm. Fig. 6.2e portrays the seed layer of precursor solution (post annealing) on FTO coated glass. Fig. 6.2f confirms the vertical growth of  $\text{BiVO}_4$  particles on the seed layer coated FTO glass (BiV-3), showing arrays of pyramids/thrones with a length of 4-8  $\mu\text{m}$ , a diameter of 200-500 nm at the bottom and a tip of about 20-50 nm (Fig. 6.2h). The agglomeration of these thorns resulted in the formation of some Sea urchin-like structures in the BiV-3 sample as shown in Fig. 6.2g. The diameter of these Sea urchin-like structures was about 20-25  $\mu\text{m}$ . Although there was no growth seen without the seed layer which means that seed layer provides the nucleation site to grow  $\text{BiVO}_4$  further.

## 6.4.2 Structure and composition

### 6.4.2.1 X-ray diffraction analysis

$\text{BiVO}_4$  exists in three crystal structures: monoclinic scheelite phase (m-s), tetragonal zircon phase (t-z), and tetragonal scheelite (t-s) phase. X-ray diffraction analysis can be used to determine the phases present in synthesized samples. Fig. 6.3a-b depict the XRD patterns of  $\text{BiVO}_4$  samples synthesized with different methods, which represent a series of diffraction peaks belonging to mostly monoclinic phase and a few tetragonal phases of  $\text{BiVO}_4$  that are in good agreement with standard data

of monoclinic  $\text{BiVO}_4$  (space group  $I2/a$ ) with cell constants of  $a=5.196 \text{ \AA}$ ,  $b=11.704 \text{ \AA}$ , and  $c=5.092 \text{ \AA}$  (JCPDS No. 00-044-0081) and tetrahedral  $\text{BiVO}_4$  (space group  $I41/amd$ ) with cell constants of  $a=7.299 \text{ \AA}$ ,  $b=7.299 \text{ \AA}$ , and  $c=6.457 \text{ \AA}$  (JCPDS No. 00-014-0133). Apart from  $\text{BiVO}_4$ , no other major peak was found in the matrix of all the three samples.



**Fig. 6.3** (a) XRD patterns of  $\text{BiVO}_4$  samples synthesized by different methods (b) XRD patterns of seed layer stage and final annealed BiV-3 sample synthesized by seed mediated method.

In Fig. 6.3a, all the diffraction peaks of sample BiV-1 and BiV-3 can be indexed to monoclinic BiVO<sub>4</sub> phase while the XRD pattern of BiV-2 contains a mixed phase pattern including tetragonal zircon and monoclinic phases. Fig. 6.3b shows the XRD reflections of the seed layer and the final product (BiV-3) which are plotted separately to clearly highlight the phase changes between these two steps. The seed layer XRD pattern has some intense peaks that come from the FTO glass substrate, almost disappeared after formation of the final phase. It can be seen that peak height at 30.6° increases significantly in final stage compared to the seed layer stage which belongs to (004) plane, determines the one-dimensional growth of BiVO<sub>4</sub> structures. Su *et al.*<sup>11</sup> also made a similar observation in their report.

#### 6.4.2.2 Raman spectroscopy

Raman spectroscopy is an efficient technique for exploring the structure and bonding in metal-oxide compounds using their vibrational characteristics. Fig. 6.4 displays the Raman spectra recorded under ambient conditions for BiV-1, BiV-2 and BiV-3 which exhibit six visible vibrational bands at 127, 210, 325, 366, 704 and 823 cm<sup>-1</sup> that correspond to the vibrational characteristics of the VO<sub>4</sub> tetrahedron and are in accordance with the interpretation of Hardcastle *et al.*<sup>12,13</sup> The intense band at 823 cm<sup>-1</sup> was ascribed to the shorter symmetric V–O stretching modes (*A<sub>g</sub>*) and the weak band at 704 cm<sup>-1</sup> to the longer (*A<sub>g</sub>*) symmetric V–O stretching modes. The asymmetric (*B<sub>g</sub>*) and symmetric (*A<sub>g</sub>*) bending vibrations of the VO<sub>4</sub> tetrahedron were observed at 325 and 366 cm<sup>-1</sup>, respectively, and external modes appear at 210, 127 cm<sup>-1</sup>. The Raman spectra of BiV-3 displays the weaker bands at 325 and 366 cm<sup>-1</sup> than other samples which could be due to the calcination at higher temperature.<sup>14</sup>

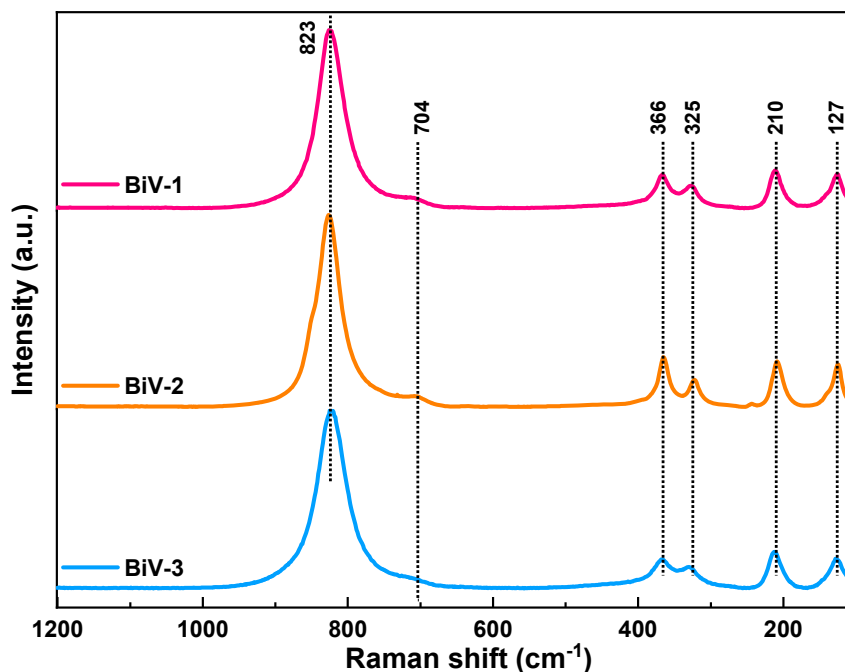
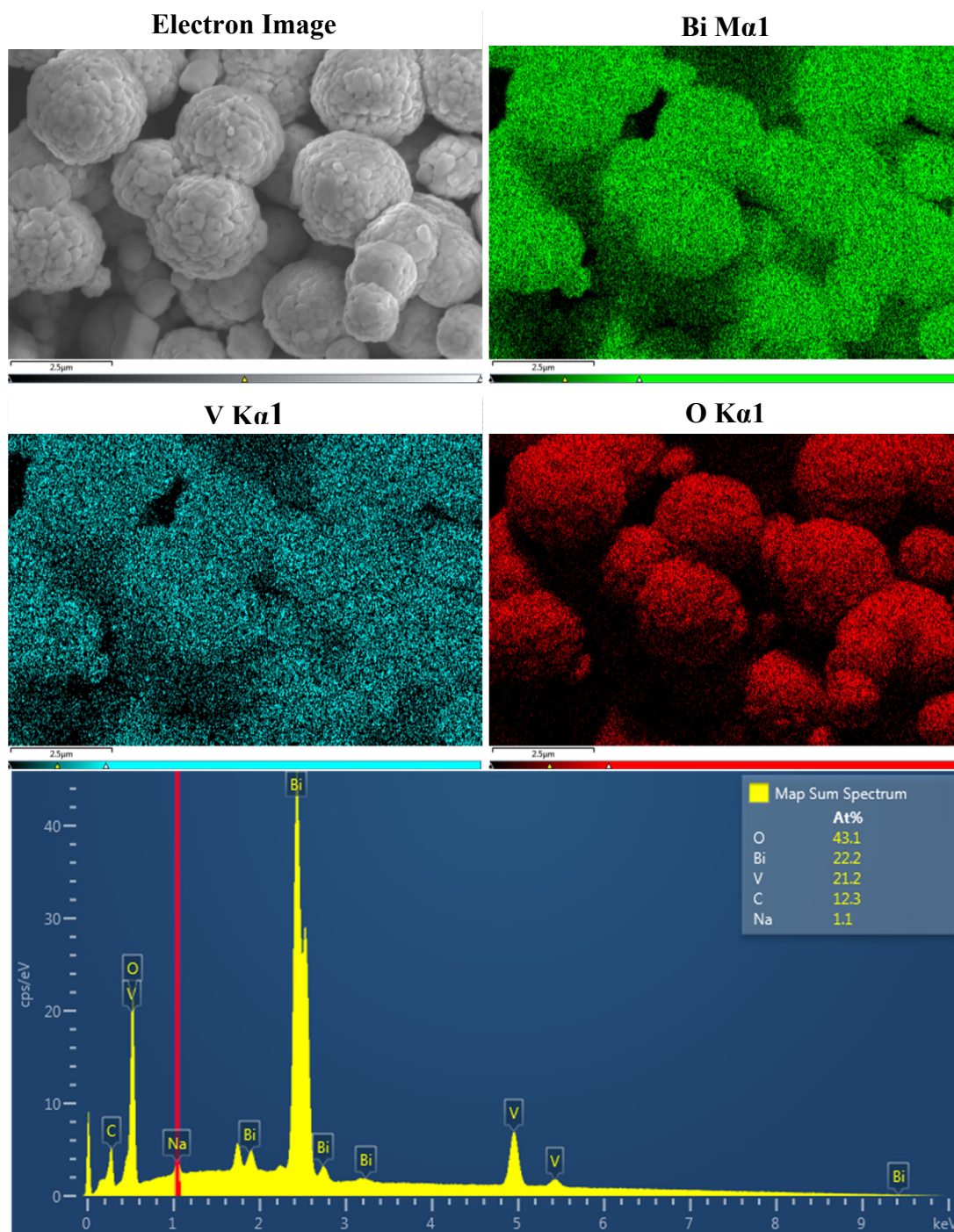


Fig. 6.4 Raman spectra of BiVO<sub>4</sub> samples synthesized by different methods, (laser 532 nm)

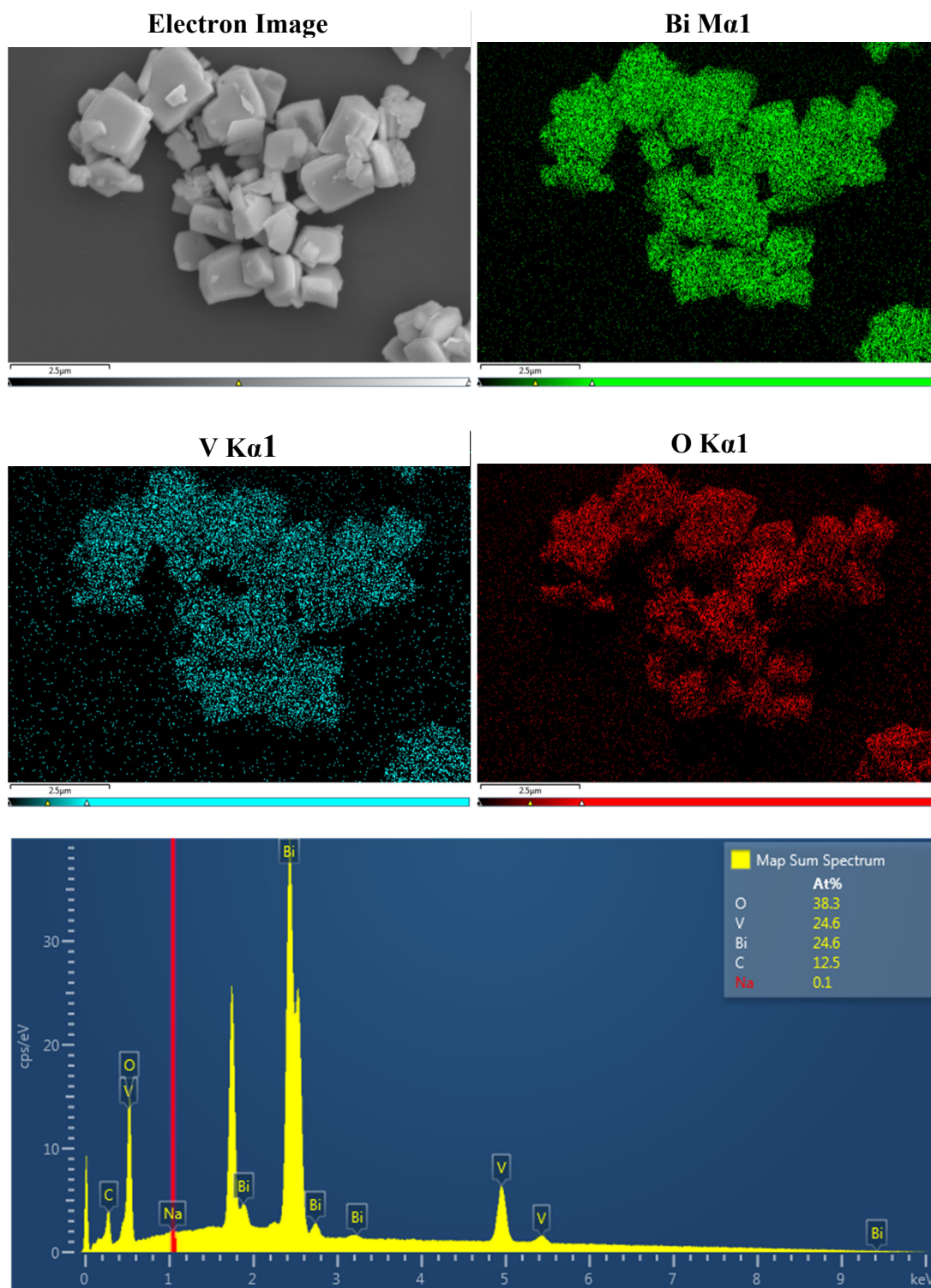
#### 6.4.2.3 Elemental mapping by EDX

The elemental composition of the as-prepared BiVO<sub>4</sub> samples was studied by the energy-dispersive X-ray spectroscopy (EDX) attached to FESEM and mapping results for BiV-1, BiV-2 and BiV-3 are shown in Fig. 6.5-6.7 respectively.

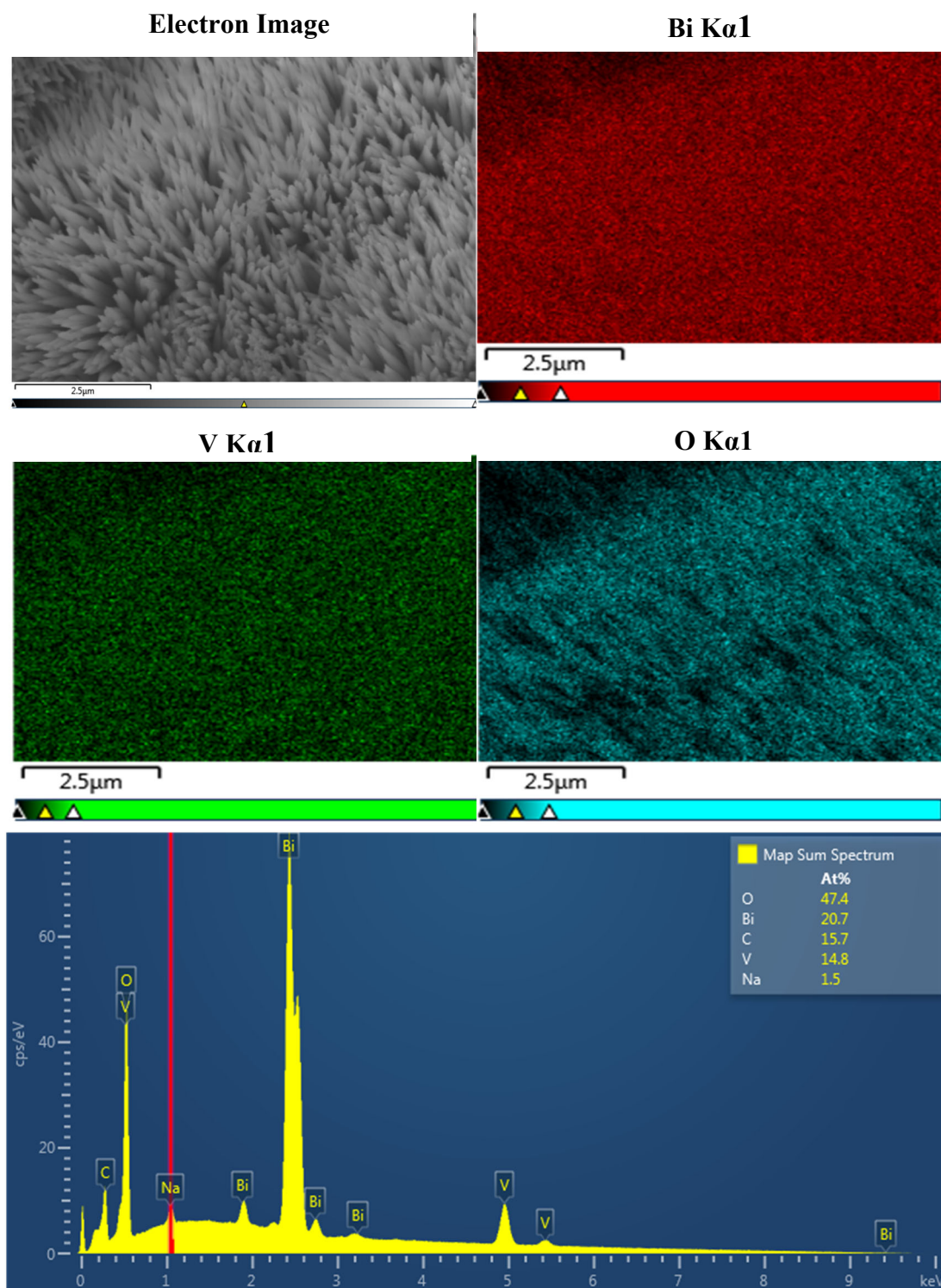
Their individual EDX elemental maps revealed a uniform distribution of bismuth (Bi) and vanadium (V), and oxygen (O) throughout the sample. The EDS analysis results find the ratio of At% of Bi:V to be almost 1:1 in both the samples, BiV-1 (Bi – 22.2%, V – 21.2%) and BiV-2 (Bi – 24.6%, V – 24.6%) indicating the absence of other compounds. Although EDX result shows the presence of ~12% carbon which may come from silicon substrate, or the solvent (methanol) used for EDX sample preparation. At% of Bi in sample BiV-3 is 6% higher than At% of V (Bi – 20.7%, V – 14.8%) implying the presence of unreacted Bismuth or other oxides in the sample.



**Fig. 6.5** FESEM image and corresponding EDX elemental mapping for Bi, V, O, and EDX spectrum for  $\text{BiVO}_4$  sample having spherical shape (BiV-1) Scale =  $2.5\mu\text{m}$



**Fig. 6.6** FESEM image and corresponding EDX elemental mapping for Bi, V, O, and EDX spectrum for  $\text{BiVO}_4$  sample having nanoplates shape (BiV-2). Scale = 2.5 μm

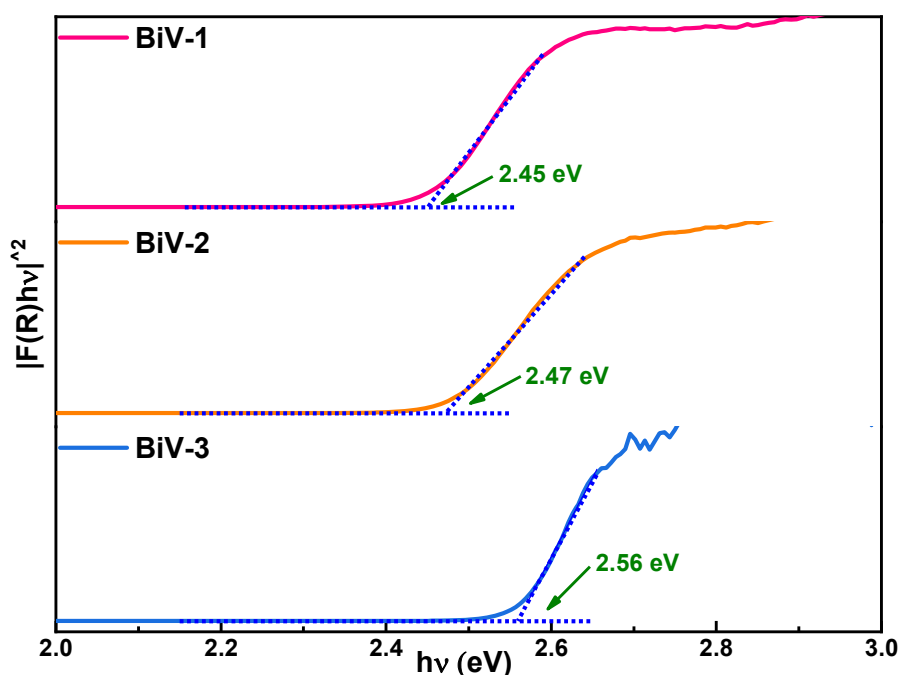


**Fig. 6.7** FESEM image and corresponding EDX elemental mapping for Bi, V, O, and EDX spectrum for  $\text{BiVO}_4$  sample having pyramid/thorns shape (BiV-3). Scale = 2.5  $\mu\text{m}$



### 6.4.3 Optical bandgap determination

The optical response of as-prepared BiVO<sub>4</sub> samples was studied by UV-Vis diffuse reflectance spectroscopy. The obtained spectra were transformed into Tauc plot and is shown in Fig. 6.8. The optical bandgap of BiVO<sub>4</sub> samples was calculated using the Kubelka-Munk function which is used to plot  $(F(R) * hv)^{1/n}$  vs. photon energy ( $hv$ ) graph, where  $F(R)$  is Kubelka-Munk function,  $v$  is light frequency and  $n=1/2$  as BiVO<sub>4</sub> follows direct absorption.<sup>15</sup> The intercept of the tangents to the plots of  $(F(R) * hv)^{1/n}$  vs. photon energy ( $hv$ ) provides the approximate bandgap of 2.45 eV, 2.47 eV and 2.56 eV for BiV-1, Biv-2 and BiV-3 which is close to the reported value (~2.4 eV) for monoclinic BiVO<sub>4</sub>.



**Fig. 6.8** Tauc plots for the band gap energy calculation, for as-prepared BiVO<sub>4</sub> samples

### 6.4.4 X-ray photoelectron spectroscopy analysis

X-ray photoelectron spectroscopy (XPS) was performed to determine the surface chemical composition and chemical states of the prepared BiVO<sub>4</sub> samples. A typical XPS analysis includes a wide energy survey scan (WESS) and a high-

resolution scan for each element possibly available in the material. All the scans were performed at minimum four different sites to reduce error in determining the elemental proportion. Figs. 6.9-6.13 show the survey scan and high-resolution spectra of Bi 4f, V 2p, C 1s, and O 1s for sample BiV-1. All the peaks were calibrated for charge correction with respect to adventitious carbon peak (C 1s at 284.8 eV).

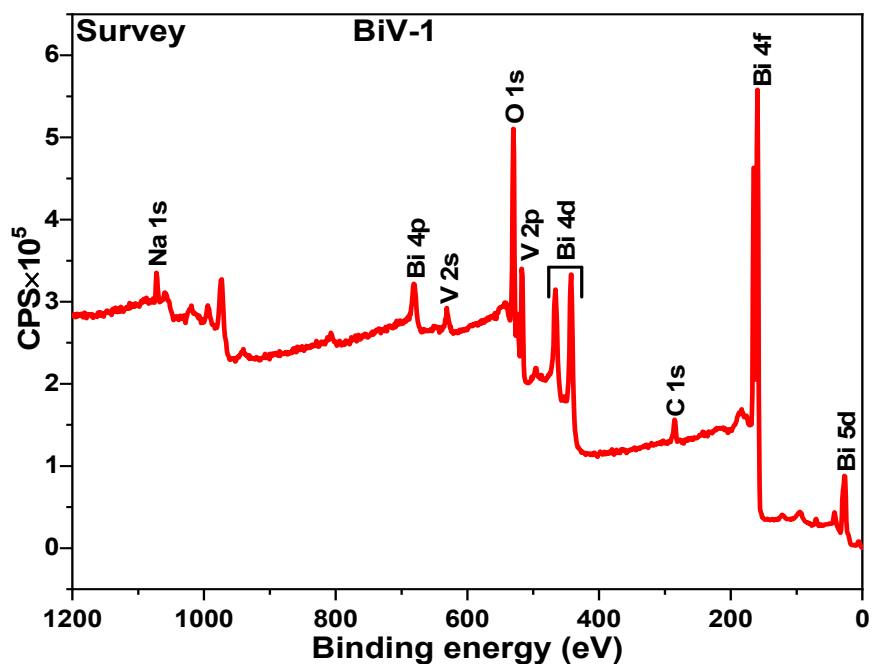


Fig. 6.9 Typical XPS survey spectra for BiV-1

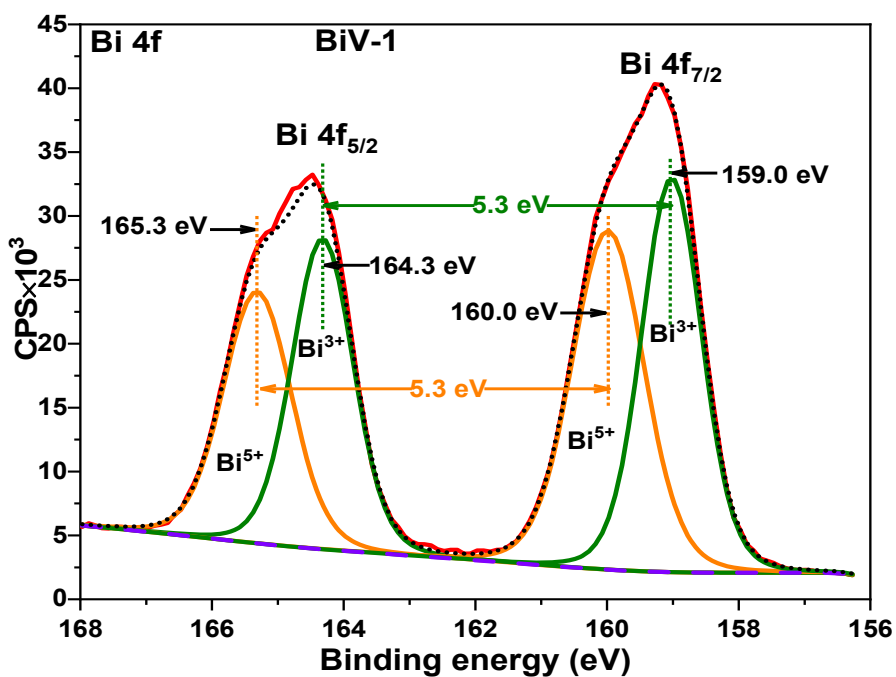


Fig. 6.10 High-resolution spectra of Bi 4f for BiV-1

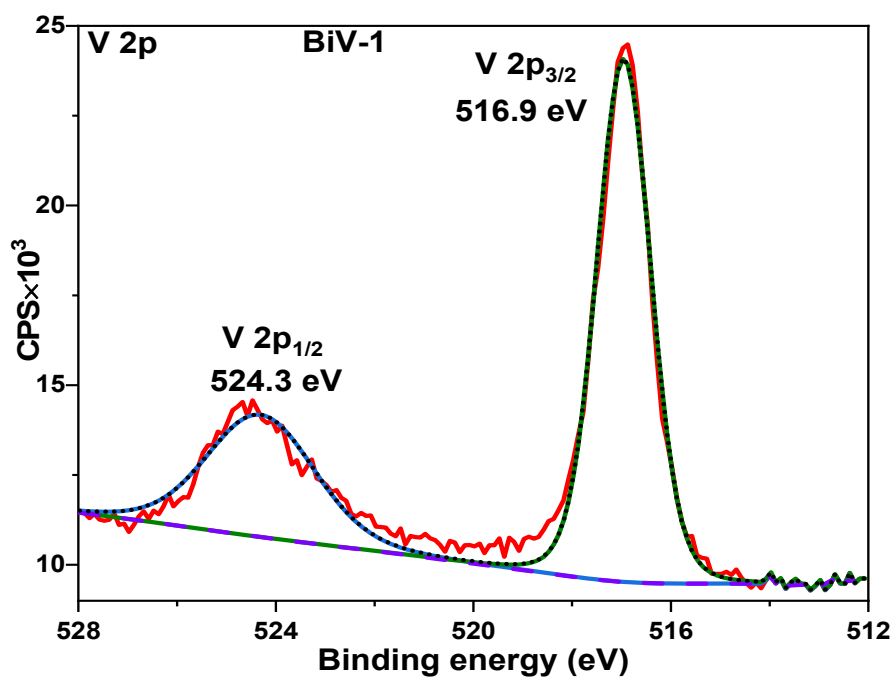


Fig. 6.11 High-resolution spectra of V 2p for BiV-1

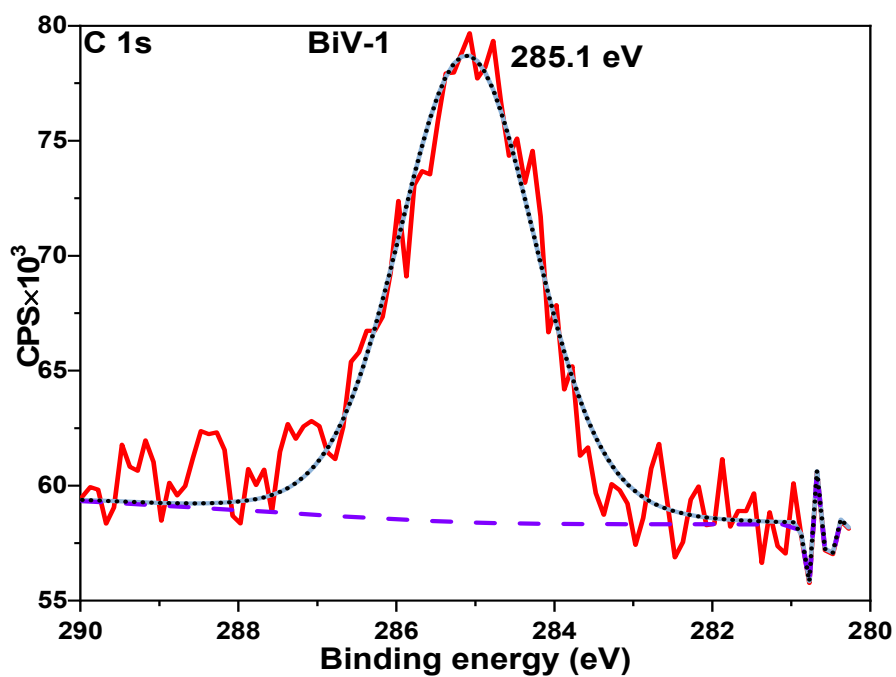


Fig. 6.12 High-resolution spectra of C 1s for BiV-1

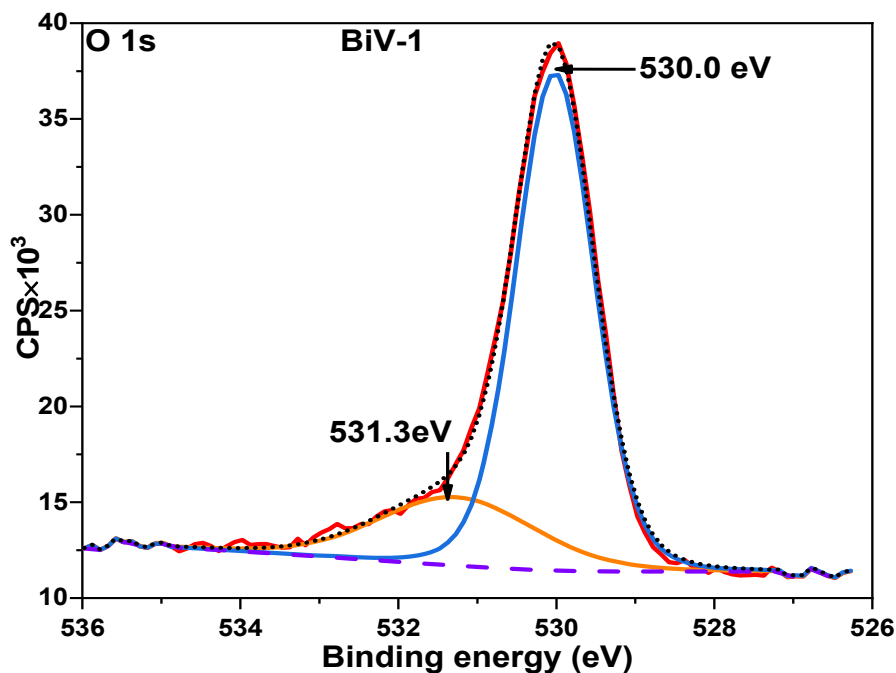


Fig. 6.13. High-resolution spectra of O 1s for BiV-1

The survey spectrum of BiV-1 (Fig. 6.9) contains various peaks including Bi 4f, V 2p, C 1s, and O 1s peaks. Fig. 6.10 reveals that the high-resolution spectrum of Bi 4f contained two sets of spin-orbit doublet peaks for the Bi 4f<sub>7/2</sub> (159.0, 160.0 eV) and Bi 4f<sub>5/2</sub> (164.3, 165.3 eV) orbitals indicating the presence of two Bi states, both close in energy to Bi<sup>3+</sup> (presumably Bi<sup>3+</sup> and Bi<sup>5+</sup>). Using the area of both states listed in Table 6.1, the ratio of the areas of the two peaks was calculated to be nearly 1:1, implying the hypothesis that there might be two distinct Bi atoms in the unit cell, resulting in two different Bi states. Although XRD pattern of the BiV-1 (Fig. 6.3a) did not contain any major phase other than BiVO<sub>4</sub>. Moreover, the separation between both sets of Bi 4f<sub>7/2</sub> and Bi 4f<sub>5/2</sub> peaks ( $\{159.0 \text{ eV}, 164.3 \text{ eV}\}$ ,  $\{160.0, 165.3 \text{ eV}\}$ ) was 5.3 eV, which is a characteristic of Bi<sup>3+</sup> state as stated by Bhatka *et al.*<sup>16</sup> All these arguments reject the dominant presence of another Bi state in BiV-1 sample. There might be some impurities present such as oxides or carbonates (*i.e.*, Bi<sub>2</sub>O<sub>4</sub>, NaBiO<sub>3</sub>) that have Bi<sup>5+</sup> states in their structure, resulting in shoulders in the XPS spectrum of

Bi 4f. Zalecki *et al.*<sup>17</sup> also observed a similar peak splitting in Bi 4f spectrum, although they found the large separation of 2.2 eV between the two Bi states but in our case this peak separation was only 1 eV. Huang and his colleagues also observed the peak splitting in Bi 4f spectrum of BiVO<sub>4</sub> and explained it in relation to pH variation of the precursor solution. According to them, alkaline pH can cause hydrolyzation of Bi<sup>3+</sup>, resulting in Bi<sup>3+</sup> to Bi<sup>5+</sup> conversion.<sup>4</sup>

Fig. 6.11 depicts that the high-resolution spectrum of V 2p that splits into two peaks at binding energies 516.9 eV and 524.3 eV which corresponds to V 2p<sub>3/2</sub> and V 2p<sub>1/2</sub> respectively, indicates the presence of V<sup>5+</sup> oxidation state in BiV-1 matrix. C 1s spectra of BiV-1 (Fig. 6.12) has a single peak at 285.11 which corresponds to adventitious carbon contamination (C-C) while O 1s spectra of BiV-2 (Fig. 6.13) splits into two synthetic peaks at BE 530.0 eV and 531.3 eV, associated to the surface lattice oxygen and adsorbed oxygen (O<sub>2</sub>, OH<sup>-</sup>), respectively.<sup>4,18</sup> Further details of peak fitting and their characteristic bond are provided in Table 6.1.

**Table 6.1.** Bi, V, C and O bonding compositions and corresponding binding energies estimated from deconvolution of high-resolution spectrum of BiV-1 obtained by XPS

Element state		BE (eV)	Characteristic bond	FWHM	Area	%
Bi 4f	Bi 4f <sub>5/2</sub>	165.31	Bi <sup>5+</sup>	1.22	1.84	20.32
	Bi 4f <sub>5/2</sub>	164.32	Bi <sup>3+</sup>	1.10	2.03	22.51
	Bi 4f <sub>7/2</sub>	159.99	Bi <sup>5+</sup>	1.29	2.62	29.03
	Bi 4f <sub>7/2</sub>	159.02	Bi <sup>3+</sup>	1.08	2.54	28.14
V 2p	V 2p <sub>1/2</sub>	524.31		2.57	1.47	31.65
	V 2p <sub>3/2</sub>	516.95	V <sup>5+</sup>	1.29	3.17	68.35
C 1s		285.11	C-C	2.04	7.47	100
O 1s		531.27	O <sub>2</sub> , OH <sup>-</sup>	2.33	4.59	21.48
		530.02	lattice oxygen	1.17	16.79	78.52

Figs. 6.14-6.18 show the survey scan and high-resolution spectra of Bi 4f, V 2p, C 1s, and O 1s for sample BiV-2. Similar to BiV-1, BiV-2 also has two sets of spin-orbit doublet peaks for the Bi 4f<sub>7/2</sub> (158.9, 159.9 eV) and Bi 4f<sub>5/2</sub> (164.2, 165.2 eV) orbitals in the high-resolution spectrum of Bi 4f. The V 2p, C 1s and O 1s of BiV-2 showed almost identical behaviour to that of BiV-1. Thus, the same explanation can be given here. Further details of peak fitting and their characteristic bond are provided in Table 6.2.

**Table 6.2.** Bi, V, C and O bonding compositions and corresponding binding energies estimated from deconvolution of high-resolution spectrum of BiV-2 obtained by XPS

Element state		BE (eV)	Characteristic bond	FWHM	Area	%
Bi 4f	Bi 4f <sub>5/2</sub>	165.21	Bi <sup>5+</sup>	1.24	2.02	17.39
	Bi 4f <sub>5/2</sub>	164.20	Bi <sup>3+</sup>	1.10	3.02	25.97
	Bi 4f <sub>7/2</sub>	159.87	Bi <sup>5+</sup>	1.29	2.82	24.33
	Bi 4f <sub>7/2</sub>	158.91	Bi <sup>3+</sup>	1.09	3.75	32.32
V 2p	V 2p <sub>1/2</sub>	524.18		2.51	1.66	32.16
	V 2p <sub>3/2</sub>	516.79	V <sup>5+</sup>	1.18	3.50	67.84
C 1s		287.16		3.30	3.18	26.53
		284.80	C-C	1.60	8.82	73.47
O 1s		531.25	O <sub>2</sub> , OH <sup>-</sup>	2.73	5.04	19.17
		529.92	lattice oxygen	1.15	21.26	80.83

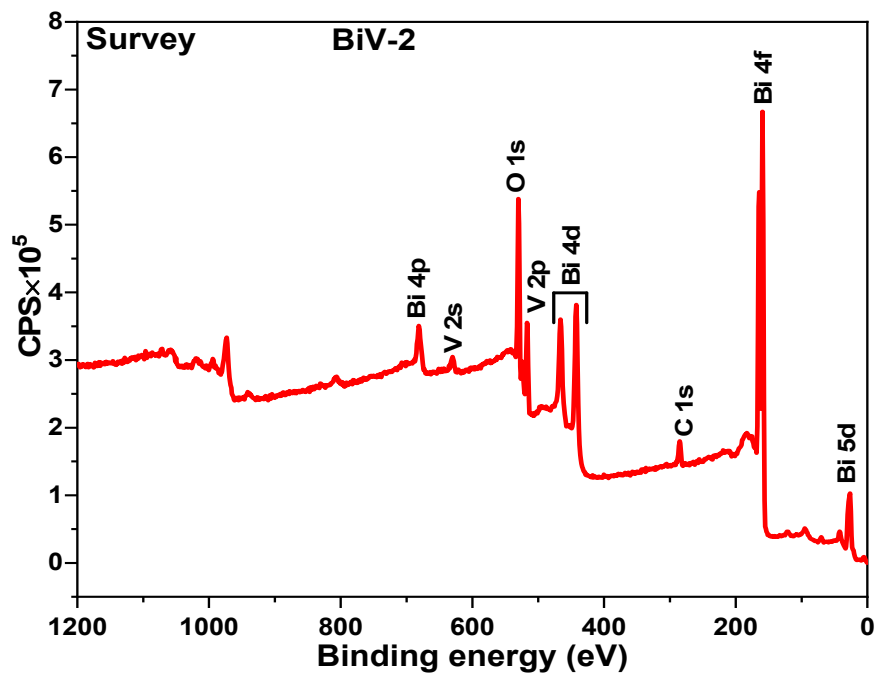


Fig. 6.14 Typical XPS survey spectra for BiV-2

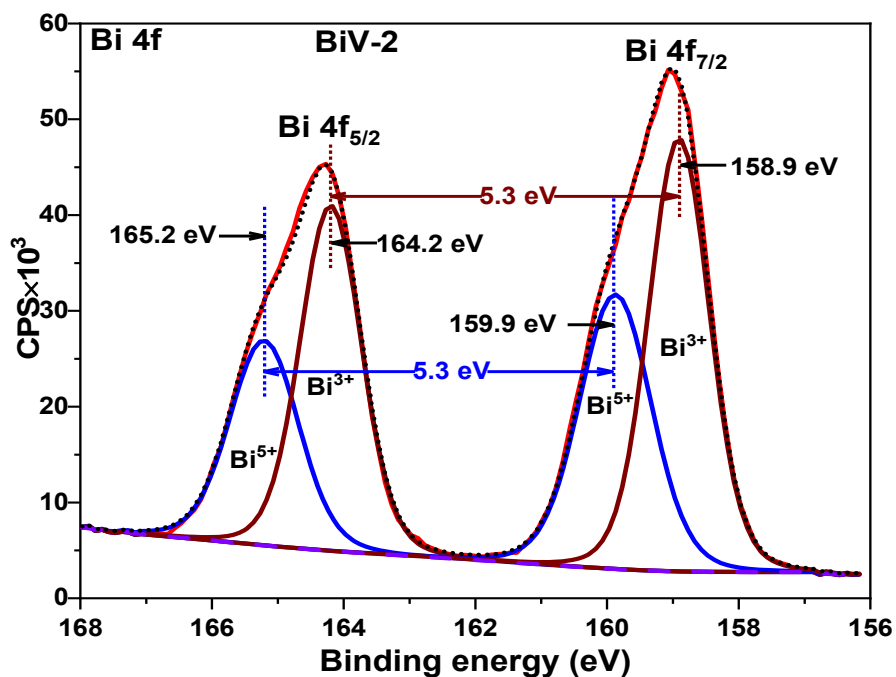


Fig. 6.15 High-resolution spectra of Bi 4f for BiV-2

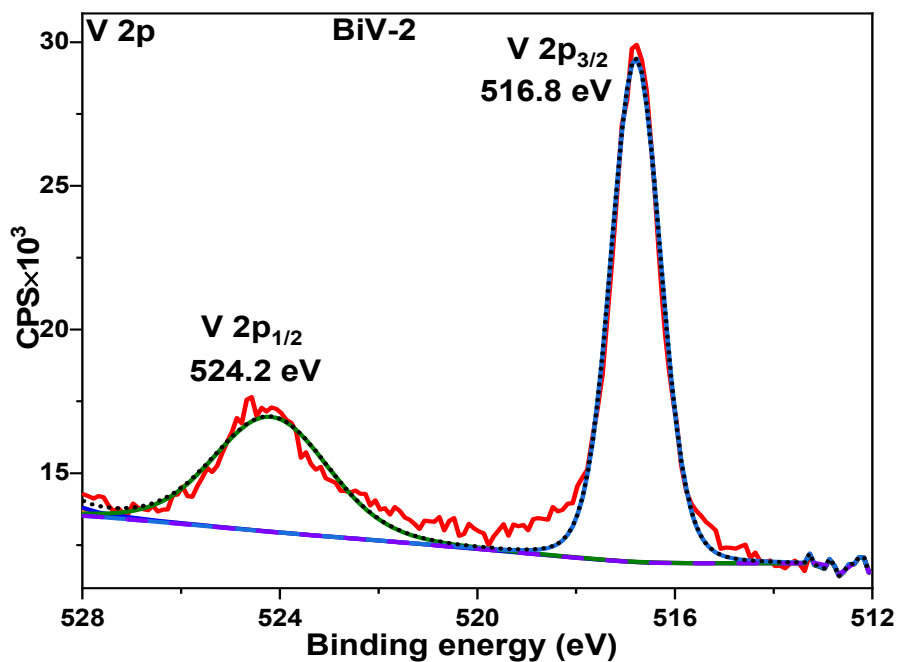


Fig. 6.16 High-resolution spectra of Bi V 2p for BiV-2

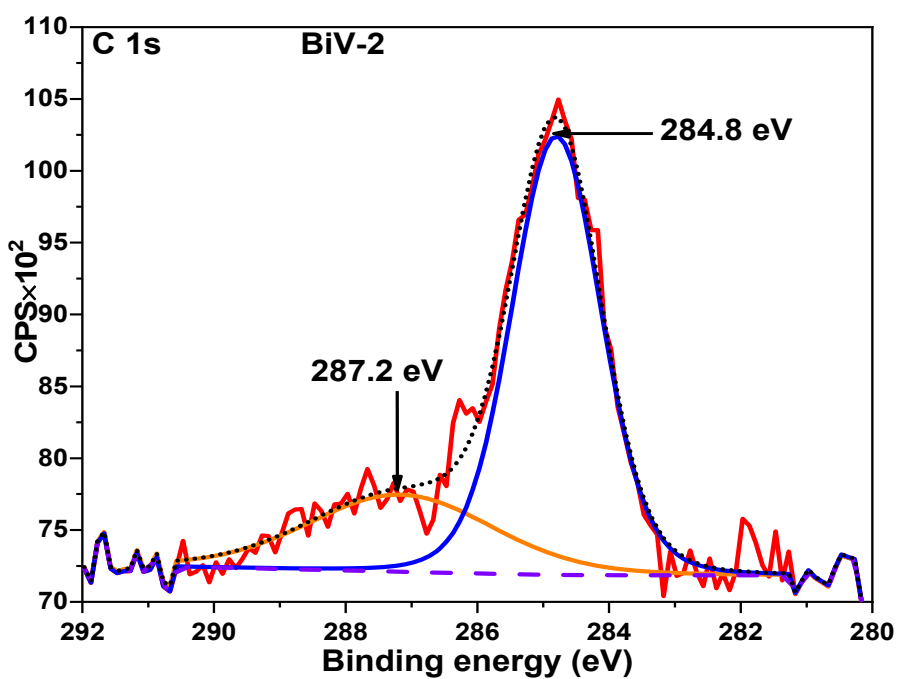


Fig. 6.17 High-resolution spectra of C 1s for BiV-2



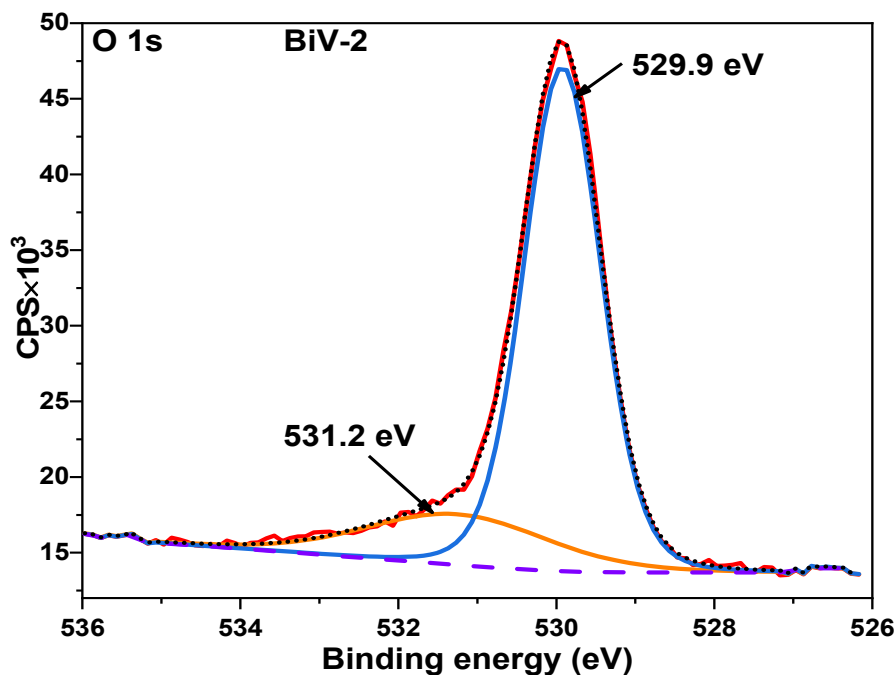


Fig. 6.18 High-resolution spectra of O 1s for BiV-2

Figs. 6.19-6.23 display the survey scan and high-resolution spectra of Bi 4f, V 2p, C 1s, and O 1s for sample BiV-3. Alike BiV-1 and BiV-2, Bi 4f spectrum of BiV-3 (Fig. 6.20) contained three sets of spin-orbit doublet peaks for the Bi 4f<sub>7/2</sub> (158.6, 159.5, 161.2 eV) and Bi 4f<sub>5/2</sub> (163.9, 164.8, 166.5 eV) orbitals in the high-resolution spectrum of Bi 4f showing the separation of 5.3 eV. This may be due to presence of other oxides along with BiVO<sub>4</sub> in the BiV-3 sample. This is in line with the EDX analysis of BiV-3 that revealed the presence of 6% higher Bi than V. Bi<sub>2</sub>O<sub>4</sub> contains mixed valence states in its structure as alternative arrangement of Bi<sup>3+</sup> and Bi<sup>5+</sup> states.<sup>19,20</sup> Although XRD pattern of the BiV-3 contain no other major phase than BiVO<sub>4</sub> but there is a possibility of peak overlapping. After a thorough examination of the XRD patterns of other bismuth oxides, the peak positioned at 26.7° was found to match with Bi<sub>2</sub>O<sub>4</sub> which is different from FTO peak at 26.4°. Thus, the Bi<sup>5+</sup> from Bi<sub>2</sub>O<sub>4</sub> may be accountable for the shifting of Bi 4f peaks towards higher binding energies.<sup>21</sup> It can be concluded that binding energy sets (158.6 eV, 163.9 eV), (159.5

eV, 164.8 eV), and (161.2 eV, 166.5 eV) are associated with monoclinic  $\text{BiVO}_4$  ( $\text{Bi}^{3+}$ ),  $\text{Bi}_2\text{O}_4$  ( $\text{Bi}^{3+}$ ) and  $\text{Bi}_2\text{O}_4$  ( $\text{Bi}^{5+}$ ), respectively.

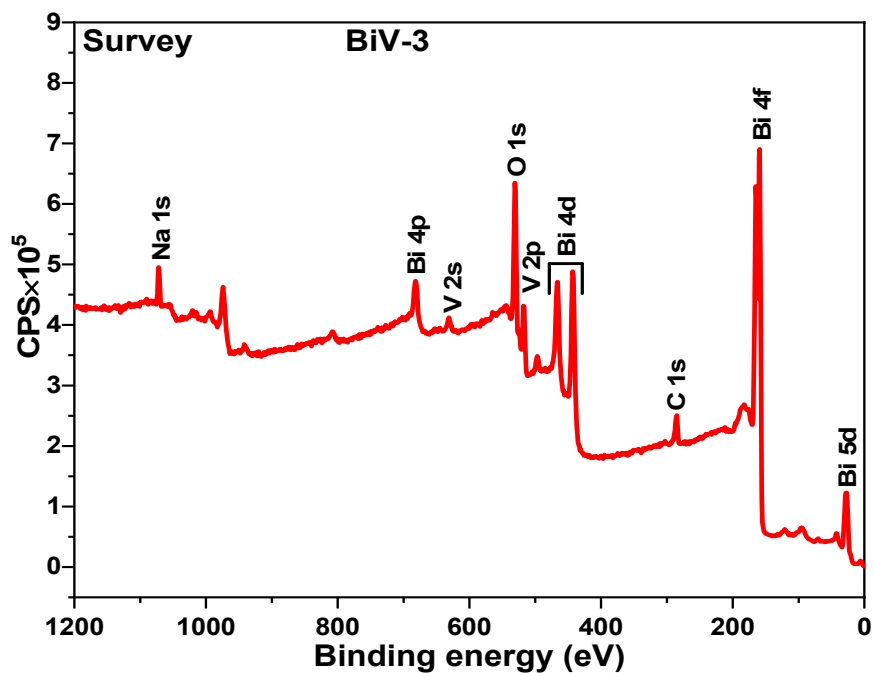


Fig. 6.19 Typical XPS survey spectra for BiV-3

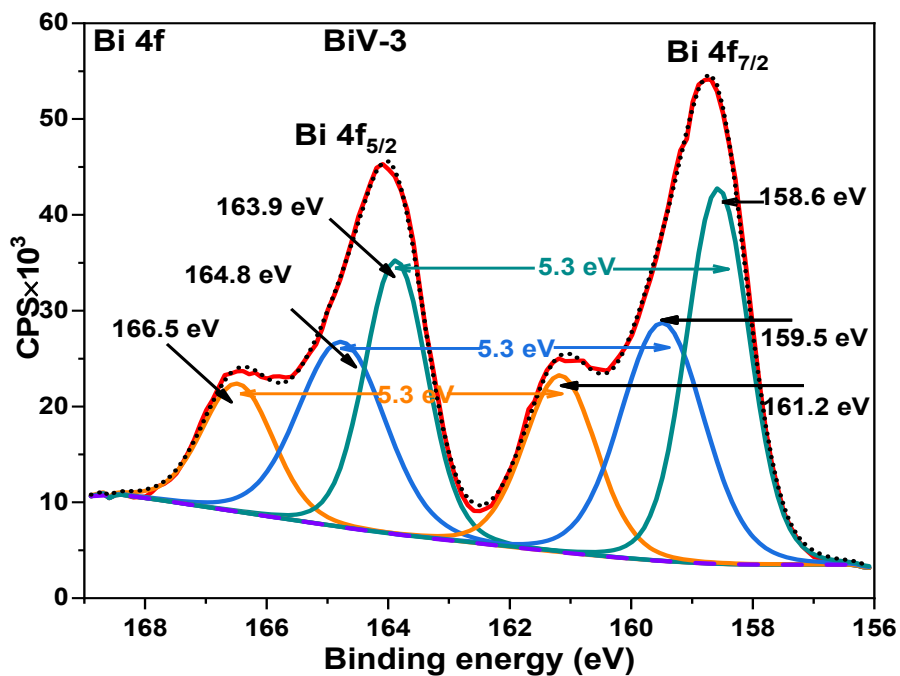


Fig. 6.20 High-resolution spectra of Bi 4f for BiV-3

The V 2p spectrum of BiV-3 (Fig. 6.21) splits into three synthetic peaks at the binding energies 516.6 eV, 518.1 eV and 524.3 eV. V  $p_{3/2}$  has two peaks at 516.6 eV and 518.1 eV which may be assigned to  $V^{5+}$  species in  $BiVO_4$  and  $V_2O_5$ , respectively<sup>22,23</sup>. Although, there was no distinct XRD peak of  $V_2O_5$  found in BiV-3 which may be due to the overlapping of peaks. Thus, it can be stated that there are some impurities present in BiV-3 film in the form of  $Bi_2O_4$  and  $V_2O_5$ .

C 1s spectra of BiV-3 (Fig. 6.22) deconvoluted in two peaks at 284.8 eV and 286.8 eV which corresponds to adventitious carbon contamination, C-C and C-O species respectively, while O 1s spectra of BiV-3 (Fig. 6.23) splits into three synthetic peaks at BE 529.8 eV, 531.3 eV, and 533.6 eV were attributed to the surface lattice oxygen and adsorbed oxygen ( $O_2$ ,  $OH^-$ ) and oxygen vacancies, respectively. Further details of peak fitting and their characteristic bond are provided in Table 6.3.

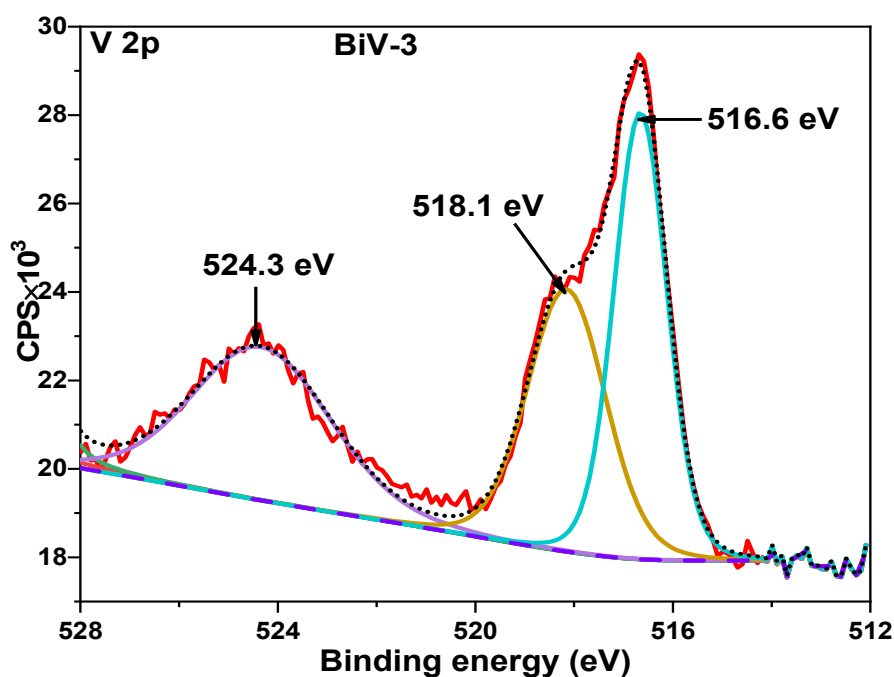


Fig. 6.21 High-resolution spectra of V 2p for BiV-3

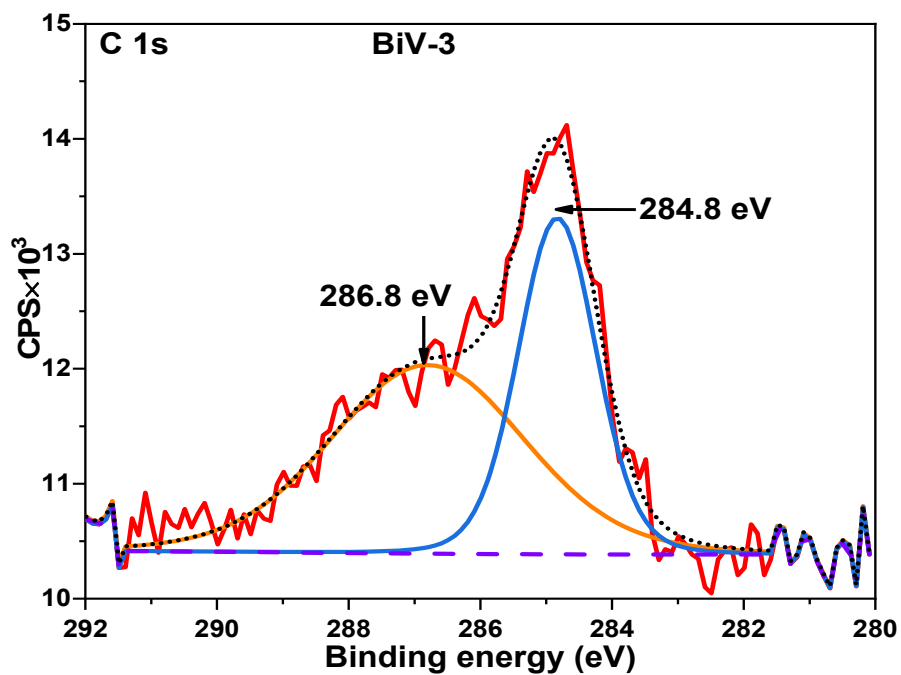


Fig. 6.22 High-resolution spectra of C 1s for BiV-3

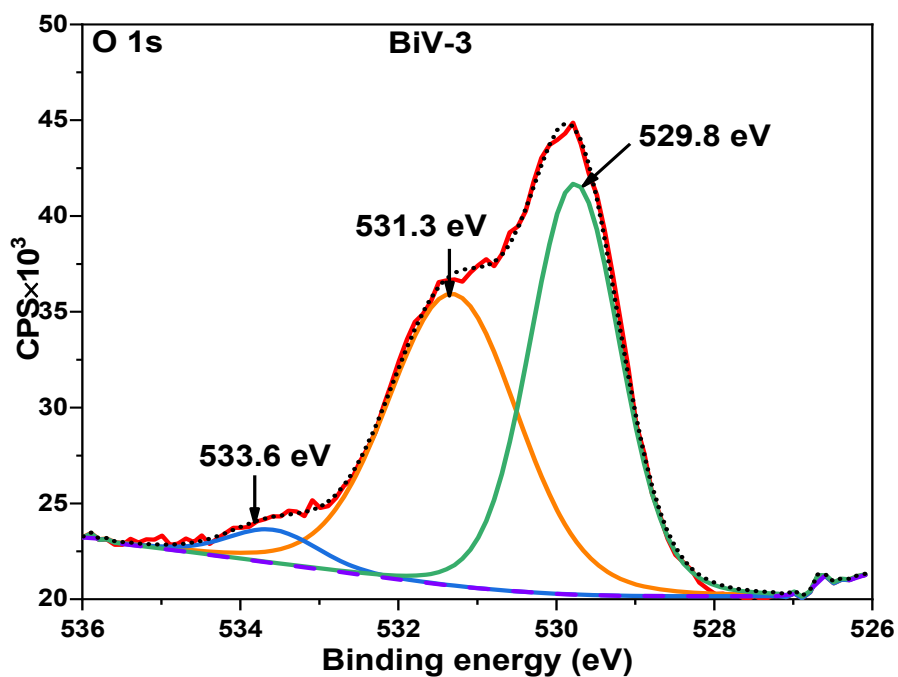


Fig. 6.23 High-resolution spectra of O 1s for BiV-3

**Table 6.3.** Bi, V, C and O bonding compositions and corresponding binding energies estimated from deconvolution of high-resolution spectrum of BiV-3 obtained by XPS

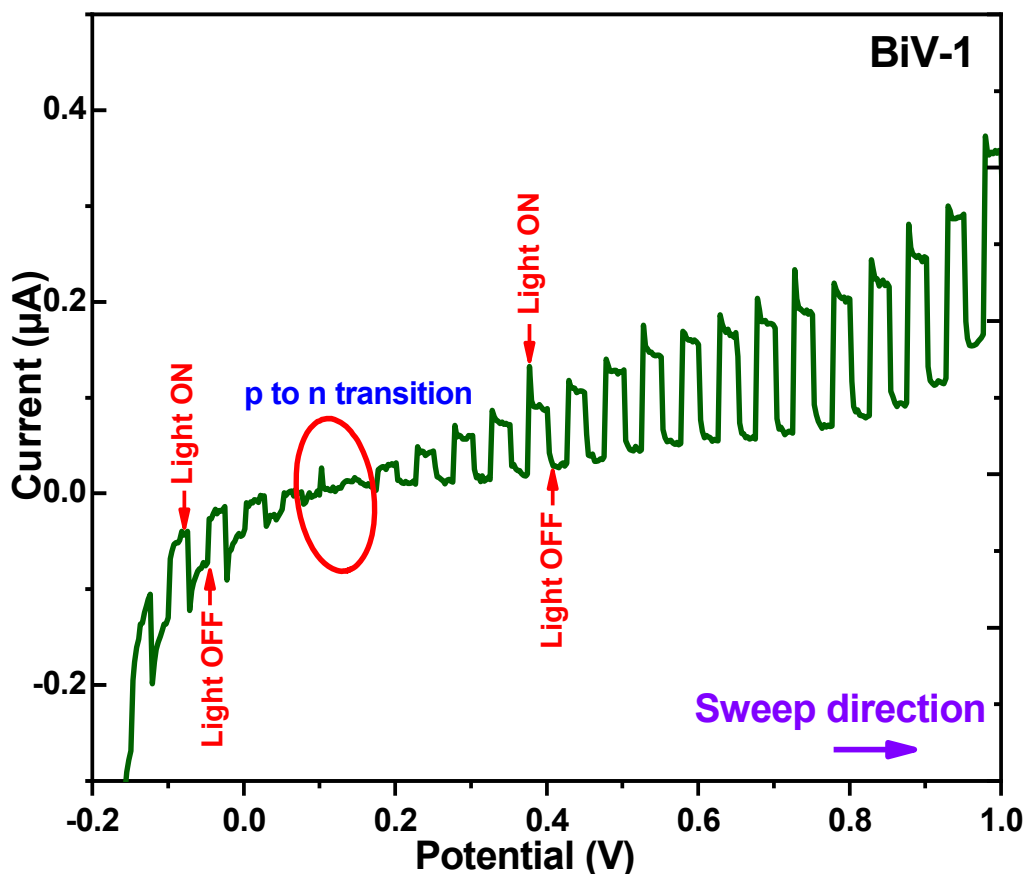
Element state		BE (eV)	Characteristic bond	FWHM	Area	%
<b>Bi 4f</b>	Bi 4f <sub>5/2</sub>	166.48	Bi <sup>5+</sup>	1.38	1.40	9.22
	Bi 4f <sub>5/2</sub>	164.76	Bi <sup>3+</sup>	1.69	2.48	16.31
	Bi 4f <sub>5/2</sub>	163.87	Bi <sup>3+</sup>	1.21	2.63	17.30
	Bi 4f <sub>7/2</sub>	161.17	Bi <sup>5+</sup>	1.41	1.98	13.03
	Bi 4f <sub>7/2</sub>	159.48	Bi <sup>3+</sup>	1.62	3.08	20.23
	Bi 4f <sub>7/2</sub>	158.57	Bi <sup>3+</sup>	1.22	3.64	23.92
<b>V 2p</b>	V 2p <sub>1/2</sub>	524.34	-	3.15	1.72	30.03
	V 2p <sub>3/2</sub>	518.15	V <sup>5+</sup> (V <sub>2</sub> O <sub>5</sub> )	1.81	1.80	31.41
	V 2p <sub>3/2</sub>	516.65	V <sup>5+</sup> (BiVO <sub>4</sub> )	1.28	2.20	38.56
<b>C 1s</b>		286.80	C-O	3.47	10.26	58.18
		284.83	C-C	1.40	7.38	41.82
<b>O 1s</b>		533.58	oxygen vacancies	1.34	1.29	3.83
		531.31	O <sub>2</sub> , OH <sup>-</sup>	1.94	16.33	48.51
		529.76	lattice oxygen	1.35	16.05	47.67

#### 6.4.5 Photoelectrochemical measurements

In this section, photoelectrochemical properties of the prepared BiVO<sub>4</sub> samples were investigated through different photoelectrochemical measurements such as linear sweep voltammetry, photocurrent at fixed potential under dark, light, and chopped irradiation. Only the results of samples BiV-1 and BiV-3 will be discussed here as the photoanode for sample BiV-2 could not be prepared due to very poor dispersion in the solvent, so it was not possible to prepare its photoanode using spray coating. An attempt was also made to obtain the BiV-2 sample by the drop-cast method but the deposited film peeled off after being put into the electrolyte, so photoelectrochemical measurements couldn't be performed for BiV-2.

### 6.4.5.1 Current-potential measurements (LSV)

Fig. 6.24 shows the linear sweep voltammogram of BiV-1 under chopped UV-vis irradiation while sweeping the bias from -1.0 to +1.0 V. It was observed that the cathodic photocurrent converted to anodic photocurrent at about +0.15 V (SCE) or +0.39 V (NHE).

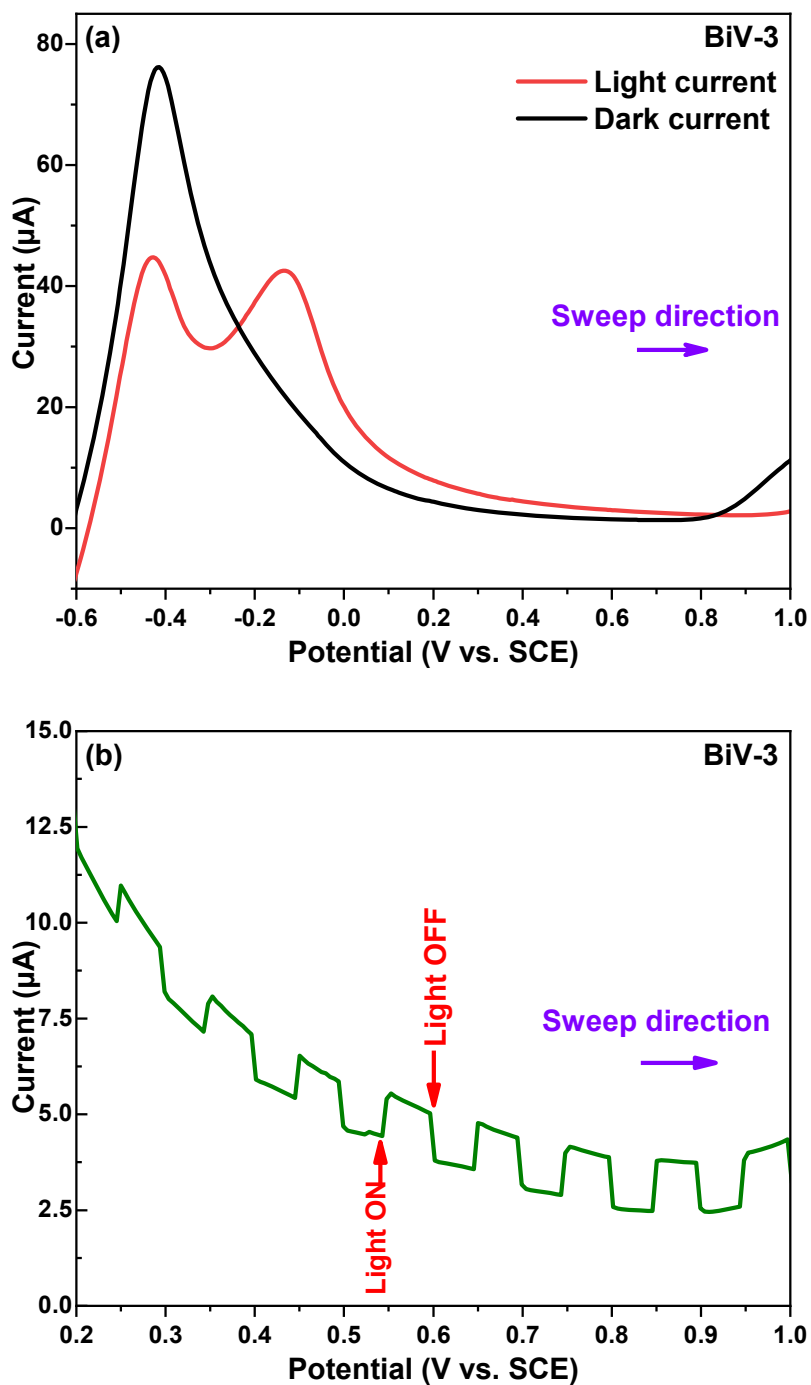


**Fig. 6.24** Chopped linear sweep voltammogram of BiV-1 from -0.2 V to +1.0 V under UV-vis irradiation. Irradiation source 450 W Xe lamp, scan rate =  $5 \text{ mV s}^{-1}$ , electrolyte 0.1 M  $\text{KClO}_4$ , 10s exposure-dark cycle.

Chen *et al.*<sup>24</sup> has also observed the similar photocurrent switching effect in  $\text{BiVO}_4$  electrodes at +0.24 V (SCE) which is consistent with the present study. They also stated that the photocurrent switching potentials can be influenced by the presence of electron donor/acceptor species. When electrode is irradiated, it behaves as a p-type semiconductor which means the bands bend downwards at the electrolyte interface, so

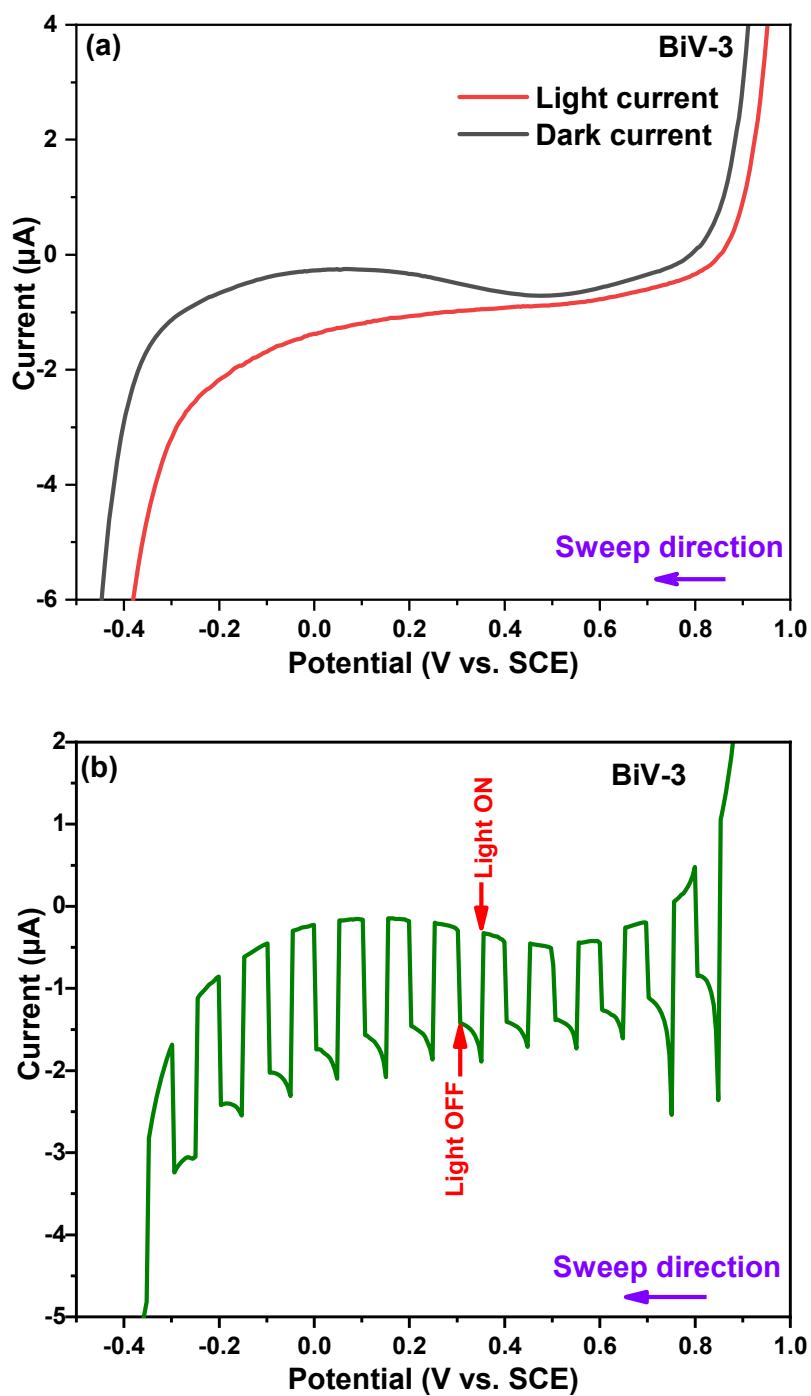
upon irradiation the electrons migrate to the surface under the influence of the space charge region and reduce the oxygen dissolved in the electrolyte resulting in cathodic photocurrents.<sup>24</sup> Fig. 6.25a depicts the photocurrent response of BiV-3 photoelectrode under dark and light conditions, whereas Fig. 6.25b displays the photocurrent response under chopped UV-vis irradiation while sweeping the bias from -1.0 to +1.0 V. It can be seen in Fig. 6.25a that there is a much larger oxidation peak at about -0.4 V in dark which turns in to two clear peaks (-0.4 & -0.15 V) during light on and shows the photocurrent switching from cathodic to anodic photocurrent at -0.24 V. Chopped LSV of BiV-3 (Fig. 6.25b) further confirms that system behaves as an n-type semiconductor in the positive applied bias when sweeping the bias from negative to positive.

The photocurrent behavior of BiV-3 electrode was investigated when sweeping the potential from positive to negative (Fig. 6.26a and b). While sweeping bias from positive to negative, we see the only cathodic photocurrent through the BiV-3 electrode, as it behaves a p-type semiconductor where the majority charge carriers are valence band holes.



**Fig. 6.25** Linear sweep voltammogram for BiV-3 while sweeping from negative to positive potential under (a) continuous light condition in the range, -0.6 V to +1.0 V, and (b) Chopped light in the range +0.2 V to +1.0 V under UV-vis irradiation. Irradiation source 450 W Xe lamp, Scan rate =  $5 \text{ mV s}^{-1}$ , electrolyte 0.1 M  $\text{KClO}_4$ , 10s exposure-dark cycle.

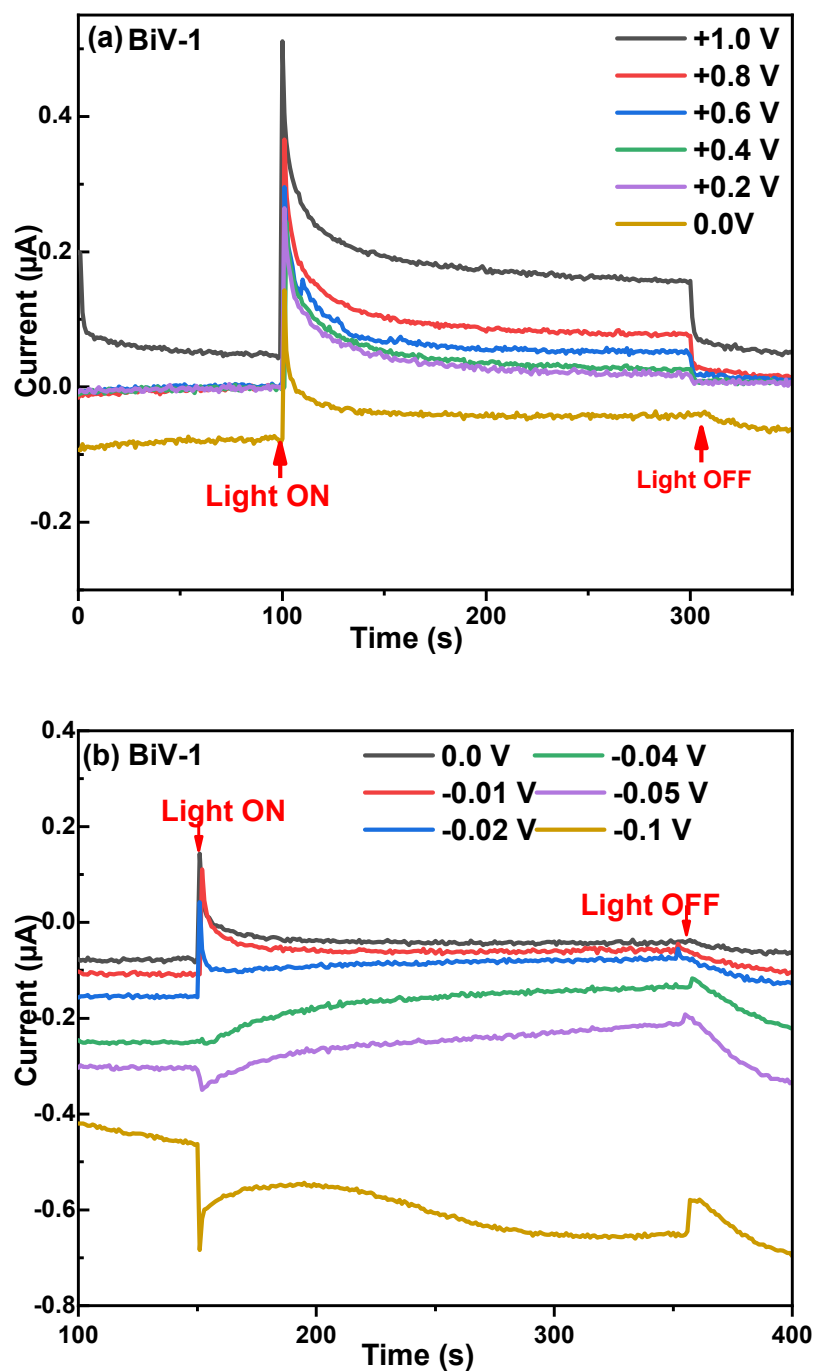




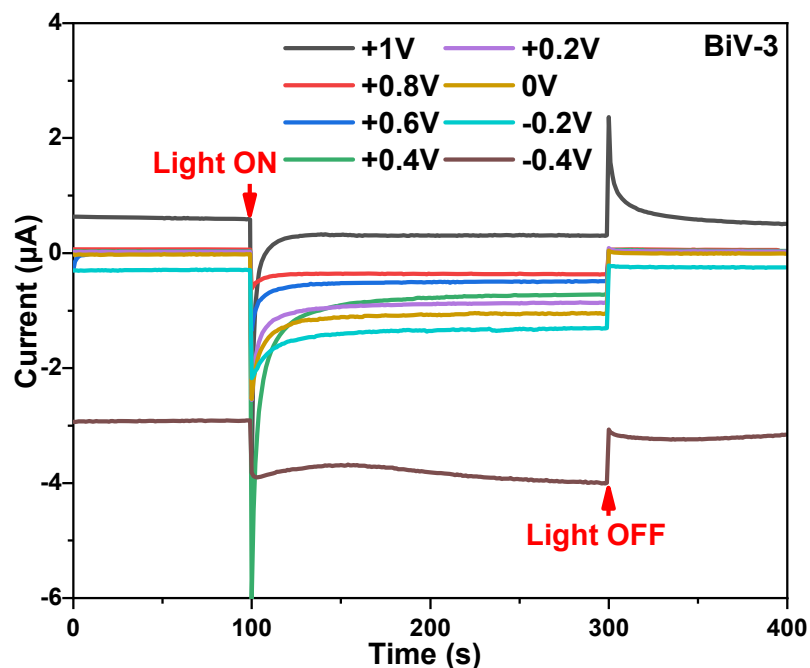
**Fig. 6.26** Linear sweep voltammogram for BiV-3 while sweeping from positive to negative potential (a) continuous light condition in the range, -0.4 V to +1.0 V, and (b) Chopped light in the range -0.4 V to +1.0 V under UV-vis irradiation. Irradiation source 450 W Xe lamp, Scan rate =  $5 \text{ mV s}^{-1}$ , electrolyte 0.1 M  $\text{KClO}_4$ , 10s exposure-dark cycle.

### 6.4.5.2 Current-time measurements at fixed potential

Fig. 6.27a-b demonstrates the photocurrent - time response recorded for BiV-1 and Fig. 6.28 for BiV-3 at certain fixed potentials.



**Fig. 6.27** Photocurrent response for BiV-1 at various potentials ranging from, (a) 1.0 V to 0.0 V, (b) 0.0 to -0.1 V. Irradiation source 450 W Xe lamp,  $\text{SR} = 5 \text{ mV s}^{-1}$ , electrolyte 0.1 M  $\text{KClO}_4$ .

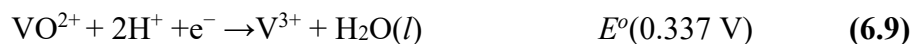
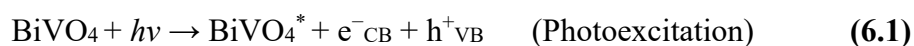


**Fig. 6.28** Photocurrent response for BiV-3 at various potentials ranging from +1.0 V to -0.4 V. Irradiation source 450 W Xe lamp, Scan rate =  $5 \text{ mV s}^{-1}$ , electrolyte 0.1 M  $\text{KClO}_4$ .

The photocurrent was measured for 200 s at each applied potential. It can be depicted from Fig. 6.27a and b that amplitude of photocurrent generated from BiV-1 electrode is not significant (nA range) and the switching potential lies somewhere between +0.2 V and -0.1 V, which are in consistent with the results obtained from liner sweep voltammetry. BiV-1 photoelectrode behaves as n-type semiconductor in the applied positive bias whereas it shows p-type photocurrent in the applied negative bias. Similar to LSV results, BiV-3 photoelectrode (Fig. 6.28) showed negative photocurrent (p-type) while measuring photocurrent at different potentials ranging from +1.0 V to -0.4 V in 200 seconds chopped UV-Vis irradiation.

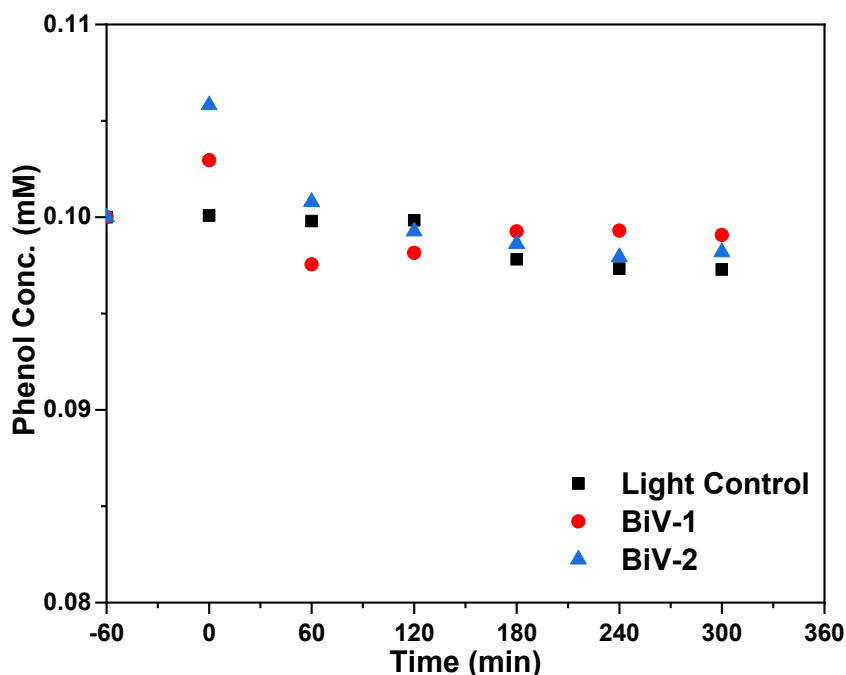
The  $\text{BiVO}_4$  samples showed both anodic (positive) and cathodic (negative) photocurrent depending on the applied potential range. The VB and CB edge position of  $\text{BiVO}_4$  has been reported as +2.9 eV and +0.5V (vs. NHE) respectively. Multiple oxidation states are possessed by both Bi (+1, +2, +3, +5) and V (+2, +3, +4, +5) so there are high chances of modification of material during electrochemical and

photoelectrochemical reactions. Additionally, prepared BiVO<sub>4</sub> samples might have some impurities of other oxides such as Bi<sub>2</sub>O<sub>3</sub>, V<sub>2</sub>O<sub>5</sub>, Bi<sub>2</sub>O<sub>4</sub> etc. which can readily dissolve in the solution and get oxidized or reduced on the availability of charge carriers with or without applying external bias. Following electrochemical or photoelectrochemical reactions (equations 6.1-6.10) possibly occurred in this PEC setup.<sup>25-28</sup>



#### 6.4.6 Photocatalytic activity

The as-prepared BiVO<sub>4</sub> samples, BiV-1 and BiV-2 were explored to evaluate their photocatalytic efficacy for the photocatalytic degradation of phenol as a model organic pollutant, under UV-Vis irradiation. The results are shown in Fig. 6.29, which reveals that BiV-1 or BiV-2 did not show any photocatalytic degradation of phenol in 5 hours of irradiation possibly due to the self-recombination.<sup>29</sup> The non-photocatalytic activity by BiVO<sub>4</sub> was further investigated using a chemical probe.



**Fig. 6.29.** Photolytic and photocatalytic phenol degradation using BiV-1 and BiV-2 samples under UV-Vis irradiation. (1kW Xe lamp, Initial phenol concentration: 0.1 mM, Photocatalyst: 100 mg L<sup>-1</sup>)

#### 6.4.7 Chemical probe study

To understand the non-photocatalytic activity by BiVO<sub>4</sub>, chemical probe study was performed to detect reactive oxygen species whether they are being generated or not. The VB edge position of BiVO<sub>4</sub> has been reported to be situated at ~+2.9 eV (vs. NHE) which, is more positive than the electrochemical potential of water oxidation (+2.73 eV, vs. NHE), hence favourable to generate the hydroxyl radicals (<sup>•</sup>OH). In a photocatalytic process photogenerated holes can either oxidize adsorbed/surface hydroxyl groups or oxidize water, resulting in <sup>•</sup>OH radicals (equations 6.11 and 6.12).



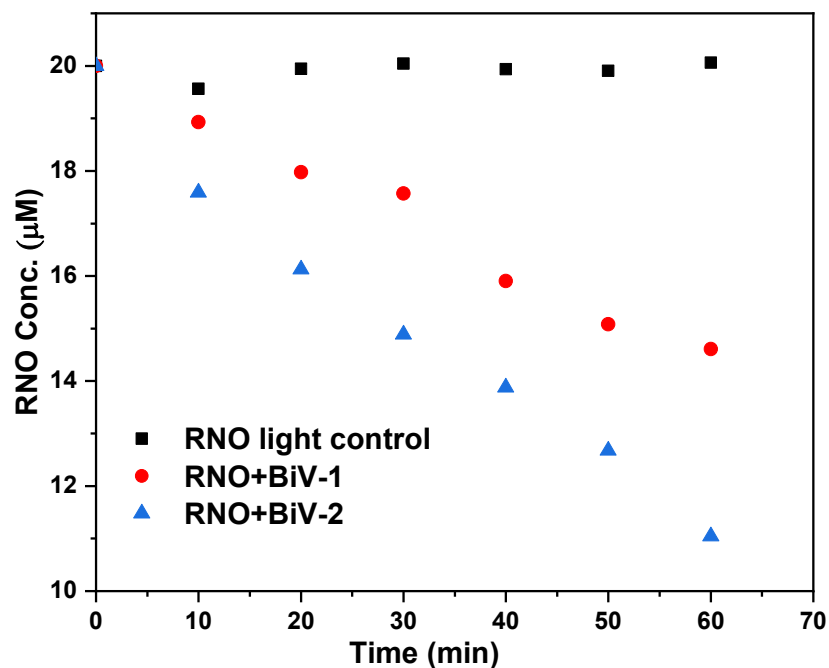
Therefore, <sup>•</sup>OH radical probe study was performed to analyse the photocatalytic activity of BiVO<sub>4</sub>. p-nitrosodimethylaniline (RNO) is being used as an

efficient scavenger for  $\cdot\text{OH}$  radicals, with the first recommendation by Kraljic and Trumbore in 1965.<sup>30,31</sup> RNO can selectively trap and scavenge the hydroxyl radicals. Baxendale and Khan<sup>32</sup> measured the absolute rate constant of the reaction between hydroxyl radicals and RNO to  $1.25 \times 10^{10} \text{ M}^{-1} \text{ s}^{-1}$ . These  $\cdot\text{OH}$  radicals can oxidize RNO by converting yellow coloured nitroso (R-N=O) group into colourless R-N=O $\cdot\text{OH}$ , where R is dimethylaniline (C<sub>8</sub>H<sub>10</sub>N) compound (equation 6.13). Therefore, the photocatalytic degradation of RNO was examined as a mean to detect the  $\cdot\text{OH}$  radicals produced by BiVO<sub>4</sub>.



The photocatalytic degradation of RNO was analysed for 60 min in the stirred tank reactor under the same conditions which was followed for phenol degradation. 200 mL of 20  $\mu\text{M}$  RNO solution was poured in stirred tank reactor with 20 mg of BiVO<sub>4</sub> photocatalysts (BiV-1 and BiV-2). In every 10 min, 3 mL sample was taken out and was quantified by measuring its absorbance at wavelength 440 nm using a UV-Vis spectrophotometer. The control experiment was done in the absence of photocatalyst. It can be seen in Fig. 6.30 that RNO concentration is getting reduced with time for both BiV-1 and BiV-2 suggesting the generation of hydroxyl radicals. In 60 min, 27% discolouration of the yellow-coloured solution was observed for BiV-1, whereas it was 45% for BiV-2, suggesting it to be more efficient than BiV-1 in generating hydroxyl radicles probably due to the presence of mixed phase BiVO<sub>4</sub> as observed in XRD spectra of BiV-2 (Fig. 6.3a). Wang *et al.* have also reported the enhanced photocurrent and photo electrocatalytic activity for mixed phase BiVO<sub>4</sub> compared to single phase BiVO<sub>4</sub>.<sup>33</sup> Although even after producing  $\cdot\text{OH}$  radicals, BiVO<sub>4</sub> did not show photocatalytic activity for phenol degradation, possibly due to its positive conduction band edge potential ( $\sim +0.5 \text{ V}$  vs. NHE) which is not enough to

reduce oxygen, so  $e^-h^+$  recombination dominates, resulting in poor photocatalytic activity.



**Fig. 6.30.** Photolytic and photocatalytic RNO degradation using BiV-1 and BiV-2 samples under UV-Vis irradiation. (Initial RNO concentration: 20  $\mu\text{M}$ , Photocatalyst: 100  $\text{mg L}^{-1}$ )

## 6.5 Conclusions

In summary, different morphologies of  $\text{BiVO}_4$  were synthesized using different methods and investigated for their physiochemical properties by FESEM, EDX, XRD, Raman, DRS, XPS, photoelectrochemical measurements and correlated to the photocatalytic activities. FESEM micrographs confirmed the sphere-like (BiV-1) and plate-like  $\text{BiVO}_4$  particles (BiV-2) which were synthesized by a hydrothermal method in a Parr reactor and pyramid/thorns-like morphology of  $\text{BiVO}_4$  (BiV-3) were vertically grown on FTO coated glass using seed-mediated method.  $\text{BiVO}_4$  spheres had an average diameter of about 2.5  $\mu\text{m}$ ,  $\text{BiVO}_4$  nano plates had a thickness of 30-70 nm, and  $\text{BiVO}_4$  pyramids/thrones had a length of 4-8  $\mu\text{m}$ , a diameter of 200-500 nm at the bottom and a tip of about 20-50 nm. The agglomeration of these pyramids

resulted in the formation of Sea urchin-like structures having an average diameter of 20-25  $\mu\text{m}$ . XRD patterns and Raman spectra confirmed the formation of  $\text{BiVO}_4$ . The XRD patterns of BiV-1 and BiV-3 had only monoclinic  $\text{BiVO}_4$  phase while BiV-2 contained a heterophase pattern including tetragonal zircon and monoclinic phases. The EDX analysis gave the ratio of At% of Bi:V to be almost 1:1 in BiV-1 (Bi - 22.2%, V-21.2%) and BiV-2 (Bi-24.6%, V-24.6%) indicating the absence of other compounds however BiV-3 had 6% more Bi atoms than V (Bi-20.7%, V-14.8%) implying the presence of unreacted Bismuth or other oxides in the sample. DRS spectra were transformed into Tauc plot which provided the approximate bandgap of 2.45 eV (BiV-1), 2.47 eV (BiV-2), and 2.56 eV (BiV-3).

XPS measurements were performed to determine the surface chemical composition and chemical states of the prepared  $\text{BiVO}_4$  samples. Interestingly, high-resolution spectrum of Bi 4f for BiV-1 and BiV-2 contained two sets of spin-orbit doublet peaks for the Bi 4f<sub>7/2</sub> (159.0, 160.0 eV) and Bi 4f<sub>5/2</sub> (164.3, 165.3 eV) indicating the presence of two Bi states ( $\text{Bi}^{3+}$  and  $\text{Bi}^{5+}$ ) due to some impurities such as oxides or carbonates (*i.e.*,  $\text{Bi}_2\text{O}_4$ ,  $\text{NaBiO}_3$ ). Likewise Bi 4f spectra of BiV-3 had three sets of spin-orbit doublet peaks suggesting the presence of other oxides along with  $\text{BiVO}_4$ . Considering the EDX results (6% higher Bi atom) and deep XRD analysis it was concluded that the other oxide may be  $\text{Bi}_2\text{O}_4$  which contains mixed valence states in its structure as alternative arrangement of  $\text{Bi}^{3+}$  and  $\text{Bi}^{5+}$  states. The V 2p spectrum of BiV-3 also indicated the presence of  $\text{V}_2\text{O}_5$ . BiV-1 displayed cathodic to anodic photocurrent switching at about +0.15 V (SCE) or +0.39 V (NHE). Surprisingly, nature of photocurrent for BiV-3 was changed with potential sweeping direction. It behaved as an n-type semiconductor (positive photocurrent) in the positive applied bias when sweeping the bias from negative to positive and vice versa. Prepared



samples were also tested for their efficacy for the photocatalytic degradation of phenol but did not show any photocatalytic degradation of phenol. To understand the non-photocatalytic activity by BiVO<sub>4</sub>, chemical probe study was performed by observing RNO photocatalytic discolouration to detect hydroxy radicals. RNO concentration is getting reduced with time for both BiV-1 and BiV-2 suggesting the generation of hydroxyl radicals. In 60 min, 27% discolouration of the yellow-coloured solution was observed for BiV-1, whereas it was 45% for BiV-2, indicating the generation of hydroxyl radicals. Despite producing  $\cdot\text{OH}$  radicals, BiVO<sub>4</sub> did not show photocatalytic activity for phenol degradation, possibly due to its positive conduction band edge potential ( $\sim+0.5$  V vs. NHE) which is not enough to reduce oxygen, so  $e^-h^+$  recombination dominates, resulting in poor photocatalytic activity.

## 6.6 References

1. Ganeshbabu, M., Kannan, N., Venkatesh, P. S., Paulraj, G., Jeganathan, K., & MubarakAli, D. Synthesis and characterization of BiVO<sub>4</sub> nanoparticles for environmental applications. *RSC Adv.* 2020, **10**, 18315–18322.
2. A., M., J., M., Ashokkumar, M. & Arunachalam, P. A review on BiVO<sub>4</sub> photocatalyst: Activity enhancement methods for solar photocatalytic applications. *Appl. Catal. A Gen.* 2018, **555**, 47–74.
3. Tokunaga, S., Kato, H. & Kudo, A. Selective preparation of monoclinic and tetragonal BiVO<sub>4</sub> with scheelite structure and their photocatalytic properties. *Chem. Mater.* 2001, **13**, 4624–4628.
4. Huang, J. G., Wang, B., Pang, S., Zhang, X. Y., Yang, X. Y., Guo, X. T., & Wang, X. S. Effects of pH value and hydrothermal time on the structure and photocatalytic activity of monoclinic-scheelite BiVO<sub>4</sub>. *Optoelectron. Adv. Mater. Rapid Commun.* 2015, **9**, 1273–1279.
5. Zhou, L., Wang, W., Zhang, L., Xu, H. & Zhu, W. Single-crystalline BiVO<sub>4</sub> microtubes with square cross-sections: microstructure, growth mechanism, and photocatalytic property. *J. Phys. Chem. C* 2007, **111**, 13659–13664.

6. Wang, X., Liu, H., Wang, J., Chang, L., Song, N., Yan, Z., & Wan, X. Additive-free solvothermal preparation, characterization, and photocatalytic activity of 3D butterfly-like BiVO<sub>4</sub>. *Res. Chem. Intermed.* 2015, **41**, 2465–2477.
7. Rather, R. A., Mehta, A., Lu, Y., Valant, M., Fang, M., & Liu, W. Influence of exposed facets, morphology and hetero-interfaces of BiVO<sub>4</sub> on photocatalytic water oxidation: A review. *Int. J. Hydrogen Energy* 2021, **46**, 21866–21888.
8. Wan, Y., Wang, S., Luo, W. & Zhao, L. Impact of preparative pH on the morphology and photocatalytic activity of BiVO<sub>4</sub>. *Int. J. Photoenergy* **2012**, 1–7.
9. Zhao, J., Yan, J., Jia, H., Zhong, S., Zhang, X., & Xu, L. BiVO<sub>4</sub>/g-C<sub>3</sub>N<sub>4</sub> composite visible-light photocatalyst for effective elimination of aqueous organic pollutants. *J. Mol. Catal. A Chem.* 2016, **424**, 162–170.
10. Xi, G. & Ye, J. Synthesis of bismuth vanadate nanoplates with exposed {001} facets and enhanced visible-light photocatalytic properties. *Chem. Commun.* 2010, **46**, 1893–1895.
11. Su, J., Guo, L., Yoriya, S. & Grimes, C. A. Aqueous growth of pyramidal-shaped BiVO<sub>4</sub> nanowire arrays and structural characterization: application to photoelectrochemical water splitting. *Cryst. Growth Des.* 2010, **10**, 856–861.
12. Hardcastle, F. D. & Wachs, I. E. Determination of vanadium-oxygen bond distances and bond orders by Raman spectroscopy. *J. Phys. Chem.* 1991, **95**, 5031–5041.
13. Sandhya Kumari, L., Rao, P. P., Radhakrishnan N. P. A., James, V., Sameera, S., & Koshy, P. Brilliant yellow color and enhanced NIR reflectance of monoclinic BiVO<sub>4</sub> through distortion in VO<sub>4</sub><sup>3-</sup> tetrahedra. *Sol. Energy Mater. Sol. Cells* 2013, **112**, 134–143.
14. He, X., Zhang, C. & Tian, D. The structure, vibrational spectra, and thermal expansion study of AVO<sub>4</sub> (A=Bi, Fe, Cr) and Co<sub>2</sub>V<sub>2</sub>O<sub>7</sub>. *Materials (Basel)*. 2020, **13**, 1628.
15. Walsh, A., Yan, Y., Huda, M. N., Al-Jassim, M. M. & Wei, S.-H. Band edge electronic structure of BiVO<sub>4</sub>: elucidating the role of the Bi s and V d orbitals. *Chem. Mater.* 2009, **21**, 547–551.
16. Bhakta, A. K., Detriche, S., Kumari, S., Hussain, S., Martis, P., Mascarenhas, R. J., Delhalle, J., & Mekhalif, Z. Multi-wall carbon nanotubes decorated with bismuth oxide nanocrystals using infrared irradiation and diazonium

- Chemistry. *J. Inorg. Organomet. Polym. Mater.* 2018, **28**, 1402–1413.
17. Zalecki, R., Woch, W. M., Kowalik, M., Kołodziejczyk, A. & Gritzner, G. Bismuth valence in a  $Tl_{0.7}Bi_{0.3}Sr_{1.6}Ba_{0.4}CaCu_2O_y$  superconductor from x-ray photoemission spectroscopy. *Acta Phys. Pol. A* 2010, **118**, 393–395.
  18. Kamble, G. S. & Ling, Y.-C. Solvothermal synthesis of facet-dependent  $BiVO_4$  photocatalyst with enhanced visible-light-driven photocatalytic degradation of organic pollutant: assessment of toxicity by zebrafish embryo. *Sci. Rep.* 2020, **10**, 12993.
  19. Liu, G., Wang, X., Liu, X., Liu, G., Cui, P., Xu, S., Zhang, C., Liu, M., & Chen, Y. One-step synthesis of a novel Z-scheme  $m-Bi_2O_4/Bi_2O_{4-x}$  heterojunction for enhanced degradation of organic dyes and phenol under visible light. *J. Mater. Sci.* 2020, **55**, 10453–10465.
  20. Cao, X., Zhao, X., Hu, J. & Chen, Z. First-principles investigation of the electronic properties of the  $Bi_2O_4(101)/BiVO_4(010)$  heterojunction towards more efficient solar water splitting. *Phys. Chem. Chem. Phys.* 2020, **22**, 2449–2456.
  21. Ma, M., Xing, Z., Zhu, X., Jiang, P., Wang, X., Lin, H., An, Y., Su, H., & Yang, S. Interface modulation of  $BiVO_4$  based photoanode with  $Bi(III)Bi(V)O_4$  for enhanced solar water splitting. *J. Catal.* 2020, **391**, 513–521.
  22. Yaw, C. S., Ruan, Q., Tang, J., Soh, A. K. & Chong, M. N. A Type II n-n staggered orthorhombic  $V_2O_5$ /monoclinic clinobisvanite  $BiVO_4$  heterojunction photoanode for photoelectrochemical water oxidation: Fabrication, characterisation and experimental validation. *Chem. Eng. J.* 2019, **364**, 177–185.
  23. Chen, L. & Feng, X. Synthesis and characterization of  $V_2O_5/BiVO_4$  cake-like microstructures. *J. Aust. Ceram. Soc.* 2019, **55**, 1067–1074.
  24. Chen, L., Chen, Y., Miao, L., Gao, Y. & Di, J. Photocurrent switching effect on  $BiVO_4$  electrodes and its application in development of photoelectrochemical glucose sensor. *J. Solid State Electrochem.* 2020, **24**, 411–420.
  25. Anon, 2021. Standard Reduction Potentials by Element. Available at: <https://chem.libretexts.org/@go/page/6649> [Accessed January 12, 2022].
  26. Singh, Shiv Prakash and Basudeb Karmakar. “A New Synthesis Approach and Properties of Bismuth Coated Spherical to Hexagonal Silver Nanoparticles in Dichroic Ag : Bismuth Glass Nanocomposites.” 2011, 1-36.

27. Armstrong, D. A., Huie, R. E., Lyman, S., Koppenol, W. H., Merényi, G., Neta, P., Stanbury, D. M., Steenken, S., & Wardman, P. Standard electrode potentials involving radicals in aqueous solution: inorganic radicals (IUPAC Technical Report). *Pure Appl. Chem.* 2015, **87**, 1139–1150 (2015).
28. Li, J., Jiang, M., Zhou, H., Jin, P., Cheung, K. M. C., Chu, P. K., & Yeung, K. W. K. Vanadium Dioxide Nanocoating Induces Tumor Cell Death through Mitochondrial Electron Transport Chain Interruption. *Glob. Challenges* 2019, **3**, 1800058.
29. Yao, X., Zhao, X., Hu, J., Xie, H., Wang, D., Cao, X., Zhang, Z., Huang, Y., Chen, Z., & Sritharan, T. The Self-Passivation Mechanism in Degradation of BiVO<sub>4</sub> Photoanode. *iScience* 2019, **19**, 976–985.
30. Kraljić, I. & Trumbore, C. N. p-Nitrosodimethylaniline as an OH Radical Scavenger in Radiation Chemistry 1. *J. Am. Chem. Soc.* 1965, **87**, 2547–2550.
31. Muff, J., Bennedsen, L. R. & Søgaard, E. G. Study of electrochemical bleaching of p-nitrosodimethylaniline and its role as hydroxyl radical probe compound. *J. Appl. Electrochem.* 2011, **41**, 599–607.
32. Baxendale, J. H. & Khan, A. A. The pulse radiolysis of p-nitrosodimethylaniline in aqueous solution. *Int. J. Radiat. Phys. Chem.* 1969, **1**, 11–24.
33. Wang, Y., Li, J., Guo, L., Zhang, B., Hou, W., & Xu, X. Mixed-phase BiVO<sub>4</sub> nanosheet achieving enhanced photoelectrocatalytic performance. *Micro Nano Lett.* 2020, **15**, 586–589.

## Chapter 7 - Conclusions and future work

### 7.1 Conclusions

The overall aim of this research was to explore the different materials as photocatalysts for water treatment and disinfection, and to correlate their physicochemical and photoelectrochemical properties to the photocatalytic activity. In this aim, two semiconductors, *i.e.*, graphitic carbon nitride (g-C<sub>3</sub>N<sub>4</sub>) and bismuth vanadate (BiVO<sub>4</sub>) were investigated as photocatalysts for their synthesis, characterization, and photocatalytic applications.

The objectives established at the beginning of the research were all met in same order to fulfil the aim and are discussed in depth in chapter 4, chapter 5, and chapter 6. Their overall conclusion are as follows:

In chapter 4, bulk and exfoliated g-C<sub>3</sub>N<sub>4</sub> samples were prepared by a simple thermal polymerization of various precursors *i.e.*, thiourea, dicyandiamide, melamine, and urea at different combinations of reaction conditions. All the obtained g-C<sub>3</sub>N<sub>4</sub> samples were characterized for their physicochemical properties by wide characterisation techniques such as XRD, FTIR, Raman, BET, and DRS. The prepared samples were compared with each other for their structural, optical, and morphological properties. The XRD patterns of melamine-derived samples at different temperatures suggested that melamine could not be fully transformed from the melem phase to the melon phase (which is elementary unit of g-C<sub>3</sub>N<sub>4</sub>) until the calcination temperature was higher than 500°C. There was a peak shift from 27.3° to 27.8° with increase in temperature indicates a structural contraction along the layer stacking direction, probably as a result of a more prolonged condensation of the carbon nitride chains at higher temperature. Increase in calcination temperature from 510°C to 650°C led to

increase in surface area from  $9.9 \text{ m}^2 \text{ g}^{-1}$  to  $33.1 \text{ m}^2 \text{ g}^{-1}$  and decrease in band gap energies from 2.75 eV to 2.54 eV, hence more available active sites, and increased light absorption (from 450 nm to 500nm) which may improve the photocatalytic activity of g-C<sub>3</sub>N<sub>4</sub>. A physical colour change from light yellow to dark yellow was also observed with increasing temperature which also represented the improved absorption in the visible light region. Increase in temperature also led to the low mass yield for final product *i.e.*, 51.1% (at 510°C), 50.2% (at 545°C), 39.1% (at 580°C) and 37.2% (at 650°C). An approximate linear relationship ( $E_g(T) = 3.5016 - 0.0015T$ ) was established between temperature and band gap energy of g-C<sub>3</sub>N<sub>4</sub>.

The urea-derived g-C<sub>3</sub>N<sub>4</sub> displayed highest specific surface area ( $52.7 \text{ m}^2 \text{ g}^{-1}$ ) than other precursor's mediated g-C<sub>3</sub>N<sub>4</sub> samples due to high evolution of ammonia and CO<sub>2</sub> gas during pyrolysis. In g-C<sub>3</sub>N<sub>4</sub> samples prepared at 545°C for 4 h, the efficiency or mass yield of precursor to g-C<sub>3</sub>N<sub>4</sub> conversion was found to be 47.5% (melamine), 33.3% (thiourea), and 4.7% (urea). Very low mass yield for urea is due to the rapid degree of polymerization and condensation. Moreover, above 550°C there was no product found in case of urea as it decomposed completely above this temperature. After exfoliation surface area and bandgap energy of exfoliated g-C<sub>3</sub>N<sub>4</sub> samples were increased compared to their bulk counterpart. Surface area increased from  $11.1 \text{ m}^2 \text{ g}^{-1}$  to  $70.4 \text{ m}^2 \text{ g}^{-1}$  (melamine), from  $39.1 \text{ m}^2 \text{ g}^{-1}$  to  $117.9 \text{ m}^2 \text{ g}^{-1}$  (thiourea) and from  $52.7 \text{ m}^2 \text{ g}^{-1}$  to  $183.9 \text{ m}^2 \text{ g}^{-1}$  (urea) whereas bandgap increased from 2.69 to 2.70 eV (melamine), from 2.56 to 2.69 eV (thiourea) and from 2.74 to 2.98 eV (urea) compared to their bulk counterpart prepared at 545°C for 4 h. Samples having favourable physicochemical properties were tested for their photocatalytic performance by degrading model organic pollutant, phenol, and *E. coli* inactivation under UV-Vis irradiation. The thiourea and urea derived exfoliated g-C<sub>3</sub>N<sub>4</sub> samples

exhibited better phenol degradation with reaction rates (rate constants) of  $1.83 \times 10^{-7}$  mol L<sup>-1</sup> min<sup>-1</sup> (TCN-exf) and  $2.14 \times 10^{-7}$  mol L<sup>-1</sup> min<sup>-1</sup> (UCN-exf) and *E. coli* disinfection (~3-log reduction) performance than all the other samples due to their high specific surface area which could be correlated with an increase in the available active sites for photocatalytic reactions. However, P25-TiO<sub>2</sub> was still outperformed the C<sub>3</sub>N<sub>4</sub> for both phenol degradation ( $k=4.48 \times 10^{-7}$  mol L<sup>-1</sup> min<sup>-1</sup>) and total *E. coli* inactivation (~6-log reduction) within 180 min.

The experimental data of *E. coli* inactivation by each g-C<sub>3</sub>N<sub>4</sub> sample were fitted with the nine models of the GInaFiT tool to get the inactivation rate. After the comparison of obtained parameters (*i.e.*, sum of squared errors (SSE), root mean sum of squared errors (RMSE), the coefficient of determination (R<sup>2</sup>) *etc.*), Weibull model was found to be the best suit for light control and MCN-exf sample, while double Weibull model was for TCN-exf and UCN-exf samples. Urea derived exfoliated g-C<sub>3</sub>N<sub>4</sub> showed faster first log reduction than other exfoliated samples (U<T<M). However, the photocatalytic efficiency demonstrated by all the g-C<sub>3</sub>N<sub>4</sub> samples is still far behind the photocatalytic efficiency of P25-TiO<sub>2</sub> tested for phenol degradation and *E. coli* disinfection.

In chapter-5, the poor photocatalytic performance of exfoliated g-C<sub>3</sub>N<sub>4</sub> was investigated through its physiochemical properties *i.e.*, bandgap energy, band edge positions, work function, photocurrent, open circuit photopotential, and flat band potential, *etc.* by EDX, DRS, XPS/UPS, and photoelectrochemistry. EDX analysis revealed the C/N ratio to be 0.72 in sample matrix and a uniform distribution of nitrogen (N) and carbon (C) also indicated the purity of synthesized material. Using the bandgap energy (2.68 eV) obtained from Tauc plot and the work function (4.28 eV) obtained from UPS study, the band edge energies for g-C<sub>3</sub>N<sub>4</sub> on the NHE scale

was calculated to be +1.51 eV (VB edge) and -1.17 eV (CB edge). The analysis of UPS results also showed that Fermi level of g-C<sub>3</sub>N<sub>4</sub> is approximately in the middle of the forbidden gap, indicating that it behaves as an intrinsic semiconductor.

A very small photocurrent (<1  $\mu\text{A}\cdot\text{cm}^{-2}$ ) and photoelectrochemical photocurrent switching (PEPS) effect was observed in photoelectrochemical results. The LSV results depicted that anodic (or positive) photocurrent switched to cathodic (or negative) photocurrent at -0.68 V (vs. SCE) or -0.44 V (vs. NHE) which again converted to anodic photocurrent at +0.05 V (vs. SCE) or +0.29 V (vs. NHE) with sweeping the bias from -1.0 to +1.0 V. Thus g-C<sub>3</sub>N<sub>4</sub> photoelectrode behaved as a p-type semiconductor in the potential range of -0.68 V to +0.05 V, beyond this region it behaved as n-type semiconductor. PEPS behavior was further confirmed by chronoamperometry and spectral response. The open circuit potential for g-C<sub>3</sub>N<sub>4</sub> electrode was measured as -0.09 V (SCE) and upon irradiation it behaved as a p-type semiconductor (positive shift of 0.28 V). The very slow change in open circuit potential indicated the slow charge separation and high surface recombination.

Electrochemical impedance spectroscopy results exhibited the high charge transfer resistance which inhibits the separation and migration of e<sup>-</sup>-h<sup>+</sup> pairs. Mott-Schottky plot had both positive and negative slope which also indicated the amphoteric nature of g-C<sub>3</sub>N<sub>4</sub>. Hence, position of Fermi level, slow change in open circuit potential and high charge transfer resistance restricts the separation and migration of charge carriers, resulting in small photocurrent and poor photocatalytic activity of g-C<sub>3</sub>N<sub>4</sub>. A schematic energy level diagram of the exfoliated g-C<sub>3</sub>N<sub>4</sub> was also proposed on the basis of obtained results from DRS, VBXPS, UPS and photoelectrochemical measurements.



In chapter 6, different morphologies of  $\text{BiVO}_4$  were synthesized using different methods and investigated for their physiochemical properties by FESEM, EDX, XRD, Raman, DRS, XPS, photoelectrochemical measurements and correlated to the photocatalytic activities. FESEM micrographs confirmed the sphere-like (BiV-1) and plate-like  $\text{BiVO}_4$  particles (BiV-2) which were synthesized by a hydrothermal method in a Parr reactor and pyramid/thorns-like morphology of  $\text{BiVO}_4$  (BiV-3) were vertically grown on FTO coated glass using seed-mediated method.  $\text{BiVO}_4$  spheres had an average diameter of about 2.5  $\mu\text{m}$ ,  $\text{BiVO}_4$  nano plates had a thickness of 30-70 nm, and  $\text{BiVO}_4$  pyramids/thrones had a length of 4.8  $\mu\text{m}$ , a diameter of 200-500 nm at the bottom and a tip of about 20-50 nm. The agglomeration of these thorns resulted in the formation of Sea urchin-like structures having an average diameter of 20-25  $\mu\text{m}$ .

XRD patterns and Raman spectra confirmed the formation of  $\text{BiVO}_4$ . The XRD patterns of BiV-1 and BiV-3 had only monoclinic  $\text{BiVO}_4$  phase while BiV-2 contained a mixed phase pattern including tetragonal zircon and monoclinic phases. The EDX analysis gave the ratio of At% of Bi:V to be almost 1:1 in BiV-1 (Bi – 22.2%, V – 21.2%) and BiV-2 (Bi – 24.6%, V- 24.6%) indicating the absence of other compounds however BiV-3 had 6% more Bi atoms than V (Bi – 20.7%, V – 14.8%) implying the presence of unreacted bismuth or other oxides in the sample. DRS spectra were transformed into Tauc plot using Kubelka-Munk function which provided the approximate bandgap of 2.45 eV (BiV-1), 2.47 eV (BiV-2), and 2.56 eV (BiV-3). XPS measurements were performed to determine the surface chemical composition and chemical states of the prepared  $\text{BiVO}_4$  samples. Interestingly, high-resolution spectrum of Bi 4f for BiV-1 and BiV-2 contained two sets of spin-orbit doublet peaks for the Bi 4f<sub>7/2</sub> (159.0, 160.0 eV) and Bi 4f<sub>5/2</sub> (164.3, 165.3 eV) indicating the presence of two Bi states ( $\text{Bi}^{3+}$  and  $\text{Bi}^{5+}$ ) due to some impurities such as oxides or carbonates

(*i.e.*, Bi<sub>2</sub>O<sub>4</sub>, NaBiO<sub>3</sub>). Likewise Bi 4f spectra of BiV-3 had three sets of spin-orbit doublet peaks suggesting the presence of other oxides along with BiVO<sub>4</sub>. Considering the EDX results (6% higher Bi atom) and deep XRD analysis it was concluded that the other oxide may be Bi<sub>2</sub>O<sub>4</sub> which contains mixed valence states in its structure as alternative arrangement of Bi<sup>3+</sup> and Bi<sup>5+</sup> states. The V 2p spectrum of BiV-3 also indicated the presence of V<sub>2</sub>O<sub>5</sub>.

BiV-1 displayed cathodic to anodic photocurrent switching at about +0.15 V (SCE) or +0.39 V (NHE). Surprisingly, nature of photocurrent for BiV-3 was changed with potential sweeping direction. It behaved as an n-type semiconductor (positive photocurrent) in the positive applied bias when sweeping the bias from negative to positive and vice versa. Prepared samples were also tested for their efficacy for the photocatalytic degradation of phenol but did not show any photocatalytic degradation of phenol.

To understand the non-photocatalytic activity by BiVO<sub>4</sub>, chemical probe study was performed by observing RNO photocatalytic discolouration to detect hydroxy radicals. RNO concentration is getting reduced with time for both BiV-1 and BiV-2 suggesting the generation of hydroxyl radicals. In 60 min, 27% discolouration of the yellow-coloured solution was observed for BiV-1, whereas it was 45% for BiV-2, indicating the generation of hydroxyl radicals. Despite producing <sup>•</sup>OH radicals, BiVO<sub>4</sub> did not show photocatalytic activity for phenol degradation, possibly due to its positive conduction band edge potential (~+0.5 V vs. NHE) which is not enough to reduce oxygen, so e<sup>-</sup>-h<sup>+</sup> recombination dominates, resulting in poor photocatalytic activity.

To summarize, this thesis provides the detailed insights into appropriate selection of precursors and reaction conditions for g-C<sub>3</sub>N<sub>4</sub> synthesis and their effect on physicochemical and photocatalytic performance of graphitic carbon nitride and

photocatalytic efficiency comparison for water treatment against P25-TiO<sub>2</sub>. Further, electronic and photoelectrochemical properties of exfoliated g-C<sub>3</sub>N<sub>4</sub> were investigated for finding out the reason behind its poor photocatalytic activity and a schematic energy band diagram was proposed. Last section was focused on BiVO<sub>4</sub> where different morphologies of BiVO<sub>4</sub> were synthesized using different methods and investigated for their physiochemical properties and correlated to the photocatalytic activities.

## 7.2 Future work and recommendations

The thesis attained the main objectives set out, by detailed investigation into the physiochemical properties of g-C<sub>3</sub>N<sub>4</sub> and BiVO<sub>4</sub>, as well as their correlation to photocatalytic water treatment. Considering the originality of this work, it should be seen as laying the foundation for future research in the field of photocatalytic water treatment, using g-C<sub>3</sub>N<sub>4</sub> and BiVO<sub>4</sub> as photocatalysts. However, there can be a plethora of potential follow up studies that can be adopted to elaborate new perspectives in this field for developing an effective visible light photocatalyst that can address energy and environmental issues in true sense. The future research directions that can be followed are as follows:

1. Even though urea-derived g-C<sub>3</sub>N<sub>4</sub> had the highest specific surface area in our research but one should avoid using urea as a precursor to g-C<sub>3</sub>N<sub>4</sub> because of it has very low efficiency in precursor to g-C<sub>3</sub>N<sub>4</sub> conversion. Also, it cannot be heated more than 550°C.
2. In this research, exfoliated g-C<sub>3</sub>N<sub>4</sub> showed better photocatalytic activity than bulk g-C<sub>3</sub>N<sub>4</sub> because exfoliation increases specific surface area drastically, thus one can explore the different methods to exfoliate g-C<sub>3</sub>N<sub>4</sub> for further

increase in specific surface area. Multiple methods have been reported so far for exfoliation of carbon nitride such as chemical exfoliation,<sup>1</sup> ultrasonic exfoliation,<sup>2</sup> gas bubble exfoliation,<sup>3</sup> etc. which can be employed for the preparation of single layer g-C<sub>3</sub>N<sub>4</sub> and may enhance the photocatalytic of g-C<sub>3</sub>N<sub>4</sub>.

3. We encountered difficulties in preparing electrodes of g-C<sub>3</sub>N<sub>4</sub> and BiVO<sub>4</sub> for photoelectrochemical measurements because of their poor dispersibility in water and organic solvents, as well their poor adhesion with FTO coated glass, thus new approaches need to explore for addressing the issue. Exfoliation of g-C<sub>3</sub>N<sub>4</sub> improves its dispersibility in water and organic solvents, hence exfoliating g-C<sub>3</sub>N<sub>4</sub> will resolve the dispersibility issue.
4. It has been established that g-C<sub>3</sub>N<sub>4</sub> and BiVO<sub>4</sub> as a single are not an effective photocatalyst because of not having appropriate band edge positions. However, g-C<sub>3</sub>N<sub>4</sub> has a very negative conduction band and BiVO<sub>4</sub> has a very positive valance band which is favourable for photocatalytic water treatment, thus a heterojunction formed with them should be investigated. Although It's been observed in our lateral studies that physical mixing of these materials does not accelerate their photocatalytic activities. Therefore in-situ deposition on FTO using electrodeposition and hydrothermal method, or some other preparation method such as mixing in an organic solvent such as methanol under ultrasonication, should be explored.<sup>4-7</sup>
5. In our case, pure BiVO<sub>4</sub> was not obtained, there were some impurities of other oxides present which might affect photocatalytic activities of BiVO<sub>4</sub>. Thus, it is recommended to prepare pure BiVO<sub>4</sub> to prevent hindrances due to impurities. Purity of BiVO<sub>4</sub> can be controlled by Bi/V ratio in the solution. In

situ deposition of BiVO<sub>4</sub> on FTO coated glass using hydrothermal method is also a better option to improve the purity of BiVO<sub>4</sub>. The final product should be given multiple washes by distilled H<sub>2</sub>O followed by methanol to remove soluble or unreacted solids.

6. Although in this work we tested photocatalysts in suspension form but using a photocatalyst suspension means that the catalyst must be removed post treatment, adding cost and complexity. Further work might consider the immobilisation of the photocatalyst on a supporting substrate such as FTO as we mentioned in the above points.

### 7.3 References

1. Zhang, M., Yang, Y., An, X., Zhao, J., Bao, Y., & Hou, L. Exfoliation method matters: The microstructure-dependent photoactivity of g-C<sub>3</sub>N<sub>4</sub> nanosheets for water purification. *J. Hazard. Mater.* 2022, **424**, 127424.
2. Ma, T., Bai, J., Liang, H., Wang, J. & Li, C. An efficient method for assembling layered g-C<sub>3</sub>N<sub>4</sub> nanosheets grow on 1D pore channels carbon fibers as a composite photocatalyst by ultrasound-assisted exfoliation and hydrothermal method. *Vacuum* 2016, **134**, 130–135.
3. Si, H., Deng, Q., Yin, C., Zhou, J., Zhang, S., Zhang, Y., Liu, Z., Zhang, J., Zhang, J., & Kong, J. *et al.* Gas exfoliation of graphitic carbon nitride to improve the photocatalytic hydrogen evolution of metal-free 2D/2D g-C<sub>3</sub>N<sub>4</sub>/graphdiyne heterojunction. *J. Alloys Compd.* 2020, **833**, 155054.
4. Rathi, V., Panneerselvam, A. & Sathiyapriya, R. A novel hydrothermal induced BiVO<sub>4</sub>/g-C<sub>3</sub>N<sub>4</sub> heterojunctions visible-light photocatalyst for effective elimination of aqueous organic pollutants. *Vacuum* 2020, **180**, 109458.
5. Safaei, J., Ullah, H., Mohamed, N. A., Mohamad Noh, M. F., Soh, M. F., Tahir, A. A., Ahmad Ludin, N., Ibrahim, M. A., Wan Isahak, W. N. R., & Mat Teridi, M. A. Enhanced photoelectrochemical performance of Z-scheme g-C<sub>3</sub>N<sub>4</sub>/BiVO<sub>4</sub> photocatalyst. *Appl. Catal. B Environ.* 2018, **234**, 296–310.
6. Sun, Z., Yu, Z., Liu, Y., Shi, C., Zhu, M., & Wang, A. Construction of 2D/2D

- BiVO<sub>4</sub>/g-C<sub>3</sub>N<sub>4</sub> nanosheet heterostructures with improved photocatalytic activity. *J. Colloid Interface Sci.* **533**, 251–258 (2019).
7. Dong, S., Lee, G. J., Zhou, R. & Wu, J. J. Synthesis of g-C<sub>3</sub>N<sub>4</sub>/BiVO<sub>4</sub> heterojunction composites for photocatalytic degradation of nonylphenol ethoxylate. *Sep. Purif. Technol.* 2020, **250**, 117202.